Archives of Environmental Protection

Vol. 52
3
2026



Polish Academy of Sciences

Institute of Environmental Engineering

Committee of Environmental Engineering

Archives of Environmental Protection

Vol. 52
3
2026

Polish Academy of Sciences
Institute of Environmental Engineering
and
Committee of Environmental Engineering

Archives of Environmental Protection is the oldest Polish scientific journal of international scope that publishes articles on engineering and environmental protection. Impact Factor of the journal, according to Clarivate Analytics Journal Citation Reports®, is **1.8** (June 2026).

ISSN 2083-4772, e-ISSN 2083-4810

Editor-in-Chief:
Czesława Rosik-Dulewska
iD 0000-0003-2698-5437
czeslawa.dulewska@ipispan.edu.pl

Editors:
Michał Bodzek
iD 0000-0001-9534-7426
michal.bodzek@ipispan.edu.pl

Joanna Surmacz-Górska
iD 0000-0002-1805-2189
joanna.s.gorska@polsl.pl

Wioletta Rogula-Kozłowska
iD 0000-0002-4339-0657
wioletta.rogula@ipispan.edu.pl

Assistant Editor (Secretary):
Jerzy Szdzuj
aep.szdzuj@ipispan.edu.pl

Address for Correspondence:
Institute of Environmental Engineering
of the Polish Academy of Sciences
ul. M. Skłodowskiej-Curie 34, 41-819 Zabrze, Poland
aep@ipispan.edu.pl

Editorial Board (with ORCID):
President:
Piotr Koszelnik
iD 0000-0001-6866-7432
pkoszel@prz.edu.pl

Members:
Adamowski Jan Franklin (Canada) 0000-0002-1242-3364
Alonso Rosa M. (Spain) 0000-0001-9046-6602
Banasik Kazimierz (Poland) 0000-0002-7328-461X
Van der Bruggen Bart (Belgium) 0000-0002-3921-7472
Corral Mosquera Anuska (Spain) 0000-0003-1925-680X
Czechowski Piotr Oskar (Poland) 0000-0001-7193-2022
Frenzel Wolfgang (Germany) 0000-0002-7697-2514
Bamwenda Gratian R.(Tanzania)
Huszar Peter (The Czech Republic) 0000-0003-2954-8347
Kulig Andrzej (Poland) 0000-0001-6122-3169
Kabsch-Korbutowicz Malgorzata (Poland)
0000-0002-8188-042X
Kyzioł-Komosińska Joanna (Poland) 0000-0001-8777-4989
Michalski Rajmund (Poland) 0000-0003-4441-7409
Miksch Korneliusz (poland) 0000-0002-2192-8647
Misiewicz Paula (United Kingdom) 0000-0003-1909-285X
Mokrzycki Eugeniusz (Poland) 0000-0003-4080-3660
Nahorski Zbigniew (Poland) 0000-0002-2340-8020
Nakamura Takashi (Japan) 0000-0002-1864-1143
Oleszek Sylwia (Poland/Japan) 0000-0001-6660-9992
Pawłowski Lucjan (Poland) 0000-0003-0628-6735
Reizer Magdalena (Poland) 0000-0002-3572-6050
Rostkowski Pawel (Norway) 0000-0001-9778-4283
Soldan Premysl (The Czech Republik) 0000-0002-8892-5117
Ultra Venecio (Philippines) 0000-0002-7980-4137
Wiatkowski Mirosław (Poland) 0000-0002-5155-0593
Winnicki Tomasz (Poland) 0000-0002-5859-7335
Włodarczyk-Makuła Maria (Poland) 0000-0002-3978-2420

Archives of Environmental Protection is indexed and abstracted in the following scientific services:
AGRICOLA, Arianta, Baidu, BazTech, BIOSIS Citation Index, CABI, CAS, EBSCO, Engineering Village, GeoRef, Google Scholar, Index Copernicus, Journal Citation Reports™, Journal TOCs, KESLI-NDSL, Naviga, ProQuest, SCOPUS, Reaxys, Ulrich's Periodicals Directory, WorldCat, Web of Science)

Website:
www.ipis.pan.pl/ipispan/pl/wydawnictwa/archives-of-environmental-protection.
Full-text articles are also available on Electronic Library Polish Academy of Sciences platform: http://journals.pan.pl/aep

Cover photo: Czesława Rosik-Dulewska

© Copyright by Polish Academy of Sciences, Institute of Environmental Engineering of the Polish Academy of Sciences, Zabrze, Poland 2025
Printed in Poland
Skład, projekt okładki, druk i oprawa: Oficyna Drukarska Jacek Chmielewski, 01-142 Warszawa, ul. Sokołowska 12A, tel. +48 22 632 83 52

Archives of Environmental Protection

Vol. 52
3
2026

Table of Contents

Effects of *Acinetobacter johnsonii* and *Rhodotorula mucilaginosa* on the migration and transformation of antimony in soil-pak choi systems. Linqiang Tian, Jiuqin Xian, Kun Liu, Qian Wang, Shixue Mei, Aijiang Yang, Wanping Bian, Aping Niu 3

Effect of a dehumidifier on the solar drying process of biomixtures based on sewage sludge. Małgorzata Helena Makowska, Sebastian Kujawiak, Damian Janczak, Ariel Antonowicz, Bartosz Kucharski 16

Comparative study of acetaminophen and 4-methoxyphenol toxicity. Marzena Matejczyk, Krzysztof Kurek, Andrzej Kaźmierczak, Piotr Ofman, Józefa Wiater, Ruslan Oblap, Paweł Kondzior, Ewelina Omelianowicz 26

Study on directional regulation of biomass pyrolysis gas coupling for hydrogen-rich fuel gas production over hydrophobic NiCo-CeO2/F-Ti3C2 catalyst. Chen Jihao, Miao Pengjie 34

Comparison of surface water treatment efficiency using integrated pressure-driven membrane processes and conventional treatment systems. Małgorzata Kabsch-Korbutowicz, Małgorzata Wolska, Marek Mołczan, Wojciech Adamski, Jacek Adam Wiśniewski, ... 45

Two decades of research on antibiotic resistance genes in global wastewater treatment systems: Critical knowledge gaps and pathways toward integrated risk management. Zhizhen Yin, Fengyang Han, Qinhui He 60

Biomass-derived activated carbons from date pits and spirulina for CO_2 and water vapor adsorption: A comparative uptake ratio study. Shaima Mahdi Al-Bazzaz, Janaen Y. Al-Saeedi, Anwar Abood AbdulHassn Abbood, Harith Y. Mahmood. 76

Development of a low-cost dissolved oxygen estimation model using calibrated arduino-based sensors. Merve Sürmen, Mehmet Kazım Yetik 88

A feasibility assessment of remediating copper contaminated soils with construction wastes. Rixiu Zhou, Quan Zhou, Chaozhen Xie, Zhenzhou Zhang, Furong Wu, Qiming Li, Fangze Shang, Yifan Hu, Zhengjie Zhu, Dianpeng Li, Shuqing An 100

Hydrodynamic cavitation as a pretreatment to enhance organic matter solubilization in orange waste prior to anaerobic digestion. Aleksandra Szaja, Agnieszka Montusiewicz, Sylwia Pasieczna-Patkowska, Elżbieta Grządka, Jerzy Montusiewicz, Magdalena Lebiocka 108

Research on the properties of waste from streets cleaning. Anna Wassilkowska, Agnieszka Generowicz, Anna Młyńska 121

© Copyright by Polish Academy of Sciences, Institute of Environmental Engineering of the Polish Academy of Sciences, Zabrze, Poland 2026

Archives of Environmental Protection
Vol. 52 no.3 pp. 3–15

PL ISSN 2083-4772
DOI: 10.24425/aep.2026.284



© 2026. The Author(s). This is an open-access article distributed under the terms of the Creative Commons Attribution-ShareAlike 4.0 International Public License (CC BY SA 4.0, https:// creativecommons.org/licenses/by-sa/4.0/legalcode), which permits use, distribution, and reproduction in any medium, provided that the article is properly cited.

Effects of *Acinetobacter johnsonii* and *Rhodotorula mucilaginosa* on the migration and transformation of antimony in soil-pak choi systems

Linqiang Tian[1] & Jiuqin Xian[1], Kun Liu[1], Qian Wang[1], Shixue Mei[1], Aijiang Yang[1], Wanping Bian[2], Aping Niu[1]*

& These authors contributed equally to this work and should be considered co-first authors.
[1] College of Resources and Environmental Engineering, Guizhou Karst Environmental Ecosystems Observation and Research Station, Ministry of Education, Key Laboratory of Karst Georesources and Environment, Ministry of Education, Guizhou University, Guiyang 550025, China.
[2] Chongqing Institute of Green and Intelligent Technology, Chinese Academy of Sciences, Chongqing, 400714, China.

*Corresponding author. E-mail: apniu@gzu.edu.cn

Keywords: Antimony accumulation; pak choi; microbial remediation; *A. johnsonii; R. mucilaginosa*

Abstract: Soil antimony (Sb) contamination poses a serious threat to the safe production of leafy vegetables and to human health. In this study, two Sb-resistant strains, *Acinetobacter johnsonii* and *Rhodotorula mucilaginos*a, were evaluated for their remediation potential in Sb-contaminated soil using pot experiments with pak choi (*Brassica chinensis L.*) under aerobic conditions. The results demonstrated that both strains significantly increased pak choi biomass, root activity, and photosynthetic pigment content through plant growth-promoting traits such as nitrogen fixation and phosphate solubilization. More importantly, they reduced Sb accumulation in pak choi by promoting the formation of residual and Fe-Mn oxide-bound Sb fractions while inhibiting the formation of humic acid-bound Sb. Notably, *R. mucilaginosa* outperformed *A. johnsonii* in both growth promotion and Sb immobilization. The superior performance of *R. mucilaginosa* is attributed to its unique ability to restructure the rhizosphere fungal community, enriching beneficial taxa such as *Mortierella and Pichia*, thereby synergistically enhancing plant resilience to Sb stress. This study provides new insights into the differential mechanisms of bacterial versus fungal remediation of Sb-contaminated soils under aerobic conditions and offers a theoretical basis for developing targeted microbial remediation strategies. The modified membrane exhibits an improved permeability of 54.4% and an average pore size of 50 nm. The ceramic membrane shows promising removal efficiency of Texas dye. Reusability tests of the manufactured membrane demonstrate stable membrane performance over five continuous filtration cycles. The membranes are cleaned by backwashing, and removal tests are conducted for further nine cycles. The membrane maintains high removal efficiency of Texas dye, as measured in chemical oxygen demand (COD), as well as hardness, during the first five cycles. This research highlights the potential of ceramic membranes for efficient, low-pressure dye removal and wastewater treatment, with enhanced durability and reusability.

Introduction

Antimony (Sb) is a toxic metalloid extensively used in the manufacturing of industrial products and has become the ninth most mined metal globally. However, Sb concentrations in soil and water bodies have increased due to natural processes and human activities such as ore mining and smelting (Li et al., 2026). Studies have shown significantly elevated Sb levels in the soil of mining areas, smelters, and shooting ranges. For instance, Sb concentrations in mining areas and surrounding soils often reach hundreds of times higher than background levels (He et al., 2025). Even agricultural and forest soils are affected by Sb contamination. Sb exhibits biotoxicity and carcinogenicity and tends to accumulate in crops. Sb contamination in farmland soil can inhibit crop growth and development (Tang et al., 2025) and pose risks to human health through the food chain, potentially inducing severe diseases such as liver disorders, cardiovascular diseases, respiratory illnesses, and cancer (Roldán et al., 2025). Therefore, it is of great significance to restore Sb-contaminated farmland.

Traditional remediation techniques for heavy metals, including physical and chemical methods, are often costly, labor-intensive, and may cause secondary pollution (Senila

et al., 2026). In contrast, bioremediation technologies have garnered widespread attention due to their low cost, operational simplicity, environmental compatibility, and strong sustainability (Ogunsola et al., 2025). Among these, microorganism-based remediation strategies have demonstrated promising application prospects in heavy metal pollution control in recent years. Microorganisms can mediate the transformation and immobilization of heavy metals through various mechanisms, such as biosorption, bioprecipitation, redox reactions, and extracellular complexation, thereby reducing their bioavailability and toxicity to plants (Pradhan et al., 2025). Furthermore, certain functional microorganisms can enhance plant growth under heavy metal stress, promoting the sustainable development of agricultural production.

Acinetobacter johnsonii, belonging to the genus *Acinetobacter*, is a common Gram-negative bacterium widely distributed in soil, water, and on plant surfaces. It can secrete various extracellular enzymes and organic acids, and possess nitrogen-fixing and phosphate-solubilizing capabilities, thereby promoting plant growth (Timková et al., 2023). *Rhodotorula mucilaginosa* (abbreviated as *R. mucilaginosa*), a unicellular eukaryote of the genus *Rhodotorula*, possesses remarkable environmental adaptability and is ubiquitously present in diverse ecosystems. It features a complex cell wall structure rich in functional groups, which contributes to its resistance to heavy metal stress (Zhang et al., 2024). Moreover, *R. mucilaginosa* can synthesize antioxidants that assist plants in scavenging reactive oxygen species (ROS) induced by heavy metals, thereby alleviating oxidative damage. Previous studies have shown that these two microorganisms exhibit promising remediation potential for heavy metal pollution, such as lead, cadmium, and arsenic (Angeles de Paz et al., 2023; Timková et al., 2023). However, research on their potential for Sb pollution remediation remains limited, necessitating further exploration of their practical remediation efficacy and underlying mechanisms for the remediation of Sb-contaminated soils.

The toxicity, mobility, and bioavailability of Sb in soil are closely related to environmental conditions, which affect the phytotoxicity and accumulation in plants. Among all various environmental factors, anaerobic and aerobic conditions have different effects on the Sb phytotoxicity. However, most previous studies have mainly focused on Sb accumulation in rice and the use of exogenous microorganisms to remediate Sb accumulation in rice, which is typically grown under anaerobic conditions (Long et al., 2023). There remains a lack of research on the use of exogenous microorganisms to remediate Sb accumulation in crops under aerobic conditions. Leafy vegetables are considered high risk crops for Sb accumulation. Pak choi (*Brassica campestris* L. ssp. *chinensis*) is one of the most common leafy vegetables, with a short growth cycle, and is typically grown under aerobic conditions. The Sb enrichment coefficient of cabbage is 0.01-0.1, which indicates the Sb absorption capacity of pak choi. To understand the environmental behavior and accumulation mechanism of Sb in soil-crops systems under aerobic conditions, pak choi, which is widely cultivated in China, is considered an ideal indicator vegetable for assessing Sb migration and transformation in soil-crops systems under aerobic conditions (Chen et al., 2025).

In our previous study, *A. johnsonii* and *R. mucilaginosa*, which exhibited high Sb-resistance, were screened from Sb-containing wastewater, and both strains were able to transform Sb(III) into Sb_2O_3 (Shi et al., 2025; Yang et al., 2024). They were used as functional microorganisms to investigate the bioavailability of Sb in soil-pak choi systems under aerobic conditions and their potential for remediating Sb-contaminated farmland. A comprehensive analysis was conducted to evaluate the remediation capabilities of these two microorganisms in Sb-contaminated farmland through indoor pak choi pot experiments. Different microbial treatment groups were established, and the growth indicators and Sb accumulation of pak choi were measured. The plant growth-promoting mechanisms were evaluated by measuring nutritional and growth-promoting indicators. The Sb accumulation mechanism was investigated by measuring Sb speciation and contents, as well as the microbial community structure, in the rhizosphere soil. This study aims to evaluate the remediation effects of *A. johnsonii* and *R. mucilaginosa* in an antimony-contaminated soil-pak choi system and to test the following hypotheses: both strains promote pak choi growth through plant growth-promoting traits such as nitrogen fixation and phosphate solubilization, while reducing antimony accumulation in pak choi by increasing the proportions of iron-manganese bound and residual antimony fractions in the soil. Moreover, *R. mucilaginosa* exhibits superior growth-promoting and antimony-immobilizing capabilities due to its ability to reshape the rhizosphere fungal community and enrich beneficial fungi such as *Mortierella* and *Pichia*.

Materials and methods

Experimental materials and strains

The pak choi variety selected was "Yellow Heart Baby Cabbage" (*Brassica chinensis* L.), characterized by its short growth cycle and strong cold tolerance. For the pot experiment, antimony (Sb) was supplied using potassium antimony tartrate ($C_4H_4KO_7Sb \cdot 1/2H_2O$) with a purity of ≥99.0%, as the chemical source of Sb (Chongqing Chuandong Chemical Group Co., Ltd., Chongqing, China).

A. johnsonii was isolated from the bottom sediment of Lengshuigou Reservoir (107.86°E, 25.97°N) in Dushan County, Guizhou Province, by our research group, while *R. mucilaginosa* was obtained from antimony mine wastewater at the outlet of Dongfeng Antimony Mine (107.73°E, 25.75°N) in Dushan County, Guizhou Province. Both strains were identified as *A. johnsonii* and *R. mucilaginosa* based on their 16S rDNA sequences. All reagents used in this study were prepared with deionized water provided by EREE deionized water equipment (Shenzhen Yiliyuan Water Treatment Equipment Co., Ltd., Shenzhen, China).The deionized water had a conductivity of <0.1 μS/cm, and all chemicals used were of analytical grade or higher purity.

Pot experiment of pak choi

Pot experiments were conducted to investigate the effects of *A. johnsonii* and *R. mucilaginosa* on the growth and Sb accumulation of pak choi (*Brassica chinensis* L.) in soils contaminated with different levels of Sb. Plastic pots were used for the pot experiment. The soil was collected from farmland near Shilihetan in Huaxi District, Guiyang City, Guizhou Province. Surface soil (0–20 cm) was collected, naturally air-dried, and then crushed. The physicochemical properties of the original

soil for pak choi cultivation were determined, and the values were as follows: pH, 5.75; organic matter content, 4.76 $mg \cdot g^{-1}$; available nitrogen, 62.23 $mg \cdot kg^{-1}$; available potassium, 257.7 $mg \cdot kg^{-1}$; available phosphorus, 7.13 $mg \cdot kg^{-1}$; and background antimony concentration, 15.92 $mg \cdot kg^{-1}$. The crushed soil was sieved through a 100-mesh sieve to preliminarily remove impurities. The preprocessed soil was packed into rectangular pots (49 cm × 18 cm × 15 cm) at 7 kg per pot. Sb solutions prepared from potassium antimonyl tartrate ($C_4H_4KO_7Sb \cdot 1/2 H_2O$) were added to the soil and thoroughly mixed to achieve exogenous Sb concentrations of 10, 50, and 100 mg/kg. Each treatment group had three replicates, and the pots were aged in a greenhouse for 30 days.

The seeds of pak choi were surface-sterilized with 0.5% NaClO solution, followed by three rinses with deionized water. The pots planted with pak choi seed were placed in a greenhouse with a diurnal temperature cycle of 20–25 °C and a relative humidity of 50%. After the pak choi seeds developed into seedlings with complete root systems, seedlings of uniform size and height were selected and transplanted into pots containing Sb-treated soil aged for 30 days. One group was inoculated with *A. johnsonii* (AJ), and another group was inoculated with *R. mucilaginosa* (RM). The group without inoculation with either microorganism was used as the control to investigate the effects of *A. johnsonii* and *R. mucilaginosa* on the growth and Sb accumulation of pak choi under Sb stress, as well as the microbial communities in rhizosphere soil. The pots were watered every two days to maintain 60% soil moisture. At the end of the pot experiment (45 days), the plants were harvested and thoroughly washed with deionized water.

The analysis of the growth indicators of pak choi and physicochemical property of rhizosphere soil

After collection, the plant roots were washed with a 20 $mmol \cdot L^{-1}$ Na-EDTA solution to remove metal ions adsorbed on the root surface, followed by thorough rinsing with deionized water and blotting dry with paper towels. Fresh weight, root weight, stem diameter, and length were recorded. A portion of the collected pak choi samples was dried at 70 °C to a constant weight and then separated into roots, stems, and leaves. These tissues were ground using an agate mortar, sieved through a 3 mm mesh, and stored in sealed plastic bags for subsequent analysis. The remaining plant samples were used to determine chlorophyll and carotenoid content. The extracted pigments were diluted to 25 ml with 96% ethanol, and the leaf tissues were removed by centrifugation. The absorbance of the extracts was measured at wavelengths of 665 nm, 649 nm, and 470 nm using a UV spectrophotometer (T6 New Century, Beijing), with 96% ethanol used as the blank control. The contents of chlorophyll a, chlorophyll b, and carotenoids were calculated using Equations (1)–(3). The sum of chlorophyll a and chlorophyll b represented the total chlorophyll content. In the equations, C_a denotes chlorophyll a, C_b denotes chlorophyll b, and C_c denotes carotenoids:

$$C_a = 13.95 \times A_{665} - 6.88 \times A_{649} \quad (1)$$

$$C_b = 24.96 \times A_{649} - 7.32 \times A_{665} \quad (2)$$

$$C_c = \frac{1000 \times A_{470} - 2.05 \times C_a - 114.8 \times C_b}{245} \quad (3)$$

After harvesting the pak choi, soil samples around the root system were collected using the quartering method. The collected soil samples were separated from residual roots. Approximately 0.5 g of soil was used for microbial community analysis. The remaining soil samples were air-dried, ground with an agate mortar, sieved through a 100-mesh sieve, and stored in sealed plastic bags for further analysis. Rhizosphere soil pH was measured using a CO_2-free distilled water extraction method and readings were taken with a calibrated pH meter after 30 min of settling following stirring. The contents of available nitrogen (N), available phosphorus (P), available potassium (K), and organic matter in the soil were determined using the alkali hydrolysis diffusion method for available N, the hydrochloric acid-ammonium fluoride method for available P, the NH_4OAc extraction method for available K, and the chromate oxidation method for organic matter, respectively. More details are provided in Text S1.

Plant growth-promoting characteristics of A. johnsonii and R. mucilaginosa

To determine the plant growth-promoting characteristics of *A. johnsonii* and *R. mucilaginosa*, their abilities to produce ammonia, fix nitrogen, solubilize phosphorus, and produce siderophores were assessed. **Ammonia production ability**: Under aseptic conditions, the activated strain was inoculated at a 2% (v/v) ratio into 50 mL of peptone water medium (the control group received no bacterial suspension). The cultures were incubated at 28-30 ℃ with shaking at 150-200 rpm for 24-72 hours. A certain amount of bacterial culture was transferred into a clean test tube, and 1-2 drops of Nessler's reagent were slowly added along the tube wall. The color change in the solution was observed. If the interface or the entire solution turned brownish-yellow, it indicated that the strain possessed ammonia-producing ability. **Nitrogen fixation ability test**: The activated bacterial suspension was spot-inoculated onto Ashby's nitrogen-free medium using an inoculation loop or a micropipette and cultured at 28-30 ℃ for 3-7 days. The formation of colonies on the medium indicated that the strain possessed nitrogen fixation ability. **Phosphate solubilization ability test**: The activated bacterial suspension was spot-inoculated onto Pikovskaya (PKO) medium and cultured at 28-30 ℃ for 3-7 days. The formation of a transparent halo (phosphorus solubilization zone) around the colonies indicated that the strain possessed phosphate-solubilizing ability. **Siderophore production test**: The activated bacterial strain was inoculated into a low-iron liquid medium and cultured in a shaker at 30 ℃ and 150 rpm for a specified duration. After centrifugation, the supernatant was collected, and Chrome Azurol S (CAS) assay detection solution was added (the control group consisted of sterilized medium without bacterial inoculation). The mixture was left to stand for a specified period, and the color change was observed. If the solution color changed from blue to orange-yellow, it indicated that the strain possessed siderophore-producing ability. The specific experimental methods and medium formulations are provided in Text S2 and Table S1.

Analysis of Sb content in pak choi and soil samples

Approximately 0.5 mg of ground plant sample was placed into a PTFE-sealed digestion vessel and digested with 68%–

70% HNO_3 and 70%–72% $HClO_4$ (5:1, v/v) at 180°C for 2 hours. Approximately 0.25 g of ground soil was digested with 1 mL of 30% hydrogen peroxide, followed by the addition of 2 mL of hydrochloric acid and 5 mL of nitric acid. The reaction was performed using a microwave digestion system (MARS 6, USA). The samples were heated at 200 °C until the digestion solution was concentrated to 2 mL. The cooled plant and soil digests were then diluted to 50 mL, and 5 mL of the diluted solution was filtered through a 0.22 μm mixed cellulose ester (MCE) membrane filter. The total Sb concentration in the soil and plant sample solutions was determined using an atomic fluorescence spectrophotometer (AFS-9800, Shanghai). The operational parameters were as follows: 5% HCl was used as the carrier solution; the reducing agent was a mixture of 2% KBH_4 and 0.5% NaOH; and the carrier gas and shielding gas flow rates were 300 mL/min and 800 mL/min, respectively.

According to the sequential extraction method, the chemical speciation of Sb in the pak choi soil was determined. The chemical forms of Sb in the rhizosphere soil of pak choi were primarily classified into the following categories: exchangeable (F1), specifically adsorbed (F2), fulvic acid-complexed (F3), humic acid-complexed (F4), poorly crystalline iron-manganese oxide-bound (F5), sulfide-bound (F6), and residual (F7) Sb (Krishnamurti and Naidu, 2003). For each extraction step, 10 mL of the extract was centrifuged at 10,000 r/min for 10 minutes, and the supernatant was filtered through a 0.22 μm membrane filter. The Sb content was then measured using an atomic fluorescence spectrophotometer (AFS-9800, Shanghai).

Analysis of soil microbial community in root zone of pak choi

To investigate the effects of *A. johnsonii* and *R. mucilaginosa* on soil microbial communities, soil samples were collected at the end of the pot experiment. Bacterial and fungal DNA was extracted using the OMEGA E.Z.N.A.™ Mag-Bind Soil DNA Kit according to the manufacturer's instructions. The concentration and quality of the extracted DNA were measured using a Qubit® 4.0 Fluorometer (Q33238, Thermo Fisher). For amplification of bacterial 16S rRNA and fungal ITS genes, the following primers were used for PCR amplification. For bacterial 16S rRNA, the primers were 341F (CCTACGGGNGGCWGCAG) and 805R (GACTACHVGGGTATCTAATCC). For fungal ITS, amplification was performed using the primers ITS1F (CTTGGTCATTTAGAGGAAGTAA) and ITS2R (GCTGCGTTCTTCATCGATGC). Following Sanger sequencing, the 16S amplified fragments and full-length sequences were aligned using the RDP Classifier against reference sequences in the Silva database, while the ITS amplified fragments and full-length sequences were aligned using Blast against reference sequences in the UNITE database. To assess bacterial and fungal diversity and relative abundance, the V3-V4 region of the bacterial 16S rRNA gene and the ITS1-ITS2 region of the fungal ITS gene were sequenced on the Illumina MiSeq platform (Shanghai Majorbio Bio-pharm Technology Co., Ltd.).

Statistical analysis

The experimental results are presented as the mean ± standard deviation of three replicates. Statistical analyses were performed using GraphPad Prism 9.0 and Origin 2021 software. Data were analyzed using one-way analysis of variance (ANOVA). Differences were considered statistically significant at $*p < 0.05$, $**p < 0.01$, and $***p < 0.001$.

Results

Effects of A. johnsonii and R. mucilaginosa inoculation on the growth and physiology of pak choi

The growth and physiological response of pak choi under antimony (Sb) stress reflect the Sb-induced phytotoxicity. To assess the effects of *A. johnsonii* and *R. mucilaginosa* on pak choi growth, we measured the fresh weight, root weight, stem diameter, and plant height under different Sb stresses. Compared to the control, both microbial treatments promoted the pak choi growth (Fig. 1 A). All inoculations enhanced root development, with the *R. mucilaginosa*-inoculated group exhibiting more robust growth (Fig. 1 A). The fresh weight of pak choi with *A. johnsonii* inoculation increased by 6.74%–168.12% at different Sb concentrations compared to the control groups, while *R. mucilaginosa* inoculation showed a greater increase of 12.05%–198.85%, overall outperforming *A. johnsonii* (Fig. 1 B). For root weight, *A. johnsonii* treatment exhibited a relatively moderate increase (2.00%–2.37%), whereas the *R. mucilaginosa* treatment demonstrated a highly significant enhancement, reaching 92.31%–374.19% (Fig. 1 C). A consistent trend was observed in stem diameter, increasing by 10.08%–20.53% and 15.63%–30.02% in the *A. johnsonii* and *R. mucilaginosa* treatment groups, respectively (Fig. 1 D). Regarding plant height, the *R. mucilaginosa* treatment remained superior to that of *A. johnsonii*, achieving a maximum increase of 25.16% (Fig. 1 E).

Analysis of key physiological indicators demonstrated that both *A. johnsonii* and *R. mucilaginosa* inoculation effectively improved the physiological status of pak choi under Sb stress, while *R. mucilaginosa* treatment generally exhibited more significant enhancement in various indicators (Fig. 2 A-C). Compared to the control groups, root vitality (Fig. 2 A) increased by 27.00%–37.58% in the *A. johnsonii* treatment and by 44.36%–50.47% in the *R. mucilaginosa* treatment, which showed a greater improvement. The change trend in photosynthetic pigment content was similar to that of root vitality. Chlorophyll contents increased by 12.05%–50.79% and 21.50%–68.69% in the *A. johnsonii* and *R. mucilaginosa* groups, respectively (Fig. 2 B), while carotenoid contents increased by 9.38%–35.14% and 21.43%–58.75%, respectively (Fig. 2 C). The effect of *R. mucilaginosa* on photosynthetic pigments was superior to that of *A. johnsonii*.

These data demonstrate that inoculation with both *A. johnsonii* and *R. mucilaginosa* can effectively promote growth and enhance the physiological performance of pak choi under Sb stresses. *R. mucilaginosa*, however, exhibited relative advantages in both growth promotion and physiological enhancement.

Growth-promoting characteristics of A. johnsonii and R. mucilaginosa

To elucidate the mechanisms by which *A. johnsonii* and *R. mucilaginosa* promote plant growth, we evaluated several key growth-promoting traits of both strains, including ammonia

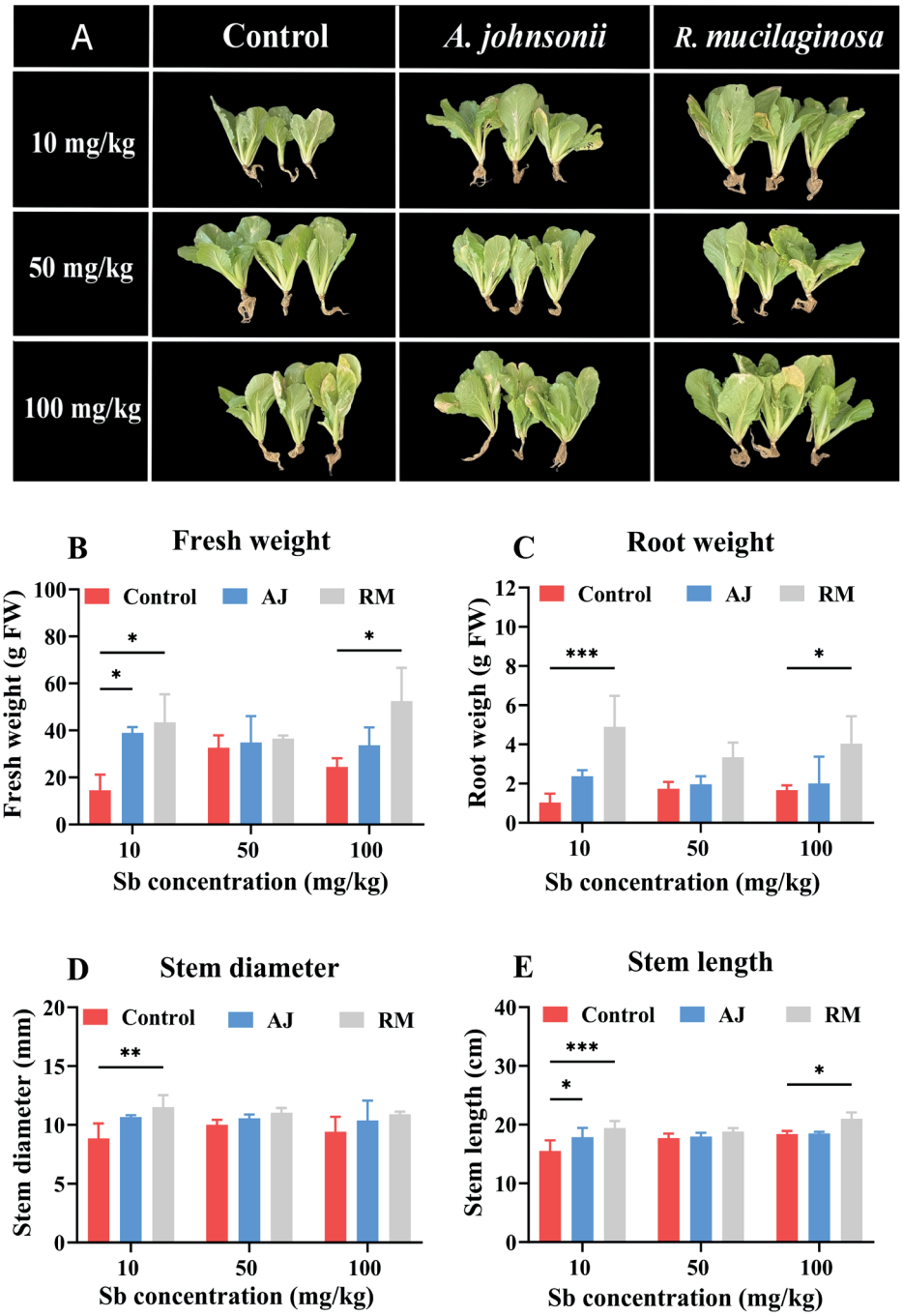


Fig 1. Growth parameters of pak choi. (A) Representative image; (B) Fresh weight; (C) Root weight; (D) Stem diameter; (E) Stem length. (AJ represents vaccination with *A. johnsonii*; RM represents vaccination with *R. Mucilaginosa*). Error bars represent standard deviations from three independent replicates. Significant differences were calculated as $^{*}p < 0.05$, $^{**}p < 0.01$, and $^{***}p < 0.001$.

production, nitrogen fixation, phosphate solubilization, and siderophore production (Fig. 2 D-G). In the ammonia production test, the solutions inoculated with both *A. johnsonii* and *R. mucilaginosa* turned brownish-yellow, confirming their ammonia-producing capability (Fig. 2 D). Both strains formed distinct colonies on Ashby's nitrogen-free medium, confirming their nitrogen-fixing capabilities (Fig. 2 E). Similarly, transparent halos (phosphorus solubilization zones) formed around the colonies of both *A. johnsonii* and *R. mucilaginosa* on the culture medium (Fig. 2 F), which is attributed to their decomposition of phosphates, confirming that both strains possess phosphate-solubilizing ability. Furthermore, after being cultured in a low-iron medium with the addition of CAS detection solution, the color of bacterial suspensions with *A. johnsonii* or *R. mucilaginosa* changed from blue to light yellow (Fig. 2 G), indicating that both strains possess the ability to produce siderophores.

Effects of A. johnsonii and R. mucilaginosa on the physicochemical properties of rhizosphere soil

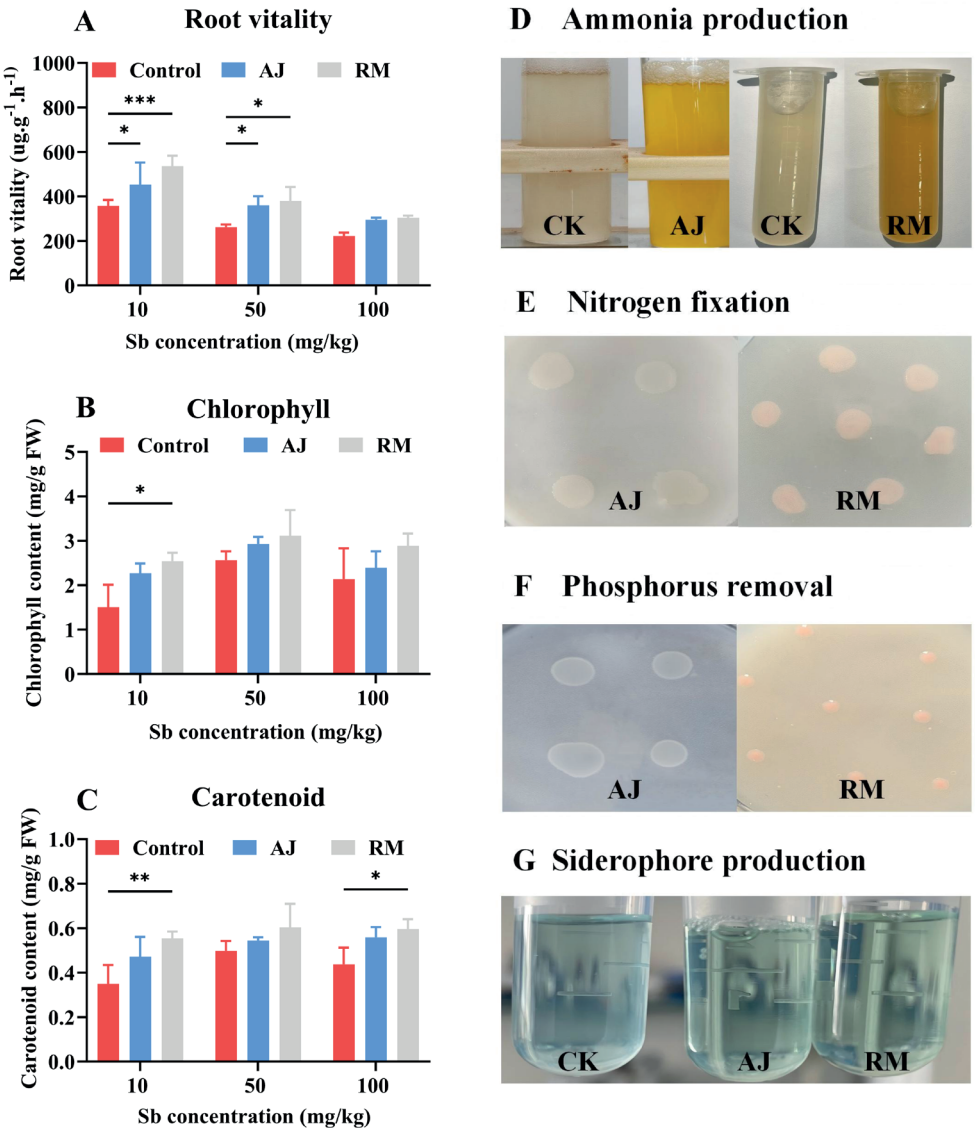


Fig 2. Physiological parameters of pak choi and plant Growth-Promoting Characteristics of *A. johnsonii* and *R. mucilaginosa*: (A) Root vitality; (B) Chlorophyll content; (C) Carotenoid content; (D) Ammonia production capacity determination; (E) Nitrogen fixation capacity determination; (F) Phosphorus solubilisation capacity determination; (G) Determination of iron carrier production ability. (AJ represents vaccination with *A. johnsonii*; RM represents vaccination with *R. Mucilaginosa*). Error bars indicate standard deviations from three replicate experiments. Significance levels denoted as *$p < .05$, **$p < .01$, and ***$p < .001$.

To elucidate the mechanisms underlying plant growth-promotion, we analyzed key physicochemical properties of the rhizosphere soil (Fig. 3). The results showed that inoculations with *A. johnsonii* or *R. mucilaginosa* exerted distinct effects on soil nutrient parameters. Soil pH was stabilized at approximately 6.0 at all treatment groups. The organic matter content in rhizosphere soil increased after *A. johnsonii* or *R. mucilaginosa* inoculations (Fig. 3 A). The *A. johnsonii* treatment group exhibited an increase of 4.09%–7.00%, while the *R. mucilaginosa* treatment showed an increase of 2.78%–7.62%, indicating that microbial inoculation promotes the accumulation of soil organic matter to some extent. Similarly, available nitrogen (Fig. 3 B) increased by 1.75%–11.98% in the *A. johnsonii* group and by 9.19%–19.96% in the *R. mucilaginosa* group compared to the control. This suggests that microbial inoculation can significantly enhance the available nitrogen content in rhizosphere soil, particularly with *R. mucilaginosa*.

In contrast, microbial inoculation significantly reduced the levels of available phosphorus and potassium in rhizosphere soil (Fig. 3 C-D). Available phosphorus (Fig. 3 C) decreased by 9.80%–15.25% and 7.84%–18.64% in the *A. johnsonii* and *R. mucilaginosa* treatment groups, respectively. A more pronounced reduction was observed for available potassium, which decreased by 53.61%–66.25% and 15.33%–44.24% in the *A. johnsonii* and *R. mucilaginosa* groups, respectively (Fig. 3 D). These results demonstrate that both *A. johnsonii* and *R. mucilaginosa* enhanced soil organic matter and available nitrogen but significantly reduced available phosphorus and potassium in the rhizosphere soil of pak choi.

Antimony content in pak choi and rhizosphere soil and antimony fractionation in rhizosphere soil

To investigate Sb migration and transformation in soil-plant system under aerobic conditions, we quantified Sb

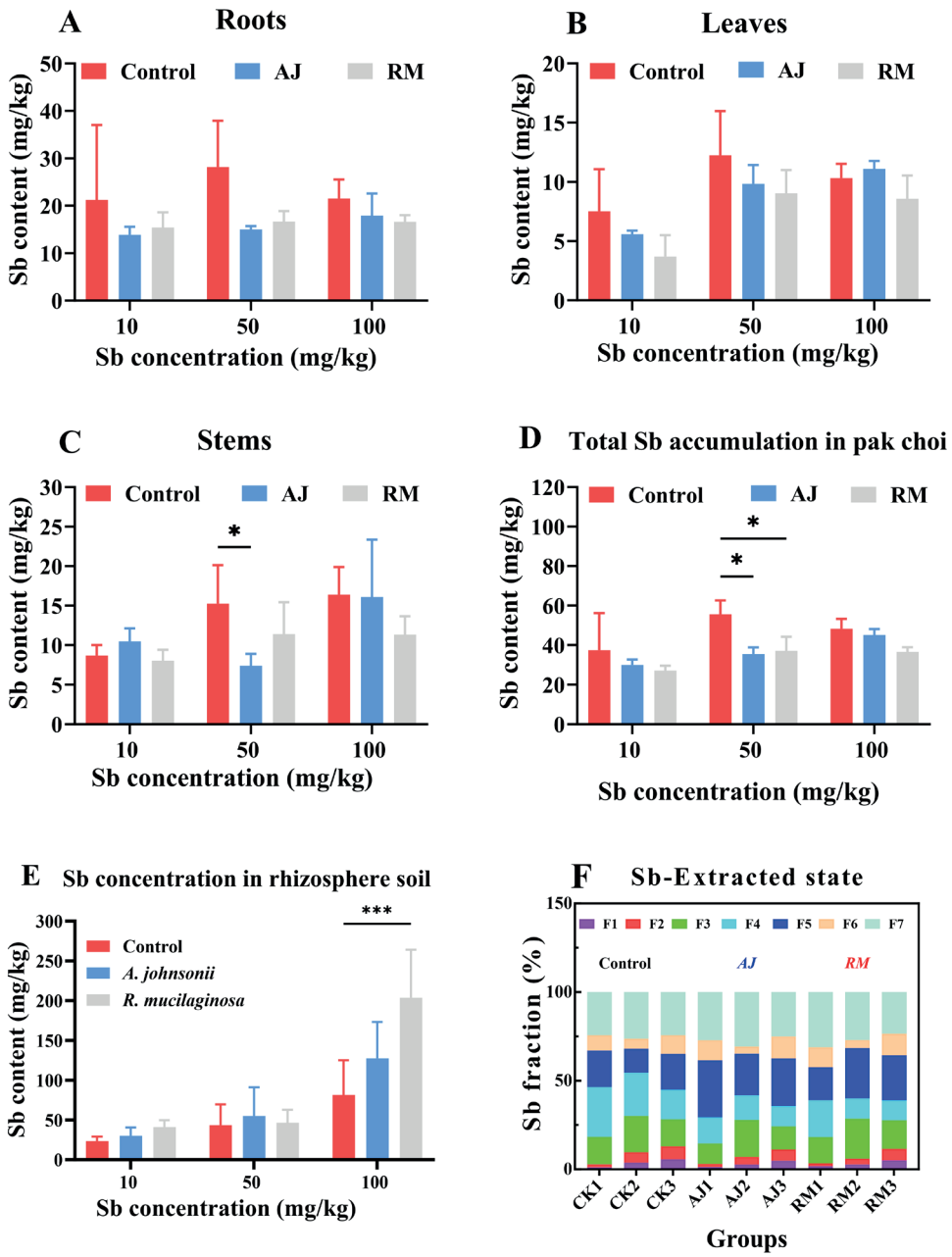


Fig 3. Illustrates the physicochemical characteristics of the soil with pak choi cultivation. (A) Organic matter content, (B) Available nitrogen, (C) Available phosphorus, and (D) Available potassium. (AJ represents vaccination with *A. johnsonii*; RM represents vaccination with *R. Mucilaginosa*). Error bars indicate standard deviations based on three parallel experiments. Significance levels were denoted as *$p < 0.05$, **$p < 0.01$, and ***$p < 0.001$.

contents in various pak choi tissues and the rhizosphere soil, and analyzed Sb speciation in rhizosphere soil (Fig. 4). In the roots, Sb content decreased by 16.65%–46.72% and 22.88%–40.75% in the *A. johnsonii* and *R. mucilaginosa* groups, respectively (Fig. 4 A). In the leaves (Fig. 4 B), Sb content decreased by 19.69% and 25.65% in the *A. johnsonii* groups with 10 and 50 mg/kg Sb treatments, respectively. In contrast, *R. mucilaginosa* reduced leaf Sb contents in all Sb treatment groups, with decreases of 17.06% - 40.75%. A similar trend was observed in the stems (Fig. 4 C). Under the 50 and 100 mg/kg Sb treatments, the Sb content in the *A. johnsonii* groups decreased by 29.55% and 1.78% compared to the corresponding control groups, respectively. Whereas *R. mucilaginosa* reduced stem Sb contents across all Sb treatment groups, with reductions of 7.36% - 30.85%. The overall Sb enrichment pattern in pak choi tissues was: root >leaf≥stem. On the whole, microbial inoculation significantly reduced total Sb content in pak choi plants (Fig. 4 D), particularly under the 50 mg/kg Sb stress, with reduction of 36.07% and 33.26% for the *A. johnsonii* and *R. mucilaginosa* treatments, respectively. These results demonstrate that both *A. johnsonii* and *R. mucilaginosa* effectively inhibited Sb uptake and accumulation in pak choi tissues. The *R. mucilaginosa* treatment exhibited relatively obvious and stable reduction on Sb accumulation in tissues at the tested Sb concentrations.

The Sb concentration in the rhizosphere soil of pak choi increased with elevated exogenous Sb levels (Fig. 4 E). Sb concentrations in the rhizosphere soil with *A. johnsonii* or

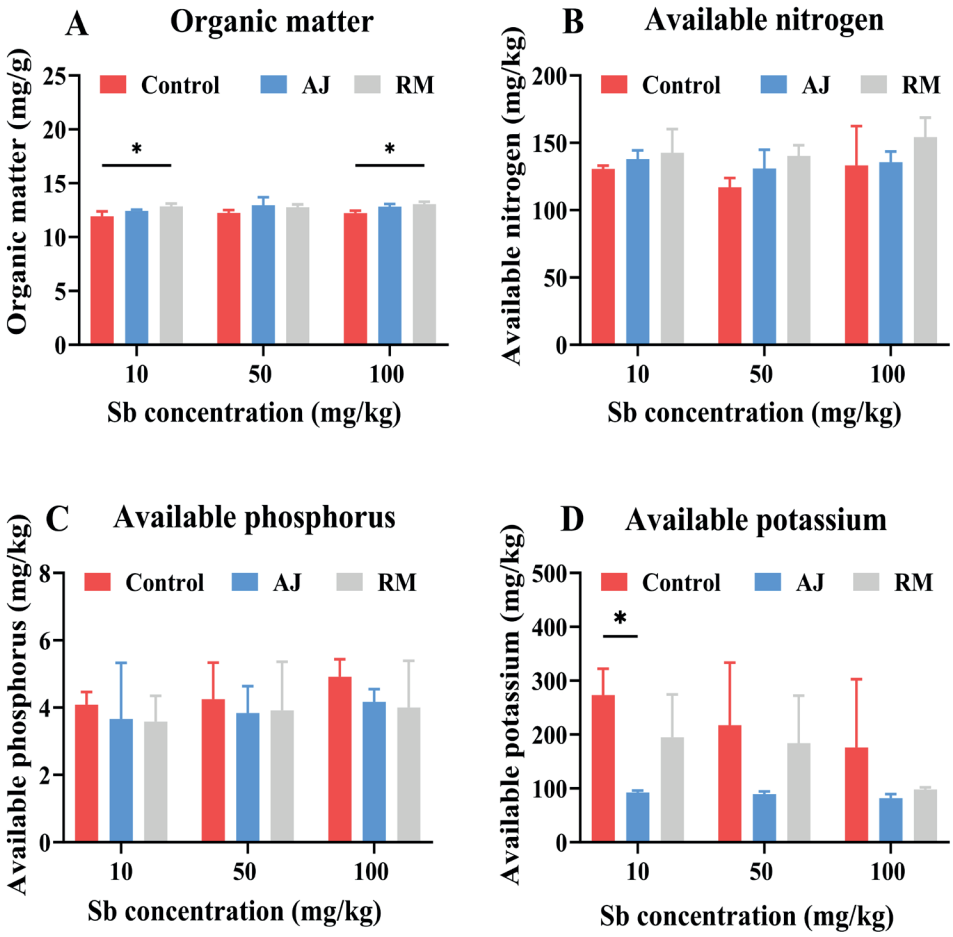


Fig 4. Accumulation content and chemical forms of Antimony in pak choi tissues and rhizosphere soil. (A) root; (B) leaves; (C) stem; (D) total Sb content; (E) rhizosphere soil; (F) chemical forms of Sb in the rhizosphere soil (F1 is the exchangeable form, F2 is the specific adsorption form, F3 is the fulvic acid-bound form, F4 is the humic acid-bound form, F5 is the weakly crystalline iron and manganese oxide-bound form, F6 is the sulfide-bound form, and F7 is the residual form). All the three groups, CK (control group), AJ and RM, were treated with 10, 50, and 100 mg/kg Sb respectively. Error bars indicate the standard deviation of three parallel experiments. Significant differences are calculated as *p < 0.05, **p < 0.01, and ***p < 0.001.

R. mucilaginosa were significantly higher than those in the control groups. In particular, Sb contents in the rhizosphere soil with *A. johnsonii* and *R. mucilaginosa* reached 127.61 and 203.75 mg/kg in the 100 mg/kg groups, with increases of 56.93% and 150.56%, respectively, which were much higher than the average Sb content in the soil.

In this study, sequential extraction was used to analyze the fractionation of Sb in the rhizosphere soil after pak choi harvest. In all treatment groups, the residual fraction (F7), weakly crystalline Fe-Mn oxide-bound fraction (F5), and humic acid-bound fraction (F4) predominated in the Sb speciation distribution (Fig. 4 F). Compared with the control groups, *A. johnsonii* and *R. mucilaginosa* inoculation significantly promoted the formation of Fe-Mn oxide-bound Sb and inhibited the formation of humic acid-bound Sb. The F5 fraction increased by 32.65%–73.73% and 24.74%–110.48% in the *A. johnsonii* and *R. mucilaginosa* groups, respectively. The F4 (humic acid-bound form) decreased by 31.02%–47.99% and 25.83%–53.26% after *A. johnsonii* and *R. mucilaginosa* inoculation, respectively. Meanwhile, the residual Sb (F7) in the *A. johnsonii* and *R. mucilaginosa* groups increased by 3.17%–24.69% and 2.74%–28.52%, respectively, compared to the control groups.

The microbial community composition in rhizosphere soil of pak choi

The rhizosphere microflora play a crucial role in modulating crop growth and heavy metal accumulation. Therefore, the microbial community in the rhizosphere was detected and analyzed through high-throughput sequencing. At the bacterial phylum level, *Pseudomonadota* and *Bacteroidota* were dominant in all groups, with their total relative abundance exceeding 50% (Fig. 5 A). Inoculation with *A. johnsonii* did not alter their combined abundance, whereas *R. mucilaginosa* increased the total relative abundance of the two phyla under different Sb stresses. At the bacterial genus level (Fig. 5 C), the dominant genera in all groups were *Sphingomonas* and *Flavisolibacter*. Neither *A. johnsonii* nor *R. mucilaginosa* inoculation had a significant effect on the total relative abundance of the two genera. However, *R. mucilaginosa* inoculation reduced bacterial diversity at the genus level.

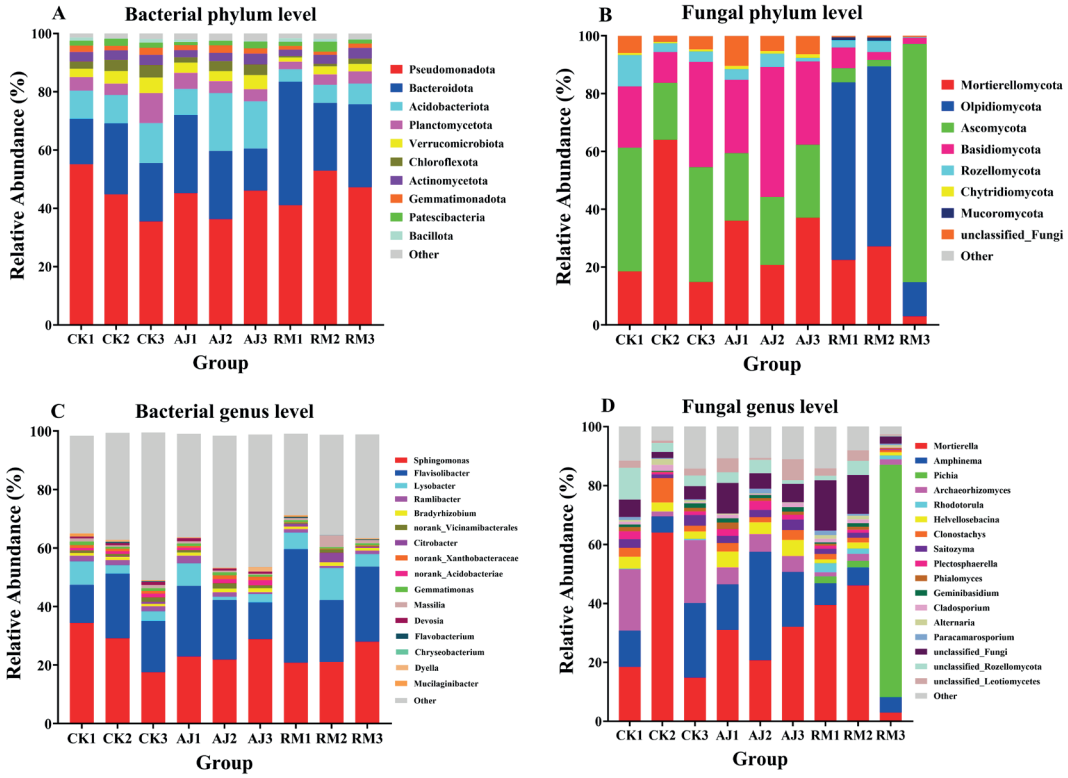


Fig 5. Taxonomic composition of bacterial and fungal communities in the rhizosphere soil of pak choi inoculated with *A. johnsonii* and *R. mucilaginosa*. (A) Bacterial phylum level; (B) Fungal phylum level; (C) Bacterial genus level; (D) Fungal genus level. (All the three groups, CK (control group), AJ and RM, were treated with 10, 50, and 100 mg/kg Sb respectively.)

At the fungal phylum level (Fig. 5 B), *Mortierellomycota*, *Ascomycota* and *Basidiomycota* were dominant in the control and *A. johnsonii*-inoculated groups, with *A. johnsonii* inoculation showing no significant impact on their total relative abundance. In contrast, the fungal community with *R. mucilaginosa* inoculation was dominated by *Olpidiomycota* or *Ascomycota,* accounting for over 60% of the abundance. At the fungal genus level (Fig. 5 D), *Mortierella, Amphinema* and *Archaeorhizomyces* were the main genera in the control and *A. johnsonii*-inoculated groups, and *A. johnsonii* inoculation had no obvious effect on the total relative abundance of dominant fungi. In contrast, *Mortierella* or *Pichia* were the dominant fungi in the group with *R. mucilaginosa* inoculation, and their relative abundance accounted for over 60%. Furthermore, *R. mucilaginosa* inoculation decreased fungal community diversity at the genus level.

The observation demonstrated that *A. johnsonii* inoculation had no significant effects on microbial communities, while *R. mucilaginosa* altered the community structure with its effect being especially significant for the fungal community. Notably, *R. mucilaginosa* inoculation reduced the abundance of certain potential pathogenic fungi, such as some *Clonostachys* and *Plectosphaerella* species, thereby further optimizing the microbial community structure. This helps mitigate the risk of pathogen infection in plants under heavy metal stress and enhances their overall resilience.

Distribution patterns and influence factors of rhizosphere microbial community

In order to study the regulatory effects of exogenous microorganisms and environmental factors on the rhizosphere microbial community, Principal Co-ordinates Analysis (PCoA) and Redundancy Analysis (RDA) were performed (Fig. 6). PCoA results revealed that inoculation with *A. johnsonii* induced a certain alteration in bacterial community structure, while exerting a relatively weaker influence on the fungal community. In contrast, *R. mucilaginosa* inoculation exerted a stronger influence on the structures of bacterial and fungal communities compared with *A. johnsonii* (Fig. 6 A-B). The influence of *R. mucilaginosa* on the fungal community was more obvious than that on the bacterial community.

RDA conducted using the ChiPlot online analysis platform further indicated a significant correlation between changes in rhizosphere nutrients and growth-promoting indicators of pak choi under the two strain treatments. RDA1 of bacteria and fungi in the groups with *A. johnsonii* inoculation explained 59.85% and 67.83% of the community variation, respectively (Fig. 6 C-D). The environmental factors of available nitrogen (HN) and available potassium (AK) showed significant associations with the microbial community variation of bacteria and fungi in the groups with *A. johnsonii* inoculation, respectively. For the groups with *R. mucilaginosa* inoculation, RDA1 accounted for 66.46% and 70.47% of the variation (Fig. 6 E-F). pH and HN were the main influencing factors for bacterial community variation, while available phosphorus (AP) and Sb were the main influencing factors for fungal community variation.

Furthermore, the explained variance of RDA2 was higher (27.45%) with *R. mucilaginosa* inoculation than that in the *A. johnsonii* treatments, indicating a stronger regulatory effect of *R. mucilaginosa* on the microbial community and a closer association of environmental factors with the

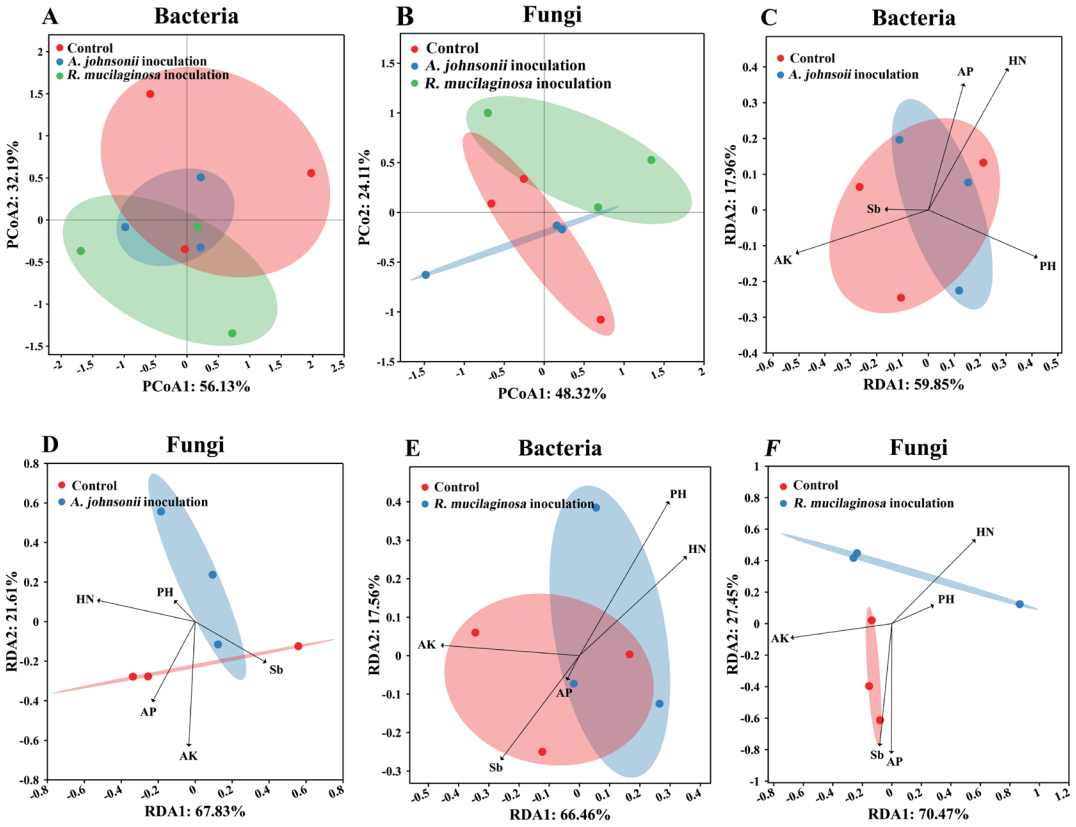


Fig 6. Analysis of the effects of A. johnsonii and R. mucilaginosa treatments on the microbial community in the rhizosphere soil of pak choi. (A, B) Principal coordinate analysis of bacterial and fungal communities; (C, D) Redundancy analysis of bacterial and fungal communities and soil physicochemical factors under A. johnsonii treatment; (E, F) Redundancy analysis of bacterial and fungal communities and soil physicochemical factors under R. mucilaginosa treatment.

microbial community in the group with *R. mucilaginosa*. The integrated PCoA and RDA results suggest that *R. mucilaginosa* exerts a more profound influence on microbial communities through synergistic interactions with environmental factors, demonstrating a particularly distinct advantage in restructuring the fungal community.

Discussion

The effectiveness of microbial remediation for heavy metal-contaminated soils varies significantly, depending on the biological characteristics, remediation mechanisms, and environmental adaptability of the microorganisms involved. Therefore, even microorganisms with "identical" remediation mechanisms might exhibit different effectiveness. Currently, research on the remediation of Sb contamination by bacteria and fungi remains limited, and the underlying mechanisms remain poorly understood. In our previous study, both *A. johnsonii* and *R. mucilaginousa* exhibited the ability to mineralize Sb(III) into Sb_2O_3, with *R. mucilaginosa* exhibiting higher Sb(III) resistance and mineralization efficiency than *A. johnsonii* (Shi et al., 2025; Yang et al., 2024). This study systematically evaluated the effects of these two strains on pak choi growth, Sb accumulation in plants, Sb speciation in soil, soil physicochemical properties, and rhizosphere microbial community.

The results demonstrated that both microorganisms can promote pak choi growth under Sb stress and effectively reduce Sb accumulation in plant tissues. However, *R. mucilaginosa* is superior to *A. johnsonii* in both promoting plant growth and reducing Sb accumulation. These findings are consistent with recent trends in microbe-assisted phytoremediation research, as multiple microorganisms have been shown to alleviate antimony stress by promoting plant growth and altering the speciation of antimony in soil (Wu et al., 2025). However, the differences in efficiency among various microorganisms also reflect a high degree of strain-specific dependence of remediation outcomes. For example, arbuscular mycorrhizal fungi (AMF) reduced antimony uptake and translocation in flax by 47% (Zrig et al., 2025), while the combination of the antimony-resistant plant growth-promoting bacterium *Bacillus* sp. D2 with Fe^{2+} reduced antimony translocation in rice stems by 67.6% (Wu et al., 2025). In comparison, *R. mucilaginosa*, which performed better in this study, resulted in even lower antimony accumulation in plant tissues, demonstrating an efficacy comparable to these reported high-efficiency remediation strategies.

Nitrogen serves as a fundamental element for chlorophyll synthesis; therefore, its availability directly influences chlorophyll content and photosynthetic efficiency. Inoculation with *A. johnsonii* or *R. mucilaginosa* significantly increased the available nitrogen content in rhizosphere soil and effectively elevated the leaf chlorophyll content. The effect was more pronounced in the *R. mucilaginosa* treatment, indicating its capacity to enhance nitrogen uptake in pak choi compared to *A.*

johnsonii. This difference is further corroborated in the study by Paul et al. (2029), in which *R. mucilaginosa* JGTA-S1 can form a tripartite interaction system by symbiotically interacting with the endophytic nitrogen-fixing bacterium *Pseudomonas stutzeri*, resulting in sustained expression of nitrogenase genes even under nitrogen-sufficient conditions. Consequently, it activates nitrogen metabolism-related transcription factors within 24 hours of colonization, providing a rapid nitrogen supply to rice (Paul et al., 2019). In contrast, although *A. johnsonii* also possesses nitrogen solubilization and heterotrophic nitrification capabilities (Jangra et al., 2024), its nitrogenase function is readily inhibited under high-nitrogen conditions. Therefore, this mechanistic difference may be a potential reason for the superior plant growth-promoting effect of *R. mucilaginosa* observed in this study.

Appropriately increasing the nutrients can promote root growth and nutrient absorption. Consistent with this, inoculation with either *A. johnsonii* or *R. mucilaginosa* distinctly decreased the contents of available phosphorus and potassium in soil, suggesting enhanced uptake of these elements by pak choi. Root vitality refers to the ability of nutrients uptake and environmental responsiveness and is a key determinant of plant growth and yield. Both *A. johnsonii* and *R. mucilaginosa* inoculations distinctly enhanced root vitality, but the effect of *R. mucilaginosa* inoculation was more pronounced. This result is highly consistent with existing studies on PGPR-mediated root system regulation. For example, Naveen and Balachandar et al. (2025) found that *Aeromonas hydrophila* QS74, owing to its abundant extracellular polymeric substance secretion capability, significantly enhances soil organic carbon, microbial activity, and aggregate stability, and improves the nutrient acquisition capacity of subsequent crops through a positive feedback mechanism of "soil conditioning–root response" (Naveen and Balachandar, 2025). Accordingly, it is further inferred that the mechanisms by which *A. johnsonii* and *R. mucilaginosa* enhance root activity are multifaceted, encompassing volatile signal transduction, rhizosphere microenvironment remodeling, and feedback regulation of the soil–plant system.

Both strains exhibit significant plant growth-promoting traits, including ammonia production, nitrogen fixation, phosphate solubilization, and siderophore synthesis. On this basis, *A. johnsonii* also produces indole compounds such as indole-3-lactic acid (ILA), and its growth-promoting chemical composition has been confirmed by mass spectrometry (Bhattacharya et al., 2024). Meanwhile, *R. mucilaginosa* RSRod01 possesses combined abilities of siderophore production, extracellular enzyme secretion, and heavy metal tolerance, and can maintain its growth-promoting activity under a salt concentration of 4% (Rahal et al., 2023). Thus, the aforementioned multiple growth-promoting traits of the two strains constitute the direct basis for their plant growth-promoting effects.

The toxicity and bioavailability of heavy metals primarily depend on their speciation in the environment. Iron-manganese oxides exhibit a strong adsorbing capacity for Sb(III) and Sb(V); however, the plant availability of these adsorbed species is significantly different. Compared to Sb(III), iron-manganese oxide-bound of Sb(V) is difficult to be absorbed by plant roots (Shao et al., 2021). In recent years, research on microbe-mediated antimony transformation has provided new approaches for reducing antimony bioavailability. For example, *Pseudomonas* sp. QJX-1, isolated from an antimony mining area, can oxidize Sb(III) to Sb(V) through the in situ formation of biogenic manganese oxides (BMO), and only the Sb(V) generated by the oxidation process can be efficiently adsorbed by BMO. The Fe(II) produced from the oxidation further forms FeOOH and mixes with BMO to constitute biogenic iron-manganese oxides (BFMO), achieving the synergistic immobilization of antimony through oxidation and adsorption (Bai et al., 2017). In addition, a team from Huazhong Agricultural University recently identified a bifunctional enzyme, AntO, that simultaneously catalyzes Sb(III) oxidation and H_2O_2 decomposition (Luo et al., 2026), providing direct molecular evidence for the enzymatic regulation of soil antimony speciation by microorganisms.

Under aerobic conditions, Sb in soil mainly exists as Sb(V). Residual Sb has low biological availability and is difficult for plants to absorb. Therefore, increases in the iron-manganese oxide-bound and residual proportions in the rhizosphere soil contribute to reducing Sb absorption by pak choi roots. Humic acid and other dissolved organic matter can significantly increase the solubility and mobility of antimony in soil through complexation and competitive adsorption, thereby raising the risk of crop uptake. Notably, the interaction effects between organic matter from different sources and iron-manganese oxides vary significantly. Straw-derived organic-inorganic composite colloids (SD-Fe/Mn) form a more stable colloidal structure with iron-manganese oxides, resulting in the near-complete stabilization (100%) of water-soluble and carbonate-extractable antimony after 35 days of treatment. In contrast, humic acid-iron-manganese colloids (HA-Fe/Mn), due to their higher carboxyl content, actually enhance colloid mobility (Zheng et al., 2024). This finding is highly consistent with the conclusion of the present study that humic acid-bound antimony increases the risk of crop uptake. *A. johnsonii* and *R. mucilaginosa* inoculation significantly increased the proportion of iron-manganese oxide-bound and residual Sb and reduced the proportion of the humic acid-bound Sb. Consequently, through their combined effects, *A. johnsonii* and *R. mucilaginosa* inoculation effectively inhibited the absorption and accumulation of Sb by pak choi.

As common resident bacterial taxa in soil, *Pseudomonadota* and *Bacteroidota* play important roles in modulating heavy metal bioavailability (Li et al., 2022). Inoculation with *A. johnsonii* did not significantly alter the total relative abundance of these two bacterial taxa at either the phylum or genus level. In contrast, *R. mucilaginosa* increased the total relative abundance of these two taxa. As key fungal taxa in the environment, *Ascomycota*, *Mortierella*, and *Pichia* play crucial roles in heavy metal immobilization, transformation, and bioremediation through their respective unique mechanisms. As a vast taxonomic group, *Ascomycota* exhibits remarkable biosorption capabilities via hyphae or yeast cells surfaces, where components such as chitin and chitosan passively bind metal ions. Furthermore, *Pichia* species can biotransform heavy metals through redox reactions and methylation, altering their mobility and toxicity (Martorell et al., 2012). *Mortierella,* a plant growth-promoting fungus, often forms mycorrhizal or endophytic associations with plants, enhancing phosphate

nutrition and plant growth, while also exhibiting significant tolerance to multiple heavy metals (such as Cd, Pb, Zn, Cu, and As) (Cui et al., 2017). *A. johnsonii* did not significantly influence the fungal community structure at phylum or genus level, but *R. mucilaginosa* significantly increased the relative abundance of *Mortierella* and *Pichia* in the rhizosphere soil and successfully established itself in the Sb-contaminated environment.

PCoA and RDA revealed that *R. mucilaginosa* inoculation significantly drove variations in bacterial and fungal communities and showed a stronger association between the community structure and environmental factors. Although *A. johnsonii* and *R. mucilaginosa* did not show obvious difference in the variation of Sb speciation in rhizosphere soil, *R. mucilaginosa* inoculation more effectively alleviated Sb accumulation in pak choi. Therefore, it is believed that the regulation of Sb accumulation in pak choi by *R. mucilaginosa* contributes to its effect on Sb speciation and the beneficial microbial community in the rhizosphere soil, while *A. johnsonii* mainly contributes to the regulation of Sb speciation alone.

Conclusions

This study demonstrates that *A. johnsonii* and *R. mucilaginosa* can significantly enhance the pak choi growth and reduce Sb accumulation in a contaminated soil–crop system through their plant growth-promoting traits, such as nitrogen fixation and phosphorus solubilization, which increase soil organic matter and available nitrogen. Critically, both strains promoted the conversion of bioavailable Sb into more stable residual and iron–manganese oxide-bound forms, thereby reducing Sb mobility and plant uptake. *R. mucilaginosa* outperformed *A. johnsonii* in enhancing plant growth and immobilizing Sb, and uniquely reshaped the rhizosphere microbial community by enriching beneficial fungi such as *Mortierella* and *Pichia*, thereby strengthening plant resilience under Sb stress. In summary, this research elucidates a synergistic mechanism of "nutrient activation–speciation stabilization–microbial regulation" underlying microbial remediation of Sb-contaminated soil, providing a theoretical and practical basis for the application of functional microorganisms in sustainable agricultural remediation. Based on the pot experiment results obtained in this study, we plan to continue this research by conducting field trials to verify the practical remediation effects of the two strains and to further dissect the mechanism by which *R. mucilaginosa* reshapes the rhizosphere fungal community. The findings can be developed into microbial remediation agents for antimony-contaminated farmland, ensuring the safety of agricultural products by reducing antimony accumulation in pak choi, with low-cost and environmentally friendly application prospects.

Declaration of competing interest

The authors declare that they have no known competing financial interests or personal relationships that could have appeared to influence the work reported in this paper.

Acknowledgements

This work was supported by the National Natural Science Foundation of China (Nos. 42567004 and 32101045) and the Introducing Talent in Guizhou University 2020 (No. 17).

References

Angeles de Paz, G., Martínez-Gutierrez, H., Ramírez-Granillo, A., López-Villegas, E.O., Medina-Canales, M.G. & Rodríguez-Tovar, A.V. (2023). Rhodotorula mucilaginosa YR29 is able to accumulate Pb2+ in vacuoles: a yeast with bioremediation potential. *World Journal of Microbiology and Biotechnology,* 39, 238. DOI:10.1007/s11274-023-03675-4.

Bai, Y., Jefferson, W.A., Liang, J., Yang, T. & Qu, J. (2017). Antimony oxidation and adsorption by in-situ formed biogenic Mn oxide and Fe-Mn oxides. *Journal of Environmental Sciences*, 54, pp. 126-134. DOI 10.1016/j.jes.2016.05.026.

Bhattacharya, E., Hazra, A., Dutta, M., Bose, R., Dutta, A., Dandapat, M., Guha, T. & Mandal Biswas, S. (2024). Novel report of Acinetobacter johnsonii as an indole-producing seed endophyte in *Tamarindus Indica* L. *Archives of Microbiology,* 206, 144. DOI:10.1007/s00203-024-03865-0.

Chen, J.-P., Qin, J., Xing, Y., Liao, Q., Pan, L.-P., Zeng, C.-C. & Liu, Y.-X. (2025). Exogenous jasmonic acid and salicylic acid enhance selenium uptake and mitigate cadmium accumulation in pak choi (*Brassica chinensis* L.) grown in selenium-rich, high-cadmium soil. *Frontiers in Plant Science*, 16(2025). DOI 10.3389/fpls.2025.1619522.

Cui, Z., Zhang, X., Yang, H. & Sun, L. (2017). Bioremediation of heavy metal pollution utilizing composite microbial agent of *Mucor circinelloides*, *Actinomucor* sp. and *Mortierella* sp. *Journal of Environmental Chemical Engineering,* 5, 4, pp. 3616-3621. DOI:10.1016/j.jece.2017.07.021.

He, J., Zhang, H., Yang, K., Li, Y., Bao, L., Gao, L. & Zhang, N. (2025). Heavy metal accumulation risk and source analysis in soils of antimony mining areas. *Scientific Reports*, 40010. DOI:10.1038/s41598-025-23789-z.

Jangra, A., Kumar, K., Maikhuri, S., Bhandari, M.S., Pandey, S., Singh, H. & Barthwal, S. (2024). Unveiling stress-adapted endophytic bacteria: characterizing plant growth-promoting traits and assessing cross-inoculation effects on *Populus deltoides* under abiotic stress. *Plant Physiology and Biochemistry*, 210. DOI:10.1016/j.plaphy.2024.108610.

Krishnamurti, G.S.R. & Naidu, R. (2003). Solid–solution equilibria of cadmium in soils. *Geoderma,* 113(1-2), pp. 17-30. DOI:10.1016/s0016-7061(02)00313-0.

Li, Q., Wang, Y., Li, Y., Li, L., Tang, M., Hu, W., Chen, L. & Ai, S. (2022). Speciation of heavy metals in soils and their immobilization at micro-scale interfaces among diverse soil components. *Science of the Total Environment*, 825. DOI:10.1016/j.scitotenv.2022.153862.

Li, Y., Zhang, R., Li, H., Wu, Q. & Cheng, H. (2026). National-scale distribution, ecological health risks, and water quality criteria for antimony in Chinese surface waters: Mining-driven pollution demands attention. *Journal of Hazardous Materials,* 502. DOI:10.1016/j.jhazmat.2025.141012.

Long, J., Zhou, D., Wang, J., Huang, B., Luo, Y., Zhang, G., Liu, Z. & Lei, M. (2023). Repeated inoculation of antimony resistant bacterium reduces antimony accumulation in rice plants. *Chemosphere*, 327. DOI:10.1016/j.chemosphere.2023.138335.

Luo, X., Lan, Y., Gao, M., Xu, M., Liu, S., Zheng, S. & Li, M., (2026). Novel bifunctional enzyme anto catalyzes antimonite oxidation and H_2O_2 decomposition in environmental antimony detoxification. *Environmental Science & Technology*, 60, 6, pp. 4606-4615. DOI:10.1021/acs.est.5c12342.

Martorell, M.M., Fernández, P.M., Fariña, J.I. & Figueroa, L.I.C. (2012). Cr(VI) reduction by cell-free extracts of *Pichia jadinii* and *Pichia anomala* isolated from textile-dye factory effluents. *International Biodeterioration & Biodegradation*, 71, pp. 80-85. DOI:10.1016/j.ibiod.2012.04.007.

Naveen, S. & Balachandar, D. (2025). Extracellular polymeric substances of plant-growth-promoting rhizobacteria modulate the positive plant-soil feedback in maize via soil conditioning. *Science of the Total Environment*, 975. DOI:10.1016/j.scitotenv.2025.179256.

Ogunsola, S.S., Oladele, O.L., Abdulraheem, T. & Cooke, C.G. (2025). Synergizing phytoremediation and geopolymerization: A sustainable waste-to-wealth approach for heavy metal-contaminated soils. *Chemosphere*, 385. DOI:10.1016/j.chemosphere.2025.144539.

Paul, K., Saha, C., Nag, M., Mandal, D., Naiya, H., Sen, D., Mitra, S., Kumar, M., Bose, D., Mukherjee, G., Naskar, N., Lahiri, S., Das Ghosh, U., Tripathi, S., Sarkar, M.P., Banerjee, M., Kleinert, A., Valentine, A.J., Tripathy, S., Sinharoy, S. & Seal, A., (2019). A Tripartite interaction among *the Basidiomycete Rhodotorula mucilaginosa*, N2-Fixing Endobacteria, and Rice Improves Plant Nitrogen Nutrition. *The Plant Cell*, 32, pp. 486-507. DOI:10.1105/tpc.19.00385.

Pradhan, N., Singh, S., Saxena, G., Pradhan, N., Koul, M., Kharkwal, A.C. & Sayyed, R. (2025). A review on microbe–mineral transformations and their impact on plant growth. *Frontiers in Microbiology*, 16. DOI: 10.3389/fmicb.2025.1549022.

Rahal, S., Menaa, B. & Chekireb, D. (2023). Characterization of *Rhodotorula mucilaginosa* RSRod01 isolated from *Trifolium* sp. Root nodules growing at a Pb-Zn mine site. *Microbiology*, 92, pp. 860-867. DOI:10.1134/s0026261723600891.

Roldán, N., Verdugo, M., Suzuki, N., Zamora, N., Quiroz, W., Gonzalez, A., Tognarelli, J. & Ogra, Y. (2025). Toxicological effects of Sb(III), Sb(V), and NMG-Sb(V) in human lung, kidney, and liver cells: cytotoxicity and fibrotic factor induction. *The Journal of Toxicological Sciences*, 50, 6, pp. 283-292. DOI:10.2131/jts.50.283.

Senila, M., Balgaradean, C. & Senila, L. (2026). Challenges in remediation of Hg-Contaminated agricultural soils: A literature review. *Agriculture*, 16, 8, pp. 849. DOI:10.3390/agriculture16080849.

Shao, Y., Sun, Q., Wang, L., Zhan, W., Zhang, H. & Zhong, H. (2021). Migration and transformation of Sb are affected by Mn(III/IV) associated with lepidocrocite originating from Fe(II) oxidation. *Journal of Environmental Sciences,* 115, pp. 308-318. DOI:10.1016/j.jes.2021.08.001.

Shi, X., Bian, W., Yang, L., Xian, J., Liu, K., Wang, Q., Yang, A., Niu, A. & Mei, S. (2025). Trivalent antimony mineralization: Mechanism and application of *Acinetobacter johnsonii*. *Archives of Environmental Protection*, 51, pp. 127-143. DOI:10.24425/aep.2025.157234.

Tang, H., Meng, G., Jiang, W., Ma, Y., Duan, R., Hassan, M.U., Altihani, F.A. & Hashem, M. (2025). Co-application of iron modified biochar and metal resistant bacteria alleviates antimony toxicity in rice by modulating morpho-physiological and biochemical traits and soil microbial activities. *Environmental Technology & Innovation*, 38. DOI:10.1016/j.eti.2025.104184.

Timková, I., Maliničová, L., Nosáľová, L., Kolesárová, M., Lorková, Z., Petrová, N., Pristaš, P. & Kisková, J. (2023). Genomic insights into the adaptation of *Acinetobacter johnsonii* RB2-047 to the heavy metal-contaminated subsurface mine environment. *Biometals*, 37, pp. 371-381. DOI:10.1007/s10534-023-00555-0.

Wu, J., Zhou, Y., Jiao, Y., Ran, M. & Li, J. (2025). Antimony-resistant plant growth-promoting bacteria and ferrous iron (Fe^{2+}) synergistically alleviate antimony stress in rice by iron plaque and metabolic regulation. *Journal of Environmental Sciences*, 164, pp. 431-441. DOI:10.1016/j.jes.2025.11.020.

Yang, L., Yang, A., Song, L., Cui, W., Bian, W., Niu, A., Xu, P., He, S., Mei, S. & Shi, X. (2024). Formation of Sb_2O_3 microcrystals by *Rhodotorula mucilaginosa. Journal of Hazardous Materials*, 469. DOI:10.1016/j.jhazmat.2024.134082.

Zhang, T.-T., Wu, A.-H., Aslam, M., Song, J.-Z., Chi, Z.-M. & Liu, G.-L. (2024). Developing *Rhodotorula* as microbial cell factories for the production of lipids and carotenoids. *Green Carbon*, 2, 4, pp. 409-420. DOI:10.1016/j.greenca.2024.09.004.

Zheng, J., Liu, L., Li, Q., Zhao, P., Liao, Q., Li, Q., Yang, Z., Si, M., Ping, Y., Xu, H. & Yang, W. (2024). In situ stabilization of antimony and arsenic in co-contaminated soil using organic matter-Fe/Mn (hydr)oxides colloids and their mineral phase transformation. *Journal of Environmental Sciences*, 156, pp. 835-848. DOI:10.1016/j.jes.2024.10.031.

Zrig, A., Korany, M.S., Sonbol, H., Alsherif, A.E., Hammouda, F., Aldailami, A.D., Mohamed, A.M.Y., Sheteiwy, S.M., Mariduena-Zavala, G.M. & Elsheikh, S.S.Y. (2025). Physiological and biochemical bases of AMF-mediated antimony stress tolerance in *Linum usitatissimum*: enhancing growth, phytochemical production, and oxidative damage resilience. *Plant, Soil and Environment*, 71, 9, pp. 650-665. DOI:10.17221/246/2025-pse.

Archives of Environmental Protection
Vol. 52 no. 3 pp. 16–25

PL ISSN 2083-4772
DOI: 10.24425/aep.2026.3673



© 2026. The Author(s). This is an open-access article distributed under the terms of the Creative Commons Attribution-ShareAlike 4.0 International Public License (CC BY SA 4.0, https:// creativecommons.org/licenses/by-sa/4.0/legalcode), which permits use, distribution, and reproduction in any medium, provided that the article is properly cited.

Effect of a Dehumidifier on the solar drying of sewage sludge-based biomixtures

Małgorzata Helena Makowska[1], Sebastian Kujawiak[1*], Damian Janczak[1], Ariel Antonowicz[2], Bartosz Kucharski[1]

[1]Poznan University of Life Sciences, Department of Hydraulic and Sanitary Engineering, Poland
[2]Poznan University of Technology, Institute of Computing Science, Poland

*Corresponding author's e-mails: sebastian.kujawiak@puls.edu.pl

Keywords: sewage sludge, solar drying, structural additives.

Abstract: One of the methods for treating sewage sludge is drying. In the Polish climate, the period from autumn to spring presents a challenge, rendering the natural sludge drying process inefficient. As an auxiliary measure, a dehumidifier can be employed, which, when combined with the use of biocomponents added to the sludge intended for drying, significantly improves the outcome of the process. The drying of sludge mixtures with additives was conducted during the autumn-winter period in a 10 m² polytunnel, divided into two sections: one unassisted and the other assisted by a dehumidifier. Sludge mixtures supplemented with walnut shells, wood chips, and sawdust, as well as sludge without additives serving as a control sample, were dried. It was found that the application of a dehumidifier, even solely during the initial phase of drying, facilitated a final reduction in the moisture content of the mixtures to 30–20% after just 40–60 days, which is sufficient for their storage, transport, or further utilization. The amount of water evaporated from the mixtures with additives in the assisted section, along with the drying rate, was several times greater. For the sludge without additives, the difference in the amount of evaporated water was as much as 30-fold. The final result achieved for the mixtures with biocomponents, owing to the initial moisture content and the structure of the material being dried, was considerably superior to that of the sludge without additives, a finding previously confirmed in earlier studies conducted under natural conditions during the spring-summer period.

Introduction

One of the stages in the sewage sludge treatment chain is drying, which significantly reduces its volume, alters its structure, promotes sludge hygienization, and increases its calorific value compared to the wet material (Bennamoun 2012; Trojanowska et al. 2012). Due to the high costs associated with drying sewage sludge using conventional methods, there has been growing interest in alternative drying techniques (Hurynovich et al. 2021, Mehrdadi et al. 2007, Przydatek et al. 2020).

Legislative developments require EU Member States to develop and implement sewage sludge management technologies, with particular emphasis on restricting landfill disposal and increasing the proportion of recovery processes. Consequently, processes involving the drying and conversion of sewage sludge into energy or fertilizer products are attracting increasing attention (Werle 2015).

Sewage sludge must be appropriately prepared prior to its natural utilization or thermal treatment (Khan et al. 2023, Mehrardi et al. 2007, Smol et al. 2020). This is necessary primarily due to its high water content, variable concentrations of heavy metals, and varying degrees of sanitary risk (Cesaro et al. 2022, Yusuf et al. 2023). Among the available drying technologies, solar systems are gaining increasing prominence, as they facilitate a reduction in water content with minimal external energy consumption. Under temperate climate conditions, solar dryers can evaporate 1 ton of water while consuming only 13–28 kWh of electrical energy, which is substantially less than conventional thermal dryers, which consume up to 1.2 kWh per kilogram of evaporated water. An additional advantage of solar drying is its suitability for small and medium-sized wastewater treatment plants, particularly in rural areas lacking access to waste heat or district heating networks (Jat Baloch et al. 2023).

The efficiency of solar drying depends on meteorological conditions, meaning that during the winter period, especially in temperate climates, it frequently requires additional support. Another crucial factor is the structure of the material being



Fig. 1. Materials used in the drying tunnel

dried; therefore, the application of additives such as wood chips, walnut shells, or sawdust can substantially improve the efficiency of water evaporation (Kujawiak et al. 2024, Makowska et al. 2025). Furthermore, the use of supplementary biocomponents can improve drying conditions during unfavorable periods, thereby enhancing the physicochemical properties of the resulting biomixture, which can subsequently be utilized for both energy recovery and fertilizer applications (Boguniewicz-Zabłocka et al. 2021, Czekała et al. 2016, Kujawiak et al. 2024a).

Structural additives optimize heat exchange within the system, limit material agglomeration, and facilitate mixing, thereby enabling the entire layer to dry uniformly throughout its cross-section (Li et al. 2021). The importance of the dryer's design and its internal microclimate parameters was highlighted by Sorrenti et al. (2022), Mathioudakis et al. (2013), and Salihoglu et al. (2007). These authors demonstrated that, particularly during periods of low insolation and high relative humidity, the use of a dehumidifier, in addition to mechanical ventilation, can be highly beneficial. It not only stabilizes the relative humidity but can also positively affect the moisture reduction in the deeper layers of the sludge, which typically dry at a significantly slower rate and are more susceptible to clumping.

Krawczyk (2019) demonstrated a clear linear correlation between the so-called drying potential of the ventilation air (defined as the difference between the water vapor saturation level at a given temperature and the current water vapor content) and the instantaneous drying rate of the sludge, particularly during the initial phase of the process, when the moisture gradient between the sludge and the ventilation air is at its peak. As the material dries and cumulative drying potential increases, the efficiency of the process decreases, which is consistent with the classical thin-layer drying model and confirms the existence of clearly defined drying phases: the rapid evaporation of free water, the transitional phase, and the final removal of bound water (An-nori et al. 2020, Bennamoun 2012). Sorrenti et al. (2022) and Bennamoun (2012) indicated that introducing additional assistance to the drying process is most effective during the first 10–20 days of the process. Therefore, the level of process assistance should be adapted to external conditions, the characteristics of the dried material, and the specific phase of drying phase.

The objective of this study was to determine the impact of employing a dehumidifier on the efficiency of the solar drying process of sewage sludge mixed with biocomponents. The study aimed to verify the hypothesis that the use of a dehumidifier as an auxiliary drying aid would improve the microclimatic parameters within the dryer, increase the rate of water evaporation from the sludge mixtures, and consequently reduce the overall drying time.

Materials and methods

The research was conducted in a naturally ventilated polytunnel measuring 2.5 x 4.0 m, located at the experimental farm of the Department of Horticulture, Poznań University of Life Sciences. Two zones were established within the tunnel: one equipped with a dehumidifier and a reference zone without a dehumidifier. Four containers measuring 0.8 x 0.9 m were placed in each zone, containing the biomixtures prepared for drying in four variants: sewage sludge supplemented with walnut shells, sewage sludge supplemented with mixed wood chips, sewage sludge supplemented with sawdust, and sewage sludge without additives (reference sample). The

Table 1: Characteristics of the dried mixtures

Symbol of the mixture	Type of supplement	Sewage sludge mass, kg	Supplement mass, kg	Total mass of the mixture, kg
MS1, BS1	Walnut shells	58.17	17.01	75.18
MS2, BS2	Wood chips	58.17	17.55	75.72
MS3, BS3	Tree sawdust	58.17	8.37	66.54
MS4, BS4	none	116.34	0	116.34



a) b)

Fig. 2. Mixtures prepared for drying; a – zone B, b – zone M

initial thickness of the mixture layer was 15 cm, and the drying surface area of each container was 0.72 m². The materials used in the study are presented in Fig 1.

The arrangement of the containers with the mixtures was designed to ensure a similar layout in both zones (Fig. 2).

In zone B, drying was carried out under natural conditions without assistance. In zone M, drying also occurred under natural conditions but was supplemented with a dehumidifier rated at 0.8 kW and equipped with adjustable capacity, which operated continuously during the first 30 days of the process. The capacity of the dehumidifier was 270 m³ of air per hour. The mixtures in both zones were manually turned once a day. A maximum of 60 liters of leachate was collected over a 24-hour period.

To monitor the air parameters inside the tunnel, automatic sensors measuring air temperature and relative humidity were installed both beneath the roof of the dryer and directly within the material being dried in each container. Measurements were recorded continuously, enabling the analysis of daily variations in temperature and humidity. External meteorological data (air temperature, relative humidity, and insolation) were obtained from the official meteorological station of the Department of Horticulture located at Poznań–Ławica. The experiment lasted 80 days, from the end of September to mid-December 2024.

The moisture content of the mixtures was analyzed at regular intervals of 2–3 days. A composite sample was collected from each container and transported to the analytical laboratory of the Department of Water and Sanitary Engineering at Poznań University of Life Sciences. The determination of total and organic suspended solids was conducted using the direct gravimetric method in accordance with the PN-EN 872 standard. Based on these measurements, the following parameters were calculated using Eqs. (1-7):

$$H_{\%} = \frac{m_{aq}}{m_w} \cdot 100\% \quad (1)$$

where: $H_{\%}$ – moisture content of the mixture, %,
m_{aq} – mass of water contained in the mixture, g,

$$m_{aq} = m_w - m_{og} \quad (2)$$

m_w – mass of the wet mixture, g,
m_{og} – total dry mass of the mixture, g,

$$W = \frac{m_{aq}}{m_w} \cdot 1000 \quad (3)$$

where: W – water content in the mixture, kg/kg,

$$\Delta W = (W_0 \cdot M_0 - W_k \cdot M_k) \cdot 10^{-3} \quad (4)$$

where: ΔW – amount of water evaporated from the mixture, kg,
W_0 – water content of the mixture before drying, g/kg,
W_k – water content of the mixture after drying, g/kg,
M_0 – total initial mass of the mixture before drying, kg,
M_k – final total mass of the mixture after drying, kg,

$$\Delta W_m = \frac{\Delta W}{M_0} \quad (5)$$

where: ΔW_m – amount of water evaporated from the mixture per unit of the total initial mass of the mixture, kg/kg,

$$\Delta W_p = \frac{\Delta W}{A} \quad (6)$$

where: ΔW_p – amount of water evaporated from the mixture per unit of drying surface area, kg/m²,
A – drying surface area, m²,

$$\Delta W_{sm} = \frac{\Delta W}{M_{sm}} \quad (7)$$

where: ΔW_{sm} – amount of water evaporated from the mixture per unit of the dry mass of the mixture, kg/kg dm,
M_{sm} – dry mass of the mixture, kg.

The research results were compiled and presented in tabular and graphical form. The coefficient of determination (R^2) was calculated for the drying curves.

The energy consumption to support the drying process was also determined in relation to the overall results achieved. The resulting indicators, calculated per unit of sludge volume, evaporated water volume, and drying surface area, were compared with data available in the literature.

Results

The course of the drying process is directly influenced by the air parameters both outside and inside the dryer. Table 2 presents the environmental parameters of the mixtures being dried in both zones of the dryer, including insolation, air temperature, and air humidity. These environmental conditions directly influenced the temperature and moisture content of the mixtures being dried.

Figure 3 presents the average daily values of air temperature inside and outside the tunnel. During the initial phase of drying, the external air temperature fluctuated from a few to over a dozen °C, and the air temperature inside the tunnel was a few degrees higher, with the MS zone containing higher temperatures than the BS zone. During the second phase of drying, when the external air temperature fell below 10 °C and occasionally below 0 °C, the temperatures inside the tunnel

Table 2: Parameters of the environment and the examined mixtures

Drying zone		Zone BS				Zone MS			
Mixture		BS1	BS2	BS3	BS4	MS1	MS2	MS3	MS4
Insolination, MJ/m²									
	min.	0.0039				0.0039			
	max.	9.3786				9.3786			
Temp. outside, ⁰C									
	min.	-1.34				-1.34			
	max.	17.51				17.51			
Temp. inside, ⁰C									
	min.	- 1.07				- 1.25			
	max.	25.82				27.90			
Humidity outside, %									
	min.	49.68				39.57			
	max.	100.00				100.00			
Temp. of mixture, ⁰C									
	initial	25.32	26.15	24.67	26.09	21.63	21.62	21.64	21.64
	final	7.49	8.12	6.85	4.44	7.98	7.98	7.99	9.02
	min.	1.20	1.00	0.73	1.34	- 0.31	- 0.51	- 0.01	0.32
	max.	25.32	36.85	26.44	26.09	28.65	43.37	36.56	28.29
Humidity of mixture, %									
	initial	67.44	68.38	76.31	86.14	72.86	69.38	77.22	86.86
	final	52.19	50.69	58.82	84.84	20.83	21.12	22.67	65.13
	min.	47.80	50.56	56.81	84.48	18.46	20.41	16.81	65.13
	max.	68.05	68.38	76.31	86.59	72.86	69.38	77.22	86.86

became comparable in both zones. Similar to the external conditions, the air temperature inside the tunnel decreased from more than 20 °C at the beginning of the process to only a few °C at the end. Overall, the difference between the initial and final air temperatures, both outside and inside the tunnel, exceeded 10 °C.

Fig. 4 presents the measured changes in air humidity inside and outside the dryer. This parameter exhibited considerable variability; however, during the operation of the dehumidifier, the humidity in the assisted MS zone was up to 40% lower than that in the unassisted BS zone. During the late autumn and winter periods, the air humidity in both zones periodically reached 100%.

The changes in air temperature and the temperature of the mixtures being dried were influenced by the variation in solar radiation intensity during the autumn-winter study period (Fig. 5).

Figure 6 illustrates the changes in the temperature of the mixtures in the BS and MS zones during the drying process, as measured by the installed sensors. Similar to the ambient air temperature, the temperature of the mixtures gradually decreased from maximum values of 30–40 °C to minimum values below 10 °C. However, in the assisted MS zone, the diurnal temperature fluctuations and the differences between consecutive days were less pronounced. A direct comparison of mixtures with identical initial compositions dried under different conditions indicates that, during the initial phase of drying (approximately the first 20–30 days), the temperature of the assisted mixtures was higher for most of the time. This was associated with the more rapid evaporation of water, further

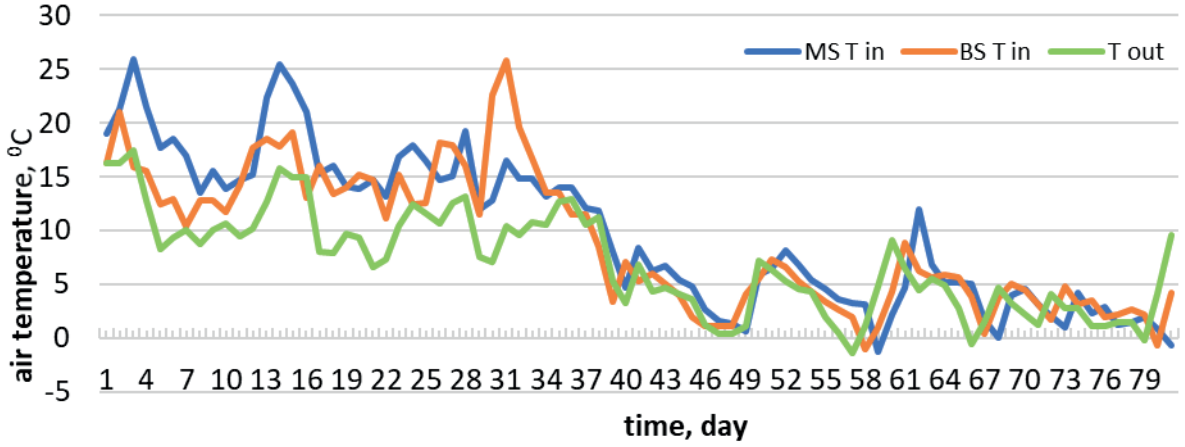


Fig. 3. Changes in air temperature inside and outside the drying room

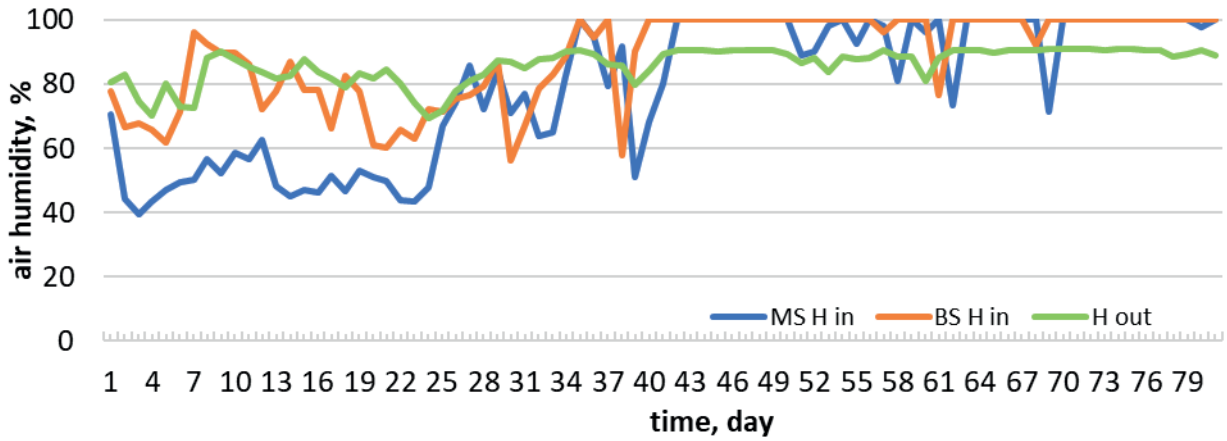


Fig. 4. Changes in air humidity outside and inside the drying room

enhanced by the operation of the dehumidifier. Although the dehumidifier was switched off after the first four weeks of the experiment, the elevated temperature of the assisted mixtures persisted for several additional days. During the second phase of drying, the temperature of the mixtures that had received assistance during the initial phase was lower than that of the unassisted mixtures.

Based on laboratory analyses of the moisture content of the mixture samples, drying curves were constructed using Eqs. (1) to (3), (Fig. 7). The drying of the mixtures in the tunnel section without the dehumidifier proceeded very slowly and inefficiently. After 80 days of the experiment, the moisture content of the sludge mixtures containing additives had decreased by more than 20percentrage points relative to the initial value, resulting in a final water content of 50–60%. In contrast, the moisture content of the sludge without additives decreased by only a few percentage points.

The drying of the identical mixtures in the tunnel section assisted by a dehumidifier proceeded considerably faster and with greater efficiency. After only 60 days, the moisture content of the mixtures had decreased to approximately 20% and was 30–40 percentage points lower than in the unassisted zone, representing a highly favorable result under autumn-winter conditions. No further significant reduction in moisture content was observed during the subsequent 20 days of drying. The drying of the sludge without additives was less effective, confirming the previously reported positive effect of additives on the efficiency of sewage sludge drying (Makowska et al. 2025). The dehumidifier was switched off after 30 days of the experiment; however, this did not adversely affect the final drying outcome, indicating that the initial drying period is crucial for modifying the structure of the material being dried and promoting water removal. Similar observations have been reported in Germany, where the application of underfloor heating or forced-air ventilation increased drying efficiency by 20-30% (https://www.eurotech.net.pl/ist.php).

Fig. 8 presents the drying rate curves for the examined mixtures. During the initial phase of the process, the drying rate in the assisted MS zone was approximately three times higher than that in the unassisted BS zone. Approximately a dozen or so days after the deactivation of the dehumidifier, the drying rate of mixtures MS1, MS2, and MS3 continued to increase. In contrast, the drying rate of the mixtures in the unassisted zone was highest in the initial phase of drying and subsequently showed only a marginal increase.

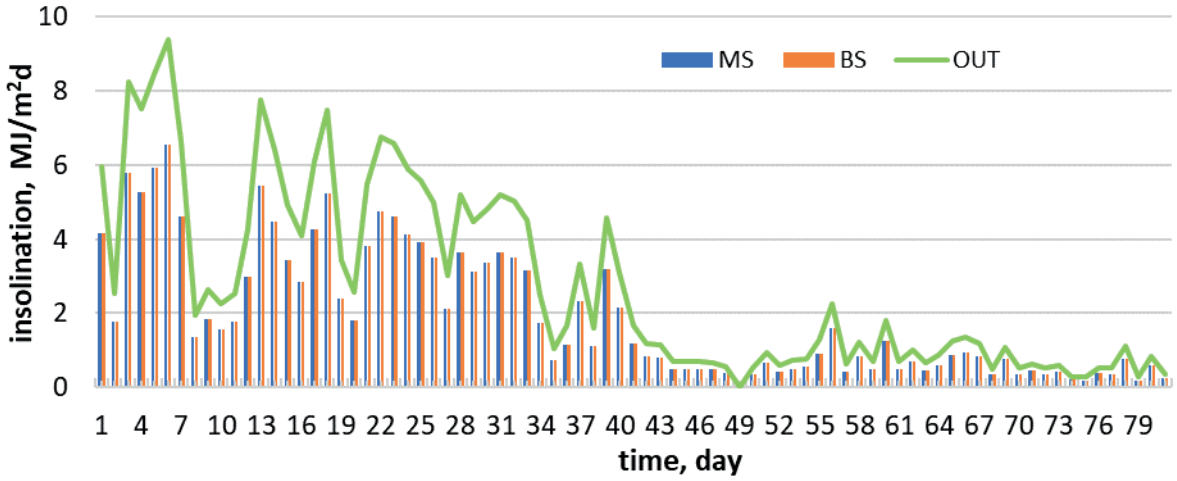


Fig. 5. Variation in solar radiation intensity during the research period; MS – assisted section, BS – unassisted section, OUT – outside the tunnel

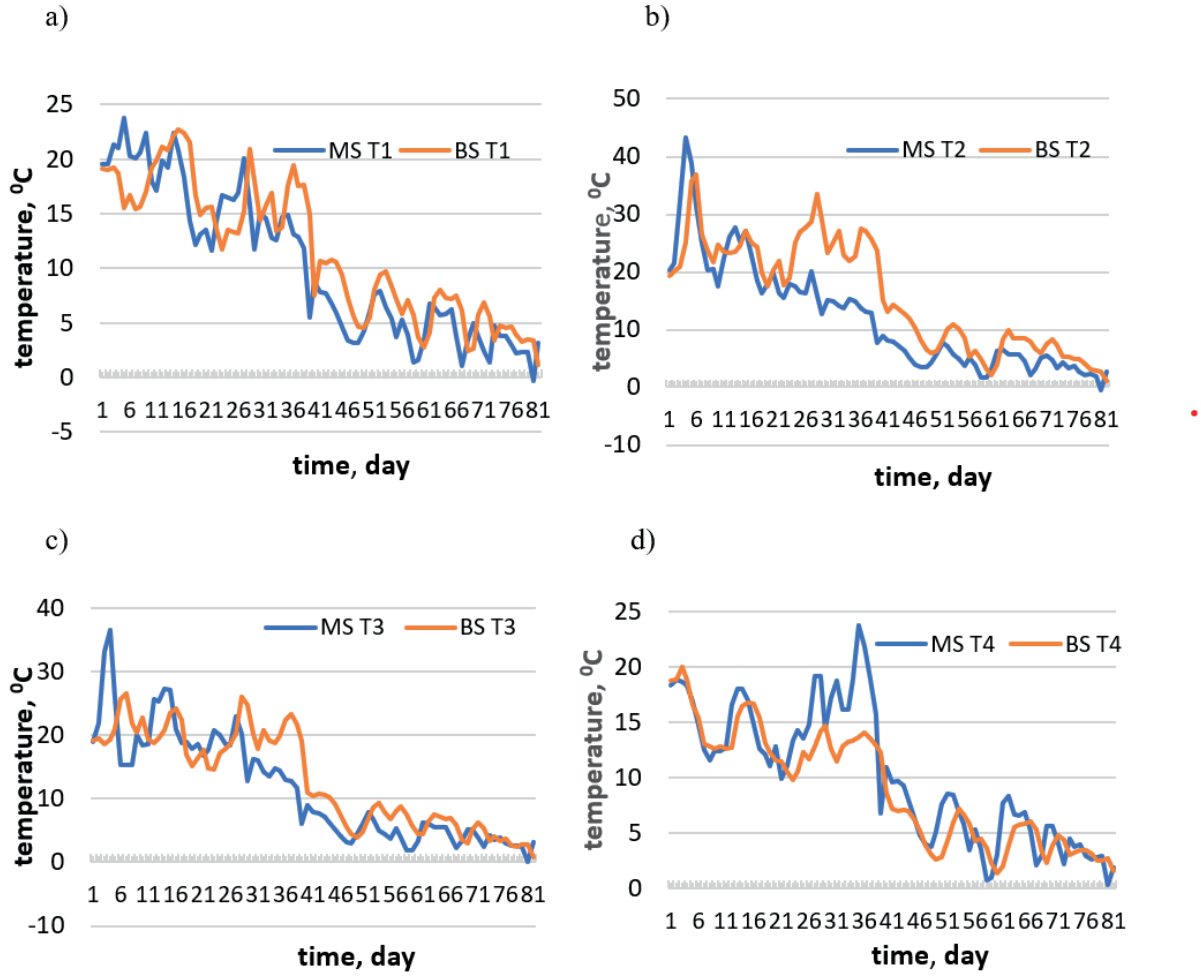


Fig. 6. Changes in the average daily temperature of the mixtures over time: a – MS1 and BS1, b – MS2 and BS2, c – MS3 and BS3, d – MS4 and BS4

A coefficient of determination greater than 0.8 is considered to indicate good fit, whereas values between 0.6 and 0.8 indicate a satisfactory fit. These correspond to correlation coefficients (the square root of the coefficient of determination) of 0.7746 and 0.8944, respectively. In general, a correlation coefficient exceeding 0.7 is regarded as indicative of a good fit. According to Szydłowski (1978), for a significance level of $\alpha = 0.05$ and the number of points in the graphs—16 and 23—the corresponding critical correlation coefficients are 0.4227 and 0.4683, respectively. In conclusion,the fitted models can be considered statistically significant and representative of the experimental data.

The drying rate of the sludge without additives in the assisted zone was comparable to that observed in the unassisted zone, demonstrating that the application of additives was responsible for improving the drying performance of the sewage sludge mixtures.

Using Eqs. (4) to (7), the amount of water evaporated during the drying of the mixtures was calculated (Fig. 9). The results showed that the total amount of evaporated water, as well as the amounts expressed per unit of the total mass and dry mass of the mixtures, was consistently greater under assisted drying than under unassisted drying. For the mixtures containing biocomponents, the amount of evaporated water in the MS zone was 1.3 to 3.4 times greater than that in the BS zone. The highest values were obtained for the mixtures containing sawdust and walnut shells in the MS zone and for the mixtures containing sawdust and wood chips in the BS zone. In the case of the sludge without additives (control sample), the difference was as much as 30-fold.

During the drying process, the organic matter content in the mixtures was also analyzed. Fig. 10 illustrates the organic matter content of the examined mixtures, expressed on a dry matter basis, at the beginning and end of the drying process. A decrease of several percentage points indicated that mineralization of organic substances occurred during drying.

An important aspect of the process is the amount of energy required to support drying. During the study, the energy consumption amounted to 1.235 kWh/kg of evaporated water. Compared with the value of 1.750 kWh/kg of evaporated water reported by Trojanowska (2010) for a dryer equipped with underfloor heating, this represents a favorable result for the proposed solution. The energy consumption per unit of drying surface area was 97.24 kWh m^2, which is significantly higher compared to 311 kWh reported for the dryer in Kłodzko (Trojanowska et al. 2012). Comparison with studies conducted in regions characterized by substantially higher solar radiation are less meaningful due to the much greater contribution of solar energy, including its storage, as reported, for example, in Chile (Poblete and Pinemal 2020).

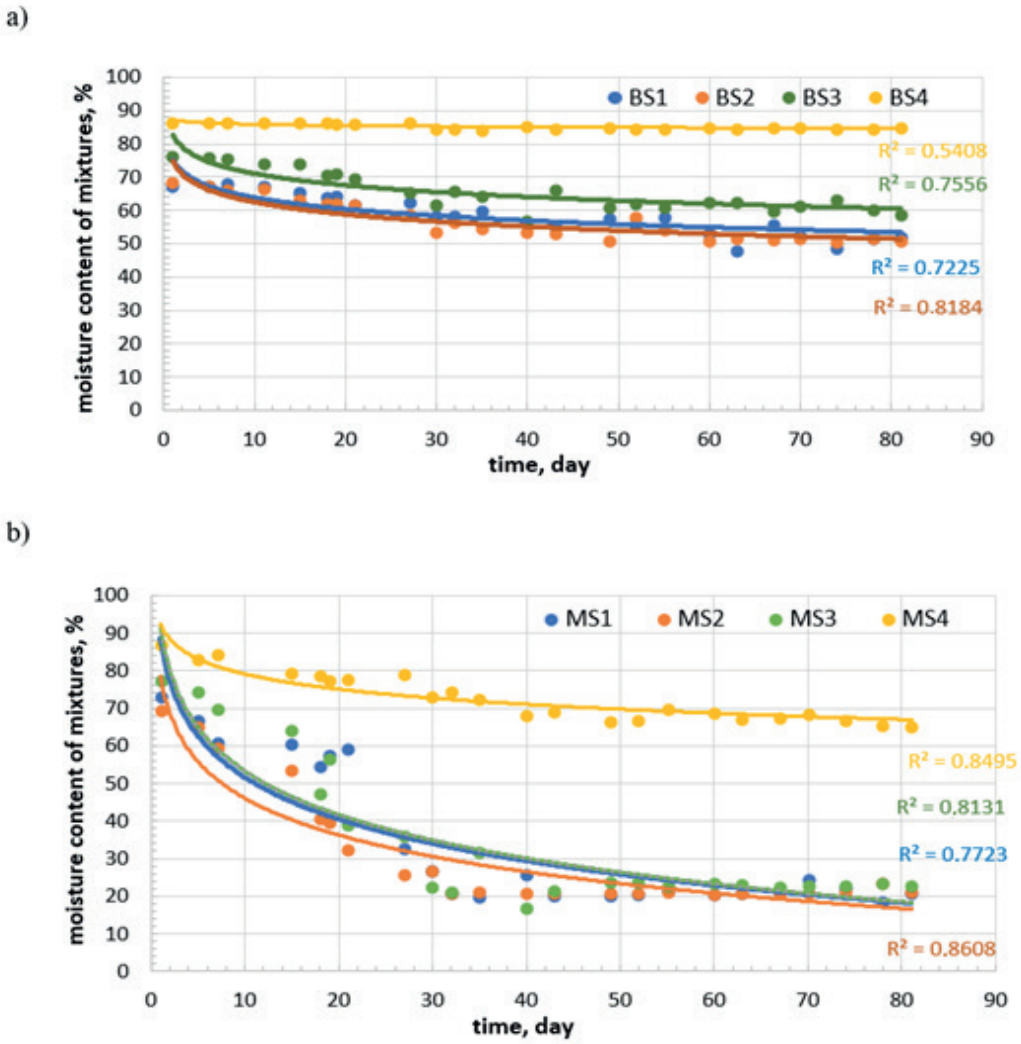


Fig. 7. Drying curves of the mixtures: a – unassisted BS section, b – assisted MS section

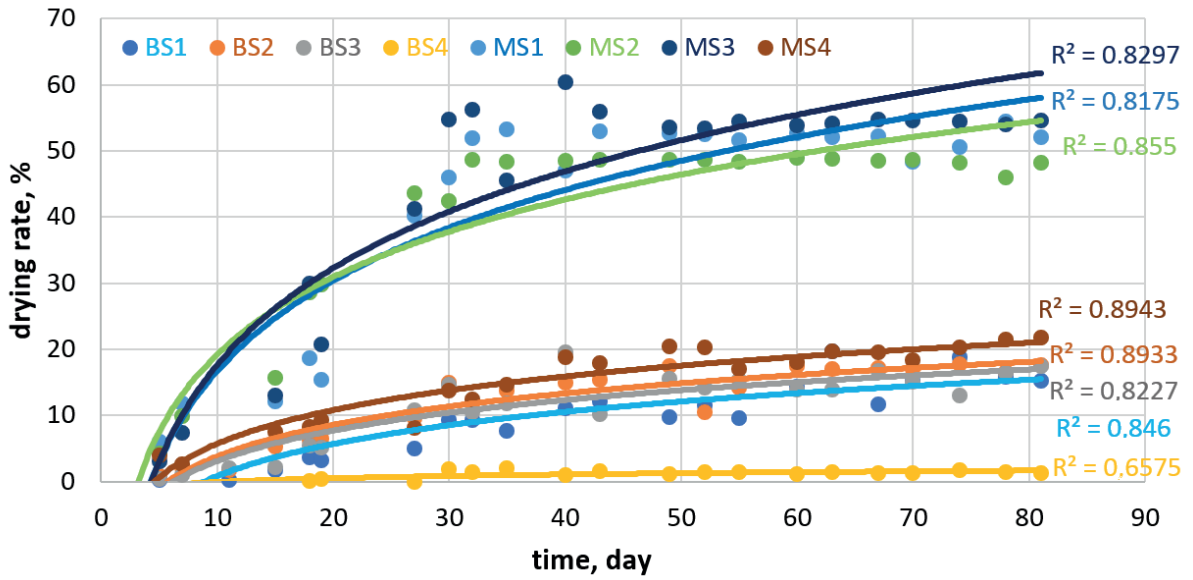


Fig. 8. Drying rate curves of the tested sludge mixtures with biocomponents

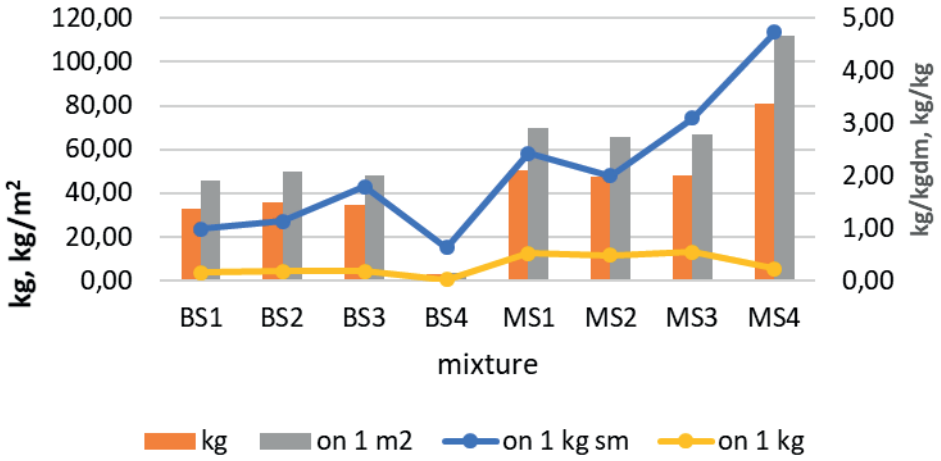


Fig. 9. Amount of water evaporated from the mixtures being dried

Conclusions

The pilot-scale study on the drying of sewage sludge with biocomponents in a polytunnel dryer clearly demonstrated the positive effect of using a dehumidifier as an auxiliary component in the drying process. During the initial 30-day drying period, the relative humidity in the assisted zone was lower, whereas the air temperature was higher than in the unassisted zone, resulting in improved drying conditions and enhanced process efficiency. After 30 days of the dehumidifier operation, the moisture content of the mixtures in the assisted zone was 20 to 30 percentage points lower than that in the unassisted zone, despite identical initial values. Although the dehumifier was switched off after this period, the moisture content of the assisted mixtures decreased to approximately 20% during the subsequent 30 days, a level sufficient for the transport and further utilization of the dried material. The uniform progression of drying following the deactivation of the dehumidifier indicates that the initial stage of the process is critical to the final drying outcome. The amount of water evaporated from the mixtures in the assisted zone was more than three times greater than in the zone without dehumidifier assistance. The study also confirmed the beneficial impact of the bio-additives on the drying process. Although drying of the sludge without additives proceeded more effectively in the assisted zone than in the unassisted zone, the process remained slow , resulting in a final reduction in moisture content of only 20%. The application of a dehumidifier as an auxiliary drying device is a simpler and less energy-intensive solution than a hybrid system based on heat pumps and underfloor heating. Combined with the use of structural additives, it may represent a favorable option for small and medium-sized wastewater treatment plants.

The proposed system is easy to implement in solar sewage sludge dryers of any size. When combined with the dryer's ventilation system (air inlets and exhaust vents) and a sewage sludge turner, it can significantly reduce the sludge drying time. A considerable reduction in the moisture content of the sludge also decreases its volume, facilitating storage when immediate utilization is not possible and reducing transport costs. Furthermore, the dried sludge can be used for energy recovery, for example, through co-incineration, provided that it meets the combustion requirements for this type of material.

Acknowledgements

This research was financed by the Polish Minister of Science and Higher Education under the Strategy of the Poznań

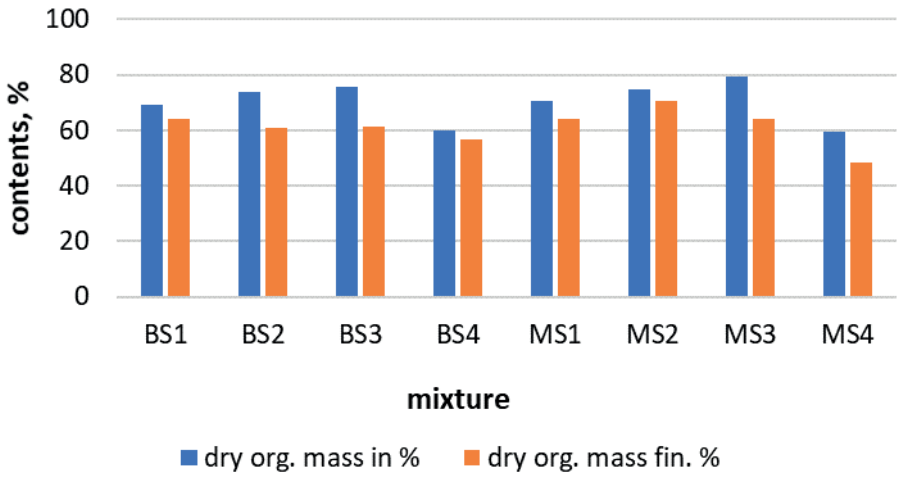


Fig. 10. Change in the dry organic matter content in the tested mixtures

University of Life Sciences for 2024–2026 to enhance scientific research and development in priority research areas. The study was supported through the Junior Grant program(Grant No 36/ PREIDUB/JUNIOR/2024.

Patents

The results presented in this publication formed the basis of Polish patent application No. P.445919, entitled „Technology for the use of natural materials in the solar drying of sewage sludge and production of sewage sludge-based briquettes".

References

An-Nori, A.; El Fels, L., Ezzariai, A.; El Gharous, M., El Mejahed, K. & Hafidi, M. (2020). Effects of solar drying on heavy metals availability and phytotoxicity in municipal sewage sludge under semi-arid climate. *Environmental Technology Innovation*, 19, 101039. DOI:10.1016/J.ETI.2020.101039

Bennamoun, L. (2012). Solar drying of wastewater sludge: A review. Renewable and *Sustainable Energy Reviews*, 16(1), pp. 1061–1073. DOI:10.1016/j.rser.2011.10.005

Boguniewicz-Zabłocka, J.; Klosok-Bazan, I. & Capodaglio, A.G. (2021). Sustainable management of biological solids in small treatment plants: Overview of strategies and reuse options for a solar drying facility in Poland. *Environmental Science and Pollution Research*., 28(19), 24680. DOI:10.1007/S11356-020-10200-9

Cesaro, A., Pirozzi, F., Zafırakou, A. & Alexandraki, A. (2022). Microplastics in sewage sludge destined to anaerobic digestion: The potential role of thermal pretreatment. *Chemosphere*, 309, 136669. DOI:10.1016/J.CHEMOSPHERE.2022.136669.

Czekała, W., Dach, J., Janczak, D., Smurzyńska, A., Kwiatkowska, A. & Kozłowski, K. (2016) Influence of maize straw content with sewage sludge on composting process. *Jurnal Water Land Development*, 301, pp. 43–49. DOI:10.1515/JWLD-2016-0020.

Eurotech (2026) https://www.eurotech.net.pl/ist.php

Hurynovich, A., Kwietniewski, M. & Romanovski, V. (2021) Evaluation of the possibility of utilization of sewage sludge from a wastewater treatment plant-case study. *Desalination Water Treatment*, 227, pp. 16–25. DOI:10.5004/dwt.2021.27199

Jat Baloch, M.Y., Zhang, W., Sultana, T., Akram, M., Shoumik, B.A., Al Khan, M.Z. & Farooq, M.A. (2023). Utilization of sewage sludge to manage saline–alkali soil and increase crop production: Is it safe or not? *Environmental Technology Innovation*. 32, 103266. DOI:10.1016/J.ETI.2023.103266.

Khan, R., Shukla, S., Kumar, M., Zuorro, A. & Pandey, A. (2023) Sewage sludge derived biochar and its potential for sustainable environment in circular economy: Advantages and challenges. *Jurnal Chemical Enginering*. 471, 144495. DOI:10.1016/J.CEJ.2023.144495.

Krawczyk, P. (2019). The relative change of drying rate as a function of the cumulative ventilation air drying potential in a thin-layer solar drying facility. *Renewable Energy*, 140, pp. 413–421. DOI:10.1088/1757-899X/556/1/012055

Kujawiak S., Makowska M., Waliszewska B., Janczak D., Brózdowski J., Czekała W. & Zyffert A. (2024): The Influence of Drying Sewage Sludge with the Addition of Walnut Shells on Changes in the Parameters and Chemical Composition of the Mixture, *Energies*, 17, 4701. DOI:10.3390/en17184701

Kujawiak, S., Makowska, M., Janczak, D., Czekała, W., Krzesiński, W., Antonowicz, A. & Kupryaniuk, K. (2024a). An Analysis of the Physicochemical and Energy Parameters of Briquettes Manufactured from Sewage Sludge Mixtures and Selected Organic Additives. *Energies*, 17(18), 4573. DOI:10.3390/en17184573

Li, Z., Zhang, H. & Yin, C. (2021). Influencing factors of the drying rate of sludge for solar drying chamber. *IOP Conference Series: Earth and Environmental Science*, 626(1), 012024. DOI: 10.1088/1755-1315/626/1/012024

Makowska M., Kujawiak S., Janczak D., Miler P. & Czekała W. (2025): Analysis of Sewage Sludge Drying Parameters Using Different Additives. *Sustainability*, 17, 6500, DOI:10.3390/su17146500

Mathioudakis, V., Kapetanios, E. & Psaroudaki, M. (2013). Sewage sludge solar drying: Experiences from the first pilot-scale application in Greece. *Desalination and Water Treatment*, 51(40–42), 7676–7684. DOI:10.1080/07373937.2012.744998

Mehrdadi, N.; Joshi, S.G.; Nasrabadi, T. & Hoveidi, H.(2007) Aplication of solar energy for drying of sludge from pharmaceutical industrial waste water and probable reuse. *International Journal Environmental Research* 1, pp. 42–48.

Poblete R. & Pinemal O. (2020): Improvement of the solar drying process of sludge using thermal storage. *Journal of Environmental Management,* 255, 109883. DOI:10.1016/j.jenvman.2019.109883

Przydatek, G. & Wota, A.K. (2020) Analysis of the comprehensive management of sewage sludge in Poland. *Journal of Material Cycles and Waste Management*, 22, pp. 80–88. DOI: 10.1007/s10163-019-00937-y

Salihoglu, N. K., Salihoglu, G. & Tüsek, A. (2007). Solar drying in sludge management in Turkey. *Renewable Energy*, 32(10), pp. 1661–1675. DOI:10.1016/j.renene.2006.08.001

Smol, M.(2020) Inventory of Wastes Generated in Polish Sewage Sludge Incineration Plants and Their Possible Circular Management Directions. *Resources*, 9, 91. DOI:10.3390/RESOURCES9080091.

Sorrenti, G., Di Girolamo, G. & Bigi, A. (2022). Enhanced sewage sludge drying with a modified solar greenhouse. *Clean Technologies*, 4(1), pp. 375–388. DOI:10.3390/cleantechnol4020025

Szydłowski H. (1978): Measurement theory. PWN, Warszawa 1978

Trojanowska K. (2010): Energy Aspects of Solar Sewage Sludge Drying. Sewage Treatment and Sewage Sludge Processing, University of Zielona Góra.

Trojanowska, M., Sadecka, Z., Myszograj, S. & Sieciechowicz, K. (2012). The effect of the method used to dry sewage sludge in solar dryers on its quality. *Environmental Engineering*, 30, pp. 84–96.

Werle, S. (2015). Sewage sludge-to-energy management in Eastern Europe: a Polish perspective. *Ecological Chemistry and Engineering* Science, 22(3), pp. 459–469. DOI:10.1515/ECES-2015-0027

Yusuf, H.H.; Roddick, F.; Jegatheesan, V.; Gao, L. & Pramanik, B.K.(2023) Tackling fat, oil, and grease FOG build-up in sewers: Insights into deposit formation and sustainable in-sewer management techniques. *Science Total Environmental*. 904, 166761. DOI:10.1016/J.SCITOTENV.2023.166761

Wpływ pochłaniacza wilgoci na proces suszenia solarnego biomieszanek na bazie osadu ściekowego

Streszczenie: Jedną z metod przeróbki osadów ściekowych jest ich suszenie. Wykorzystanie w tym celu energii słonecznej jest korzystne pod względem ekonomicznym oraz umożliwia stosowanie procesu suszenia w małych i średnich obiektach oczyszczających ścieki. Jednak w polskim klimacie problemem jest okres roku od jesieni do wiosny, kiedy intensywność promieniowania słonecznego i temperatura powietrza spadają i proces naturalnego suszenia jest mało efektywny. Jako wspomaganie, zamiast dodatkowego ogrzewania suszarni słonecznej, można zastosować pochłaniacz wilgoci, który w połączeniu z wykorzystaniem biokomponentów dodawanych do osadu przeznaczonego do suszenia zdecydowanie poprawia efekt procesu. Suszenie mieszanek osadu z dodatkami przeprowadzono w okresie jesienno- zimowym, w tunelu ogrodowym o powierzchni 10 m^2 , podzielonym na dwie sekcje: bez wspomagania i ze wspomaganiem pochłaniaczem wilgoci. Suszono mieszanki osadu z dodatkiem łupin orzecha włoskiego, zrębków drzewnych i trocin oraz osad bez dodatków będący próbą kontrolną. Stwierdzono, że zastosowanie pochłaniacza wilgoci już tylko w pierwszej fazie suszenia pozwoliło na końcowe obniżenie wilgotności mieszanek do 30-20% już po 40–60 dniach, co jest wystarczające dla ich magazynowania, transportu lub dalszego wykorzystania. Ilość odparowanej wody z mieszanek z dodatkami w sekcji ze wspomaganiem, podobnie jak szybkość suszenia, była kilkukrotnie większa. Dla osadu bez dodatków różnica w ilości odparowanej wody była nawet 30-to krotna. Efekt końcowy uzyskany dla mieszanek z biokomponentami ze względu na wyjściowe uwodnienie i strukturę suszonego materiału był zdecydowanie lepszy, niż dla osadu bez dodatków, co stwierdzono już we wcześniejszych badaniach, prowadzonych w warunkach naturalnych w okresie wiosenno-letnim.

Archives of Environmental Protection
Vol. 52 no. 3 pp. 26–33

PL ISSN 2083-4772
DOI: 10.24425/aep.2026.3674



© 2026. The Author(s). This is an open-access article distributed under the terms of the Creative Commons Attribution-ShareAlike 4.0 International Public License (CC BY SA 4.0, https:// creativecommons.org/licenses/by-sa/4.0/legalcode), which permits use, distribution, and reproduction in any medium, provided that the article is properly cited.

Comparative study of acetaminophen and 4-methoxyphenol toxicity

Marzena Matejczyk[1*], Krzysztof Kurek[2], Andrzej Kaźmierczak[3], Piotr Ofman[4], Józefa Wiater[5], Ruslan Oblap[6], Paweł Kondzior[1], Ewelina Omelianowicz[1]

[1]Bialystok University of Technology, Faculty of Civil Engineering and Environmental Sciences, Department of Chemistry, Biology and Biotechnology, Bialystok, Poland.
[2]Medicał University of Bialystok, Department of Gastroenterology and Internal Medicine, Bialystok, Poland
[3]Department of Cytophysiology, Institute of Experimental Biology Faculty of Biology and Environmental Protection, University of Łódź,, Poland.
[4]Bialystok University of Technology, Department of Environmental Engineering Technology, Bialystok, Poland
[5]Department of Agri-Food Engineering and Environmental Management, Bialystok University of Technology, Bialystok, Poland
[6]Jan Kochanowski University in Kielce, Collegium Medicum, Department of Surgical Medicine with the Laboratory of Medical Genetics, Kielce, Poland

*Corresponding author's e-mails: Marzena Matejczyk, e-mail: m.matejczyk@pb.edu.pl

Keywords: biodegradation; acetaminophen; 4-methoxyphenol; toxicity; soil; water.

Abstract: Acetaminophen (APAP, paracetamol) is one of the most widely used human drugs, and simultaneously, one of the most frequently detected pharmaceutical micropollutants in environmental matrices. The major metabolites of acetaminophen are generally considered to be glucuronide and sulfate conjugates, p-aminophenol, hydroquinone, and NAPQI, while 4-MP may occur as one of the transformation products under specific environmental degradation pathways. Determining and comparing the toxicity of these compounds is crucial for environmental and public health. In this study, the toxicity of APAP and 4-MP was assessed using two model microorganisms, *Escherichia coli* ATCC-25922 and *Candida albicans* ATCC-1023, based on growth inhibition. The susceptibility of microorganisms belonging to the human microbiome (*E. coli*, *E. hormaechei*, *S. epidermidis*, *L. rhamnosus*, and *C. albicans*) to both compounds was determined by calculating the minimum inhibitory concentrations (MICs). Genotoxicity was estimated using the genotoxin-sensitive *recA* promoter in *E. coli* RFM443 *recA*::*luxCDABE*. Reactive oxygen species (ROS) production was measured in *E. coli* exposed to both compounds at concentrations of 0.1, 1, 10, 100, and 1000 mg·L^{-1} as an oxidative stress indicator. Comparative analysis revealed similar sensitivity of *E. coli* and *C. albicans* to both compounds at 100 mg·L^{-1}, though at 10 mg·L^{-1}, 4-MP exerted a stronger inhibitory effect on both strains than APAP. MIC assays showed that *E. coli* and *E. hormaechei* were more sensitive to 4-MP than to APAP, while no significant differences were observed for the remaining strains. APAP demonstrated a stronger genotoxic effect than 4-MP in *E. coli* cells. ROS data indicate that oxidative stress is the primary molecular mechanism underlying the toxicity and genotoxicity of both compounds. Future studies should investigate the toxicity of APAP and 4-MP mixtures under environmentally relevant exposure conditions.

Introduction

The contamination of water resources with pharmaceuticals and their metabolites is a significant global problem. Pharmacologically active compounds, including antibiotics and hormones, have been detected in all aquatic and water-related compartments (Lunghi et al. 2025), causing negative effects on living organisms and having long-term consequences for human health through the development of antimicrobial resistance (AMR) (Ossowicz-Rupniewska et al., 2023). In response to these threats, the European Union has established a comprehensive legal framework for the protection of water resources, most notably through the Water Framework Directive 2000/60/EC and Council Directive 98/83/EC on the quality of water intended for human consumption, implemented in Poland through the Water Law Act (Dz. U. poz. 2294, 2017, Cybulski et al. 2021, Szymański et al., 2026).

The environmental concern is acetaminophen, a fully synthetic aromatic amide of the aniline derivative class, with

a para-substituted benzene ring bearing a hydroxyl and an acetamido group. APAP is one of the most widely consumed over-the-counter analgesic and antipyretic agents worldwide (Chacón et al. 2022), marketed under several trade names, of which acetaminophen, paracetamol, and N-acetyl-p-aminophenol (APAP) are the most widely recognized. Its molecular formula is $C_8H_9NO_2$, and its molecular weight is 151.16 $g \cdot mol^{-1}$. The compound is a white, odorless, crystalline solid with moderate water solubility (1:70 at room temperature; 1:20 at 100°C), a pK_a of 9.5–9.7, and an octanol-water partition coefficient of 3.2. These physicochemical properties facilitate its mobility and persistence in aquatic environments (IARC, 1990; Mészáros et al. 2022).

Conventional wastewater treatment technologies, including the activated sludge process, frequently fail to achieve complete removal of APAP, resulting in its continuous discharge into surface waters and soils. Concentrations in surface waters reach up to 10 $\mu g \cdot L^{-1}$, in groundwater used for drinking water supply up to 1.89 $\mu g \cdot L^{-1}$ (Li et al. 2014; Pandey et al. 2024), in contaminated soils below 100 $\mu g \cdot kg^{-1}$, and in biosolids up to 1400 $\mu g \cdot kg^{-1}$ (Chacón et al. 2022; Tomczyk and Urbaniak 2025), with the highest recorded concentration reaching approximately 107 $\mu g \cdot L^{-1}$. Evidence of paracetamol bioaccumulation in both flora and fauna, together with its detection at substantial concentrations in multiple environmental matrices, underscores the risks this compound poses to ecological balance and human health (Pandey et al. 2025). Numerous studies have demonstrated that APAP induces reproductive disruption, DNA damage, and oxidative stress in aquatic organisms, and has been associated with nephrotoxicity, myocardial infarction, hepatic damage, and impaired fetal development in humans and animals (Li et al. 2014; Pandey et al. 2024). Paracetamol use during pregnancy may increase the risk of attention-deficit/hyperactivity disorder (ADHD) and autism spectrum disorder (ASD; Bührer et al. 2021). Furthermore, regular paracetamol use has been associated with a 28% higher risk of developing liver cancer (Tian et al. 2024).

Experimental studies have shown that the major metabolites of APAP include glucuronide and sulfate conjugates, p-aminophenol, hydroquinone, and NAPQI. In turn, a study by Li et al. (2014), which utilized both ^{14}C isotope labeling and LC-MS/MS techniques, and other studies confirmed the presence of 4-MP as one of the transformation products formed through specific environmental degradation pathways (Li et al. 2014; Żur et al. 2018; Chacón et al. 2022; Yisau et al. 2024; Pandey et al. 2024, 2025; Fig. 1). The possible biodegradation pathway of APAP, with 4-MP as a one of the metabolites formed, is presented in Fig. 1 (adapted from Żur et al. 2018 and Pandey et al. 2025).

4-MP is widely used across multiple industrial sectors, including the pharmaceutical, agricultural, and cosmetic industries, and has been detected in aquatic and terrestrial environments at concentrations ranging from $ng \cdot L^{-1}$ to $\mu g \cdot L^{-1}$. Studies have shown that 4-MP inhibits the synthesis of DNA, RNA, and proteins, causing skin irritation, disruption of reproductive function, and exhibiting mutagenic, genotoxic, and carcinogenic properties in both humans and animals (Asakawa et al. 1994; Miyachi et al. 2005; Rahman et al. 2017; Saeed et al. 2024). Despite the widespread environmental occurrence of paracetamol, comparative toxicological data on its effects on soil microorganisms and the human microbiome remain scarce. In this experimental work, we tested the following research hypothesis: 4-MP, the transformation product formed as a result of acetaminophenol degradation in soil, exhibits toxic, genotoxic, and oxidative stress-inducing activity. The present study comparatively assessed the toxicity, genotoxicity, and oxidative stress-generating potential of APAP and 4-MP using strains of *E. coli* ATCC-25922 and *C. albicans* ATCC-10231. Based on minimum inhibitory concentration (MIC) values, the susceptibility of microorganisms constituting the human microbiome was further compared among *E. coli*, *E. hormaechei*, *S. epidermidis*, *L. rhamnosus*, and *C. albicans*. The results contribute to understanding the impact of paracetamol and its

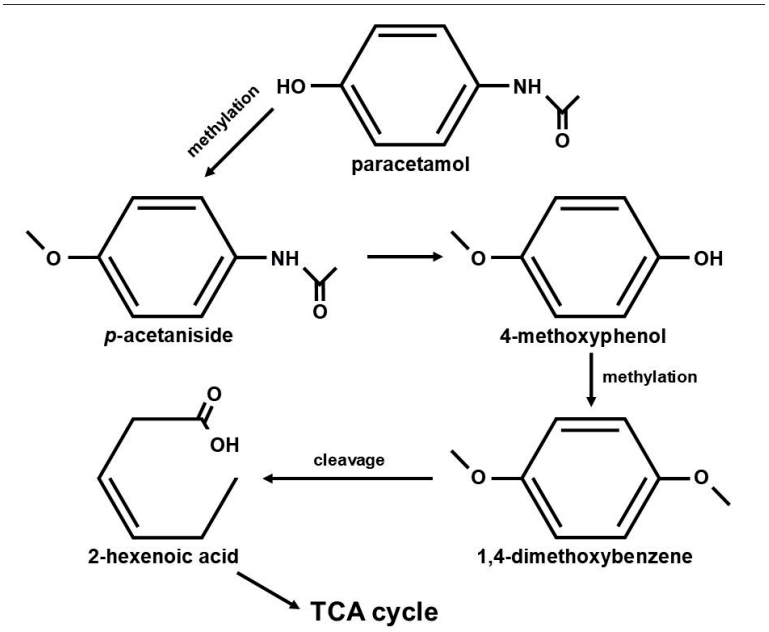


Fig. 1. Possible biodegradation pathway of APAP with 4-MP as a one of the metabolites formed (adapted from Żur et al. 2018 and Pandey et al. 2025).

transformation product on environmental microorganisms and biodegradation efficiency.

Materials and Methods

Chemical Compounds

The concentrations of 0.01, 0.1, 1, 10, 100, and 1000 $mg \cdot L^{-1}$ were selected based on literature data reporting environmentally detected levels of paracetamol and its biodegradation metabolites (Li et al. 2014; Pandey et al. 2024). The inclusion of higher concentrations was intended to determine whether the toxicological mechanism of both compounds is concentration-dependent. Acetaminophen and 4-methoxyphenol were purchased from Sigma-Aldrich (UK) and dissolved in dimethyl sulfoxide (DMSO) prior to use. In the samples studied, the final DMSO concentration was 10%. Solvent controls were included in the experimental systems used in the studies.

Microorganisms

The study was conducted during the academic year 2024/2025 using microorganisms purchased from the American Type Culture Collection (ATCC, USA). The toxicity of APAP and 4-MP was assessed based on the antimicrobial activity of both compounds against two model microorganisms: the bacterium *E. coli* ATCC-25922 and the fungus *C. albicans* ATCC-10231. Oxidative stress, based on reactive oxygen species (ROS) generation, was additionally measured in *E. coli* ATCC-25922. The genotoxicity of both compounds was determined using the *E. coli* RFM443 *recA:luxCDABE* biosensor strain. For the determination of MIC values, a broader panel of microorganisms representing the natural human microbiome was employed, comprising *E. coli* ATCC-25922, *Enterobacter hormaechei* ATCC-700323, *Staphylococcus epidermidis* ATCC-12228, *Lacticaseibacillus rhamnosus* ATCC-53103, and *C. albicans* ATCC-10231.

Rationale for the Selection of Microorganism Strains

The study was conducted using microorganisms belonging to the human microbiome to investigate the effects of the drug and its transformation product, 4-MP, on the natural human microbiota. When ingested as a drug, APAP is metabolized in the human body, enters the bloodstream, and reaches the tissues and organs, affecting not only the gut microbiome but also the microbiome of the entire body. Furthermore, when immunity is compromised, there is excessive proliferation of microbiome microorganisms and the emergence of opportunistic infections, which are also caused by strains of *E. coli*, *C. albicans*, and *S. epidermidis* - the subjects of our study.

Justification for the Selection of Biological Assays Used in the Experiments

The toxicity (inhibition of microbial culture growth and determination of MIC values), genotoxicity, and oxidative stress (based on ROS synthesis values) tests conducted in this study were aimed at determining the toxic and genotoxic potential of both tested chemical compounds (APAP and 4-MP). The determination of ROS synthesis levels served as the basis for confirming oxidative stress as the primary mechanism of toxicity and genotoxicity of the chemical compounds studied in this work.

Measurement of Antimicrobial Activity

Antimicrobial activity was established based on the growth inhibition of both microorganisms, cultivated at 37°C in Luria-Bertani (LB) medium containing tryptone ($10\ g \cdot L^{-1}$), yeast extract ($5\ g \cdot L^{-1}$), and NaCl ($10\ g \cdot L^{-1}$) (pH 7.0). On the following day, the cultures were refreshed by dilution with fresh LB medium and incubated in a shaking water bath (130 rpm) at 37°C until reaching the logarithmic growth phase (OD_{600} = 0.2). Subsequently, in 96-well plates, 100 µl of bacterial or fungal cultures were mixed with 100 µl of appropriate concentrations of APAP and 4-MP. Control samples contained no chemicals. The plates were then incubated at 37°C for 24 and 48 h. Nalidixic acid (NA), a quinolone antibiotic that acts by inhibiting bacterial DNA gyrase and disrupting DNA replication, was used as a genotoxic standard. The growth of bacterial and fungal cultures following treatment was assessed spectrophotometrically at 600 nm using a GloMax® microplate reader (Promega, MA, USA), and the results were expressed as a percentage of growth inhibition or stimulation relative to the control. All experiments were performed in at least three independent series, with six replicates per sample in each series.

Determination of Minimum Inhibitory Concentration (MIC)

MIC values for APAP and 4-MP were determined using *E. coli* ATCC-25922, *E. hormaechei* ATCC-700323, *Staphylococcus epidermidis* ATCC-12228, *Lacticaseibacillus rhamnosus* ATCC-53103, and *C. albicans* ATCC-10231. Microorganisms were cultivated overnight in Müller-Hinton medium (MHM) at 37°C. The following day, cultures were refreshed with fresh MHM and incubated at 37°C until reaching the logarithmic growth phase (OD_{600} = 0.2). Subsequently, a drop of each culture was placed on Müller-Hinton agar (MHA) containing appropriate concentrations of the drugs, ranging from 10 $mg \cdot mL^{-1}$ to 0.01 $\mu g \cdot mL^{-1}$. Control samples contained no chemicals. Plates were incubated at 37°C for 24 and 48 h, after which the presence or absence of microbial growth was recorded.

Genotoxicity Assay

To determine the genotoxic potency of both compounds, the *E. coli* RFM443 *recA:luxCDABE* biosensor strain, carrying a plasmid construct with a genotoxin-sensitive *recA* promoter fused to the *luxCDABE* reporter gene, was used. The strain was cultivated overnight in LB medium at 37°C. The following day, the culture was diluted with fresh LB medium and incubated at 37°C with shaking (130 rpm) until reaching the logarithmic growth phase (OD_{600} = 0.2). Subsequently, 100 µl of *E. coli* RFM443 *recA:luxCDABE* culture was mixed with 100 µl of appropriate concentrations of APAP and 4-MP in white 96-well plates and incubated for 2 h at 37°C. Luminescence was measured at time 0 (immediately upon addition of the tested compounds) and after 2 h of incubation using a GloMax® microplate reader (Promega, MA, USA). The luminescence signal was normalized to the OD_{600} value according to the formula: $Lc = L / OD_{600}$, where Lc is the corrected luminescence and L is the raw luminescence value. Results are expressed as a percentage of *recA* promoter activity relative to the control at time 0 (100%). All experiments were

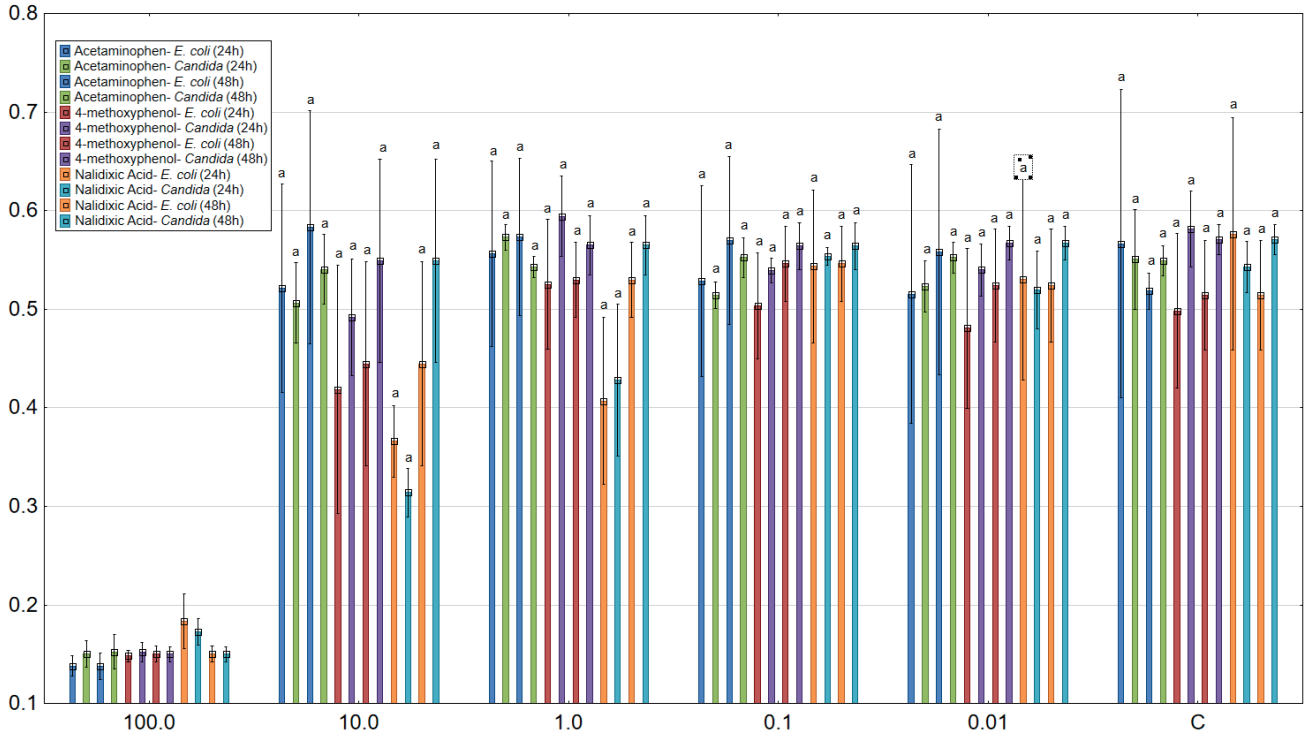


Fig. 2. Percentage inhibition of *E. coli* and *C. albicans* culture growth after 24 h and 48 h exposure to acetaminophen, 4-methoxyphenol, and nalidixic acid at concentrations of 0.01, 0.1, 1, 10, and 100 mg•L_{-1} compared to the control (100%). Note: a – statistically significant differences at $p \leq 0.05$. Data are presented as mean ± SD; error bars indicate the SD of three independent replicates (n = 3).

performed in three independent series, with six replicates per sample in each series.

Determination of Intracellular ROS Levels

To confirm oxidative stress as a mechanism underlying the toxicity and genotoxicity of the tested compounds, intracellular ROS levels were determined in *E. coli* ATCC-25922 cells using 2′,7′-dichlorofluorescein diacetate (DCFH-DA) (Sigma-Aldrich, UK). Both compounds were tested at concentrations of 0.01, 0.1, 1, 10, and 100 mg·L^{-1}. *E. coli* was cultivated overnight in LB medium at 37°C, then refreshed with fresh LB medium and incubated at 37°C with shaking (130 rpm) until reaching the logarithmic growth phase (OD_{600} = 0.2). Subsequently, 200 µl of a mixture of *E. coli* culture and appropriate concentrations of APAP and 4-MP were added to black 96-well plates. Control samples contained no chemicals; NA was used as a reference standard. DCFH-DA was added to a final concentration of 5 µM, and the plates were incubated at 37°C for 3 h. Thereafter, DCF fluorescence intensity was measured using a GloMax® microplate reader (Promega, MA, USA) at an excitation wavelength of 485 nm and an emission wavelength of 535 nm. Results were expressed as a percentage of ROS increase relative to the untreated control. All experiments were performed in three independent series, with six replicates per sample in each series.

Statistical Analysis

Prior to statistical analyses, the assumptions of normality and homogeneity of variance were verified. Data normality was assessed using the Shapiro–Wilk test, while homogeneity of variances was evaluated using Levene's test. In cases where the assumption of homogeneity of variance was not met, the Brown–Forsythe test was applied. For growth inhibition experiments, one-way ANOVA was applied, followed by Tukey's honestly significant difference (HSD) post hoc test. For *recA* promoter induction in *E. coli* RFM443 *recA::luxCDABE* and ROS synthesis, Student's t-test for independent samples was applied. All statistical tests were two-tailed and evaluated at a significance level of $\alpha \leq 0.05$. Statistical calculations were performed using Statistica software, version 13.3.

Results

Antimicrobial Activity of APAP and 4-MP

At 100 mg·L^{-1}, both *E. coli* and *C. albicans* showed growth inhibition exceeding 70% after 24 and 48 h of incubation (Fig. 2). At APAP concentrations of 0.01–10 mg·L^{-1}, slight growth inhibition was detected after 24 h, reaching a maximum of 8% in *C. albicans* at 10 mg·L^{-1}. In *E. coli*, APAP at concentrations of 0.01–10 mg·L^{-1} stimulated growth after 48 h, reaching over 12% at 10 mg·L^{-1}. At 10 mg·L^{-1}, 4-MP inhibited the growth of both strains by over 16% after 24 and 48 h, with stronger inhibition observed in *E. coli* after 24 h compared to APAP.

Minimum Inhibitory Concentration (MIC) Values for APAP and 4-MP

The MIC analysis revealed comparable antimicrobial activity of acetaminophen and 4-methoxyphenol against the tested bacterial strains and *C. albicans*. An exception was observed for *L. rhamnosus*, against which acetaminophen demonstrated greater growth inhibition (MIC = 5 mg·mL^{-1})

Table 1: MIC values (mg•mL¹) of APAP, 4-MP, and kanamycin (control) against microorganisms after 24 and 48 h of incubation.

Chemicals	*E. coli* (Gram−)	*E. hormaechei* (Gram−)	*S. epidermidis* (Gram+)	*L. rhamnosus* (Gram−)	*C. albicans*
Acetaminophen	5	5	10	5	10
4-methoxyphenol	5	5	10	10	10
Kanamycin	0.1	<0.1	0.1	<0.1	0.2

than 4-MP (MIC = 10 mg·mL^{-1}). Comparison of the MIC values with those of the positive control, kanamycin, indicated that the antimicrobial efficacy of the classic antibiotic exceeded that of acetaminophen and 4-MP by more than an order of magnitude (Table 1).

Genotoxic effect of APAP and 4-MP

Genotoxic activity after 2 h of exposure indicated that APAP elevated E. coli RFM443 recA:luxCDABE expression more than 4-MP, with differences of approximately 20% at 1 and 10 mg·L^{-1} and over 10% at 100 mg·L^{-1} (Fig. 3). NA at 1 mg·L^{-1} elicited the highest level of induction among the tested compounds, exceeding 150% relative to the control.

Intracellular ROS Levels

At concentrations of 0.1, 1, 10, and 100 mg·L^{-1}, APAP increased ROS levels in *E. coli* cells by 13%, more than 10%, 14%, and more than 18%, respectively, compared to the corresponding ROS levels induced by 4-MP. The strongest ROS induction was observed in cultures treated with NA at 1, 10, and 100 mg·L^{-1}, reaching over 120%, over 150%, and approximately 200% of the control, respectively (Fig. 4).

Discussion

Paracetamol (APAP, acetaminophen) is one of the most frequently detected pharmaceutical contaminants in water and soil environments, where it undergoes biodegradation, resulting in the formation of its metabolites, including 4-methoxyphenol (4-MP). Both APAP and its metabolite have adverse effects on living organisms and bioaccumulate in their cells (bacteria, fungi, and unicellular algae) and tissues (plants and animals), thereby disrupting the proper functioning of ecosystems. This study compares the biological activity of paracetamol and its transformation product, 4-MP. Drug metabolites often exhibit higher mobility, distinct toxicities, and greater persistence than their parent compounds; therefore, studying their activity is very important for determining environmental safety.

In this experiment, a comparative analysis of the antimicrobial activity of APAP, 4-MP and nalidixic acid (NA,

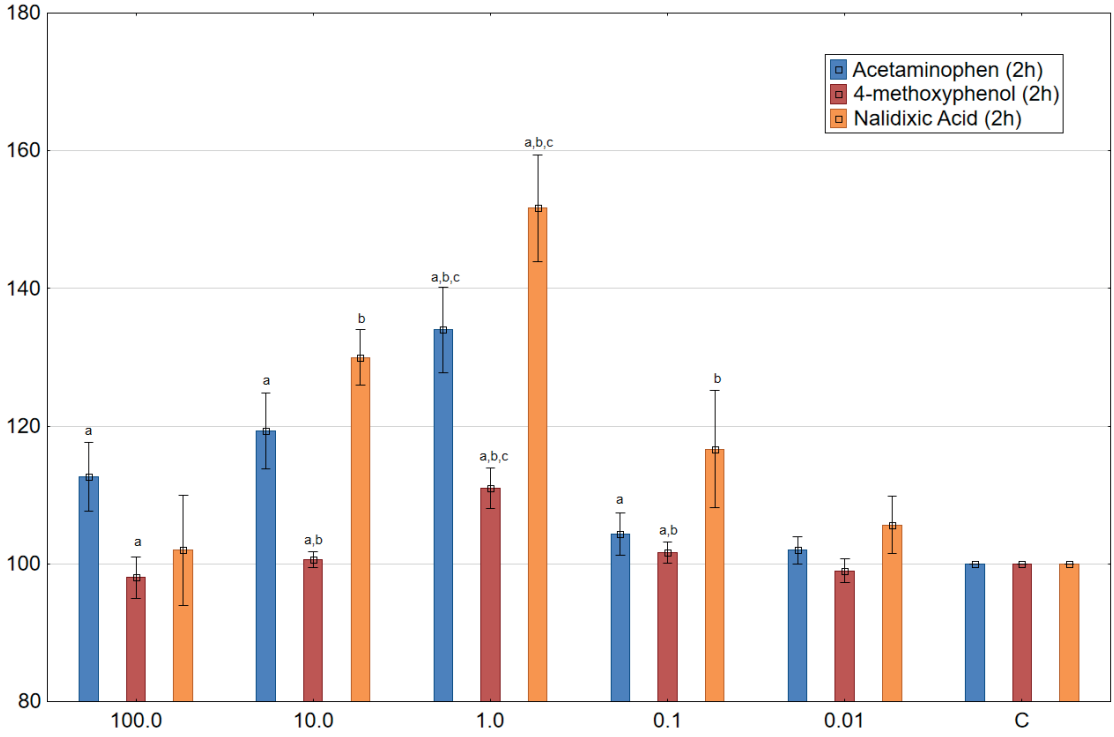


Fig. 3. Activity of E. coli RFM443 *recA::luxCDABE* after 2 h exposure to acetaminophen, 4-methoxyphenol, and nalidixic acid at concentrations of 0.01–100 mg•L¹, relative to the control (100%). Statistically significant differences ($p \leq 0.05$): (a) acetaminophen vs. 4-methoxyphenol; (b) 4-methoxyphenol vs. nalidixic acid; (c) nalidixic acid vs. acetaminophen. Data are presented as mean ± SD (n = 3); error bars indicate SD

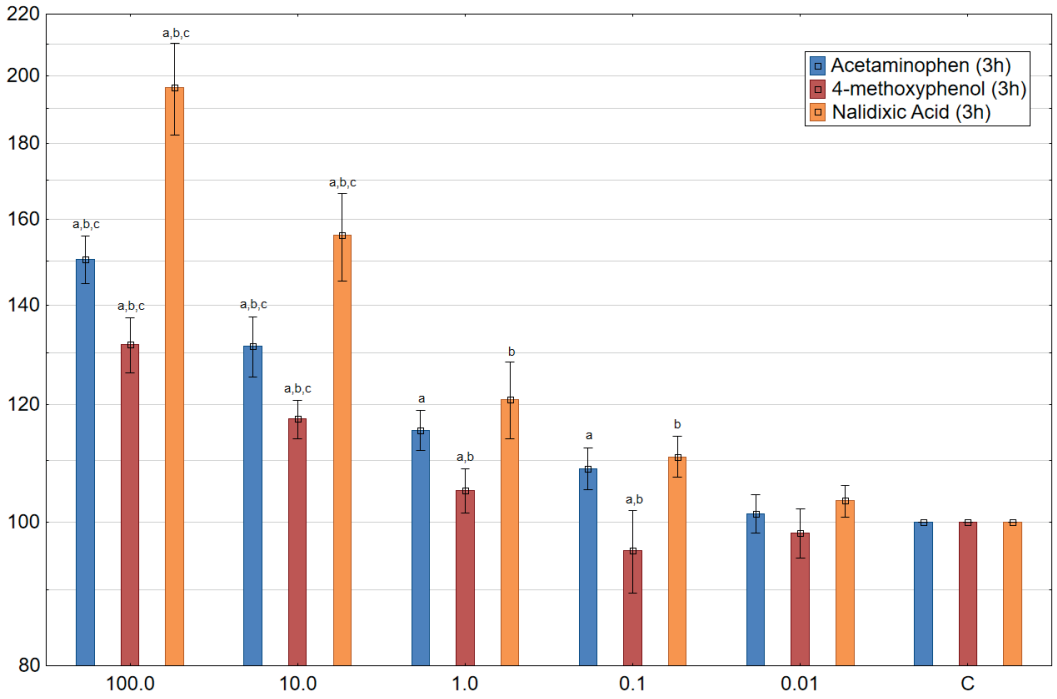


Fig. 4. ROS levels (%) in E. coli after 3 h exposure to acetaminophen (APAP), 4-methoxyphenol (4-MP), and nalidixic acid (NA) at concentrations of 0.01–100 mg•L¹, relative to the untreated control (100%). Statistically significant differences ($p \leq 0.05$): (a) APAP vs. 4-MP; (b) 4-MP vs. NA; (c) NA vs. APAP. Data are presented as mean ± SD (n = 3); error bars indicate SD.

used as a positive control) revealed the sensitivity of both *E. coli* and *C. albicans* strains to paracetamol and 4-MP, with the highest toxic effect observed at a concentration of 100 mg L^{-1} after 24 h and 48 h. 4-MP applied at a lower concentration of 10 mg L^{-1} exerted a stronger inhibitory effect on both *E. coli* and *C. albicans* strains compared to APAP, indicating broader and more potent biological activity of the transformation product relative to APAP. For all three compounds, i.e., APAP, 4-MP, and nalidixic acid (NA, used as a positive control), a concentration-dependent inhibition of microbial growth was observed, whereby increasing concentrations of each compound consistently and predictably suppressed microbial viability, regardless of exposure duration. Furthermore, varying sensitivities to acetaminophen, APAP, and NA were observed in the two microorganisms studied, *E. coli* and *C. albicans*. This is likely due to differences in the chemical structures and activities of the compounds tested, as well as structural differences between the cells: *E. coli* is a bacterium, whereas *C. albicans* is a eukaryotic fungal cell. MIC tests were performed to determine the sensitivity of a larger group of microorganisms (*E. coli*, *E. hormaechei*, *S. epidermidis*, *L. rhamnosus*, and *C. albicans*) to the chemical compounds under investigation. The results showed that the sensitivity of the tested microorganisms to APAP and 4-MP is species-dependent and dose-dependent. We demonstrated that as the concentration of APAP and 4-MP increases, a bactericidal effect occurs in a greater number of the tested microorganisms. These results are consistent with those reported by previous authors (Torequl et al. 2025), who demonstrated that paracetamol and its derivatives exhibit antimicrobial activity against Gram-positive and Gram-negative bacteria, fungi, and drug-resistant strains. Moreover, antiviral and antiprotozoal activity has been reported for this compound. Toxicological profiling of acetaminophen has revealed that this drug has the potential to damage organs, particularly the liver and lungs, *via* a mechanism involving oxidative stress.

Using the genotoxicity-sensitive *recA* promoter assay in *E. coli*, we demonstrated that paracetamol, 4-MP, and NA, tested individually, exhibited genotoxic effects. Among the chemical compounds tested (except at a concentration 100 mg L^{-1}), the strongest genotoxic response was detected for NA, a known genotoxicity standard. Comparative analysis of the genotoxic potential of APAP and 4-MP revealed a stronger genotoxic effect for the parent drug relative to 4-MP. Within the range of APAP, 4-MP, and NA concentrations tested, a positive correlation was observed between the measured ROS concentration and the level of genotoxicity of the compounds in *E. coli*. ROS generation and oxidative stress represent the primary molecular mechanism underlying the toxicity and genotoxicity of test compounds, as confirmed by earlier studies (Żur et al. 2018; Kirkland et al. 2021; Jaeschke et al. 2021; Torequl et al. 2025). ROS and oxidative stress lead to DNA damage and genotoxic effects. The strongest genotoxic effect and induction of ROS synthesis were detected for APAP. These findings demonstrate a robust and consistent concentration-dependent induction of oxidative stress, indicating that ROS overproduction constitutes a central and reproducible mechanism of cellular damage for both the parent drug and its metabolite across the tested concentration range (0.01–100 mg L^{-1}).

Analysis of the relationship between test compound concentration and *recA::luxCDABE* promoter activity in *E. coli* (genotoxicity assay) provided additional insight into the

nature of these genotoxic responses. The result for APAP was negligible, suggesting the absence of a concentration-dependent genotoxic response, which may reflect the cytotoxicity-masking effect at higher concentrations, as proposed by Kirkland et al. (2021). A statistically non-significant positive result was observed for 4-MP indicating a lack of a relationship between concentration and DNA damage induction. In contrast, NA also displayed statistically non-significant results, which may reflect the complex and non-dynamic nature of genotoxic responses at higher concentrations, potentially attributable to cytotoxic interference. Taken together, these data suggest that while oxidative stress induction follows a concentration-response pattern for all compounds, genotoxic effects, as measured by *recA* promoter activation, exhibit more complex, compound-specific relationships with concentration.

In the period between 2019 and 2025, an increasing number of studies have addressed the possible carcinogenic effects of paracetamol. In 2019, the California Office of Environmental Health Hazard Assessment (OEHHA) initiated an investigation into the potential carcinogenic risk associated with paracetamol use. In 2021, an independent research group led by Jaeschke et al. published findings demonstrating that, at recommended therapeutic doses, only small amounts of the paracetamol metabolite N-acetyl-p-benzoquinone imine (NAPQI) are formed in the human body and that such quantities are unlikely to exert harmful effects under normal conditions. It is only in cases of acetaminophen overdose that substantially higher levels of NAPQI are produced and glutathione is depleted, potentially resulting in mitochondrial dysfunction and DNA damage, although exclusively at doses that induce cell death (Jaeschke et al. 2021; Torequl et al. 2025). Kirkland et al. (2021), however, argue that the cytotoxic effects of this drug manifest prior to the induction of permanent genetic damage, suggesting that the genotoxic and carcinogenic risk under therapeutic conditions remains limited. More conclusive evidence of toxicity and genotoxicity has emerged for the metabolite 4-MP. Based on the current state of knowledge, methoxyphenols are recognized as genotoxins and mutagens capable of inhibiting the synthesis of nucleic acids and proteins (Saeed et al. 2024). The results obtained in the present study, confirming the genotoxic nature of 4-MP, are consistent with previously published findings.

Conclusions

1. The results of the conducted studies demonstrated that both compounds – the parent drug, paracetamol, and its transformation product, 4-MP, exhibit toxic and genotoxic properties in *Escherichia coli* bioassays.
2. The results obtained support the hypothesis that 4-MP, as a transformation product of APAP, exhibits toxic and genotoxic activity and generates oxidative stress in *E. coli* cells similarly to the parent drug.
3. The diverse chemical structures of the tested compounds - APAP, 4-MP, and the standard (NA) - affected their activity against the tested *E. coli* strains. The analysis of ROS level detected oxidative stress, which is likely one of the main mechanisms underlying the toxicity and genotoxicity of APAP and 4-MP. The relationship between ROS synthesis, as an indicator of oxidative stress, and the genotoxic effect is most clearly observed at a concentration of 10 mg L^{-1} for the tested chemical compounds APAP, 4-MP, and NA.
4. There is an environmental risk that paracetamol and 4-MP, because of their toxic and genotoxic activities, may disrupt the quantitative and qualitative composition of soil and activated sludge microbiota, leading to impairment of their biological functions.
5. Another possible situation in the environment is that drugs and their transformation products present in environmental matrices may interact in various ways with other micropollutants (pesticides, pharmaceutical residues), forming complexes of unknown and unpredictable biological activity, which may negatively affect the proper functioning of ecosystems and pose a threat to living organisms.

Funding

This work was financially supported by Ministry of Education and Science, Poland, under research project number WZ/WB-IIS/14/2026 (Teta 0601000171).

Declaration of Competing Interest

The authors declare that they have no known competing financial interests or personal relationships that could have influenced the work reported in this paper.

Acknowledgements

The authors are very grateful to Professor Shimshon Belkin and his team at the Institute of Life Sciences, The Hebrew University of Jerusalem, Jerusalem, Israel, for E. coli RFM443 recA:luxCDABE bacteria strain.

References

Asakawa E., Hirose M., Hagiwara A., Takahashi S. & Ito N. (1994). Carcinogenicity of 4-methoxyphenol and 4-methylcatechol in F344 rats. *Int. J. Cancer* 56(1), pp. 146–152. DOI:10.1002/ijc.2910560126

Bührer C., Endesfelder S., Scheuer T. & Schmitz T. (2021). Paracetamol (acetaminophen) and the developing brain. Int. *J. Mol. Sci.* 22, 11156. DOI:10.3390/ijms222011156

Chacón F.J., Cayuela M.L. & Sanchez-Monedero M.A. (2022). Paracetamol degradation pathways in soil after biochar addition. *Environ. Pollut.* 307, 119546. DOI:10.1016/j.envpol.2022.119546

Cybulski J., Witczak A. & Pokorska-Niewiada K. (2021). The effect of water and sewage treatment on reducing residues of selected organochlorine pesticides in Szczecin (Poland). *Water Air Soil Pollut.* 232, 310. DOI:10.1007/s11270-021-05261-6

Jaeschke H., Murray F.J., Monnot A.D., Jacobson-Kram D., Cohen S.M., Samuel, Jerry F. Hardisty, J.F., Atillasoy, E., Hermanowski-Vosatka, A., Kuffner, E., Wikoff, D., Chappell, G.A., Bandara, S.B., Deore, M., Kumar Pitchaiyan, S. & Eichenbaum, G. (2021). Assessment of the biochemical pathways for acetaminophen toxicity: Implications for its carcinogenic hazard potential. *Regul. Toxicol. Pharmacol.* 120, 104859. DOI:10.1016/j.yrtph.2020.104859

Kirkland D., Kovochich M., More S.L., Murray F.J. & Monnot A.D. (2021). A comprehensive weight of evidence assessment of published acetaminophen genotoxicity data: Implications for its carcinogenic hazard potential. *Regul. Toxicol. Pharmacol.* 122, 104892. DOI:10.1016/j.yrtph.2021.104892

Li J., Ye Q. & Gan J. (2014). Degradation and transformation products of acetaminophen in soil. *Water Res.* 49, 44–52. DOI:10.1016/j.watres.2013.11.008

Lunghi C., Valetto M.R., Caracciolo A.B., Bramke I., Caroli S., Bottoni P., Castiglioni S., Crisafulli S., Cuzzolin L., Deambrosis P., Giunchi V., GrisottoJ., Marcomini A., Moretti U., Murgia F., Pandit J., Polesello S., Poluzzi E., Romizi R., Scarpa N., Scroccaro G., Sorrentino R., Sundstron A., Wilkinson J. & Paolone G. (2025). Call to action: Pharmaceutical residues in the environment: threats to ecosystems and human health. *Drug Saf.* 48, 315–320. DOI:10.1007/s40264-024-01497-3

Miyachi T. & Tsutsui T. (2005). Ability of 13 chemical agents used in dental practice to induce sister-chromatid exchanges in Syrian hamster embryo cells. *Odontology* 93, 24–29. DOI:10.1007/s10266-005-0055-8

Ossowicz-Rupniewska P. E., Kucharska E., Klebeko J., Kopciuch E., Bilska K. & Janus E. (2023). Effect of the type of amino acid on the biodegradation of ibuprofen derivatives. *Arch. Environm. Protect*. 49, 4, 46–69. DOI:10.24425/aep.2023.148685

Pandey B., Pandey A.K., Tripathi K. & Dubey S.K. (2024). Biodegradation of acetaminophen: Microcosm centric genomic-proteomic-metabolomics evidence. *Bioresour. Technol.* 401, 130732. DOI:10.1016/j.biortech.2024.130732

Pandey B., Pandey A.K., Bhardwaj L. & Dubey S.K. (2025). Biodegradation of acetaminophen: Current knowledge and future directions with mechanistic insights from omics. *Chemosphere* 372, 144096. DOI:10.1016/j.chemosphere.2025.144096

Rahman M.M., Balkhoyor H.B. & Asiri A.M. (2017). Phenolic sensor development based on chromium oxide-decorated carbon nanotubes for environmental safety. *J. Environ. Manag.* 188, 228–237. DOI:10.1016/j.jenvman.2016.12.008

Saeed M., Marwani H.M., Rabbee M.F., Alfaifi S.Y., Khan M.M.R. & Rahman M. M. (2024). Fabrication of 4-methoxyphenol chemical sensor with graphene oxide conjugated binary Co3O4/Y2O3 nanocomposite by linear sweep voltammetry. *Microchem. J.* 207, 112231. DOI:10.1016/j.microc.2024.112231

Szymański K., Piekarski J., Sidełko R. & Janowska B. (2026). Removal efficiency of selected micropollutants from municipal wastewater using disc cloth filters – a case study. *Arch. Environm. Protect.* 52, 1, 36–47. DOI:10.24425/aep.2026.158382

Tian L., Mi N., Wang L., Huang C. & Fu W. (2024). Regular use of paracetamol and risk of liver cancer: a prospective cohort study. *BMC Cancer* 24, 33. DOI:10.1186/s12885-023-11767-5

Tomczyk P. P. & Urbaniak M. (2025). Silent threat – the ecological dangers of NSAIDs in aquatic ecosystems. *Arch. Environm. Protect.* 51, 4,144–158. DOI:10.24425/aep.2025.157235

Torequl Islam M., Chowdhury R., Bhuia S., Al Hasan S., Akbor S., Farhad F., Domiciano C. B., Silva D. A. & Coutinho H. D. M. (2025). Antimicrobial potentials and challenges of paracetamol: A comprehensive reassessment based on database reports. *Pharm. Sci. Adv.* 3, 100070. DOI:10.1016/j.pscia.2025.100070

Yisau Y.S., Al-Makishah N.H. & El-Fetouh Barakat M.A. (2024). Microbial degradation of paracetamol in pharmaceutical wastewater: a review. *Am. J. Environ. Sci.* 20, 31–47. DOI:10.3844/ajessp.2024.31.47

Żur J., Piński A., Marchlewicz A., Hupert-Kocurek K., Wojcieszyńska D. & Guzik U. (2018). Organic micropollutants paracetamol and ibuprofen—toxicity, biodegradation, and genetic background of their utilization by bacteria. *Environ. Sci. Pollut. Res.* 25, 21498–21524. DOI:10.1007/s11356-018-2517-x

Porównanie toksyczności acetaminofenu i 4-metoksyfenolu

Streszczenie: Acetaminofen (APAP, paracetamol) jest jednym z najczęściej stosowanych leków przeznaczonych dla ludzi, a jednocześnie jest jednym z najczęściej wykrywanych mikrozanieczyszczeń farmaceutycznych w matrycach środowiskowych. 4-MP jest jednym z produktów transformacji acetaminophenolu powstającym w określonych ścieżkach degradacji środowiskowej. Porównanie toksyczności tych związków ma kluczowe znaczenie dla ochrony środowiska i zdrowia publicznego. W niniejszym badaniu toksyczność APAP i 4-MP oceniono przy użyciu dwóch modelowych mikroorganizmów, *E. coli* ATCC-25922 i *C. albicans* ATCC-1023, w oparciu o hamowanie wzrostu hodowli. Wrażliwość mikroorganizmów należących do mikrobiomu człowieka (*E. coli*, *E. hormaechei, S. epidermidis, L. rhamnosus* i *C. albicans*) na oba związki określono poprzez obliczenie minimalnych stężeń hamujących (MIC). Genotoksyczność oszacowano przy użyciu wrażliwego na genotoksyny promotora *recA* w *E. coli* RFM443 *recA::luxCDABE*. Wytwarzanie reaktywnych form tlenu (ROS) zmierzono w *E. coli* poddanej działaniu obu związków w stężeniach 0,1, 1, 10, 100 i 1000 $mg \cdot L^{-1}$, jako wskaźnika stresu oksydacyjnego. Analiza porównawcza wykazała podobną wrażliwość *E. coli* i *C. albicans* na oba związki w stężeniu 100 $mg \cdot L^{-1}$, chociaż w stężeniu 10 $mg \cdot L^{-1}$ 4-MP wywierał silniejsze działanie hamujące na oba szczepy niż APAP. W testach MIC wykryto, że szczepy *E. coli* i *E. hormaechei* były bardziej wrażliwe na 4-MP niż na APAP, natomiast w przypadku pozostałych szczepów nie zaobserwowano istotnych różnic. APAP wykazał silniejsze działanie genotoksyczne niż 4-MP w komórkach *E. coli*. Dane dotyczące ROS wskazują, że stres oksydacyjny jest głównym mechanizmem molekularnym leżącym u podstaw toksyczności i genotoksyczności obu związków. Biorąc pod uwagę uzyskane wyniki przyszłe badania powinny dotyczyć toksyczności mieszanin APAP i 4-MP w warunkach narażenia odpowiadających warunkom środowiskowym.

Archives of Environmental Protection
Vol. 52 no. 3 pp. 34–44

PL ISSN 2083-4772
DOI: 10.24425/aep.2026.3676



© 2026. The Author(s). This is an open-access article distributed under the terms of the Creative Commons Attribution-ShareAlike 4.0 International Public License (CC BY SA 4.0, https:// creativecommons.org/licenses/by-sa/4.0/legalcode), which permits use, distribution, and reproduction in any medium, provided that the article is properly cited.

Directional Regulation of Biomass Pyrolysis Gas Coupling for Hydrogen-Rich Fuel Gas Production over a Hydrophobic NiCo-CeO_2/F-Ti_3C_2 Catalyst

Chen Jihao[1,2], Miao Pengjie[1,2*]

[1]College of Energy and Chemical Engineering, Xinjiang Institute of Technology, Aksu 843100, China
[2]Xinjiang Key Laboratory of New Energy and Energy Storage Technology,
Xinjiang Institute of Technology, Aksu 843100, China

*Corresponding author's e-mails:37743386@qq.com

Keywords: Ti_3C_2 MXene; CeO_2; Ni-Co alloy; biomass hydrogen production; hydrophobicity.

Abstract: A key challenge in hydrogen-rich fuel gas production via biomass pyrolysis gas coupling is catalyst hydrothermal deactivation. In this study, hydrophobic F-Ti3C2 MXene nanosheets are prepared by a combination of HF-HCl etching and perfluorooctanesulfonic acid (PFOS) modification. Using the nanosheets as the support, CeO2 promoters and Ni-Co alloy active components are loaded via impregnation, nitrogen calcination and hydrogen reduction processes. Finally, a catalyst with high activity and high hydrophobicity is successfully prepared. The performance of the catalyst is tested in a fixed-bed reactor. The effects of total NiCo loading, Ni/Co molar ratio, and Ce loading on CO/CH4 conversion and H2 selectivity are systematically investigated. The catalyst is characterized by X-ray diffraction (XRD), scanning electron microscopy (SEM), X-ray photoelectron spectroscopy (XPS), and contact angle measurements, and the mechanisms of underlying its activity and hydrophobicity enhancement are

Introduction

Driven by the dual goals of carbon peaking and carbon neutrality, as well as energy structure transformation, the high-efficiency resource utilization of renewable energy has become a global research hotspot (Gyimah et al. 2024). Biomass is a renewable carbon source that can be converted into solid, liquid and gaseous fuels. It has abundant reserves and remarkable carbon-neutrality characteristics. Its pyrolysis conversion technology is one of the important approaches to addressing fossil energy shortage and environmental problems (Wang et al. 2024). Therefore, developing efficient biomass pyrolysis gas conversion technologies is of great practical significance. It can upgrade biomass pyrolysis gas into high-value-added clean energy, thereby optimizing the energy structure and protecting ecological environment. The pyrolysis gas produced by biomass is mainly composed of CH_4, CO, CO_2, C_2/C_3 hydrocarbons, and H_2O. It has extremely high conversion potential. Hydrogen-rich fuel gas can be prepared through the coupled reforming of biomass pyrolysis gas. The key to this technology is the synergistic occurrence of multiple reactions. These reactions include CH_4 reforming, CO water-gas shift reaction, and C_2/C_3 hydrocarbon cracking. They can achieve efficient enrichment of hydrogen (Wang et al. 2024). However, water is involved in the hydrogen production process from biomass pyrolysis gas, causing problems such as sintering of catalyst active components and hindrance of mass transfer (Guo et al. 2025). Thus, developing catalysts with both high activity and strong hydrophobicity is one of the keys to realizing the industrialization of hydrogen-rich fuel gas production via biomass pyrolysis gas coupling.

Chen et al. (2023) prepared a hydrophobic Fe_2O_3@ SiO_2-xHDTMS catalyst via a room-temperature solid-phase method for light hydrocarbon synthesis. The hydrophobic long-chain alkyl groups of HDTMS can graft onto the SiO_2 surface, replacing polar hydroxyl groups. This treatment increased the maximum contact angle of the catalyst to 155.2°, achieving superhydrophobicity. Khojasteh et al. (2024) modified SiO_2 with perfluorooctyltriethoxysilane (PFOS) to prepare a superhydrophobic glass coating. PFOS provides low surface energy groups and increases surface

roughness. The water contact angle of the coating reached 144°. Ma et al. (2024) etched Cu/ZnO/Al_2O_3 with NaOH, and then prepared superhydrophobic catalysts via MTMS modification and PFOTES grafting, respectively, for syngas-to-methanol conversion. PFOTES exhibited better hydrophobic performance than MTMS. The contact angles of both catalysts exceeded 150°. These catalysts can rapidly remove surface water molecules and improve the hydrothermal stability of the catalysts. Bootpakdeetam et al. (2024) loaded cobalt and ruthenium onto a SiO_2 support. After calcination, the supported catalyst was treated with a PFOS-toluene solution to prepare a superhydrophobic Co-Ru/SiO_2 catalyst for Fischer-Tropsch synthesis. PFOS grafted onto the support surface via siloxane bonds. The catalyst showed a contact angle of over 150° and a sliding angle of less than 5°. It effectively repelled water generated during the reaction, thereby avoiding cobalt oxidation and deactivation. The CO conversion rate increased to 38%. Benkacher et al. (2025) modified Algerian palygorskite (A-Pal) with triethoxyoctylsilane (TEOS) to prepare a hydrophobic O-Pal material. Silane molecules replaced hydroxyl groups and introduced hydrophobic octyl groups. This effectively improved the dispersion and compatibility of the material in hydrophobic biopolymers. In summary, silane-based hydrophobic groups such as HDTMS, PFOS, MTMS, and TEOS can endow modified catalysts with excellent water resistance.

The support is a key factor governing catalyst stability and, in the present context, also provides the platform for hydrophobic-group grafting. Therefore, it directly determines the stability of the catalyst in the complex pyrolysis gas atmosphere. Conventional supports, including Al_2O_3, SiO_2, and ZrO_2, have been widely employed; however, each exhibits inherent limitations. γ-Al_2O_3 possesses strong hydrophilicity and a relatively limited specific surface area, whereas SiO_2 provides a high specific surface area but suffers from relatively poor mechanical strength and insufficient stability. ZrO_2 exhibits good thermal stability, but its relatively simple pore structure can restrict mass transfer. All these supports have certain defects. Two-dimensional nanomaterials can serve as ideal materials for catalyst preparation. They have the advantages of ultra-large specific surface area, abundant pore structures, and adjustable surface properties. Two-dimensional MoS_2 loaded with Ni has a specific surface area of up to 680 m^2/g. Meanwhile, hydrophobic groups such as fluoro and alkyl groups can be grafted onto the MoS_2 surface. This improves water resistance. Moreover, the interlayer structure can inhibit carbon deposition and agglomeration (Wei et al. 2019). Two-dimensional Ti_3C_2 MXene constructs a porous structure through etching modification. Ti_3C_2 loaded with Ni-Ce has high conductivity. It can promote electron transfer and enhance catalytic activity. Meanwhile, its surface -OH and -F functional groups enable hydrophobic group grafting. In addition, the layered structure can enhance the stability of active components. It has great advantages in the application of hydrogen production from biomass pyrolysis gas (Reghunath et al. 2023). Therefore, two-dimensional nanomaterials not only have high-efficiency active component dispersion capacity and structural stability, But they can also meet modification requirements such as hydrophobic group grafting and active component/promoter loading. High activity and strong hydrophobicity of the catalyst are achieved through multi-performance synergy.

Aiming at the drawbacks of existing hydrophobically modified catalysts, most of which are based on traditional supports such as silica and palygorskite, and adopt single-component metal active sites, these catalysts are prone to sintering of active components and failure of hydrophobic layers under high-temperature water vapor environments. Meanwhile, conventional supports, including Al_2O_3, SiO_2, and ZrO_2 have inherent deficiencies such as strong hydrophilicity, single pore structures, and poor metal dispersion. In this work, two-dimensional Ti_3C_2 MXene nanosheets are used as the support to construct a novel fluorinated hydrophobic NiCo-CeO_2/F-Ti_3C_2 catalyst for coupled hydrogen production from biomass pyrolysis gas. Compared with the reported silane-modified hydrophobic catalytic systems, this work has three prominent innovations and differentiated advantages.

First, layered F-Ti_3C_2 supports are fabricated via HF-HCl co-etching combined with PFOTS perfluorosilane fluorination modification. The two-dimensional layered MXene skeleton provides abundant anchoring sites for metal species, while covalently grafted perfluoroalkyl chains construct a stable hydrophobic interface with low surface energy, fundamentally inhibiting hydrothermal poisoning caused by water vapor adsorption. Second, CeO_2 promoters and Ni-Co bimetallic alloy active centers are simultaneously loaded on the hydrophobic support. Different from the existing single-Ni or single-Co catalytic systems, the synergistic effect of the bimetallic alloy and the reversible Ce^{3+}/Ce^{4+} redox cycle of cerium-based oxides synergistically enhance the activities of CH_4 reforming, the water-gas shift reaction, and light hydrocarbon cracking. Third, hydrophobic interface regulation, bimetallic alloy catalysis, and rare-earth promoter modification are integrated into one system. Relying on the highly conductive layered structure of MXene to accelerate interfacial electron transfer, the catalyst achieves high CO and CH_4 conversion rates as well as high H_2 selectivity, and greatly improves the hydrothermal stability of the catalyst at high temperature. This study provides a new strategy for designing anti-deactivation catalysts for efficient hydrogen production from biomass pyrolysis gas.

Experimental section

Experimental reagents

Ti_3AlC_2 powder (purity ≥ 98%, particle size 400 mesh) and perfluorooctyltriethoxysilane (PFOTS, purity ≥ 97%) were purchased from Aladdin Reagent Co., Ltd. Hydrogen fluoride (HF, mass fraction 40%), hydrochloric acid (HCl, mass fraction 37%), cerium nitrate ($Ce(NO_3)_3·6H_2O$, purity ≥ 99%), nickel nitrate ($Ni(NO_3)_2·6H_2O$, purity ≥ 99%), cobalt nitrate ($Co(NO_3)_2·6H_2O$, purity ≥ 99%), and absolute ethanol (C_2H_5OH, purity ≥ 99.7%) were purchased from Sinopharm Chemical Reagent Co., Ltd.

The power density and rated power parameters of all experimental testing equipment are listed in Section 2.3.

Preparation of catalysts

Preparation of Ti_3C_2 MXene two-dimensional nanosheet support

A total of 100 mL of 10 mol/L HF solution is taken and slowly added to a polytetrafluoroethylene beaker containing 5

g of Ti_3AlC_2 powder. The mixture is stirred at room temperature for 24 h to etch and remove the Al layer in Ti_3AlC_2. Then, 50 mL of 8 mol/L HCl solution is added, and stirring is continued for 6 h to enhance the etching effect. A crude Ti_3C_2 MXene product is obtained. The crude product is centrifuged and washed with deionized water. The washing process is repeated until the pH value of the supernatant reaches 6-7. The washed precipitate is dried in a vacuum oven at 60 °C for 12 h. The resulting Ti_3C_2 MXene two-dimensional nanosheet support is obtained and denoted as Ti_3C_2.

Preparation of fluoro-group modified Ti_3C_2 MXene support

A total of 2 g of Ti_3C_2 MXene two-dimensional nanosheets is weighed and dispersed in 50 mL of absolute ethanol. The mixture is ultrasonically dispersed for 30 min to form a uniform suspension. Then, 0.4 g of PFOTS is added, and the mixture is stirred at room temperature for 6 h for hydrophobic group grafting. The product is vacuum-dried at 120 °C for 8 h. The fluoro-group-modified Ti_3C_2 MXene support is obtained and denoted as F-Ti_3C_2.

Preparation of CeO_2/F-Ti_3C_2 support

The corresponding mass of cerium nitrate is calculated and weighed according to the designed Ce loading. A homogeneous cerium nitrate solution is prepared. A total of 2.0 g of F-Ti_3C_2 support is weighed and placed in a beaker. The cerium nitrate solution is slowly added dropwise onto the F-Ti_3C_2 support. The mixture is stirred at room temperature for 4 h. The mixture is then vacuum-dried at 120 °C for 12 h. The dried sample is transferred into a muffle furnace and calcined at 290 °C for 2 h under nitrogen atmosphere. The calcination is performed to ensure the complete decomposition of cerium nitrate into CeO_2. The CeO_2/F-Ti_3C_2 support is obtained.

Preparation of NiCo-CeO_2/F-Ti_3C_2 catalyst

The corresponding masses of nickel nitrate and cobalt nitrate are calculated and weighed according to the total NiCo loading and molar ratio. A homogeneous solution is prepared with the weighed nickel nitrate and cobalt nitrate. CeO_2/F-Ti_3C_2 support is weighed. The prepared solution is slowly added dropwise onto the CeO_2/F-Ti_3C_2 support. The mixture is stirred at room temperature for 6 h. The mixture is then vacuum-dried at 120 °C for 12 h. The dried sample is placed into a muffle furnace and calcined at 260 °C for 1.5 h under nitrogen atmosphere. After calcination, the sample is reduced at 290 °C for 2 h under hydrogen atmosphere. The NiCo-CeO_2/F-Ti_3C_2 catalyst is obtained.

Activity evaluation of catalysts

Figure 1 shows the process flow diagram of catalyst activity evaluation. The fixed-bed reactor is a quartz tube with and inner diameter 10 mm and a length of 500 mm. The programmed heating furnace is equipped with a heating tube with a rated power density of 12 W/cm^2, a maximum heating power of 1.8 kW, and a temperature control accuracy is ±1°C. The gas chromatograph is equipped with a thermal conductivity detector (TCD) and a flame ionization detector (FID), with a rated power of 60 W and 120 W, respectively, ensuring stable and continuous online detection of gas components. The gas chromatograph is equipped with a thermal conductivity detector (TCD) and a flame ionization detector (FID), and The gas products are analyzed using a GC-2014c gas chromatograph, and the detailed testing conditions are listed in the table 1. It can simultaneously detect components such as H_2, CO, CO_2, CH_4 and C_2/C_3 hydrocarbons. A total of 0.5 g of catalyst (40-60 mesh) is weighed and uniformly loaded in the middle part of the quartz tube of the fixed-bed reactor. The upper and lower ends of the catalyst are filled with quartz wool to prevent catalyst particles from being blown away by the gas flow. The nitrogen cylinder is opened, and the flow rate is adjusted to 50 mL·min^{-1}. The reactor is purged for 30 min to remove air inside the reactor. Then, the temperature of the reactor is raised to 600 °C. The nitrogen cylinder is closed, and the simulated biomass pyrolysis gas cylinder is opened. The flow rate is adjusted to 25 mL·min^{-1}. The pyrolysis gas contacts the catalyst for the coupling hydrogen production reaction. The product components are determined by gas chromatography.

Calculation of evaluation indexes

CH_4 conversion rate, CO conversion rate, and H_2 yield are used as the indexes for evaluating catalyst performance. The calculation formulas are as follows:

CO conversion: $$X_{CO} = \frac{n_{CO,\,in} - n_{CO,\,out}}{n_{CO,\,in}} \times 100\%$$

CH_4 conversion: $$X_{CH_4} = \frac{n_{CH_4,\,in} - n_{CH_4,\,out}}{n_{CH_4,\,in}} \times 100;$$

H_2 yield: $$Y_{H_2} = \frac{n_{H_2,\,out}}{\left(n_{CO,\,in} - n_{CO,\,out}\right) + 2\left(n_{CH_4,\,in} - n_{CH_4,\,out}\right)} \times 100\%$$

Catalyst characterization tests

(1) X-ray diffraction (XRD) test: XRD is used to analyze the phase composition, existing forms of metals, and crystallinity. Cu target Kα radiation is adopted. The tube voltage is set at 40 kV, and the tube current is set at 40 mA. The scanning range is 2θ= 5°-80°. The scanning rate is 5°·min^{-1}. The step size is 0.02°.

Table 1: Operating conditions of GC

Detector	TCD	FID
Chromatographic column	Chromosorb 101, 3 m×1/8 inch stainless steel packed column	Porapak Q, 3 m×1/8 inch stainless steel packed column
Gasification chamber temperature (ºC)	360	360
Column box temperature (ºC)	80	80
Detector temperature (ºC)	100	150
Determination of gases	CO_2, H_2, CO	CH_4, C_2/C_3

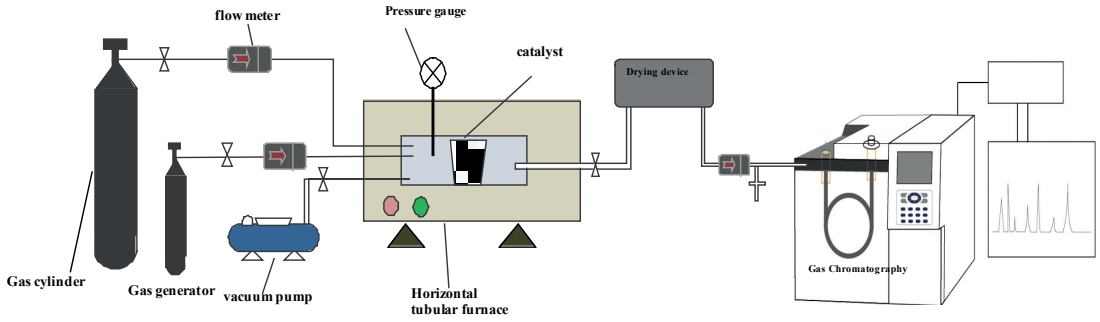


Fig. 1. Process flow diagram of catalyst activity evaluation

(2) Scanning electron microscopy (SEM) test: SEM is used to observe the microscopic morphology. The accelerating voltage is 10 kV, and the magnification is 5000-50000 times. The secondary electron imaging mode is employed. The samples are subjected to gold-spraying treatment before the test. The gold-spraying thickness is 5-10 nm.

(3) X-ray photoelectron spectroscopy (XPS) test: XPS is used to analyze the surface chemical composition and element valence states. Al target Kα radiation (hv=1486.6 eV) is used. The vacuum degree is ≤ 1×10^{-9} Pa. The binding energy is calibrated using C 1s (284.8 eV). The full-spectrum scanning range is 0-1200 eV. The high-resolution scanning range is adjusted according to target elements.

(4) Contact angle test: The contact angle test is used to evaluate the hydrophobicity. The sessile drop method is adopted. The test temperature is 25 °C, and the humidity is 50%. The volume of deionized water droplets is 5 μL. Each sample is tested 3 times, and the average value is taken as the final contact angle.

Results and discussion

Characterization analysis of Ti_3C_2 and F-Ti_3C_2 supports

XRD analysis

Figure 2 shows the XRD patterns of Ti_3AlC_2, Ti_3C_2, and F-Ti_3C_2. The pristine Ti_3AlC_2 phase exhibits strong diffraction peaks at 2θ=9.5°, 19.0°, and 39°. These peaks correspond to its (002), (004), and (104) crystal planes, respectively. The Ti-C layers and Al layers in Ti_3AlC_2 stack alternately. This is a typical characteristic of the MAX phase (Guénolé et al. 2022). For the Ti_3C_2 two-dimensional nanosheets obtained by HF-HCl etching, the strong peaks of the original Ti_3AlC_2 basically disappear. A distinct characteristic peak of Ti_3C_2 appears near 2θ=6.5°. This indicates that the Al atomic layer is effectively stripped and the structure of Ti_3AlC_2 is disassembled. 10. Two-dimensional sheet-dispersed Ti_3C_2 is successfully obtained. The diffraction peaks of fluorine-modified F-Ti_3C_2 shift to lower angles at small 2θ values, and the peak heights also decrease. According to the Bragg equation (2dsinθ=nλ), this indicates that the interlayer spacing d increases (Guan et al. 2020). This suggests that fluorine groups intercalate between the layers and widen the interlayer distance. The decrease in peak height reflects a reduction in the crystal domain size of Ti_3C_2 and a slight decrease in layered order. These two phenomena together confirm the successful fluoro-group modification.

SEM analysis

Figure 3 shows the SEM images of Ti_3AlC_2, Ti_3C_2, and F-Ti_3C_2. Figure 3(a) corresponds to Ti_3AlC_2 powder. It presents a bulk aggregation morphology, with fine particles attached to its surface. It is a typical dense bulk structure of the MAX phase. Figure 3(b) corresponds to Ti_3C_2 MXene two-dimensional nanosheets obtained by HF-HCl etching. Clear and uniformly dispersed two-dimensional layered structures are observed, with gaps between the layers. Meanwhile, the surface of the nanosheets is relatively smooth without obvious impurities. This indicates that the etching process is relatively complete and that the two-dimensional layered structure is successfully exfoliated (Hasan et al. 2025). Figure 3(c) shows F-Ti_3C_2 obtained by PFOTS modification. It still maintains a complete two-dimensional layered structure, with only a slightly rough surface. This is attributed to the hydrophobic film formed by PFOTS grafting via siloxane bonds. The film has no obvious particles and uniformly covers the surface. The comparison shows that HF-HCl etching of Ti_3AlC_2 can successfully obtain a layered structure with clear two-dimensional morphology. Subsequent PFOTS modification can uniformly form a hydrophobic film while maintaining its two-dimensional layered structure (Zhou et al. 2022).

XPS analysis

Figure 4 shows the XPS spectra of Ti_3C_2 and F-Ti_3C_2. Characteristic peaks of F 1s, O 1s, C 1s, and Ti 2p are observed in the survey spectrum of pristine Ti_3C_2 in Figure 4(a). This

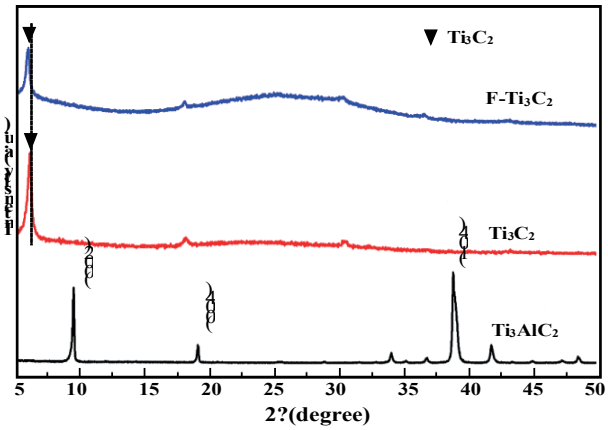


Fig. 2. XRD patterns of Ti3AlC2, Ti_3C_2 and F-Ti_3C_2

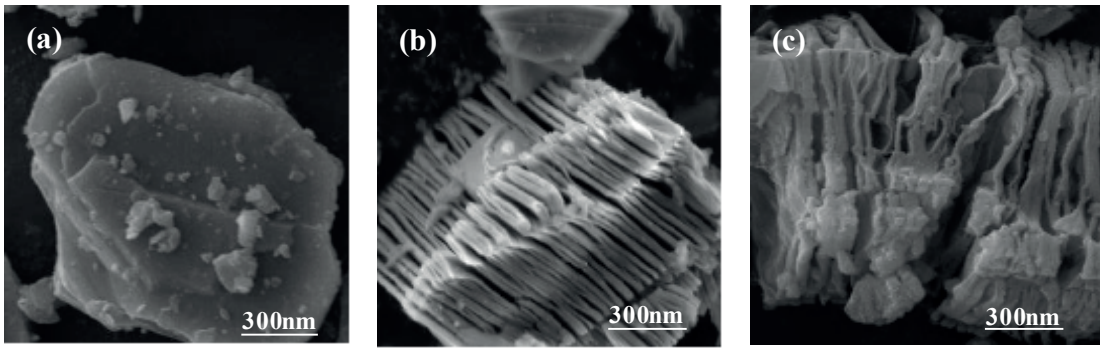


Fig. 3. SEM of Ti_3AlC_2, Ti_3C_2 and F-Ti_3C_2

confirms the formation of typical MXene surface functional groups such as Ti-F and Ti-O/Ti-OH on Ti3C2 after HF-HCl etching. It provides direct evidence that the Al layer is effectively etched. Characteristic peaks of Ti^{2+} (Ti-C, 454.8 eV/460.5 eV), Ti^{3+} (Ti-O/Ti-X, 456.2 eV/462.0 eV), and Ti^{4+} (TiO_2, 458.6 eV/464.3 eV) are obtained by peak fitting of the high-resolution Ti 2p spectrum in Figure 4(b). The appearance of the Ti^{4+} peak is attributed to slight oxidation on the Ti3C2 surface. The fitted peak of the Ti-X (X=F/O) bond reflects the diversity of surface functional groups after etching(Li et al. 2020). The C 1s spectrum in Figure 4(c) can be deconvoluted into C-C (284.8 eV), C-O (286.0 eV), and Ti-C (281.6 eV) peaks. As the characteristic skeleton bond of Ti3C2, the Ti-C bond shows a sharp peak and a significant proportion. This indicates that the layered structure of MXene is not destroyed (Zeng et al. 2024). The O 1s spectrum in Figure 4(d) is further fitted into Ti-O-Ti (529.8 eV), Ti-OH (531.2 eV), and surface-adsorbed oxygen (532.5 eV) peaks. It shows that the surface of pristine Ti_3C_2 is dominated by hydrophilic functional groups such as hydroxyl and oxy groups as active sites (Huang et al. 2020).

Figure 4(e) shows the survey spectrum of F-Ti_3C_2 after PFOTS modification. The intensity of the F 1s peak is significantly enhanced compared with that of pristine Ti_3C_2. A characteristic Si-O peak appears in the O 1s spectrum. This provides evidence that PFOTS molecules are successfully grafted onto the surface of Ti_3C_2. Two characteristic peaks of C-F (688.0 eV) and C-Ti-F_X (685.5 eV) are fitted from the high-resolution F 1s spectrum in Figure 4(k). The C-F bond is the typical bonding form of perfluoroalkyl groups in PFOTS molecules. The C-Ti-F_X peak indicates that PFOTS forms chemical bonding with Ti sites on the Ti_3C_2 surface, which supports the formation of chemical bonding rather than simple physical adsorption. New characteristic peaks of -CF_2-

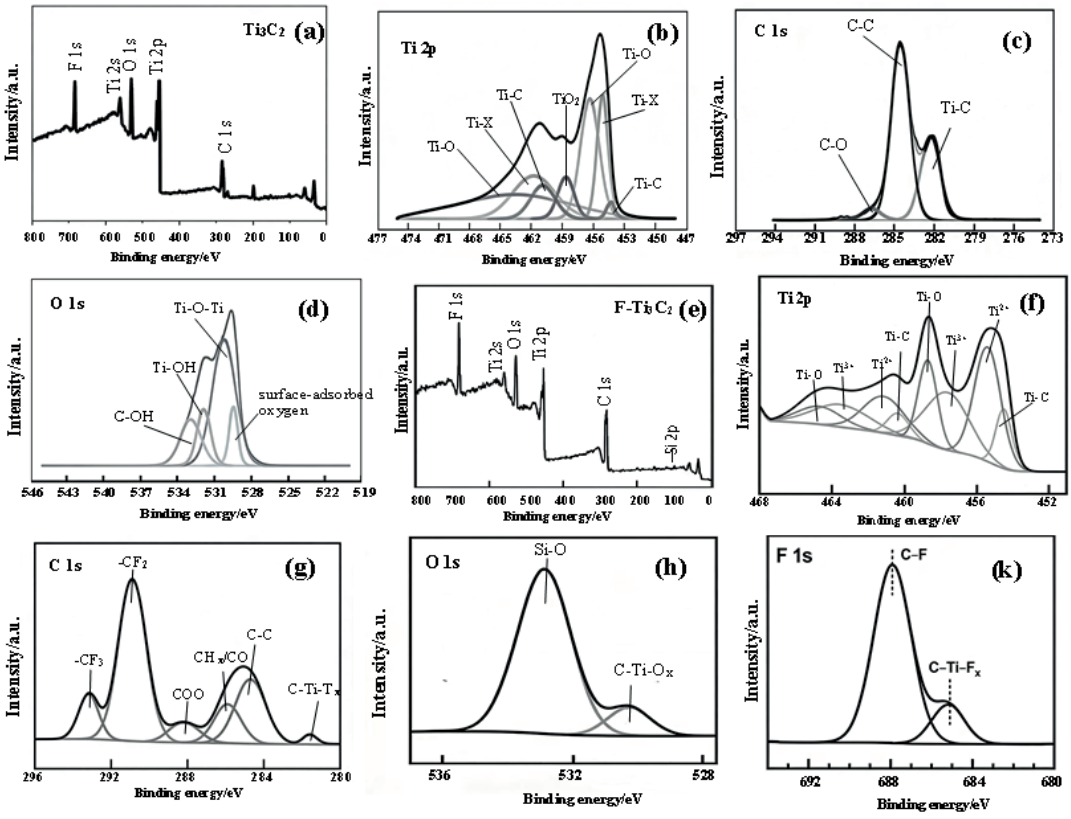


Fig. 4. XPS spectra of Ti_3C_2 and F-Ti_3C_2: (a)-(d) correspond to the survey spectrum and high-resolution spectra of Ti, C and O for Ti_3C_2; (e)-(k) correspond to the survey spectrum and high-resolution spectra of Ti, C, O and F for PFOTS-modified F-Ti_3C_2.

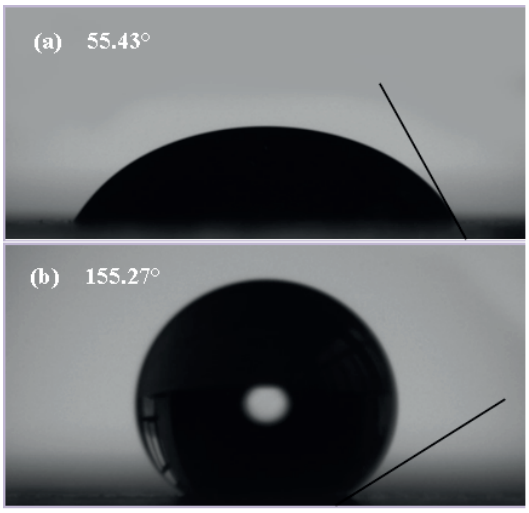


Fig. 5. The contact angle test results of Ti_3C_2 and F-Ti_3C_2

(291.0 eV) and -CF_3 (293.5 eV) appear in the C 1s spectrum deconvolution in Figure 4(g). These are characteristic carbon peaks of the perfluorooctyl chain in PFOTS. Meanwhile, the appearance of CH_X/CO (285.5 eV) and COO (288.0 eV) peaks corresponds to the alkyl and ester groups in PFOTS molecules. The retention of the Ti-C (281.6 eV) peak indicates that the main framework of Ti3C2 is not destroyed. The Si-O (532.0 eV) peak becomes the main peak in the O 1s spectrum deconvolution in Figure 4(h). It replaces the dominant position of Ti-OH in pristine Ti_3C_2. This indicates that PFOTS is covalently bonded to the hydroxyl groups on the Ti3C2 surface through a Si-O-Ti condensation reaction. The grafting of hydrophobic functional groups is thus achieved. The proportion of Ti^{4+} in the Ti 2p spectrum deconvolution of F-Ti_3C_2 in Figure 4(f) increases slightly. This is speculated to be caused by slight oxidation on the surface. However, the strong signal of the Ti–C main peak still indicates the structural integrity of MXene.

In summary, the XPS characterization results show that PFOTS modification introduces hydrophobic functional groups onto the Ti_3C_2 surface via Si–O–Ti bonds without destroying the main layered structure of Ti_3C_2. Meanwhile, it promotes the transformation of Ti_3C_2 surface functional groups from hydrophilic groups (-OH, -O-) to hydrophobic ones. Thus, the hydrophobicity of the Ti_3C_2 interface is achieved.

Contact angle analysis

Figure 5 shows the contact angle test results of Ti_3C_2 and F-Ti_3C_2. The contact angle of Ti_3C_2 is only 55.43°, indicating that pristine Ti_3C_2 has strong hydrophilicity. This is because a large number of hydroxyl groups exist on its surface. These groups are prone to adsorb water vapor. The contact angle of F-Ti_3C_2 support modified by PFOTS increases significantly to 155.27°. This demonstrates that the hydrophobicity of Ti_3C_2 is greatly improved after fluoro-group modification. It meets the standard of strong hydrophobicity. A hydrophobic film forms on the surface of modified F-Ti_3C_2. Combined with the determination results in Figure 4(g), the -CF_3 and -CF_2- groups have extremely strong hydrophobicity and can effectively repel water molecules. They can inhibit water vapor adsorption and condensation on the support surface. Meanwhile, combined with the SEM image in Figure 3(c), the formation of the hydrophobic film does not block the interlayer gaps of Ti_3C_2. It does not affect the subsequent loading of promoters and active components. The above results confirm that fluoro-group modification can significantly enhance the hydrophobicity of Ti_3C_2 support(Yang et al. 2025).

Optimization of catalyst preparation parameters and activity evaluation

Coupling evaluation experiments for hydrogen-rich fuel are conducted at 600 °C. CO conversion, CH_4 conversion ,and H_2 selectivity are used as the evaluation indicators. The optimal preparation parameters of the NiCo-CeO_2/F-Ti_3C_2 catalyst are screened. These parameters include NiCo metal loading, Ni/Co molar ratio, and Ce loading. The stability of the optimal catalyst is then evaluated.

Effects of NiCo metal loading on CO/CH_4 conversion and H_2 selectivity

Catalysts of NiCo/F-Ti_3C_2 are prepared. The total loadings of NiCo are set at 5%, 8%, 13%, and 17%. The Ni/Co molar

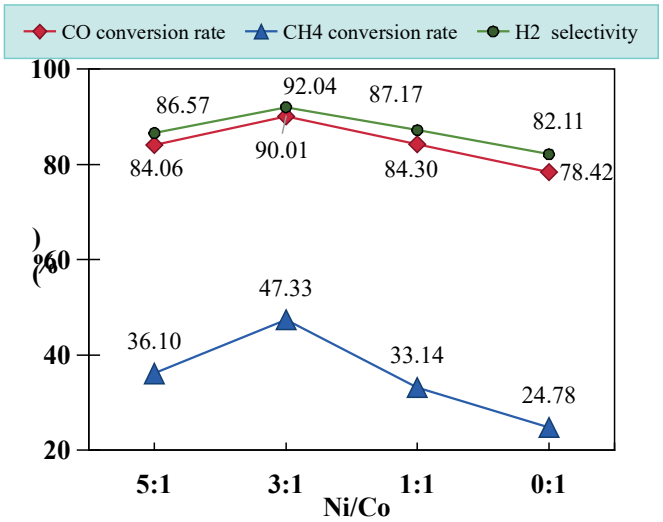


Fig. 6. Effects of NiCo loading on CO/CH4 conversion and H_2 selectivity

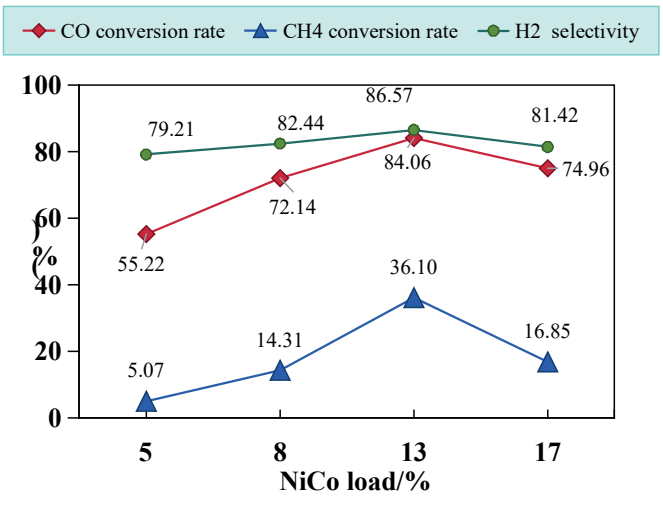


Fig. 7. Effects of Ni/Co molar ratio on CO/CH4 conversion and H_2 selectivity

ratio is controlled at 3:1. The results of the activity evaluation are shown in Figure 6. It can be seen from Figure 6 that CO conversion, CH_4 conversion, and H_2 selectivity all show a trend of first increasing and then decreasing with the increase in NiCo loading. The CO conversion, CH_4 conversion, and H_2 selectivity reach their peak values when the NiCo loading is 13%. The peak values are 79.21%, 36.10%, and 84.06%, respectively. The main reason is that a 13% NiCo loading can form a large number of Ni-Co alloy active sites. The interaction between the active sites and the support can efficiently activate the C–O bonds of CO and C-H bonds of CH_4. This improves the conversion efficiency and H_2 selectivity. When the loading increases to 17%, excessive NiCo metals agglomerate. This leads to a decrease in the exposure of active sites (Masoudpanah et al. 2025). It also blocks the pores of the support, hindering the contact between reactants and active sites as well as the desorption of H_2. Finally, all performance indicators decrease. Therefore, 13% is determined as the optimal NiCo loading.

Effects of Ni/Co molar ratio on CO/CH_4 conversion and H_2 selectivity

NiCo/F-Ti_3C_2 catalysts are prepared. The Ni/Co molar ratios are set at 5:1, 3:1, 1:1 and 0:1. The total NiCo loading is controlled at 13%. The results of the activity evaluation are shown in Figure 7. It can be observed from Figure 7 that, with the Ni/Co molar ratio changing from 5:1 to 0:1, both CO conversion and CH_4 conversion show a trend of first increasing and then decreasing. H_2 selectivity also first increases to a peak and then decreases continuously. When the Ni/Co molar ratio is 3:1, the CO conversion, CH_4 conversion, and H_2 selectivity reach 90.01%, 47.33%, and 92.04%, respectively. These values are the maximum within the entire ratio adjustment range. From the perspective of active sites and the alloy formation mechanism, when the Ni/Co molar ratio is 3:1, the proportion of nickel-dispersed active sites and the formation of nickel-cobalt alloys in the system reach a balance. The synergistic effect of the two types of sites maximizes the adsorption and activation efficiency of CO and CH_4 as well as the selectivity of H_2 generation. Thus, the catalytic performance reaches its peak. When the Ni/Co molar ratio is higher than 3:1 (e.g., 5:1), the formation of nickel-cobalt alloys is limited, and the proportion of nickel active components is relatively high. Nickel is prone to agglomeration, leading to a reduction in the number of effective active sites. Therefore, the conversion effect and selectivity are poor. When the Ni/Co molar ratio is lower than 3:1 (e.g., 1:1), the increase in Co content promotes the formation of more nickel-cobalt alloys. The proportion of nickel-dispersed active sites decreases accordingly, and the total number of active sites is reduced. The catalytic performance further declines. When the ratio continues to decrease to 0:1, only cobalt active sites remain in the system. Cobalt is not only prone to self-agglomeration but also cannot achieve high-efficiency catalysis like nickel or nickel-cobalt alloys. Finally, the CO conversion, CH_4 conversion, and H_2 selectivity all remain at the lowest level. In summary, the optimal Ni/Co molar ratio is 3:1.

Effects of Ce loading on CO/CH_4 conversion and H_2 selectivity

Ce is first loaded onto the F-Ti_3C_2 support. The Ce loadings are set at 3%, 5%, 8%, and 11%. Then, NiCo metals are loaded onto the support. The total NiCo loading is controlled at 13%, and the Ni/Co molar ratio is fixed at 3:1. The NiCo-CeO_2/F-Ti_3C_2 catalysts are prepared via calcination under a nitrogen atmosphere followed by reduction under a hydrogen atmosphere. The results of the activity evaluation are shown in Figure 8.

It can be observed from Figure 8 that, with the Ce loading increasing from 2% to 11%, CO conversion, CH_4 conversion, and H_2 selectivity all show a trend of increasing significantly to a peak and then decreasing continuously. When the Ce loading is 5%, all catalytic performance indicators reach their maximum within the entire adjustment range. It achieves the optimal preparation effect of hydrogen-rich fuel gas. From the perspective of the catalytic mechanism, the core function of CeO_2 is to regulate the dispersion of Ni-Co alloy active metals. It improves the effective utilization and catalytic activity of active sites. When the Ce loading is lower than 5%, the content of CeO_2 is insufficient, and its regulating effect on the dispersion of Ni-Co alloys is limited. Some Ni-Co metals are

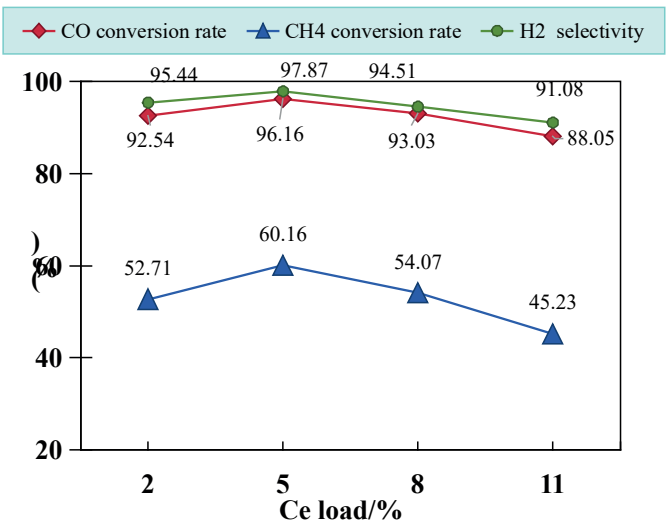


Fig. 8. Effects of Ce loading on CO/CH4 conversion and H_2 selectivity

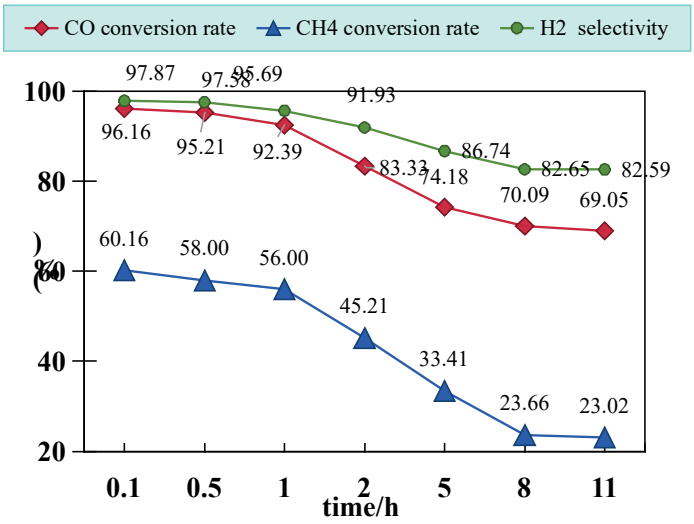


Fig. 9. Evaluation of the optimal NiCo-CeO_2/F-Ti_3C_2 catalyst

prone to agglomeration, leading to a reduction in the number of effective active sites. The catalytic performance cannot be fully exerted. When the Ce loading is higher than 5%, excessive CeO_2 cannot further optimize the dispersion of Ni-Co alloys. Instead, it aggregates on the support surface and blocks the pores. This hinders the mass transfer process of reactants and products, and the catalytic efficiency of active components decreases significantly. The catalytic performance continues to decrease with the increase in Ce loading. In summary, the optimal Ce loading is 5%.

Stability evaluation of the optimal NiCo-CeO_2/F-Ti_3C_2 catalyst

The optimal catalyst is prepared with a Ce loading of 5%, a NiCo loading of 13% and a Ni/Co molar ratio of 3:1. A stability test is conducted on this catalyst. CO conversion, CH_4 conversion, and H_2 selectivity are measured at different time intervals. The measurement results are shown in Figure 9.

Figure 9 shows that, for the optimal catalyst, CO/CH_4 conversion and H_2 selectivity decrease only slightly within 0-1 h, maintaining a stable trend. The performance indicators drop rapidly with a significant decrease within 1-8 h. The performance stabilizes without obvious fluctuations within 8-11 h. At the initial 6 minutes of the reaction, CO conversion reaches 96.16%. CH_4 conversion reaches 60.16%, and H_2 selectivity reaches 97.87%. After 11 h, CO conversion maintains at 69.05%, CH_4 conversion remains at 23.02%, and H_2 selectivity remains at 82.59%. Within 0-1 h, the catalytic performance attenuates slightly. The hydrophobic surface structure is assumed to remain relatively intact during this stage. The overall structure of the catalyst and the catalytic efficiency of active centers do not undergo substantial changes. The performance decline is therefore extremely small. Within 1-8 h, the high-temperature reaction environment causes thermal decomposition of fluoro-based hydrophobic groups on the Ti_3C_2 surface. The hydrophobic properties of the support are thereby weakened, which may lead to aqueous-phase poisoning of the catalyst. This results in a rapid decline of conversion and selectivity. Within 8-11 h, the support structure and hydrophobic groups of the catalyst undergo irreversible structural changes. A dynamic balance is achieved between slight carbon deposition and water vapor poisoning. The catalytic function of the active components is not completely lost, and they can still participate in the hydrogen production reaction. Therefore, all catalytic performance indicators tend to izestabilize without significant fluctuations. In summary, the optimal catalyst exhibits stage-specific catalytic stability during the 11 h stability test. Performance attenuation is slight in the early stage, with good structural integrity. Performance drops sharply in the middle stage, which may be attributed to structural damage and poisoning effects. Performance stabilizes in the later stage after a balance between poisoning and catalytic processes is achieved. Overall, it has certain potential for long-term catalytic applications.

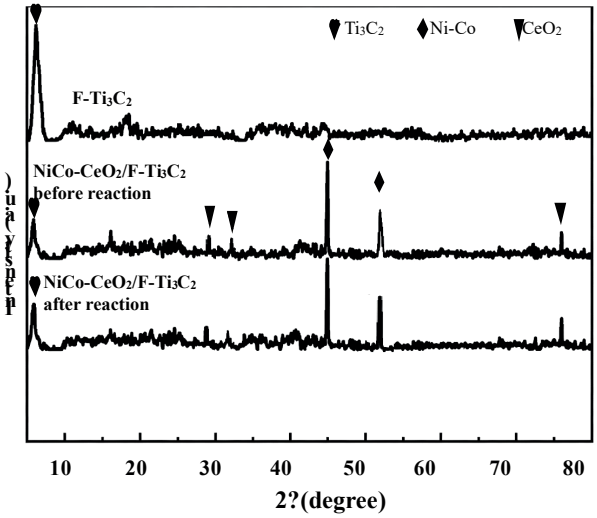


Fig. 10. XRD patterns of F-Ti_3C_2, the optimal NiCo-CeO_2/F-Ti_3C_2 before reaction and after 0.1 h of

Catalyst characterization analysis

XRD analysis

It can be seen from Figure 10 that, in the XRD patterns of the optimal NiCo-CeO_2/F-Ti_3C_2 catalyst before and after the reaction, besides the characteristic diffraction peaks of Ti_3C_2, there are obvious characteristic diffraction peaks of CeO_2 (Kanmaz et al. 2025). The peaks are located at 2θ=28.6°, 33.1°, and 76.7°. This indicates that the successfully loaded Ce forms a stable oxide phase. The characteristic diffraction peaks of the Ni-Co alloy appear in the patterns (Rai & Hegde 2024). The peaks are located at 2θ=44.5° and 51.7°. This demonstrates that the oxides of Ni and Co are successfully reduced to the Ni-Co alloy. In addition, the characteristic diffraction peaks of the Ni-Co alloy have high intensity, indicating that the Ni-Co alloy has good crystallinity. The characteristic diffraction peaks of CeO_2 have low intensity, suggesting that CeO_2 is uniformly dispersed without obvious agglomeration. The characteristic peaks of the optimal catalyst show little change before and after the reaction. This indicates that the catalyst has good structural stability.

SEM analysis

Figures 11(a)-(c) show the SEM characterization results of the optimal NiCo-CeO_2/F-Ti_3C_2 catalyst. The results are obtained under the hydrogen-rich atmosphere of biomass pyrolysis gas at 600 °C. The three states are the unreacted

Table 2: XPS analysis of Ni, Co, O and Co for the optimal catalyst

optimal catalyst	Ni^0/Ni^{2+} molar ratio	Co^0/Co^{2+} molar ratio	O_{ads}/O_{total} (at.%)	Ce^{3+}/Ce^{4+} molar ratio
unreaction	1.55	1.17	26.1	0.28
after 8h reaction	2.06	1.49	18.6	0.17

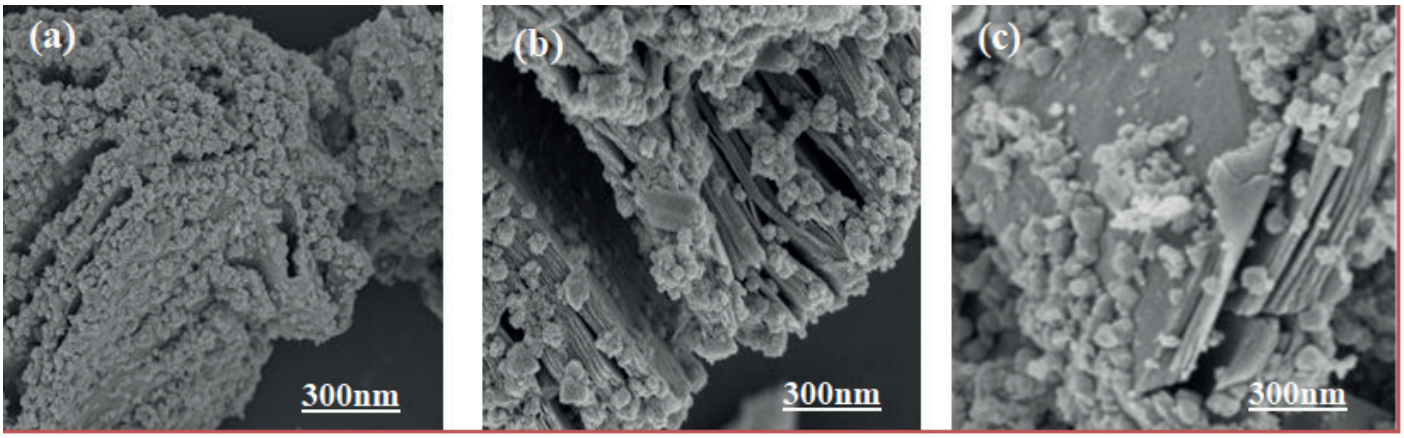


Fig. 11. SEM images of the optimal NiCo-CeO_2/F-Ti_3C_2 catalyst

catalyst, the catalyst reacted for 1 h, and the catalyst reacted for 8 h. For the unreacted catalyst (Figure 11 (a)), the active metal particles are uniformly dispersed on the support surface at the nanoscale. No obvious agglomeration is observed. The hydrophobicity imparted by fluoro-group modification endows the catalyst surface with a rough micromorphology, which provides highly dispersed active sites. After 1 h of reaction (Figure 11 (b)), the active particles show slight agglomeration, and some small particles fuse together. The catalyst structure remains intact. The catalyst surface still presents a fuzzy and rough state, indicating that the fluoro-based hydrophobic groups are not largely destroyed and the hydrophobicity is retained. When the reaction time is extended to 8 h (Figure 11 (c)), the agglomeration degree of active particles increases significantly. Large particle aggregates form on the support surface. Meanwhile, the support surface changes from rough to smooth and flat. This may be because the fluoro-based hydrophobic groups undergo thermal decomposition and are removed at 600 °C. The long-term thermal effect promotes further migration and fusion of active particles, eventually leading to significant changes in the surface morphology and active particle distribution of the catalyst (Liu et al. 2022). The changes in catalyst morphology further support the stability evaluation results in Figure 9.

XPS analysis

Table 2 presents the XPS analysis results of the optimal catalyst before the reaction and after 8 h of reaction. The changes in the valence states of various elements and adsorbed oxygen clearly reflect the structural evolution and activity decay mechanism of the catalyst under the hydrogen-rich atmosphere of biomass pyrolysis gas at 600 °C. In the unreacted catalyst, the molar ratios of Ni^0/Ni^{2+} and Co^0/Co^{2+} are 1.55 and 1.17, respectively. After 8 h of reaction, these two ratios increase to 2.06 and 1.49, respectively. This indicates that Ni and Co elements are reduced to their metallic states during the high-temperature reaction process (Zhang et al. 2024). Although metallic Ni and Co are the active centers of the catalytic reaction, combined with the particle agglomeration observed in the SEM characterization, the aggregation of metallic species leads to a decrease in the effective exposure of active sites.

The proportion of adsorbed oxygen (O_{ads}) in the total oxygen decreases from 26.1% to 18.6%. As a key active oxygen species in the catalytic reaction, the sharp reduction in its content significantly weakens the adsorption and activation ability of the catalyst for the reactants of biomass pyrolysis gas. The molar ratio of Ce^{3+}/Ce^{4+} decreases from 0.28 to 0.17, indicating an increase in the proportion of Ce^{4+}. The Ce^{3+}/Ce^{4+} redox cycle is the core of the cocatalytic effect of cerium dioxide promoter (Gong et al. 2025). The reduction in the efficiency of this cycle further weakens the promoting effect of the promoter on the main catalytic reaction (Mathew & Devi 2024). The comprehensive changes in the valence states of the above elements and oxygen species, together with the agglomeration of catalyst morphology and the decomposition of hydrophobic groups, constitute the internal reasons for the catalytic activity first decreasing sharply and then stabilizing during the reaction process.

Contact angle analysis

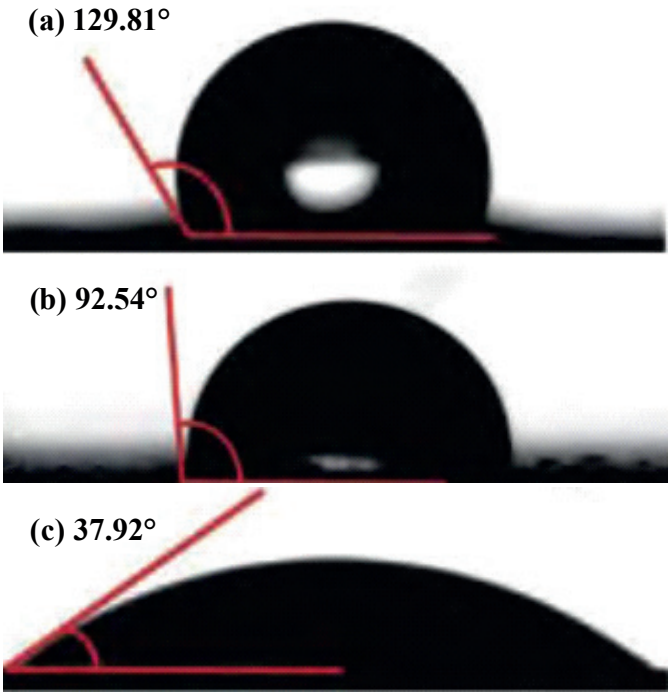


Fig. 12. S. Contact angle measurement results of the optimal catalyst in unreacted state, after 1 h of reaction and after 8 h of reaction

Figures 12(a)-(c) show the contact angle measurement results of the optimal catalyst in the unreacted state, after 1 h of reaction, and after 8 h of reaction. The contact angle values decrease from 129.81° to 92.54° and then to 37.92°. This trend is highly correlated with the catalytic activity evolution of the hydrogen production reaction in the aqueous phase of biomass pyrolysis gas. The contact angle of the unreacted catalyst is much larger than 90°. The strong hydrophobic surface constructed by fluoro-group modification and the uniformly dispersed active particles can resist the adsorption and agglomeration of water vapor in the reaction system (Zhang et al. 2025). This avoids the coverage of active sites by water film and ensures sufficient contact between CO, CH_4, and active centers. Thus, the catalyst exhibits excellent initial activity. After 1 h of reaction, the contact angle is slightly larger than 90°. The hydrophobicity decreases significantly. This is because some fluoro-based hydrophobic groups decompose under high temperature. Meanwhile, the slight agglomeration of active particles reduces the surface roughness (Chen 2026). A small amount of water vapor begins to adsorb and occupy the active sites. The catalytic activity shows an initial sharp decline. After 8 h of reaction, the contact angle drops sharply to 37.92°. The catalyst surface becomes hydrophilic (Chen & Wang 2026). The fluoro-based groups may have substantially decomposed under the synergistic effect of high temperature and water vapor. Severe particle agglomeration makes the surface tend to become smooth. A large amount of water vapor adsorbs to form a water film. It not only blocks the active sites but also hinders the diffusion of reactants. It also inhibits the hydrogen production reaction. As a result, the catalytic activity drops continuously and sharply during 1-8 h. The subsequent stable activity is related to the substantial decomposition of hydrophobic groups and the dynamic equilibrium of water vapor adsorption.

Conclusions

This study prepares hydrophobic F-Ti_3C_2 MXene two-dimensional nanosheets. The preparation involves HF-HCl solution etching and perfluorooctyltriethoxysilane(PFO TS) modification. The F-Ti_3C_2 MXene serves as the catalyst support. CeO_2 promoters and Ni-Co alloy active components are loaded onto the support. The loading process adopts the impregnation method combined with nitrogen calcination and hydrogen reduction. A catalyst with both high activity and strong hydrophobicity is obtained. A fixed-bed reactor is used to evaluate the catalyst performance for hydrogen-rich gas production. The effects of total NiCo loading, Ni/Co molar ratio, and Ce loading on CO/CH_4 conversion and H_2 selectivity are investigated. Characterization techniques including XRD, SEM, XPS, and contact angle measurement are applied to analyze the catalytic mechanism. The main conclusions are as follows:

(1) The NiCo-CeO_2/F-Ti_3C_2 catalyst exhibits optimal performance under the following parameters: the total NiCo loading is 13%, the Ni/Co molar ratio is 3:1, and the Ce loading is 5%. In the initial reaction stage, the catalyst achieves a CO conversion rate of 96.16%, a CH_4 conversion of 60.16%, and an H_2 selectivity of 97.87%. The catalyst shows excellent performance in hydrogen production from biomass pyrolysis gas.

(2) The optimal catalyst has a contact angle of 129.81° , showing strong hydrophobicity. XRD characterization confirms the presence of characteristic peaks of the Ni-Co alloy and CeO_2 after nitrogen calcination and hydrogen reduction. SEM characterization reveals an intact two-dimensional layered structure of the catalyst and uniform dispersion of the active components. XPS analysis before and after the reaction indicates changes in the valence states of the elements. The Ce^{3+}/Ce^{4+} redox cycle efficiency decreases, which impairs the catalyst performance. The catalyst maintains high and stable catalytic activity within 0-1 h, during which the hydrophobic groups remain relatively intact.

(3) The hydrophobic interface constructed by fluoro-group modification effectively resists the hydrothermal deactivation of the catalyst and improves the efficiency of biomass pyrolysis gas conversion. Future work will focus on preparing protective carbon films to protect the hydrophobic groups and prevent them from being damaged during the reaction. This strategy will extend the stable reaction time of the catalyst.

Acknowledgments: This work was financially supported by the Key Industrial Talent Support Project of Xinjiang Uygur Autonomous Region (No. XJRC-2025-GX-ZDCY-04), the Regional Collaborative Innovation Program (Science and Technology Aid to Xinjiang) of Xinjiang Uygur Autonomous Region (No. 2025E02036), and the Xinjiang Uygur Autonomous Region Natural Science Foundation (Youth Fund, Southern Xinjiang United Fund) (Grant No. 20271161766).

Conflicts of Interest: The authors declare no conflict of interest.

References

Benkacher, N., Iggui, K., Mekhania, Z. A., Benhamida, A., Djermoune, A., Merzeg, F. A., Satha, H. & Layachi, A. (2025). Influence of surface modification of Algerian palygorskite with triethoxyoctylsilane as a hydrophobic agent for enhanced performance, *Journal of Coatings Technology and Research*, 22, 6, pp.2105–2118. DOI:10.1007/s11998-025-01102-x.

Bootpakdeetam, P., Igboenyesi, O. V., Dennis, B. H. & MacDonnell, F. M. (2024). Superhydrophobic Surface Modification of a Co-Ru/SiO Catalyst for Enhanced Fischer-Tropsch Synthesis, *Catalysts,* 14, 9, pp.638. DOI:10.3390/catal14090638.

Chen, J. (2026). Preparation of NiFe-CeLaOx/HAP catalyst and its performance and mechanism for high-efficiency methanation of coal pyrolysis gas, *Energy Sources, Part A: Recovery, Utilization, and Environmental Effects,* 48, 1, 2595287. DOI:10.1080/15567036.2025.2595287.

Chen, J. & Wang, J. (2026). Research Progress in Photocatalytic Degradation of Cyclic Pollutants by Electrospun Black TiO / Ag@SiO Nanofiber Membranes, *Inorganics,* 14, 5, 131. DOI:10.3390/inorganics14050131.

Chen, Z., Meng, Y., Lu, J., Zhou, W., Yang, Z. & Zhou, A. (2023). The Effect of Hydrophobically Modified Iron Catalysts with Hexadecyltrimethoxysilane on Fischer-Tropsch Synthesis, *Chemistry Select,* 8, e202202903. DOI:10.1002/slct.202202903.

Gong, Y., Qi, W., Lu, W., Chang, Q., Xie, Y., Wang, J. & Deng, X. (2025). Construction of CeO2/Ti3C2Tx heterojunction with antibacterial and antioxidant capabilities for diabetic wound healing, *Journal of Colloid and Interface Science*, 689, 137247. DOI:10.1016/j.jcis.2025.03.036.

Guan, Y., Zhang, M., Qin, J., Ma, X., Li, C. & Tang, J. (2020).

Hydrophilicity-Dependent Distinct Frictional Behaviors of Different Modified MXene Nanosheets, *The Journal of Physical Chemistry* C, 124, 25, pp.13664–13671. DOI:10.1021/acs.jpcc.0c01551.

Guénolé, J., Taupin, V., Vallet, M., Yu, W. & Guitton, A. (2022). Features of a nano-twist phase in the nanolayered Ti3AlC2 MAX phase, Scripta Materialia, 210. DOI:10.1016/j.scriptamat.2021.114425.

Guo, H., Wang, Z., Kang, K. & Li, D. (2025). Production of Hydrogen-Rich Syngas via Biomass-Methane Co-Pyrolysis: Thermodynamic Analysis, *Polymers,* 17, 19, pp.2695. DOI:10.3390/polym17192695.

Gyimah, J., Nyantakyi, G. & Isaac, S. H. (2024). The effect of renewable energy on carbon emissions through globalization, *Heliyon*, 10, e26894. DOI:10.1016/j.heliyon.2024.e26894.

Hasan, M. Z., Haque, M. H., Ali, M. A., Hossain, M. M. & Uddin, M. M. (2025). Structural, optical, and photocatalytic efficacy of Ti3C2 and M2C (M=Ti, V, Cr, Nb) MXene materials synthesized by etching technique, *AIP Advances*, 15, 3. DOI:10.1063/5.0251436.

Huang, K., Li, C., Li, H., Ren, G., Wang, L., Wang, W. & Meng, X. (2020). Photocatalytic Applications of Two-Dimensional Ti3C2 MXenes: A Review, *ACS Applied Nano Materials*, 3, 10, pp.9581 − 9603. DOI:10.1021/acsanm.0c02481.

Kanmaz, ., Köksal, O. K., Apaydin, G., Tomakin, M. & Cengiz, E. (2025). Investigation of radiation shielding properties of CeO2 thin films prepared at different molarities, *Physica Scripta*, 100, pp.035945. DOI:10.1088/1402-4896/adb349.

Khojasteh, H., Mazhari, M.-P., Heydaryan, K., Aspoukeh, P., Ahmadiazar, S., Hamad, S. M. & Shaikhah, D. (2024). Enhancing glass surface hydrophobicity: the role of Perfluorooctyltriethoxysilane in advanced surface modification, *Journal of Sol-Gel Science and Technology*, 112, pp.857–869. DOI:10.1007/s10971-024-06593-5.

Li, Q., Zhou, J., Li, F. & Sun, Z. (2020). Novel MXene-Based Hierarchically Porous Composite as Superior Electrodes for Li-Ion Storage, *Applied Surface Science*, 530, 147214. DOI:10.1016/j.apsusc.2020.147214.

Liu, Z., Zhao, Y., Li, S., Sun, T., Liu, H., Wang, K. & Chen, X. (2022). CeO2/Ti3C2Tx MXene Nanostructures for Microwave Absorption, *ACS Applied Nano Materials*, 5, 4, pp.5764–5775. DOI:10.1021/acsanm.2c00829.

Ma, F., Liu, J., Chen, K. & Cheng, Z. (2024). Thermal Stability Improvement of Cu-Based Catalyst by Hydrophobic Modification in Methanol Synthesis, *Processes,* 12, 9, pp.2008. DOI:10.3390/pr12092008.

Masoudpanah, S. M., Koohdar, H. R., Derakhshani, M., Ranjbar, K., Sarkar, T. & Aslibeiki, B. (2025). Enhancement of microwave absorption performance of MOF-derived NiCo2O4 by adding Ti3C2Tx MXene, *Journal of Materials Science: Materials in Electronics*, 36, 1184. DOI:10.1007/s10854-025-15264-2.

Mathew, S. & Devi, S. K. R. (2024). Rationally designed CeO2 decorated Ti3C2 MXene interface for efficient water splitting and enhanced supercapacitor performance, Colloids and Surfaces A: *Physicochemical and Engineering Aspects*, 684, 133170. DOI:10.1016/j.colsurfa.2024.133170.

Rai T., Y. & Hegde, A. C. (2024). Electrodeposition and Electrocatalytic Study of Ni–Co Alloy Coatings, *Protection of Metals and Physical Chemistry of Surfaces*, 60, 6, pp.1084–1093. DOI:10.1134/S2070205124702514.

Reghunath, B. S., Rajasekaran, S., Mathew, S., Pinheiro, D., Devi, S. K. R., Jung, S., Jayaraman, T. & Choi, M. Y. (2023). Two-dimensional Ti3C2 MXene for photocatalytic hydrogen production: A review, *Bulletin of the Korean Chemical Society*, 44, pp.969–988. DOI:10.1002/bkcs.12783.

Wang, T., Zhou, T., Li, C., Song, Q., Zhang, M. & Yang, H. (2024). Development Status and Prospects of Biomass Energy in China, *Energies*, 17, 17, pp.4484. DOI:10.3390/en17174484.

Wang, Y., Shen, G., Wang, C., Gao, F., Wang, J. & Shen, M. (2024). Mechanistic insights into the deactivation of Pd/BEA methane combustion catalysts by hydrothermal aging, *Molecular Catalysis*, 558, pp.114027. DOI:10.1016/j.mcat.2024.114027.

Wei, C., Liu, C., Gao, L., Sun, Y., Liu, Q., Zhang, X. & Guo, J. (2019). MoS nanosheets decorated Ni (OH) 2 nanorod array for active overall water splitting, *Journal of Alloys and Compounds*. DOI:10.1016/j.jallcom.2019.05.071.

Yang, P., Wang, J., Ning, F., Qi, L., Chen, J. & Zhang, X. (2025). The electrowetting-on-dielectric and photothermal performance of the porous Ti3C2@PVDF composite and dehumidification application, *Colloids and Surfaces A: Physicochemical and Engineering Aspects*, 714, pp.136556. DOI:10.1016/j.colsurfa.2025.136556.

Zhang, H., Bao, L., Pan, Y., Du, J. & Wang, W. (2024). Interface reconstruction of MXene-Ti3C2 doped CeO2 nanorods for remarked photocatalytic ammonia synthesis, *Journal of Colloid and Interface Science*, 675, pp.130–138. DOI:10.1016/j.jcis.2024.07.008.

Zhang, W., Wang, Y., Jiao, Z., Wang, W., Ge, Y., Wang, C., Sun, L. & Zhou, C. (2025). Rapid detection and anti-humidity NO2 sensor at room temperature based on CeO2/few-layer Ti3C2 MXene composite, *Microchemical Journal*, 216, 114742.

Zeng, F., Chen, H., Mei, Y., Ye, L., Zhuang, S., Pu, N. & Wang, L. (2024). Performance and mechanism of sulfonamide-antibiotic adsorption by Ti3C2 MXene, *New Journal of Chemistry*, 48, 38, pp.16742–16752. DOI:10.1039/d4nj03341h.

Zhou, L., Qi, H., Lei, Y., Yu, J., Guo, B. & Zhang, D. (2022). Ti3C2 MXene induced high tribological performance of polyimide/polyurea copolymer at a wide temperature range, *Applied Surface Science*, 608, 155157. DOI:10.1016/j.apsusc.2022.155157.

Archives of Environmental Protection
Vol. 52 no. 3 pp. 45–59

PL ISSN 2083-4772
DOI: 10.24425/aep.2026.3677



© 2026. The Author(s). This is an open-access article distributed under the terms of the Creative Commons Attribution-ShareAlike 4.0 International Public License (CC BY SA 4.0, https:// creativecommons.org/licenses/by-sa/4.0/legalcode), which permits use, distribution, and reproduction in any medium, provided that the article is properly cited.

Comparison of surface water treatment efficiency using integrated pressure-driven membrane processes and conventional treatment systems

Małgorzata Kabsch-Korbutowicz[1]*, Małgorzata Wolska[1,2], Marek Mołczan[1], Wojciech Adamski[1], Jacek Adam Wiśniewski[1]

[1]Wrocław University of Science and Technology, Poland
[2]AGH University, Faculty of Geo-Data Science, Geodesy, and Environmental Engineering

*Corresponding author. E-mail: malgorzata.kabsch-korbutowicz@pwr.edu.pl

Keywords: microfiltration, ultrafiltration, nanofiltration, surface water treatment, separation efficiency

Abstract: Pressure-driven membrane techniques are increasingly being applied to natural water treatment as an alternative to conventional physico-chemical processes. This makes it essential to compare the effectiveness of these two approaches, particularly under long-term operational conditions. In the preliminary phase of the study, short-term tests were conducted to select the most suitable membranes based on their separation and transport properties: two out of three microfiltration (MF) membranes, two out of three ultrafiltration (UF) membranes, and one out of two nanofiltration (NF) membranes were chosen for subsequent long-term tests. During these long-term evaluations, the efficiency of surface water treatment in integrated MF+NF and UF+NF systems was assessed and compared with the performance of a conventional treatment train comprising coagulation, sedimentation, filtration, and adsorption.

The results indicate that integrated MF+NF and UF+NF systems achieve significantly higher treatment efficiency than conventional processes, with, for example, dissolved organic carbon (DOC) reduction of 93% in membrane systems compared with 50% using conventional methods. Membrane processes also enable highly effective removal of specific microorganisms, which is not achievable using traditional treatment methods. Additionally, integrated MF+NF and UF+NF systems reduce water salinity and achieve water softening, whereas conventional systems tend to increase salinity. An analysis of operational costs revealed that the UF+NF system is nearly 50% less expensive to operate than the MF+NF system. Nevertheless, both membrane-based systems remain several times more costly than conventional water treatment.

Introduction

Freshwater is one of the most important environmental resources, essential for the proper functioning of all living organisms and for all sectors of industry. In Europe, the majority of freshwater is abstracted from surface water bodies: approximately 75% of total water abstraction originates from rivers and reservoirs, while 25% comes from groundwater (Water resources of Europe 2025). Water is primarily used in three main sectors: agriculture, industry, and households. For potable water production, approximately 65% of the supply is derived from groundwater, whereas 35% comes from surface water sources (Europe's water in figures 2027).

Conventional surface water treatment typically involves a sequence of physico-chemical processes designed to remove physical, chemical, and microbiological contaminants. The most commonly applied unit processes include coagulation, flocculation, sedimentation, rapid sand filtration, adsorption on activated carbon, and disinfection. These conventional treatment methods have been successfully used for decades, particularly in municipal water supply systems. However, they present several limitations in the context of contemporary environmental, health, and technological challenges. Their effectiveness depends strongly on the characteristics and concentrations of pollutants, as well as on the composition of the water matrix (Knap-Bałdyga, and Zubrowska-Sudoł 2023). Moreover, these processes generate sludge and backwash water that require appropriate management and disposal (Zielina and Dąbrowski 2021). Coagulation involves the addition of chemical reagents, the residuals of which may contribute to secondary pollution (García-Avila et al. 2025). Similarly, chemical disinfection may lead to the formation of disinfection by-products (DBPs), some of which are potentially toxic or carcinogenic (Srivastav et al. 2020).

In response to the limitations of conventional technologies, low-pressure membrane processes began to be widely implemented in the 1990s (Li & Visvanathan 2017). Compared with conventional surface water treatment, microfiltration (MF) and ultrafiltration (UF) offer several advantages, including stable production of high-quality treated water, reduced or no chemical consumption, compact system design, and ease of automation (Aziz et al. 2024). These processes are particularly effective in removing protozoa (e.g., *Cryptosporidium*), whereas their efficiency in removing bacteria and, especially, viruses may be limited (Bodzek et al. 2019). Furthermore, low-pressure membrane processes are generally ineffective in removing low-molecular-weight organic compounds of both natural and anthropogenic origin, which may contribute, among other effects, to water color.

Nanofiltration (NF) has also been applied in drinking water treatment. Due to the specific separation properties of NF membranes, this process enables the removal of low-molecular-weight organic compounds, including emerging contaminants, and allows partial water softening and salinity reduction (Guo et al. 2022). However, membrane fouling remains a major operational challenge in NF system design and operation, affecting both the separation and transport properties of the membranes. Counteracting this phenomenon or mitigating its intensity significantly impacts the operational costs of membrane processes. As stated by Hong and Elimelech (1997), the presence of natural organic matter (NOM) in water causes calcium ions, responsible, among other things, for water hardness, to form a dense gel layer with high resistance on the NF membrane surface, thereby intensifying membrane fouling. To mitigate fouling intensity in NF systems, primarily through the removal of NOM, pretreatment using either conventional processes (Kim et al. 2011) or low-pressure membrane techniques is widely applied (Liu et al. 2021).

The application of membrane separation processes in drinking water treatment is limited by operational costs, particularly those associated with energy consumption and membrane fouling. Energy consumption in membrane separation processes has been reduced through the use of increasingly advanced (modified) membranes. The average energy consumption of the UF process is 0.29 kWh/m³ (Lidén and Persson 2016). In the case of NF, it is approximately 1 kWh/m³ (Fan et al. 2020), which is nearly 50% lower than that of RO. For this reason, among others, NF is widely used for freshwater treatment when only softening is required. For comparison, the energy consumption of conventional water treatment systems ranges from 0.6 to 0.8 kWh/m³, depending on the plant size and the type of filtration used (Skoczko 2025).

Regardless of whether conventional physico-chemical processes or membrane-based technologies are employed for water purification, treated surface water must undergo chemical disinfection to prevent secondary microbial contamination within the distribution system. The effectiveness of disinfection and, in particular, the formation and speciation of DBPs are strongly influenced by the concentration and characteristics of organic matter remaining in the treated water (Li et al. 2017; Pietrzyk and Papciak 2017). Numerous studies have shown that the amount of disinfection by-products formed is proportional to the UV_{254} absorbance value (Valenti-Quiroga et al. 2024; Wang et al. 2024). Therefore, the effective removal of organic matter in processes preceding disinfection is crucial to ensuring water safety.

The presence and type of organic matter also affect the degree of membrane fouling and, consequently, the reduction of permeate flux. In particular, the structure of NOM has been indicated as the main factor influencing the extent of membrane fouling (Zularisam et al. 2006). Additionally, membrane durability and permeate quality are determined by operational conditions, including the method and frequency of backwashing and/or chemical cleaning procedures.

The analyses of the effectiveness of membrane separation processes and conventional treatment systems presented in the

Table 1: Raw water characteristics

Parameter	Unit	Min value	Max value
Temperature	°C	12.0	17.4
Conductivity	µS/cm	563	740
Suspended solids	mg/L	1.6	16.6
Turbidity	NTU	2.9	17.8
Color	mg Pt/L	8.96	13.66
UV_{254}	m^{-1}	9.4	16.87
TOC	mg C/L	4.05	4.99
DOC	mg C/L	3.96	4.92
BDOC	mgC/L	0.31	1.39
Total hardness	mg $CaCO_3$/L	161	290
SO_4^{2-}	mg/L	27.1	86.4
Cl^-	mg/L	34.1	50.8
Clostridium perfringens	CFU/100 cm^3	0	78
E. coli	CFU/100 cm^3	0	25
Coliform bacteria	CFU/100 cm^3	3	2420
Total cell count (TCC)	cell/mL	37,971	293,069

literature do not allow for a direct comparison of these two approaches, as the studies were conducted using different water sources. In contrast, the present study was carried out in parallel using two treatment systems processing the same water, making it possible to compare both treatment efficiency and operational costs.

Therefore, the aim of this study was to compare the efficiency and costs of surface water treatment using conventional physico-chemical processes with those of integrated systems combining low-pressure membrane processes (microfiltration or ultrafiltration) and nanofiltration. The research was conducted under long-term operational conditions and included membranes made of different materials, enabling the identification of those with the most favorable separation and transport properties.

Materials and Methods

Raw water

The study was conducted to compare the effectiveness of surface water treatment using pressure-driven membrane processes (microfiltration, ultrafiltration, and nanofiltration) with a conventional treatment system comprising sequential coagulation, sedimentation, rapid sand filtration, and granular activated carbon adsorption. The water used in the study was sourced from a surface water body supplying a town in south-western Poland. The feedwater for each treatment system is characterized in Table 1.

Membrane processes

The membrane process tests were conducted in two stages. The first stage aimed to evaluate the separation and transport properties of microfiltration, ultrafiltration, and nanofiltration membranes. Preliminary tests were performed using three types of microfiltration modules, three types of ultrafiltration modules, and two types of nanofiltration modules. In the second stage, the membranes selected during the preliminary tests in each category were employed in long-term experiments to assess the suitability of integrated MF+NF and UF+NF processes for water treatment. The application of integrated MF+NF and UF+NF systems resulted from the need for partial softening of treated freshwater without complete demineralization.

All membrane modules used in the study were supplied by PolymemTech (Warsaw, Poland). The characteristics of the membrane modules are summarized in Table 2.

Preliminary membrane tests were conducted over a period of 5 hours, while the long-term experiments using sequential systems were carried out for 71 days (MF+NF) and 90 days (UF+NF). All short-term experiments were performed in duplicate. Prior to the main experiments, the membranes were conditioned at the operating pressure for 45 minutes using tap water. During filtration cycles with capillary and tubular modules, the membranes were backwashed every 10 minutes for 1 minute. At the end of each filtration cycle, the membranes were chemically cleaned with a 1% citric acid solution.

Filtration with MF and UF membranes was preceded by pre-treatment of the raw water using 20 μm bag filters. For the NF tests, the feedwater was pre-treated using the MF3 microfiltration membrane.

In the long-term experiments, to minimize membrane fouling, the MF and UF modules were supplied with feedwater pre-treated using a 20 μm bag filter, a UV lamp, and a 10 μm cartridge filter. The ceramic micro- and ultrafiltration membranes were backwashed with permeate every 10 minutes for 1 minute and chemically cleaned weekly with NaOCl (200 mg Cl_2/L) and citric acid (pH 2.8).

Table 2: Membrane modules characteristics

Process	**Microfiltation**		
module symbol	**MF1**	**MF2**	**MF3**
membrane material	polypropylene (PP)	polypropylene (PP)	ceramic (α Al_2O_3)
mean pore diameter, μm	0.2	0.2	0.2
module configuration	spiral wound	capillary	tubular
membrane surface, m^2	1.8	0.5	1.26
Process	**Ultrafiltration**		
module symbol	**UF1**	**UF2**	**UF3**
membrane material	modified polytetrafluoroethylene (TFM)	polyethersulfone (PES)	ceramic
cut-off, kDa	1.5-3.5	20	50
module configuration	spiral wound	spiral wound	tubular
membrane surface, m^2	2.4	1.8	0.7
Process	**Nanofiltration**		
module symbol	**NF1**	**NF2**	
membrane material	poliamide (PA)	modified polytetrafluoroethylene (TFM)	
cut-off, Da	200	200-300	
module configuration	spiral wound	spiral wound	
membrane surface, m^2	7.9	7.9	

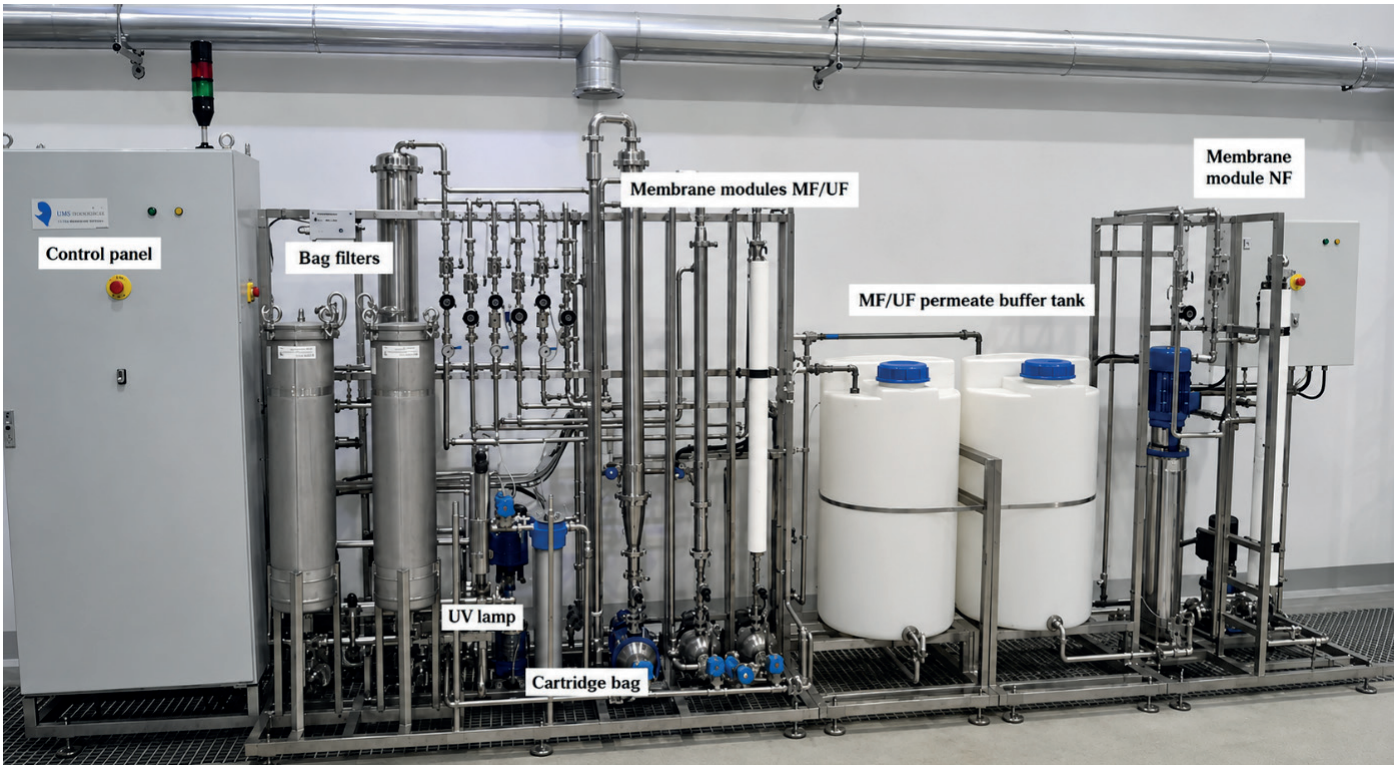


Fig. 1. Experimental set-up of the membrane system

All membrane processes were operated at constant pressures as follows:

- Short-term tests: 1.3 bar for MF, 3.05 bar for UF, and 3 bar for NF;
- Long-term tests: 1.9 bar for MF, 3 bar for UF, and 3.2 bar for NF.

The parameters applied in the short-term and long-term tests were determined based on preliminary studies and the operating conditions achievable within the pilot-scale installation.

All experiments were performed using the setup shown in Figure 1.

Conventional water treatment train

An experiment to evaluate the effectiveness of surface water treatment using a conventional treatment system was conducted in a continuous-flow system with a capacity of 2.95–3.05 m³/h, as illustrated in Figure 2. The treatment train consisted of coagulation, sedimentation, rapid sand filtration, and adsorption on granular activated carbon (GAC), with the operating parameters summarized in Table 3.

The system was operated continuously, and the process parameters remained largely stable throughout the study, except for minor adjustments in reagent dosages. The activated carbon was loaded into the filters two months prior to the start of the experiments, allowing it to develop biological activity.

Analytical methods

To evaluate the effectiveness of the individual treatment processes, the following parameters were measured in the raw water and in samples collected after each process step: temperature, conductivity, color, turbidity, suspended solids concentration, absorbance at 254 nm, dissolved organic carbon (DOC) concentration, total hardness, sulphate and chloride ion concentrations, and the presence of coliform bacteria, *Escherichia Coli* (*E. coli*), and *Clostridium perfringens*. All

Table 3: Operational parameter of conventional unit processes

Process:	Contact time (min)	Reagent	Dose, mg/L
Coagulation:		polyaluminium chloride of 65% basicity	1.94-2.89
Rapid mixing	2-3		
Flocculation	17-21		
Sedimentation	115-125	-	-
Sand filtration	18-25 (rate 5 m/h)	sand	-
Adsorption by GAC	18-25 (rate 5 m/h)	GAC WG-12 (specific surface area 968 m^2/g)	-
Stabilisation	-	H_2SO_4	2.1-3.5
Disinfection	-	NaOCl	0.7-1.0

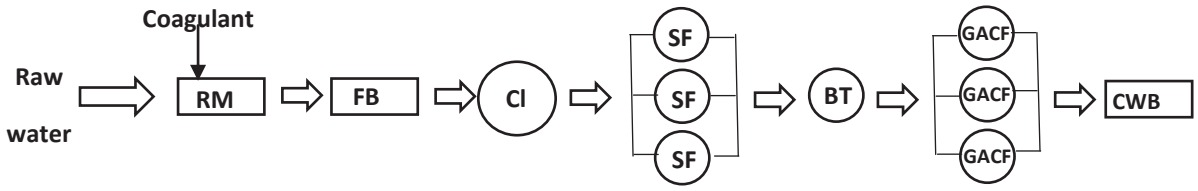


Fig. 2. Experimental set-up of the conventional water treatment train (RMT – rapid mixing tank, FB – flocculation basin, Cl – clarifier, SF – sand filter, BT- buffer tank, GACF – granular activated carbon filter, CWB – clean water basin)

analyses were conducted in accordance with current standard methods. Based on UV_{254} and DOC measurements, the specific UV absorbance (SUVA) was calculated. The analytical error of the performed measurements did not exceed 2%.

The molecular weight distribution of organic substances was determined using size-exclusion chromatography (SEC), following the procedure described in detail by Allpike et al. (2005). The SEC results were also presented as three-dimensional UV absorbance spectra (3D spectra) over the full wavelength range, allowing inferences regarding the properties of the organic substances.

For the long-term evaluation of both the membrane processes and the conventional treatment system, cytometric analyses were performed to determine total cell counts (TCC), the proportion of damaged cells, and the concentration of biodegradable dissolved organic carbon (BDOC). DNA staining was conducted using SYBR Green (SG) to quantify TCC and propidium iodide (PI) to assess damaged cells. Cytometric measurements were carried out using a BD Accuri™ C6 flow cytometer (BD Biosciences, USA).

Operational costs analysis

The comparison of the conventional water treatment system with the integrated membrane systems also included an analysis of the operational costs of each technological configuration.

Operational costs were determined based on measurements conducted during the study. The systems were equipped to monitor energy consumption, the volume of water used for rinsing, and the amount of reagents used for membrane cleaning. These measurements were used to determine the average consumption of energy, reagents, and consumable materials. Costs were then calculated using the unit prices of the individual materials applicable during the study period and incurred by the company. Unit prices were based on the company's supply contracts for reagents, energy, and other consumable materials. For the integrated membrane processes, the operational costs comprised:

1. Pre-treatment, including the operating costs of the bag filter system, cartridge filters, and the water heater and/or UV disinfection lamp.
2. Operation of MF, UF, and NF membranes, covering energy consumption and the costs associated with membrane rinsing (periodic chemical cleaning costs were not included).
3. Idle operation, encompassing the control and electrical systems of the installation.
4. Membrane replacement, assuming a service life of five years.

For the conventional treatment system, operational costs included:

1. Energy consumption for water pumping and mixing, covering the power supply for pumps, mixers, and reagent dosing pumps.
2. Reagent consumption, including coagulants, sodium hydroxide for pH adjustment, sodium hypochlorite, oxygen for ozone generation, and activated carbon.

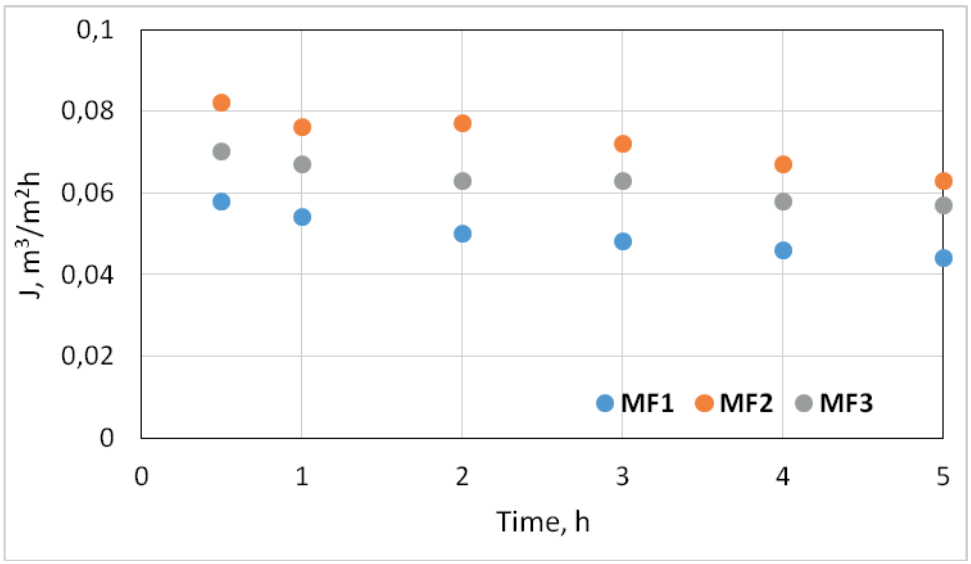


Fig. 3. Short-term permeate flux profiles for microfiltration membranes

Average reagent dosages used during system operation were adopted for cost estimation.

3. Filter backwashing, including the energy costs of blowers and pumps used for water and air backwashing.
   All costs were estimated based on 2025 prices.

Results and discussion

Evaluation of the transport and separation properties of micro-, ultra-, and nanofiltration membranes: a short-term study

To preliminarily assess the suitability of the membranes, their transport and separation properties were evaluated in short-term experiments. Analysis of the transport performance of the microfiltration modules showed that permeate flux was influenced by both the membrane material and the module configuration and operating mode (Figure 3, Table 4).

In the case of microfiltration membranes, which, according to the literature (Mulder 1996), are the most susceptible to fouling because they exhibit the highest convective transport among the three membrane types investigated (MF, UF, NF), detailed measurements of permeate flux were performed to analyze the kinetics of this phenomenon. Analysis of the permeate flux decline profiles over time showed that none of the membranes exhibited a rapid initial drop in hydraulic performance, which would indicate complete pore blocking. Instead, all membranes exhibited a gradual decline in performance throughout the experiment, indicating a mixed-mode fouling mechanism (intermediate blocking, adsorption, and cake layer formation).

For the polypropylene (PP) membranes, a significantly higher permeate flux was recorded in the capillary module (MF2) than in the spiral-wound module (MF1). This difference resulted from the fact that the capillary module was operated with periodic backwashing, whereas backwashing was not possible in the spiral-wound configuration. Despite the lower absolute permeate flux observed for the membrane in module MF1 compared with MF2, the relative decline in hydraulic performance after 5 hours of filtration was comparable for both systems, amounting to 23.8% and 27.9% for MF1 and MF2, respectively.

A comparison of the transport properties of PP and ceramic membranes, both operated with systematic backwashing (modules MF2 and MF3), revealed higher hydraulic performance for the polymeric membrane. This finding is somewhat unexpected, as PP membranes are generally considered hydrophobic (Ariono and Kusuma Wardani 2017), whereas ceramic membranes are typically regarded as strongly hydrophilic (Gu et al. 2022). Polypropylene is widely used as a membrane material due to its chemical stability, low cost, and good mechanical properties. Moreover, surface modification can render PP highly hydrophilic (Gryta 2021), which may lead to an increased permeate flux during the filtration of aqueous solutions. Although no information was available from the manufacturer of the membrane used in module MF2 regarding its surface treatment, it can reasonably be assumed that the membrane had undergone hydrophilization.

Analysis of the transport properties of the ultrafiltration membranes indicated that the highest permeate flux was achieved with the ceramic membrane installed in the tubular UF3 module, whereas the lowest flux was recorded for the TFM membrane in the spiral-wound UF1 module. The observed differences are attributable to both the membrane material (PTFE, PES, and ceramic) and the substantially different molecular weight cut-off (MWCO) values: 1.5–3.5 kDa for UF1, 20 kDa for UF2, and 50 kDa for UF3. Moreover, the tubular membrane in the UF3 module was subjected to systematic backwashing, which effectively limited the formation of a fouling layer and contributed to maintaining a higher permeate flux.

It is also noteworthy that, despite the absence of backwashing during the operation of the UF1 module (MWCO 1.5–3.5 kDa), the permeate flux remained nearly constant throughout the 5-hour test. This suggests that the retained particles were sufficiently large to prevent internal pore blocking and were continuously removed from the membrane surface by the circulating feed stream, thereby minimizing fouling.

For the nanofiltration membranes, both systems exhibited stable permeate flux throughout the experimental period. However, superior transport performance was observed for the NF1 membrane. Although the two tested membranes have similar molecular weight cut-off values, they differ in terms of membrane material. The membrane in the NF1 module was fabricated from polyamide, a highly hydrophilic polymer (El-Gendi 2022), which may account for its higher hydraulic performance.

Furthermore, no decline in permeate flux was recorded for either membrane during the short-term tests, indicating the absence of fouling under the applied operating conditions. This favorable performance may also be attributed to the pre-treatment of the feed solution using a ceramic microfiltration

Table 4: Permeate flux for membranes tested in short-term experiments

	Permeate flux, m^3/m^2h			
	min	max	mean	SD
MF1	0.043	0.056	0.048	0.0039
MF2	0.067	0.093	0.078	0.0066
MF3	0.054	0.071	0.063	0.005
UF1	0.028	0.028	0.028	0
UF2	0.049	0.069	0.058	0.0079
UF3	0.136	0.152	0.143	0.0075
NF1*	0.013	0.013	0.013	0
NF2*	0.009	0.009	0.009	0

* preceded by MF3

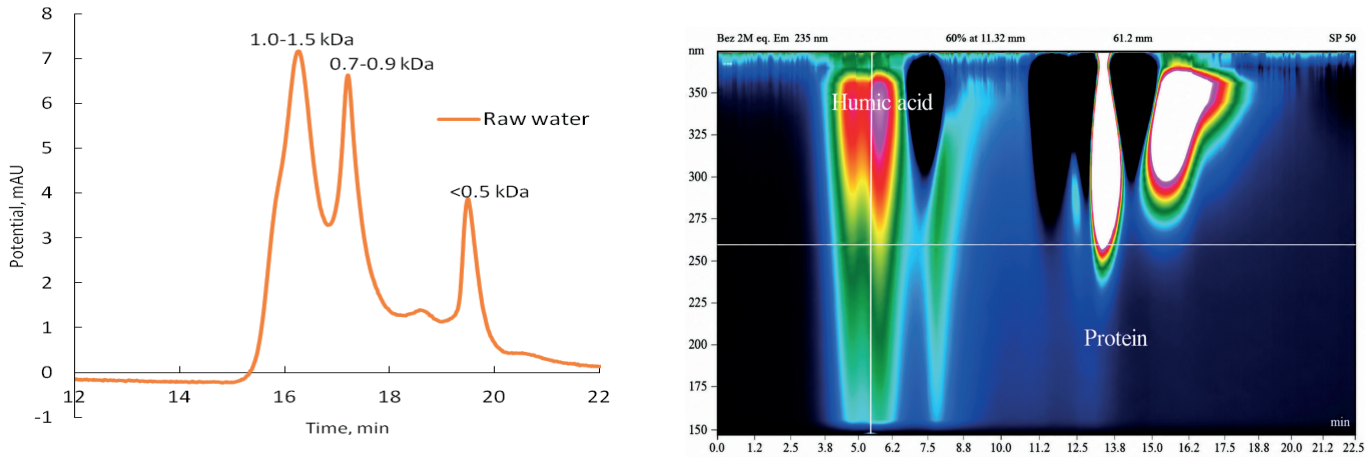


Fig. 4. Particle size distribution (a) and 3-D absorbance spectra (b) for the surface water

membrane, which likely reduced the fouling potential of the feed stream.

The selection of membranes for further long-term testing was based not only on their transport properties but, above all, on their effectiveness in removing specific groups of pollutants from the surface water.

The raw water was characterized by a moderate concentration of organic matter (DOC < 5 mg C/L). Size exclusion chromatography (SEC) analysis indicated that the organic fraction consisted primarily of humic acids with molecular weights of approximately 1 kDa and proteins with molecular weights below 0.15 kDa (Figure 4). These findings are consistent with the SUVA values, which ranged from 2.4 to 3.4 L/mg·m, suggesting the presence of a mixture of humic substances with varying molecular weights.

As shown in Table 5, among the microfiltration membranes tested, the best water treatment performance was achieved with the MF3 ceramic membrane. All membranes provided more than 90% removal of suspended solids and more than 95% turbidity reduction. Since particles larger than 5 µm are primarily responsible for water turbidity (Folorunso et al. 2022), such high turbidity removal efficiencies were expected for all tested membranes. Moreover, the removal of suspended solids and turbidity remained stable throughout each filtration cycle.

In contrast, the removal efficiency of organic matter by the microfiltration membranes was significantly lower. It did not exceed 35% for color, 19% for UV absorbance at 254 nm, 18% for TOC, or 17% for DOC. Similarly low organic matter removal efficiencies for microfiltration have also been reported by Metsämuuronen et al. (2014). This limited performance results from the relatively large membrane pore size (0.2 µm) and the low molecular weight of the organic compounds present in the treated water.

At the same time, for the parameters characterizing organic matter content (TOC, DOC, color, and UV_{254}), a gradual increase in separation efficiency was observed over the course of the process. This effect was most likely associated with membrane fouling and, in particular, with the formation of an additional dynamic (cake) layer on the membrane surface. A similar phenomenon was reported by Celik et al. (2022).

Ultrafiltration tests (Table 5) demonstrated that only the dense UF1 membrane enabled significant removal of organic matter, achieving approximately 76% reduction in DOC, 82% reduction in color, and 75% reduction in UV_{254} absorbance. Particle size distribution analysis of the raw water (Fig. 4a) indicated that compounds with molecular weights in the range of 0.9–1.5 kDa predominated. Considering the manufacturer-declared molecular weight cut-off (MWCO) of 1.5–3.5 kDa for the UF1 membrane, these compounds were removed with high efficiency.

Spectrophotometric analysis (Fig. 4b) further confirmed the presence of humic acids in the raw water, in addition to proteins and fulvic acids. Humic acids were effectively retained by the dense UF membrane. The observed decrease in color and UV_{254} absorbance is directly related to the removal of humic substances, which contain aromatic rings and conjugated double bonds in their structure (Gomes de Melo et al. 2016).

In contrast, the UF2 and UF3 membranes achieved more than 90% removal of suspended solids and turbidity; however, their efficiency in removing organic matter was comparable to that observed for the microfiltration membranes. For example, TOC and DOC removal did not exceed 20%. The MWCO

Table 5: Removal efficiency of selected water quality parameters using microfiltration and ultrafiltration membranes

Parameter	Retention coefficient, %					
	MF1	MF2	MF3	UF1	UF2	UF3
Turbidity	95.9-97.4	97.5-98.1	98.4-99.2	89.6-97.1	94.4-97.6	89.6-97.1
TOC	6.3-7.7	8.6-13.6	11.2-17.7	74.1-78.0	9.2-22.5	14.9-19.4
DOC	5.1-7.0	7.8-10.7	10.5-17.0	74.1-77.6	14.1-20.4	13.4-18.6
Color	26.4-34.8	27.5-33.2	25.7-34.1	79.6-86.1	26.8-33.5	20.6-26.8
UV_{254}	11.2-13.4	9.7-12.5	12.1-19.1	70.7-76.5	13.1-18.8	10.7-15.1

Table 6: Removal efficiency of selected water quality parameters using nanofiltration membranes

Parameter	Retention coefficient, %	
	NF1	NF2
TOC	93.2-96.0	96.1-97.4
DOC	93.3-95.9	95.9-97.4
Color	94.9-96.8	96.1-96.6
UV_{254}	88.0-96.5	94.9-96.1
Hardnes	29.4-33.3	31.7-33.0
Conductivity	39.9-48.2	39.3-47.0
Cl^-	3.9-9.7	6.4-11.2

values of these membranes were 20 kDa (UF2) and 50 kDa (UF3), which, given the relatively low molecular weight of the organic compounds present in the treated water, explains their limited separation performance. Similar conclusions were reported by Prihartini Aryanti et al. (2025), who demonstrated that only tight ultrafiltration membranes are effective for the removal of natural organic matter (NOM) from surface waters.

During the short-term experiments with nanofiltration modules, the surface water was pretreated using the MF3 ceramic microfiltration membrane. As a result, the feed stream supplied to the NF modules was practically free of suspended solids.

As shown in Table 6, both nanofiltration membranes achieved organic matter removal efficiencies exceeding 90%, with slightly higher retention observed for the NF2 membrane. In addition, nanofiltration reduced water hardness by more than 30%. SEC analysis of the NF permeate (Figure 5) indicated that it mainly contained proteins with molecular weights below 0.15 kDa.

The high efficiency of organic matter removal is consistent with findings of other researchers (Liu et al. 2021, Yuksekdag et al. 2023), who have demonstrated that organic macromolecules, due to their relatively high molecular weight (compared to the MWCO of NF membranes) and their negative charge, are effectively retained during nanofiltration.

Although the NF1 and NF2 membranes have similar MWCO values, they differ in membrane material: NF1 is made of polyamide, whereas NF2 is fabricated from modified polytetrafluoroethylene (PTFE). The latter material is more hydrophobic, which may contribute to a lower permeate flux but, at the same time, may reduce convective transport of organic compounds through the membrane, potentially enhancing their retention.

Transport and separation properties of micro-, ultra-, and nanofiltration membranes in long-term testing

Given that the primary objective in selecting the treatment technology was to produce high-quality treated water, membranes for long-term experiments were selected primarily on the basis of their separation performance. The results of the short-term experiments indicated that the MF3 microfiltration, UF3 ultrafiltration, and NF2 nanofiltration membranes exhibited the best separation properties, and these were therefore selected for extended testing.

Before assessing the overall surface water treatment efficiency of the integrated membrane systems, long-term experiments were conducted using both the best-performing membranes (MF3 and UF3) and membranes with lower separation efficiency (MF1 and UF2). As shown in Figure 6, the separation performance of both micro- and ultrafiltration membranes remained largely unchanged throughout the test period. This stability was observed for membranes subjected to backwashing (MF3 and UF3) as well as for those operated without this cleaning procedure (MF1 and UF2).

For turbidity removal, the microfiltration membranes achieved average reductions of 92.5% (MF1) and 90.5% (MF3), while the ultrafiltration membranes reduced turbidity by 97.1% (UF2) and 95.4% (UF3). In contrast, the low molecular weight of the organic compounds present in the water resulted in limited removal during long-term experiments: DOC reduction reached only 17.2%, 27.0%, 31.1%, and 29.7% for MF1, MF3, UF2, and UF3, respectively. Among the removed organic matter, nearly half was biodegradable, with average BDOC removal efficiencies of 44.7%, 43.6%, 46.3%, and 44.8% for MF1, MF3, UF2, and UF3, respectively.

Throughout the long-term experiments, all tested low-pressure membranes achieved complete (100%) retention of *Escherichia coli* and *Clostridium perfringens* spores. Similarly, the removal efficiency of total cell counts (TCC) was close to 100%, regardless of membrane type. Nevertheless, some bacteria were still detected in the permeate, with the microfiltration membranes allowing several times more bacterial passage than the ultrafiltration membranes

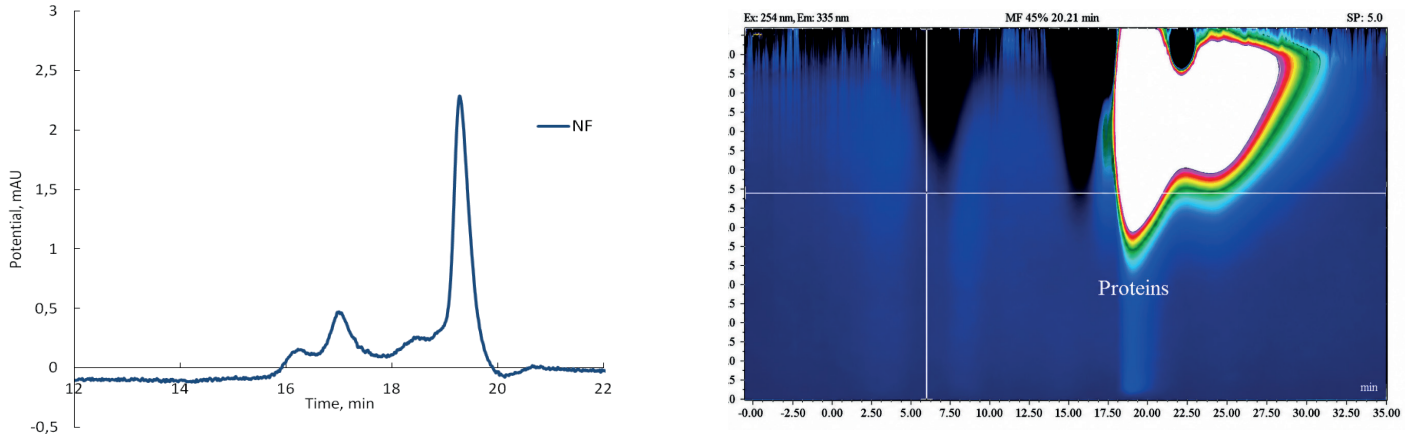


Fig. 5. Particle size distribution (a) and three-dimensional absorbance spectra (b) of NF2 nanofiltration permeate

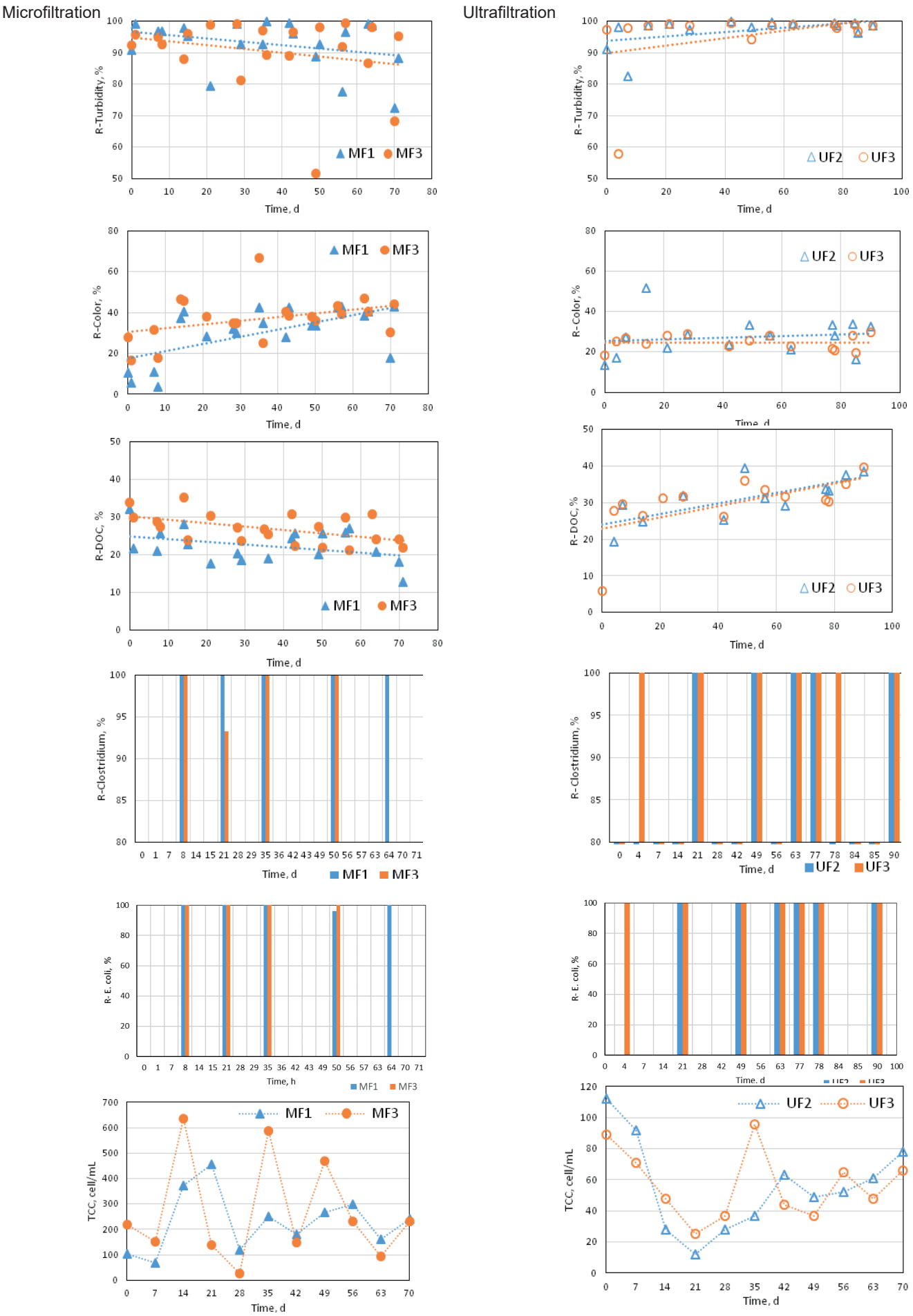


Fig. 6. Separation properties of micro- and ultrafiltration membranes during long-term experiments

(Figure 6). The significantly higher bacterial removal efficiency observed for both ultrafiltration membranes may help reduce the required disinfectant dosage in subsequent stages of water treatment.

Long-term testing with the MF and UF membranes confirmed that MF3 and UF3 exhibit the best separation performance. Consequently, in evaluating the effectiveness of surface water treatment in an integrated system, these membranes were used for pretreatment prior to filtration with the NF2 nanofiltration membrane. Regardless of the pretreatment applied, the nanofiltration process ensured water softening, which was the primary objective of incorporating nanofiltration into the treatment train. At the same time, the reduction in salinity (degree of demineralization) resulting from NF did not necessitate remineralization of the treated water, which may be required when reverse osmosis (RO) is used. (Gao et. al. 2022).

These experiments also enabled a comparison of the performance of the integrated membrane system and that of a conventional treatment system comprising coagulation, sedimentation, rapid sand filtration, and activated carbon adsorption. Long-term experiments on surface water treatment using integrated MF3–NF2 and UF3–NF2 processes (Figure 7) showed that, during the initial stage of operation, pretreatment with the UF membrane provided higher hydraulic performance of the NF2 membrane, although this advantage diminished over time. In contrast, when nanofiltration was preceded by microfiltration, the permeate flux of the NF2 membrane remained nearly constant throughout the experiment.

A comparison of the surface water treatment efficiency of the integrated membrane processes with that of the conventional treatment system (Figure 8) shows that, over long-term experiments, the membrane processes achieved substantially higher removal of organic matter. Specifically, average reductions of more than 95% in color, 93% in DOC, and 93% in UV_{254} absorbance were observed, compared with 76%, 50%, and 61%, respectively, for the conventional treatment system.

Long-term experiments also demonstrated that the treated water quality in the MF+NF and UF+NF systems was comparable, regardless of whether microfiltration or ultrafiltration was used as the low-pressure membrane pretreatment step. In the conventional treatment system, despite confirmed microbiological activity in the adsorption beds, the removal of biodegradable dissolved organic carbon (BDOC) was nearly 50% lower than that achieved by membrane systems, with similar results obtained regardless of the type of low-pressure membrane used for pretreatment.

Significant differences between the treatment systems were also observed in terms of total cell count, which directly affects the required disinfectant dosage. Only the integrated UF+NF system reduced cell counts to a level sufficient to ensure biological stability. In contrast, water treated by the conventional system contained 15 and 5 times more cells than water treated by the UF+NF and MF+NF systems, respectively.

Furthermore, treatment using integrated membrane systems achieved average reductions of 21% in total hardness and 76% in sulfate concentration. The removal of these inorganic components by nanofiltration also led to a substantial decrease in water conductivity—43% for MF+NF and 45% for UF+NF, which could not be achieved with the conventional treatment system. As shown in Figure 9, none of the unit processes in the conventional system effectively removes inorganic ions, and coagulation could even increase water salinity. For example, the use of polyaluminium chloride as a coagulant led to a 6% increase in conductivity.

The study also enabled a comparison of the removal efficiency of different fractions of organic compounds present in the water. Particle size distribution analysis (Figure 10) showed that, following conventional water treatment, the relative proportions of the individual fractions remained similar to those in the raw water. Treatment with low-pressure membrane processes slightly reduced the overall organic matter content and partially removed the larger fractions with molecular weights above 1.0–1.5 kDa. In contrast, nanofiltration effectively retained most of the organic matter, allowing only low-molecular-weight natural organic matter (NOM) with molecular weights below 0.15 kDa to remain in

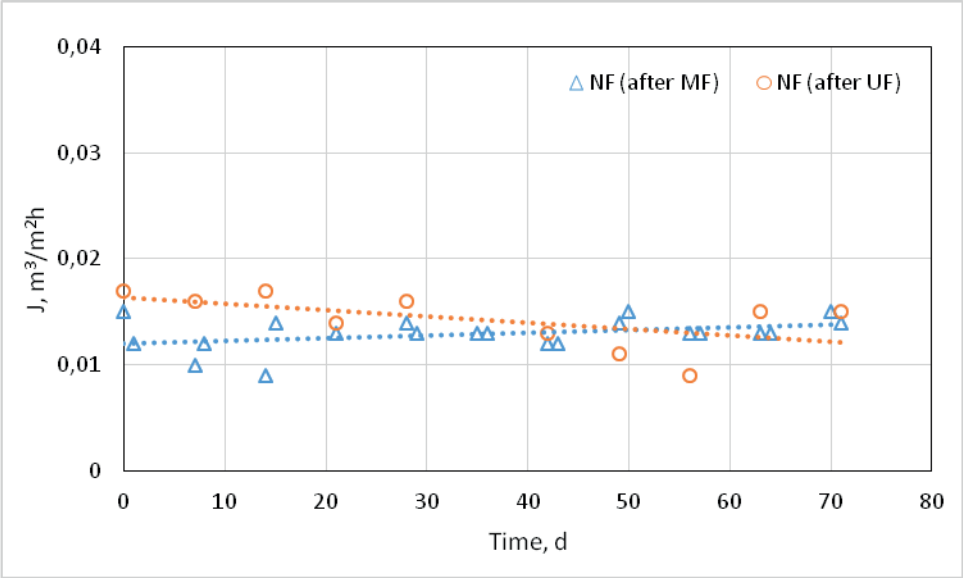


Fig. 7. Effect of surface water pretreatment on NF membrane permeate flux during long-term tests

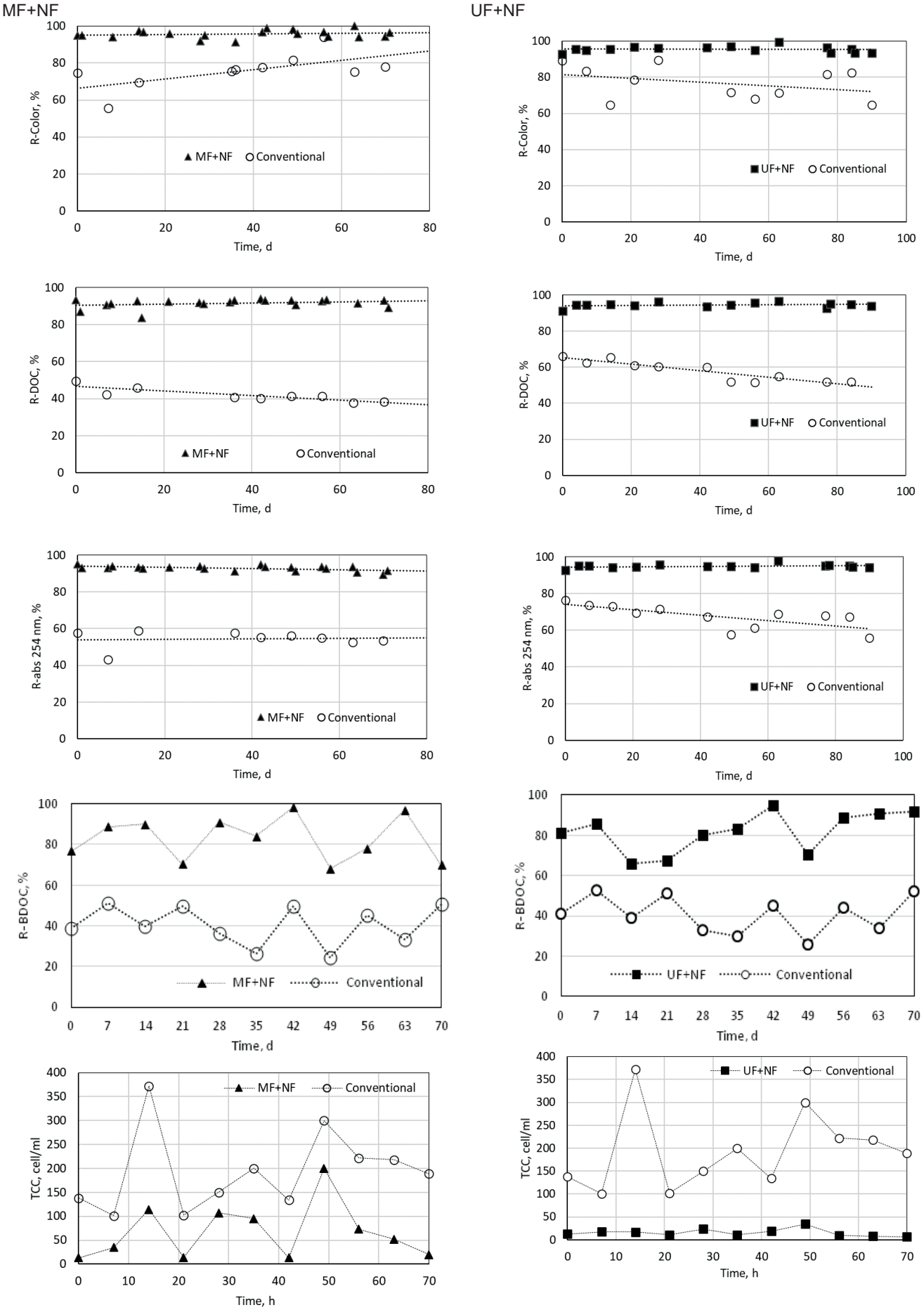


Fig. 8. Comparison of water treatment efficiencies of MF+NF and UF+NF membrane processes with a conventional system comprising coagulation, sedimentation, rapid sand filtration, and granular activated carbon adsorption

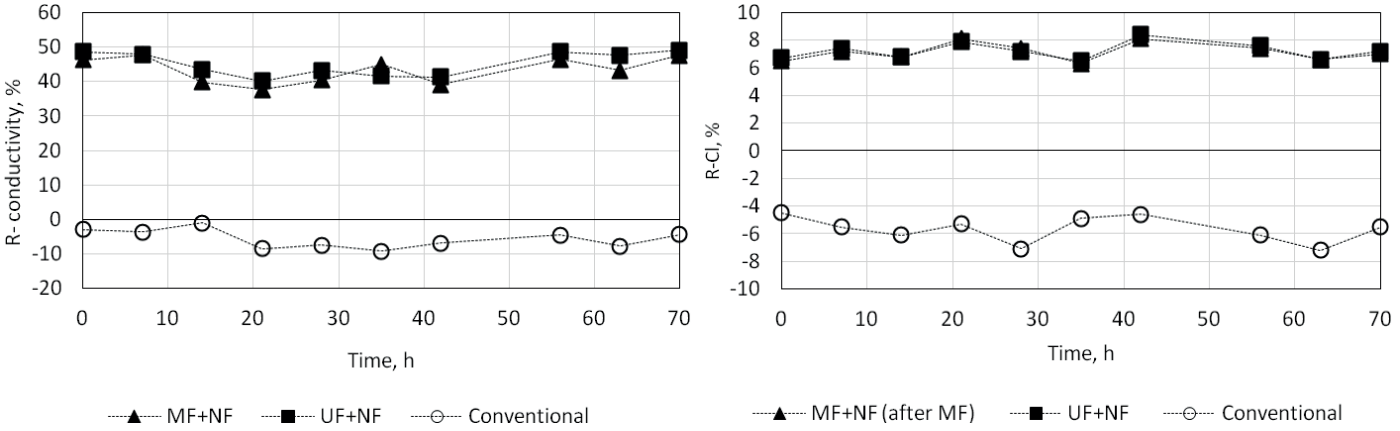


Fig. 9. Effect of water treatment method on conductivity (a) and chloride ion concentration (b)

the permeate.

The substantial effect of nanofiltration on the removal of medium- and high-molecular-weight organic substances is reflected in the average concentrations of the individual fractions in the feed water and in the treated water from each treatment system. As shown in Figure 11, pretreatment with ultrafiltration prior to nanofiltration enhanced the removal of particles with molecular weights above 0.7–0.9 kDa. In contrast, the conventional treatment system achieved average removal efficiencies of only 69.1% and 71.4% for particles in the 0.7–0.9 kDa and 1.0–1.5 kDa molecular weight ranges, respectively.

It should also be noted that the lowest molecular weight fraction (<0.15 kDa) was removed less efficiently in all systems, with removal efficiencies ranging from 2.4 to 40.4% for the conventional system, from 1.4 to 31.4% for the MF+NF system, and from 9.8 to 44.8% for the UF+NF system. The marked reduction in organic matter achieved with the integrated MF+NF and UF+NF systems significantly lowers the risk of disinfection by-product formation (Chaukura et al. 2020).

The removal of medium- and high-molecular-weight organic substances in the integrated membrane systems resulted in a marked increase in the proportion of biodegradable dissolved organic carbon (BDOC) within the total organic carbon (TOC) fraction (Figure 12). In contrast, the conventional water treatment system showed only a negligible increase in the BDOC fraction. A high proportion of biodegradable organic matter in the treated water indicates that these compounds are readily available to microorganisms in the distribution system, thereby increasing the risk of secondary microbial growth within the water supply network (Ndiongue et al. 2005).

Costs analysis

The costs of water treatment in the conventional system included coagulation, filtration, and adsorption, with the unit costs for each stage summarized in Table 7.

The cost of coagulation in the conventional system depended primarily on the type of coagulant used and, to a lesser extent, on its dosage, with higher costs associated with pre-hydrolyzed coagulants.

In the integrated membrane systems (MF+NF and UF+NF), electricity consumption accounted for the largest share of total operational costs, exceeding 90%. The overall water treatment costs in these systems (Table 8) varied considerably, largely due to the need to heat the feed water to maintain stable permeate flux. During periods of declining feed water temperature, the

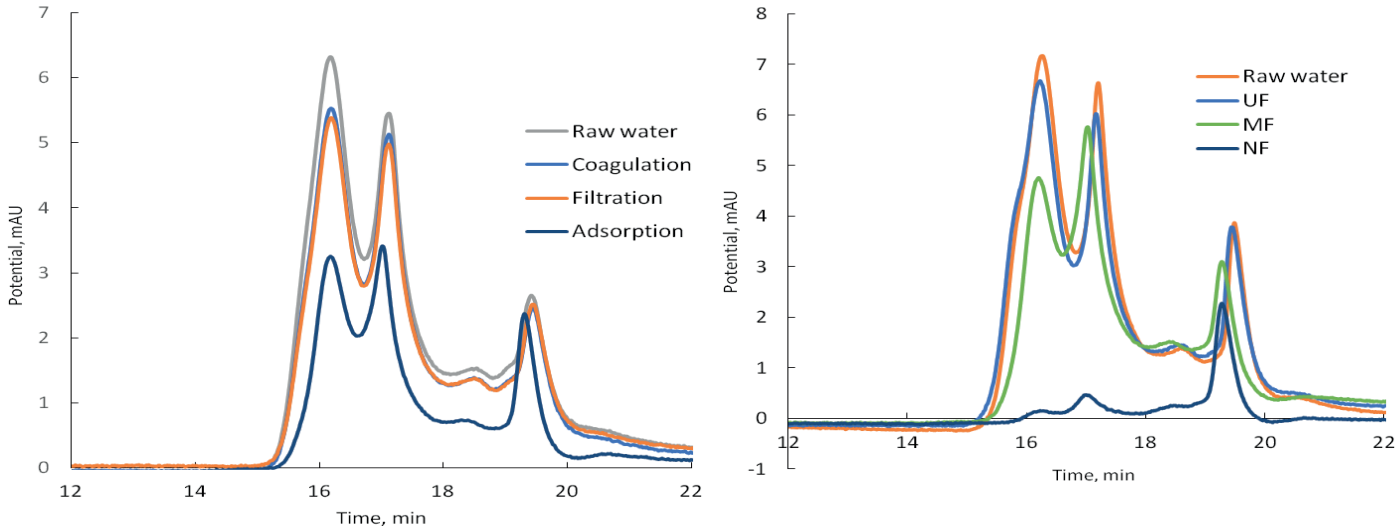


Fig. 10. Size exclusion chromatography of water treated by conventional processes (a) and membrane processes (b)

Table 7: Unit operational costs of the conventional water treatment system (euro/m³)

Process / operation	Water intake	Coagulation	Filtration	Adsorption
Unit cost	0.02	0.03–0.06	0.03	0.03

Table 8: Costs of integrated membrane processes (euro/m³)

Process	MF+NF	UF+NF
With heating (to 5°C)	7.70–15.20	4.73–9.23
Without heating	6.72	4.16

feed water was heated to 5 °C. This was intended to reduce the adverse effect of increasing water viscosity on membrane hydraulic performance.

The operational costs observed in this study were substantially higher than those reported by other researchers (Othman et al. 2021), likely due to the higher operating pressures applied during microfiltration and ultrafiltration. Additionally, the MF+NF system incurred higher operational costs than UF+NF system, reflecting the significantly lower permeate flux achieved with microfiltration.

Eliminating the water heating step prior to MF and UF processes can considerably reduce treatment costs. However, even without water heating, the cost of the MF+NF system remains approximately 33 times higher than that of the conventional water treatment system, while the cost of the UF+NF system is approximately 20 times higher.

It should also be noted that these cost estimates are associated with considerable uncertainty due to the relatively small scale of the experimental setup.

Conclusions

The study demonstrated that:

- Integrated membrane systems (MF+NF and UF+NF) achieved significantly higher removal of organic matter, with average reductions exceeding 95% for color, 93% for DOC, and 93% for UV_{254} absorbance, compared with 76%, 50%, and 61%, respectively, for the conventional treatment system.
- Surface water treatment using integrated membrane systems removed biodegradable dissolved organic carbon (BDOC) more effectively than conventional treatment system.
- Integrated membrane systems removed microorganisms far more efficiently than the conventional treatment systems; water treated by the conventional system contained 15 and 5 times more cells than water treated by the UF+NF and MF+NF systems, respectively.
- Treatment using the integrated MF+NF and UF+NF systems reduced water salinity and achieved water softening, whereas the conventional treatment system increased water salinity.

Acknowledgments

This research was funded by the National Center for Research and Development (Grant No. PBS3/B9/44/2015, *Research on the effectiveness of new water treatment technology as a step towards a shift in thinking about water utility sector* (WODTECH)). The work was carried out through the collaboration of both project consortium members: Wrocław Municipal Waterworks and Drainage Company and Wrocław University of Science and Technology.

References

Allpike, B.P., Heitz, A., Joll, C.A., Kagi, R.I., Abbt-Braun, G., Frimmel, F.H. & Amy, G. (2005). Size exclusion chromatography

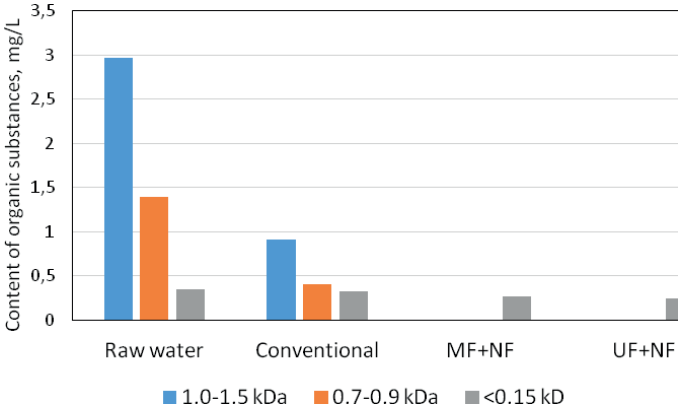


Fig. 11. Average concentrations of organic substance fractions in raw water and in water treated by conventional and integrated membrane systems

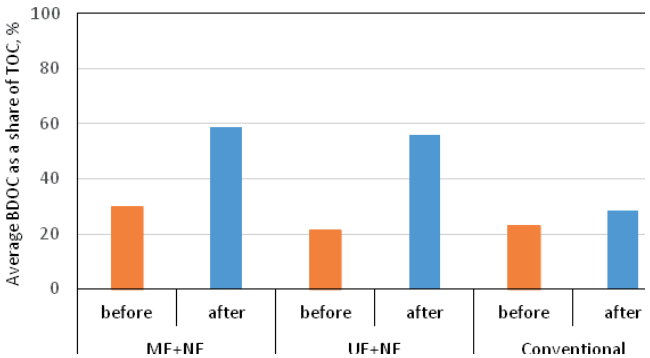


Fig. 12. Average proportion of BDOC in TOC for raw and treated water

to characterize DOC removal in drinking water treatment. *Environmental Science & Technology*, 39, 7, pp. 2334-2342. DOI:10.1021/es0496468

Ariono, D. & Kusuma Wardani, A. (2017). Modification and applications of hydrophilic polypropylene membrane. *IOP Conf. Series: Materials Science and Engineering*, 214, 012014. DOI:10.1088/1757-899X/214/1/012014.

Aziz, S., Rehman Mazhar, A., Ubaid, A., Hamza Shah, S. M., Riaz, Y., Talha, T. & Won Jung, D. (2024). A comprehensive review of membrane based water filtration techniques, *Applied Water Science,* 14, 169. DOI:10.1007/s13201-024-02226-y.

Bodzek, M., Konieczny, K. & Rajca, M. (2019). Membranes in water and wastewater disinfection – review, *Archives of Environmental Protection*, 45, pp. 3–18. DOI:10.24425/aep.2019.126419.

Celik, S. O., Tufekci, N. & Koyuncu, I. (2022). Self-forming dynamic membrane filtration for drinking water treatment, *Water Supply,* 22, 1624–1637. DOI:10.2166/ws.2021.329.

Chaukura, N., Marais, S. S., Moyo, W., Mbali, N., Thakalekoala, L. C., Ingwani, T., Mamba, B. B., Jarvis, P. & Nkambule, T.T.I (2020). Contemporary issues on the occurrence and removal of disinfection byproducts in drinking water - A review, *Journal of Environmental Chemical Engineering*, 8, 103659. DOI:10.1016/j.jece.2020.10365932.

El-Gendi, A. (2022) A critical review of the preparation, characterization and applications of polyamide membranes, *Desalination and Water Treatment*, 255, pp. 120–135. DOI:10.5004/dwt.2022.28333.

Europe's water in figures. An overview of the European drinking water and waste water sectors (2017). (https://www.eureau.org/resources/publications/1460-eureau-data-report-2017-1/file (6.03.2026)).

Fan, G., Li, Z., Yan, Z., Wei, Z., Xiao, Y., Chen, S. & Chang, H. (2020). Operating parameters optimization of combined UF/NF dual-membrane process for brackish water treatment and its application performance in municipal drinking water treatment plant. *Journal of Water Process Engineering*, *38*, 101547. 10.1016/j.jwpe.2020.101547

Folorunso, O.P, Omotoso, T. & Aribisala, J.O. (2022). Effect of particle size distribution on turbidity and river water quality, *Journal of Engineering, Technology and Innovation*, 1, pp. 01–07. https://jetipublications.com/media/media/Vol_1_Iss_2_Paper_3_PSD_effect_on_WQ_9ClIOHN.pdf.

García-Avila, F., Encalada-Alvear, T., Alvarez-Altamirano, L. M., Aviles-Anazco, A., Valdiviezo-Gonzalez, L. & Alfaro-Paredes, E. (2025). Human health risk assessment of aluminium in water treated with aluminium-based coagulants in a rural area, *Results in Engineering*, 25, 104200. DOI:10.1016/j.rineng.2025.104200.

Gomes de Melo, B. A., Lopes Motta, F. & Andrade Santana, M. H. (2016). Humic acids: Structural properties and multiple functionalities for novel technological developments, *Materials Science and Engineering C,* 62, pp. 967–974. http://dx.doi.org/10.1016/j.msec.2015.12.001.

Gryta, M. (2021). Application of polypropylene membranes hydrophilized by plasma for water desalination by membrane distillation, *Desalination*, 515, 115187. DOI:10.1016/j.desal.2021.115187.

Gu, Q., Chiang Albert Ng, T., Bao, Y., Yong Ng, H., Ching Tan, S. & Wang, J. (2022). Developing better ceramic membranes for water and wastewater Treatment: Where microstructure integrates with chemistry and functionalities, *Chemical Engineering Journal,* 428, 130456. DOI:10.1016/j.cej.2021.130456.

Guo, H., Li, X., Yang, W., Yao, Z., Mei, Y., Elfa Peng, L., Yang, Z., Shao, S. & Tang, C. Y. (2022). Nanofiltration for drinking water treatment: a review, *Front. Chem. Sci. Eng.*, 16, pp. 681–698. DOI:10.1007/s11705-021-2103-5.

Hong, S. & Elimelech, M. (1997). Chemical and physical aspects of natural organic matter (NOM) fouling of nanofiltration membranes. *Journal of Membrane Science*, 132(2), pp. 159-181. DOI:10.1016/S0376-7388(97)00060-4.

Horváthová, E. (2022). Analysis of drinking water treatment costs – with an application to groundwater purification valuation. *One Ecosystem*, 7, e82125. DOI: 10.3897/oneeco.7.e82125.

Kim, E.-S., Liu, Y. & Gamal El-Din, M. (2011). The effects of pretreatment on nanofiltration and reverse osmosis membranę filtration for desalination of oil sands process-affected water, *Separation and Purification Technology*, 81, pp. 418–428. DOI:10.1016/j.seppur.2011.08.016.

Knap-Bałdyga, A. & Zubrowska-Sudoł, M. (2023). Natural organic matter removal in surface water treatment via coagulation - current issues, potential solutions, and new findings, *Sustainability*, 15, 13853. DOI: 10.3390/su151813853.

Li, C., Wang, D., Xu, X. & Wang, Z. (2017). Formation of known and unknown disinfection by-products from natural organic matter fractions during chlorination, chloramination, and ozonation, *Science of the Total Environment*, 587–588, pp. 177–184. DOI:10.1016/j.scitotenv.2017.02.108.

Li, L. & Visvanathan, C. (2017). Membrane technology for surface water treatment: advancement from microfiltration to membrane bioreactor, *Rev. Environ. Sci. Biotechnol*., 16, pp.737–760. DOI:10.1007/s11157-017-9442-1.

Lidén, A., & Persson, K. M. (2016). Feasibility study of advanced NOM-reduction by hollow fiber ultrafiltration and nanofiltration at a Swedish surface water treatment plant. *Water*, *8*(4), 150. https://doi.org/10.3390/pr11051300

Liu, D., Cabrera, J., Zhong, L., Wang, W., Duan, D., Wang, X., Liu, S. & Xie, Y.F. (2021). Using loose nanofiltration membrane for lake water treatment: A pilot study, *Front. Environ. Sci. Eng.,* 15, 69. DOI:10.1007/s11783-020-1362-6.

Liu, M., Wang, S., Wang, T., Duan, M., Su, Y., Han, H., Lin, X. & Li, Z. (2021). Application of microfiltration–nanofiltration combined technology for drinking water advanced treatment in a large-scale engineering project, *AQUA — Water Infrastructure, Ecosystems and Society*, 70, pp. 619–636. DOI:10.2166/aqua.2021.020.

Metsämuuronen, S., Sillanpää, M., Bhatnagar, A. & Mänttäri, M. (2014). Natural organic matter removal from drinking water by membrane technology, *Separation and Purification Reviews*, 43, 1-61. DOI:10.1080/15422119.2012.712080.

Mulder, M. (1996), *Basic Principles of Membrane Technology*, second ed., Kluwer Academic London, 1996.

Ndiongue, S., Huck, P.M. & Slawson, R.M. (2005). Effects of temperature and biodegradable organic matter on control of biofilms by free chlorine in a model drinking water distribution system, *Water Research*, 39, pp. 953–964. DOI:10.1016/j.watres.2004.12.019.

Othman, N.H., Alias, N.H., Fuzil, N.S., Marpani, F., Shahruddin, M.Z., Chew, C.M., David Ng, K.M., Lau, W.J. & Ismail, A.F. (2021). A review on the use of membrane technology systems in developing countries, *Membranes*, 1, 30. DOI:10.3390/membranes12010030.

Pietrzyk, A., & Papciak, D. (2017). The influence of the properties of organic compounds on the efficiency of water treatment processes - theoretical basis. *Czasopismo Inżynierii Lądowej, Środowiska*

i Architektury/Journal of Civil Engineering, Environment and Architecture. DOI:10.7862/rb.2017.234 (in Polish)

Prihartini Aryanti, P. T., Adi Nugroho, F., Lugito, G. & Khoiruddin, K. (2025). Tight ultrafiltration membranes: Advancing separation technologies for water and wastewater treatment, *Separation and Purification Technology,* 367, 132892. DOI:10.1016/j.seppur.2025.132892.

Skoczko, I. (2025). Energy efficiency analysis of water treatment plants: current status and future trends. *Energies*, *18*(5), 1086. https://doi.org/10.3390/en18051086

Srivastav, A. L., Patel, N. & Kumar Chaudhary, V. (2020). Disinfection by-products in drinking water: Occurrence, toxicity and abatement, *Environmental Pollution*, 267, 115474. DOI:10.1016/j.envpol.2020.115474.

Valenti-Quiroga, M., Cabrera-Codony, A., Emiliano, P., Valero, F., Monclús, H. & Martin, M. J. (2024). In-depth analysis of natural organic matter fractions in drinking water treatment performance: Fate and role of humic substances in trihalomethanes formation potential. *Science of The Total Environment*, *954*, 176600. https://doi.org/10.1016/j.scitotenv.2024.176600

Wang, K., Mukundan, R. & Gelda, R. K. (2024). Modeling source water disinfection byproducts formation potential using environmental variables. *JAWRA Journal of the American Water Resources Association*, *60*(1), 163-175. https://doi.org/10.1111/1752-1688.13172

Water resources of Europe (2025). (https://water.europa.eu/freshwater/europe-freshwater/freshwater-themes/water-resources-europe (6.03.2026)).

Yuksekdag, A., Korkut, S., Kaya, R., Emin Pasaoglu, M., Turken, T., Agtas, M., Evren Ersahin, M., Ozgun, H. & Koyuncu, I. (2023). Upgrading of conventional water treatment plant by nanofiltration for enhanced organic matter removal, *Separation and Purification Technology*, 325, 124766. DOI:10.1016/j.seppur.2023.124766.

Zielina, M. & Dąbrowski, W. (2021). Energy and water savings during backwashing of rapid filter plants, *Energies*, 14, 3782. DOI:10.3390/en14133782.

Zularisam, A. W., Ismail, A. F. & Salim, R. (2006). Behaviours of natural organic matter in membrane filtration for surface water treatment—a review. *Desalination*, *194*(1-3), 211-231. 10.1016/j.desal.2005.10.030

Porównanie skuteczności oczyszczania wód powierzchniowych z wykorzystaniem zintegrowanych ciśnieniowych procesów membranowych oraz systemów konwencjonalnych

Ciśnieniowe techniki membranowe są coraz częściej stosowane w uzdatnianiu wód naturalnych jako alternatywa dla konwencjonalnych procesów fizyczno-chemicznych. Sprawia to, że niezbędne staje się porównanie skuteczności obu tych podejść, szczególnie w warunkach długotrwałej eksploatacji. W fazie wstępnej badań przeprowadzono testy krótkookresowe, aby na podstawie właściwości separacyjnych i transportowych wyłonić najodpowiedniejsze membrany: do dalszych badań długofalowych wybrano dwie z trzech membran do mikrofiltracji (MF), dwie z trzech do ultrafiltracji (UF) oraz jedną z dwóch do nanofiltracji (NF). Podczas wspomnianych testów długookresowych oceniano efektywność oczyszczania wód powierzchniowych w zintegrowanych układach MF+NF oraz UF+NF, a następnie porównano ją ze skutecznością konwencjonalnego układu technologicznego obejmującego koagulację, sedymentację, filtrację oraz adsorpcję. Wyniki wskazują, że zintegrowane układy MF+NF lub UF+NF pozwalają na uzyskanie znacznie wyższej efektywności oczyszczania niż procesy konwencjonalne; przykładowo, redukcja rozpuszczonego węgla organicznego (DOC) wyniosła 93% w systemach membranowych wobec 50% w metodach konwencjonalnych. Procesy membranowe umożliwiają również wysoce skuteczne usuwanie specyficznych mikroorganizmów, co jest nieosiągalne przy zastosowaniu tradycyjnych metod uzdatniania. Ponadto zintegrowane układy MF+NF oraz UF+NF obniżają zasolenie wody i zapewniają jej zmiękczenie, podczas gdy systemy konwencjonalne wykazują tendencję do zwiększania zasolenia. Analiza kosztów eksploatacyjnych wykazała, że układ UF+NF jest o niemal 50% tańszy niż układ MF+NF. Niemniej jednak oba systemy oparte na technikach membranowych pozostają kilkukrotnie droższe od konwencjonalnego uzdatniania wody. Badania pokazały, że zastosowanie zintegrowanych procesów membranowych pozwala na uzyskanie wody o lepszej jakości niż w wypadku użycia procesów konwencjonalnych.

Archives of Environmental Protection
Vol. 52 no. 3 pp. 60–75

PL ISSN 2083-4772
DOI: 10.24425/aep.2026.3678



© 2026. The Author(s). This is an open-access article distributed under the terms of the Creative Commons Attribution-ShareAlike 4.0 International Public License (CC BY SA 4.0, https:// creativecommons.org/licenses/by-sa/4.0/legalcode), which permits use, distribution, and reproduction in any medium, provided that the article is properly cited.

Two decades of research on antibiotic resistance genes in global wastewater treatment systems: Critical knowledge gaps and pathways toward integrated risk management

Zhizhen Yin*, Fengyang Han, Qinhui He

Key laboratory of Pollutant Chemistry and Environment Treatment, School of Resources and Environment, Yili Normal University, China

*Corresponding author's e-mails: yinzhizhen123@163.com

Keywords: ARGs, wastewater, bibliometrics.

Abstract: Wastewater treatment plants serve as both barriers against and gateways for the environmental dissemination of antibiotic resistance genes (ARGs), yet the scientific community's collective research priorities over the past two decades have shaped – and been shaped by – critical knowledge gaps that now constrain effective risk management. Through systematic analysis of 2,894 publications (2004-2024) from the Web of Science Core Collection, this study identifies three fundamental imbalances that undermine progress toward resistance control. First, a source-research misalignment: livestock wastewater, responsible for >50% of global antibiotic consumption, accounts for merely 5.55% of research attention, while municipal wastewater – with lower selective pressure – dominates at 68.98%, leaving the most significant resistance reservoir critically understudied. Second, a mechanism-application disconnect: fundamental research on horizontal gene transfer predominantly utilizes hospital-derived clinical isolates, yet hospital wastewater research constitutes only 25.47% of publications, limiting the translational value of mechanistic insights. Third, a risk-investment mismatch: although "super resistance genes" (mcr-1, blaNDM) with demonstrated clinical impact have emerged as post-2020 research hotspots, targeted control technologies remain in early development, with 78% of treatment studies focusing on conventional processes that are inadequate for high-risk gene elimination. China leads global output (1,184 articles, 40.9%) but exhibits lower average citations (24.1), suggesting a scale-depth trade-off. Temporal analysis reveals three paradigm shifts—from mechanism cognition (2004-2007), through technical standardization (2008-2013), to risk management (2014-2024) – with current emphasis on "pollution," "surveillance," and "generation" signaling integration of resistome research with intelligent early-warning technologies.
Addressing these imbalances requires: (1) rebalancing research investment toward livestock-associated resistance through targeted funding mechanisms; (2) developing translational frameworks that connect mechanistic insights (e.g., MGE-mediated transfer) to source-specific intervention design; and (3) prioritizing technology development for high-risk gene elimination (tet, mcr-1, blaNDM) over incremental optimization of conventional processes. This analysis transforms bibliometric patterns into actionable scientific priorities, providing a roadmap for transitioning from reactive monitoring to proactive resistance control

Introduction

Since Alexander Fleming, a British microbiologist, discovered and successfully isolated penicillin in 1928, antibiotics have been applied in human medicine, livestock breeding, and agricultural production for over ninety years. However, the widespread and often excessive use of antibiotics has led to their persistent residues in environmental matrices, creating an ecological selection pressure that drives the evolution and dissemination of antibiotic-resistant bacteria (ARB) and ultimately results in the continuous accumulation and spread of antibiotic resistance genes (ARGs) in the environment (Malayil et al. 2022, Murray et al. 2022). Unlike chemical pollutants, ARGs, as an emerging class of biological contaminants, exhibit significant environmental persistence and biological activity. They can propagate across different bacterial strains, environmental compartments, and even organisms via horizontal gene transfer (HGT) through mobile genetic elements (MGEs) such as integrons and transposons (Ben et al. 2017, Jian et al. 2021). Their expression directly confers resistance to bacteria, substantially elevating the risk of clinical treatment failure (Chen et al. 2013, Rizzo et al. 2014). The World Health Organization has unequivocally stated that infections caused by multidrug-resistant pathogens pose a major threat to global public health security (Murray et al. 2022).

In this context, wastewater treatment plants (WWTPs) have been confirmed to act both as sinks for ARGs and as

secondary emission sources disseminating them into the natural environment (Michael-Kordatou et al. 2018). The high organic load, complex microbial communities, and biofilm microenvironments within activated sludge systems provide ideal conditions for the horizontal gene transfer of ARGs (Zhao et al. 2025). Therefore, a thorough understanding of the distribution characteristics, transmission mechanisms, and control strategies of ARGs in wastewater treatment systems has become a critical research topic in the field of environmental microbiological safety.

Bibliometrics, a core method of scientometrics since its formal introduction by Pritchard in 1969, has demonstrated a powerful capacity for constructing knowledge maps across multiple disciplines. This method systematically deconstructs the knowledge architecture, paradigm shifts, and interdisciplinary intersections of academic literature based on authoritative databases and statistical analysis (Qian et al. 2015, Parida et al. 2021, Magro et al. 2020, Cadore et al. 2020). It has been successfully applied to research on emerging pollutants such as perfluorinated compounds and microplastics (Chen et al. 2022, Zhong et al. 2023, Zheng et al. 2019). However, systematic bibliometric analyses specifically focusing on ARG research in wastewater remain relatively scarce. Existing reviews predominantly concentrate on specific technological advancements, lacking a comprehensive, macro-scale revelation of the imbalances in research power dynamics and the evolutionary patterns of research hotspots within this field (Wen et al. 2024, Zheng et al. 2018, Tiernoa et al. 2017). Critical questions remain unanswered: Is there a structural imbalance in research investment across different wastewater sources (municipal, hospital, livestock)? How has research shifted over time? These issues lack quantitative evidence derived from knowledge mapping.

Addressing this gap, the present study conducts a systematic bibliometric and visual analysis of global research on ARGs in wastewater treatment systems. Utilizing 2,894 publications indexed in the Web of Science Core Collection from 2004 to 2024 as the data source, and employing VOSviewer and CiteSpace for analysis, this study aims to: (1) analyze annual publication trends and characteristics of highly cited papers to delineate the field's development trajectory; (2) identify core countries, institutions, and journals to reveal the landscape of research forces; and (3) track the migration trajectory of research hotspots and identify structural imbalances through keyword burst detection, timezone mapping, and cluster analysis.

This investigation is expected to provide a systematic knowledge framework for future ARG-related research and offer a reference for risk management and technological innovation concerning ARGs in wastewater treatment systems.

Materials and Methods

Visualization Tools

This study employs VOSviewer (version 1.6.20) and CiteSpace (version 6.3.R1) to conduct a bibliometric analysis and visual presentation of the retrieved data. VOSviewer, developed by the team of van Eck and Waltman at Leiden University in the Netherlands, excels in network construction and multi-dimensional visualization of large-scale literature data, effectively revealing the co-occurrence structures and clustering characteristics of research themes (Jiang et al. 2022). CiteSpace focuses on detecting the knowledge evolution trajectory and research frontiers within a scientific domain. Through citation network analysis, keyword co-occurrence, and timezone mapping, it identifies pivotal node literature, core research forces, and evolutionary trends of hotspots (Xu et al. 2022, Zare et al. 2022). The combined use of these two tools provides complementary insights, enabling a systematic presentation of the knowledge structure and evolutionary patterns of this field.

Data Sources and Search Strategies

This study utilized the Web of Science Core Collection as the data source, with the retrieval time span set from January 1, 2004, to May 1, 2024. The retrieval strategy employed a topic search, with the specific search query formulated as: TS = ("antibiotic resistance gene") AND TS = ("wastewater treatment"). The document types were limited to Articles and Reviews, yielding a total of 2,894 relevant publications. The full records and cited references of all these publications were exported in plain text format, serving as the foundational dataset for subsequent analyses.

To further investigate the distribution characteristics of ARG research across different wastewater sources, a secondary classification was performed on the 2,894 publications. Based on an analysis of abstracts and keywords, the publications were categorized into four groups: municipal wastewater, hospital wastewater, livestock breeding wastewater, and other types of wastewaters. This classification aims to reveal the disparities in research attention paid to ARG issues originating from different pollution sources, thereby providing data to underpin the identification of a "structural imbalance" in the research landscape.

Results

Publication Trends and Highly Cited Articles: A Two-Decade Analysis

Annual Publication Trends

Annual publication output and citation frequency of scholarly literature serve as core indicators for assessing the developmental trajectory of a scientific field (Liu et al. 2021, Zhang et al. 2022). Since 2004, both the annual number of publications and citation frequency in global research on ARGs in wastewater have exhibited a sustained and rapid growth trend, indicating increasingly widespread academic attention to this field (Figure 1a).

Based on publication trends and key milestone events, the research trajectory of ARGs in wastewater can be delineated into four phases.

The Initial Exploration Phase (2004–2010): During this period, annual publications numbered fewer than 50, and research lacked a systematic framework, primarily focusing on the ecological effects of clinical antibiotic residues. ARG detection relied mainly on traditional culture-based methods and conventional polymerase chain reaction (PCR), with research efforts concentrated predominantly in the medical field (Schwartz et al. 2006, Silva et al. 2006).

The Policy-Driven Phase (2011–2014): The World Health Organization's global call to combat antibiotic resistance in 2011 and the release of the Global Action Plan on Antimicrobial

Resistance in 2014 catalyzed an initial paradigm shift in research (Grimbs et al. 2017, Millet et al. 2011). The research scope expanded from clinical settings to environmental matrices, PCR detection techniques became standardized, and research focus gradually shifted toward point-source pollution represented by wastewater treatment plants, although the publication growth rate remained relatively modest (Rizzo et al. 2013, Michael et al. 2013).

The Deepening Breakthrough Phase (2015–2019): Multidisciplinary integration propelled the annual publication growth rate to 15%. Key advancements manifested in three dimensions: First, the characterization of ARG environmental distribution systematically revealed the abundance profiles of ARGs in environments such as wastewater treatment plants and livestock farms (Guo et al. 2017, Ma et al. 2021). Second, methodological innovations in detection technology, particularly the application of metagenomics, transcended the target limitations of PCR and enabled comprehensive profiling of ARGs (Zhu et al. 2023, Zhao et al. 2018). Third, theoretical advancements in transmission mechanisms systematically elucidated horizontal gene transfer and biofilm-mediated effects (Zhang et al. 2024, Yang et al. 2019).

The Exponential Growth Phase (2020–2024): Research entered a rapid development trajectory, with publication volume increasing exponentially. Research foci exhibited three major shifts: from single-compartment investigations to quantification of multi-source contributions, with systematic assessments of ARG input fluxes from hospital, agricultural, and municipal wastewater (Yang et al. 2024, Zhang et al. 2024); from optimization of conventional treatment processes to exploration of emerging technologies, with cutting-edge approaches such as CRISPR gene editing and single-molecule tracking being applied to ARG mitigation (Wang et al. 2025, Brown et al. 2024); and from phenomenological descriptions to mechanistic elucidations, with continuous deepening of research on ARG transmission pathways and driving factors (Liang et al. 2022, Madhogaria et al. 2024, Zheng et al. 2017).

However, with the diversification of research foci, internal imbalances have become increasingly prominent. As shown in Figure 1(b), global research on ARG pollution across different wastewater matrices exhibits significant uneven distribution. The latest bibliometric data indicate that municipal wastewater treatment plants, as a hotspot for ARG research, account for 68.98% of related publications, far exceeding the proportions for medical wastewater (25.47%) and livestock wastewater (5.55%). This pronounced gradient disparity in scientific research output reveals a critical blind spot in environmental governance: although agriculture and animal husbandry represent the primary sectors for antibiotic use, research investment into the migration and transformation mechanisms of ARGs in livestock wastewater and agricultural environments remains notably insufficient. This situation serves as a warning that future research should establish a comprehensive "human-animal-environment" monitoring network to address the lag in risk assessment of agricultural-source antibiotic resistance pollution.

China ranks first globally in this research domain in both total publications (1,184 articles) and total citations (28,476 citations), underscoring its central position in the field of ARGs in wastewater research.

Core Themes of Highly Cited Literature

Highly cited literature reflects the foundational knowledge and core concerns of a research field. Table 1 summarizes the top 10 most frequently cited studies. Concerning environmental distribution and fate, Zhang et al. (2015) revealed the multi-source input, transport, transformation, and dynamic behavior of antibiotics in the environment through multimedia modeling and first proposed a potential correlation between antibiotic discharge and ARG enrichment. Baquero et al. (2008) comprehensively reviewed the distribution, sources, and transmission mechanisms of antibiotics and ARGs in aquatic environments from a macro perspective, explicitly identifying water systems as key reservoirs for resistance dissemination.

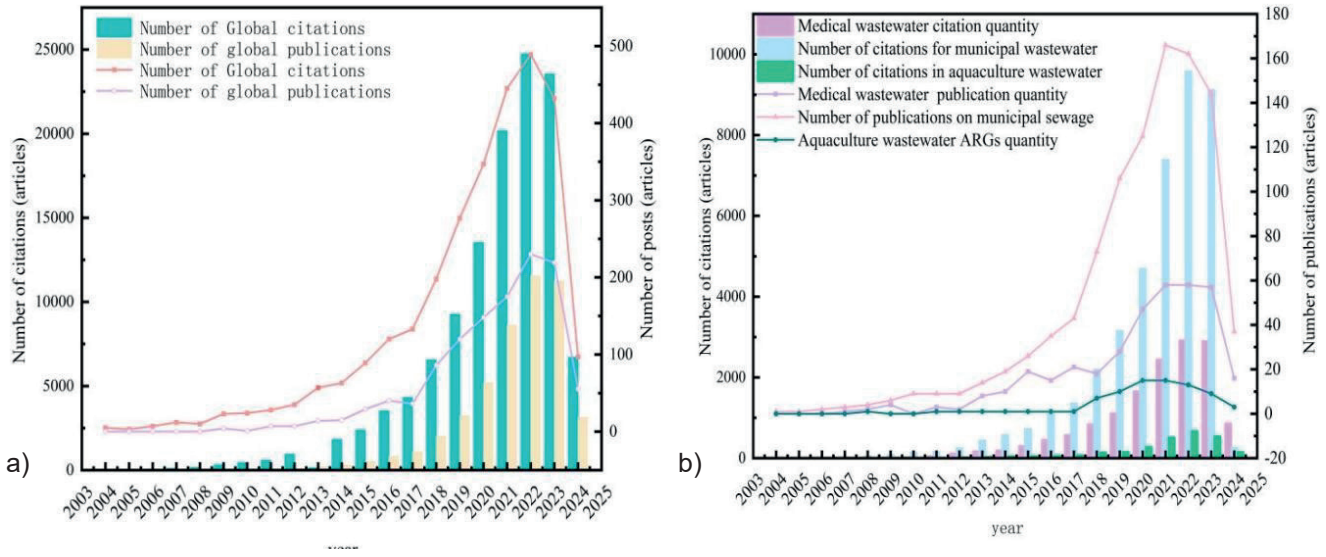


Fig 1. (a) The global and Chinese publication and citation quantities from 2004 to 2024 (b)The publication and citation quantities of ARGs in municipal wastewater, medical wastewater, and livestock farm wastewater globally.

Pruden et al. (2006), investigating a wastewater treatment plant in Colorado, USA, employed high-throughput quantitative PCR to elucidate the dynamics of ARGs during treatment processes, laying the conceptual foundation for ARGs as "emerging environmental contaminants".

In terms of pollution source apportionment, Rodriguez-Mozaz et al. (2015) comparatively analyzed the distribution characteristics of antibiotics and ARGs in municipal wastewater and hospital wastewater from a Chinese city, finding that their input contributions to receiving water bodies significantly exceeded background levels and confirming hospital wastewater as a crucial source of riverine ARG pollution. Guo et al. (2017) employed metagenomic approaches to identify 18 major classes and 578 ARG subtypes in a full-scale wastewater treatment plant, quantifying ARG persistence and removal efficiencies and thereby providing high-resolution data for process efficacy assessment. Karkman et al. (2017) detected the dominance of sulfonamide and tetracycline ARGs in antibiotic production wastewater and found a significant correlation between the abundance of class 1 integrons (intI1) and sulfonamide resistance gene levels, revealing the critical role of mobile genetic elements in ARG dissemination.

Regarding control strategies and mechanisms, Wang et al. (2020) systematically reviewed the concentration ranges of antibiotics (10^{-3}–10^{4} μg/L) and ARGs (10^{4}–10^{12} copies/L) in municipal wastewater treatment plants, noting that the removal efficiencies of ARGs by anaerobic and aerobic treatment processes varied depending on gene type and structural configuration. Mao et al. (2015) further discovered that optimizing microbial community structure could significantly enhance ARG removal efficiency, providing a theoretical basis for bioaugmentation strategies.

In terms of journal distribution, among the aforementioned top 10 highly cited publications, *Water Research* accounts for four, while *Environmental Science & Technology and Science of the Total Environment* each account for two, indicating that these three journals possess core influence in the ARG-wastewater research field. Regarding the evolution of research themes, early highly cited literature (2006–2013) primarily focused on the environmental distribution and conceptual establishment of ARGs; the mid-phase (2015–2017) concentrated on pollution source apportionment and process evaluation; and more recent studies (2018–2020) have increasingly emphasized transmission mechanisms and control strategies. This evolutionary pattern corroborates the research phase delineation presented in Section 3.1.1.

Distribution of Core Research Forces by Country, Institution, and Journal

Leading Countries by Publication Output

The number of publications indexed in SCI and their citation frequencies serve as important indicators for evaluating a country's scientific research capacity and academic influence (Liu et al. 2021). Figure 2a illustrates the distribution of the top 20 countries by publication output in the global research field of ARGs in wastewater. Worldwide, authors contributing to this field are primarily concentrated in China, the United States, Germany, India, Spain, Canada, Poland, the United Kingdom, Portugal, and Australia. China leads globally with 1,184 publications, accounting for 40.9% of the total publications, the United States ranks second with 440 publications, Germany (153 publications), India (150 publications), and Spain (135 publications) occupy the third to fifth positions, respectively (Figure 2a).

China's leading position in this field is driven by multiple factors (Kümmerer et al. 2009, Ren et al. 2023). First, policy guidance: sustained investment through policy documents such as the National Action Plan to Contain Antimicrobial Resistance (2016–2020, 2022–2025) has provided institutional support for ARG research. Second, problem-driven impetus: China accounts for approximately 50% of global antibiotic usage, with prominent ARG pollution issues in intensive livestock farming areas and in surrounding environments of wastewater treatment plants, catalyzing substantial applied

Table 1: Information about top 5 highly cited papers.

Rank	Journal	title	Author	Year	Citations	Country
1	Environmental science & technology	Comprehensive Evaluation of Antibiotics Emission and Fate in the River Basins of China: Source Analysis, Multimedia Modeling, and Linkage to Bacterial Resistance	Zhang Q.Q.	2015	2741	China
2	Science of the total environment	Urban wastewater treatment plants as hotspots for antibiotic resistant bacteria and genes spread into the environment: A review	Rizzo L.	2013	1571	Italy
3	Water research	Urban wastewater treatment plants as hotspots for the release of antibiotics in the environment: A review	Michael I .	2012	1417	Cyprus
4	Current opinion in biotechnolog	Antibiotics and antibiotic resistance in water environments	Baquero F.	2008	1407	Spain
5	Environmental science & technology	Antibiotic resistance genes as emerging contaminants: Studies in northern Colorado	Pruden A.	2006	1330	USA

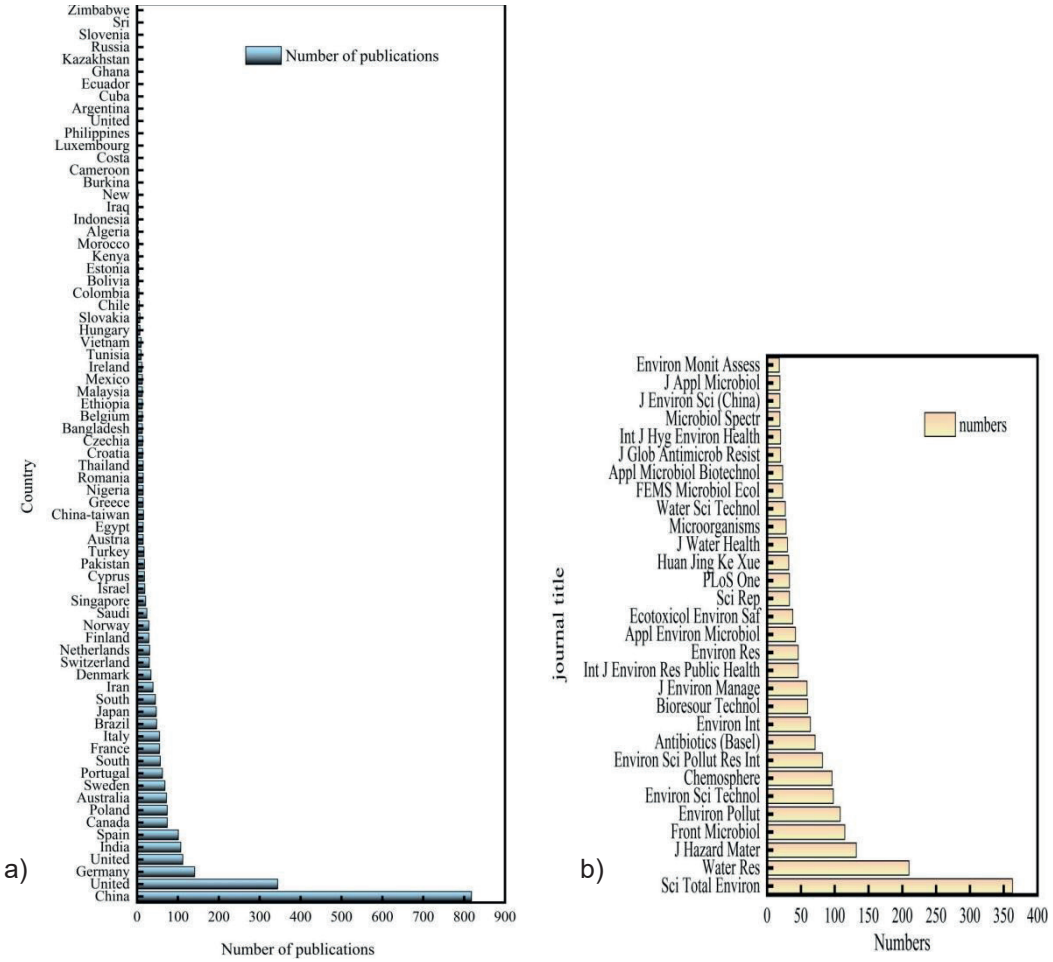


Fig 2. (a) Number of national publications (b)Number of journal publications.

research (Zhang et al. 2015). Third, technological advancement: declining costs of metagenomic sequencing have enabled large-scale environmental surveys.

Notably, despite China's leading publication output, its average citations per publication (24.1) are lower than those of the United States (32.5) and Germany (29.8), indicating room for improvement in research "depth" and "impact" (based on Web of Science data statistics). However, in terms of total citations, China far surpasses all other countries with 28,476 citations, underscoring its substantial overall contribution to the field despite the dilution effect commonly associated with large publication volumes.

Regarding country-specific research themes (based on keyword co-occurrence analysis), Chinese research predominantly focuses on process optimization and pollution status surveys, such as evaluating ARG removal efficiencies of different treatment technologies. In contrast, the United States and European countries demonstrate stronger influence in elucidating transmission mechanisms and health risk assessment, including mediation mechanisms of mobile genetic elements and associations between ARGs and clinical resistance (Cacace et al. 2019, Garner et al. 2024). This configuration—characterized by a pattern of "leadership in scale" coexisting with a "need to catch up in depth," along with differentiated distribution of research themes—provides a foundation for future complementary advantages through international collaboration.

Core Research Institutions

Based on an analysis of publication output by research institutions in the global field of ARGs in wastewater (Table 2), the Chinese Academy of Sciences ranks first worldwide with 245 publications, surpassing the second-ranked institution by 116.8%, underscoring its central position in this research domain. Following sequentially are the University of Chinese Academy of Sciences (113 publications), the Research Center for Eco-Environmental Sciences (101 publications), Tsinghua University (76 publications), and Harbin Institute of Technology (70 publications). Among the top 10 institutions by publication output, Chinese research institutions occupy seven positions, forming a comprehensive research cluster centered around institutions affiliated with the Chinese Academy of Sciences, spanning fundamental research, technological innovation, and engineering practice.

The dominant position of Chinese research institutions in this field benefits from their well-defined division of labor and collaborative framework. The Research Center for Eco-Environmental Sciences focuses on environmental behavior and fate analysis of ARGs, Tsinghua University possesses advantages in technological innovations such as membrane

Table 2: Top 10 Institutions in Global and Chinese Research on ARGs in Wastewater from 2004 to 2024 by Number of Published Papers

Top 10 global contributors	Publication volume	Top 10 contributors in China	Publication volume
Chinese academy of sciences	245	Chinese academy of sciences	245
University of chinese academy of sciences	113	University of chinese academy of sciences	113
Research center for eco environmental sciences	101	Research center for eco environmental sciences	101
Tsinghua university	76	Tsinghua university	76
Harbin institute of technology	70	Harbin institute of technology	70
Centre national de la recherche scientifique cnrs	56	Tongji university	55
Tongji university	55	Zhejiang university	53
Universidade catolica portuguesa	55	Institute of Urban Environment, Chinese Academy of Sciences	50
Zhejiang university	53	Ministry of agriculture rural affairs	50
Indian institute of technology system iit system	50	University of hong kong	44

separation, and Harbin Institute of Technology has developed distinctive strengths in engineering practice areas including disinfection process optimization. This complete chain of "fundamental research—technological development—engineering application" provides systematic support for China's continued production of high-quality research outputs in the ARG-wastewater field.

Highly Influential Authors

Table 3 lists the top eight scholars by publication output in the global research field of ARGs in wastewater, whose research directions encompass the core dimensions of this field. Su et al. (2017) applied metagenomics to urban sewage in China, revealing 381 widely shared resistance genes with seasonal variation, and suggesting that the core resistome is associated with human gut microbiota and may spread via sewage disposal. Manaia et al. (2018) focused on tracking methodologies for ARB and ARGs in municipal wastewater treatment plants, providing a theoretical foundation for establishing standardized monitoring approaches. As a corresponding author, Pruden et al. (2024), through metagenomic sequencing of 12 wastewater treatment plants across six continents, revealed significant inter-gene variability in ARG removal efficiencies, with total ARG abundance and clinically relevant ARGs being higher in Asian wastewater compared to Europe and North America. Yang et al. (2023), as the corresponding author, elucidated the inhibitory effects of high organic loads and oxytetracycline concentrations on nitrifying bacteria, demonstrating that adjusting process parameters could reduce relative ARG abundance by 63.2%. Liu et al. (2023) systematically evaluated the inactivation of ARB and inhibition of plasmid-mediated horizontal gene transfer by peroxymonosulfate. The research of these scholars collectively constitutes the core knowledge contribution network of this field.

Major Publishing Journals

The distribution of journals publishing research on ARGs in global wastewater systems is presented in Figure 2b. *Science of the Total Environment* ranks first with 363 publications (accounting for 12.5%), emphasizing the investigation of ARG distribution, dissemination, and removal mechanisms from an environmental systems perspective. *Water Research* ranks second with 210 publications (7.25%), focusing on the behavioral mechanisms of ARGs in aquatic environments and process optimization. *Journal of Hazardous Materials* ranks third with 132 publications (4.56%), with a primary focus on targeted treatment technologies for ARGs in high-risk scenarios such as pharmaceutical and livestock wastewater.

From the perspective of journal functional differentiation, ARG research has formed a complete knowledge chain encompassing "mechanisms—technologies—risks." *Frontiers in Microbiology* (115 publications, 3.97%) elucidates ARG hosts and horizontal transfer mechanisms from a microbial ecology perspective, *Environmental Pollution* (108 publications, 3.73%) emphasizes ARG distribution characteristics and ecological risk assessment, *Environmental Science & Technology* (98 publications, 3.39%) advances treatment technology innovation, and *Chemosphere* (96 publications, 3.32%) primarily evaluates ARG removal efficiencies through laboratory-scale simulation studies. The differentiated positioning of these journals collectively promotes the multidimensional development of ARG research.

Regarding the journal distribution of highly cited literature (Table 1), *Water Research* accounts for four publications, while *Environmental Science & Technology* and *Science of the Total Environment* each account for two, further confirming the core influence of these three journals in the ARG-wastewater research field.

Table 3: Top 8 authors with the highest number of publications on ARGs in wastewater worldwide from 2004 to 2024 by Number of Published Papers

Author	Number of publications	Title	Total citations	Average citations
Su J.Q	65	Metagenomics of urban sewage identifies anextensively shared antibiotic resistome in China	212	78.22
Manaia C. M.	52	Antibiotic resistance in wastewater treatment plants: Tackling the black box	5853	112.56
Zhang T.	42	Plasmid Metagenome Reveals High Levels of Antibiotic Resistance Genes and Mobile Genetic Elements in Activated Sludge	3807	90.64
Yang M.	39	Unveiling the threshold values of organic and oxytetracycline loadings for nitrification recovery of a full-scale pharmaceutical wastewater treatment system	1840	47.18
Pruden A.	37	Antibiotic resistance genes as emerging contaminants: Studies in northern Colorado	4614	124.7
Harnisz M.	34	Antibiotic resistant Escherichia coli in hospital and municipal sewage and their emission to the environment	1511	44.44
Liu Y.	33	Removal of antibiotic resistant bacteria, genes and inhibition of plasmid-mediated horizontal transfer by peroxymonosulfate: Efficiency and mechanisms	1325	40.15
Schwartz T.	33	Real-time PCR detection of Pseudomonas aeruginosa in clinical and municipal wastewater and genotyping of the ciprofloxacin-resistant isolates	5420	164.24

3.3 Evolution of Research Hotspots and Analysis of Structural Imbalance

Analyzing research hotspots requires not only revealing the temporal migration trajectory of academic attention but also discerning its spatial imbalance across different wastewater types. This section systematically examines the evolutionary patterns of research foci in ARG-wastewater studies over the past two decades through keyword burst detection, timezone mapping, and cluster analysis, while elucidating the structural mismatch between "hot topics" and "cold sources."

Keyword Burst Analysis

Keyword burst refers to the phenomenon where the frequency of a specific term appearing in academic literature exhibits a concentrated surge within a particular time frame. This indicator reflects the intensity of research attention and the prominence of research themes, with longer burst durations indicating more sustained academic interest in that direction.

Bibliometric analysis based on CiteSpace reveals significant temporal heterogeneity and thematic evolutionary characteristics in keyword bursts within ARG-wastewater research from 2004 to 2024 (Table 4). Among these, "antimicrobial resistance" (2004–2015), "tetracycline resistance" (2007–2018), and "Escherichia coli" (2004–2016) represent the three research threads with the longest durations and highest burst intensities.

"Tetracycline resistance" emerged as the most representative long-term hotspot in this field, with a burst intensity of 20.42 and a duration of 12 years (2007–2018). The formation of this phenomenon is driven by multiple factors. First, massive usage—global annual tetracycline production reached 5,000 tons by 2015, with widespread applications in livestock breeding, agricultural production, and clinical treatment (Kümmerer et al. 2009). Second, environmental persistence—tetracycline antibiotics exhibit soil half-lives of up to 180 days, and their corresponding resistance genes show removal efficiencies of only 20%–40% in wastewater treatment systems. Third, co-selection mechanisms—tetracycline resistance genes are frequently co-localized with heavy metal resistance genes on plasmids, enabling synergistic enrichment under metal contamination (Ren et al. 2023).

Notably, despite the prolonged prominence of tetracycline resistance research, its primary source—livestock breeding wastewater—accounts for merely 5.55% of overall studies in this field (Figure 1b). This pronounced mismatch between "hot topics" and "cold sources" profoundly reveals the structural imbalance characterizing current ARG research. The decline in this hotspot's prominence after 2018 does not signify problem resolution but rather reflects a shift in research focus toward "super resistance genes" with higher clinical risk and greater transmission capacity (such as blaNDM-1, mcr-1), exemplifying a "risk-oriented escalation" of research priorities.

Escherichia coli, serving as an indicator organism, sustained research attention for 13 years (2004–2016) with a burst intensity of 18.18. This bacterium's 20-minute division cycle enables rapid characterization of resistance phenotypes, with approximately 40% of clinical isolates carrying multidrug resistance plasmids (Yin et al. 2025), establishing it as a key model strain for investigating environmental transmission of ARGs.

During the 2020–2024 period, research focus significantly shifted toward ecological risk prevention and control, with three interconnected emerging hotspots: "pollution" (burst intensity 18.76), "surveillance" (burst intensity 15.32), and "generation" (burst intensity 12.45), marking the deep

integration of environmental resistomics and intelligent monitoring technologies. The "pollution" theme concentrates on elucidating pollution mechanisms and innovating monitoring technologies. Yan et al. (2024) employed multi-omics approaches to reveal co-evolutionary patterns of ARGs and metal resistance genes in sewage-irrigated paddy fields. Soni et al. (2024) developed a microfluidic chip-based rapid capture system for resistant bacteria and established a transmission risk index based on mobile genetic element abundance. The emergence of the "surveillance" direction signifies a strategic shift in research emphasis from "passive response" to "active early warning." Dong et al. (2024), through 18-month dynamic monitoring of wastewater systems, revealed spatiotemporal distribution patterns of ARGs, with source apportionment models indicating that 78.4% of ARG host bacteria originate from the human gut microbiome. Gholipour et al. (2023) systematically outlined four major bottlenecks confronting current wastewater surveillance efforts. Addressing these challenges, the World Health Organization launched an antibiotic resistance gene source tracing initiative in 2023, proposing a three-tier technical framework comprising metagenomic census, culturomics-based host resolution, and mobile genetic element risk assessment. The emergence of the "generation" hotspot stems from fundamental inquiries into the environmental behavior mechanisms of antibiotic resistance genes. Bengtsson-Palme et al. (2021) modeled resistance emergence, suggesting the environment plays a minor role in most scenarios, yet large uncertainties demand more quantitative data for targeted interventionsMadhogaria et al. (2024) proposed an "adsorption-resistance coupling" theory, demonstrating that biosorption processes drive adaptive evolution of ARGs by altering antibiotic bioavailability.

3.3.2. Time-Zone View Analysis

While Section 3.1.1 delineated the research trajectory into four phases based on publication trends and policy milestones, keyword time-zone mapping offers a complementary perspective centered on the evolution of research content itself. As revealed below, this content-based analysis condenses the trajectory into three phases, reflecting the intrinsic cognitive progression of the field from fundamental mechanisms to technical standardization and ultimately to systematic risk management. These two frameworks are not contradictory but rather illuminate different facets of the field's development—the former capturing external drivers, the latter capturing internal intellectual shifts.

Compared to keyword burst analysis, time-zone mapping provides a more intuitive visualization of keyword occurrence frequency and temporal distribution characteristics, facilitating the tracking of dynamic evolutionary trajectories of research hotspots (Figure 3). The time-zone map constructed in this study reveals a clear phased progression in the evolution of research hotspots within ARG-wastewater studies.

Phase I (2004–2007): Mechanism Cognition Stage. Research hotspots predominantly centered on "antibiotic resistance," "bacteria," and *Escherichia coli*. During this

Table 4: Keywords with the Strongest Citation Bursts

Keywords	Year	Strength	Begin- End	2004~2024
escherichia coli	2004	18.18	2004-2016	
Antibiotic resistance	2004	15.73	2004-2015	
identification	2004	7.13	2004-2012	
tetracydine resistance	2007	20.42	2007-2018	
determinants	2007	7.61	2007-2016	
bacteria	2004	9.47	2008-2016	
sewage treatmentplants	2009	9.9	2009-2018	
sewage	2009	7.23	2009-2016	
enterobacteriaceae	2009	6.17	2009-2017	
real time pcr	2009	5.73	2009-2016	
solid phase extraction	2009	5.48	2009-2015	
activated sludge	2006	6.94	2010-2014	
strains	2011	12.61	2011-2016	
south china	2011	6.07	2011-2018	
integrons	2009	7.17	2012-2018	
resistance	2009	5.16	2012-2014	
molecular characterization	2013	6.55	2013-2016	
municipal waste water	2012	5.15	2014-2019	
sewage treatment plant	2008	6.23	2015-2019	
point source	2015	5.43	2015-2018	
china	2014	8.42	2017-2018	
receiving river	2017	7.41	2017-2018	
pollution	2020	6.19	2020-2022	
surveillance	2021	5.63	2021-2024	
generation	2021	5.5	2022-2024	

phase, studies primarily investigated plasmid-mediated resistance gene transmission mechanisms, revealing plasmids as core vectors for resistance dissemination (Szczepanowski et al. 2004, Tennstedt et al. 2005). Foundational research encompassed detection methodologies for resistant bacteria and resistance mechanisms, while preliminary assessments of treatment process efficacy compared ARG removal efficiencies across different technologies (Garcia et al. 2007).

Phase II (2008–2013): Technical Standardization Stage. Research hotspots expanded to include "wastewater," "activated sludge," "gene," "fate," and "effluent." During this period, researchers focused on transmission mechanisms linking ARGs and mobile genetic elements (Zhai et al. 2016, Zhang et al. 2011). Significant methodological standardization advances occurred, with applications of PCR, quantitative PCR, and metagenomic technologies substantially enhancing monitoring accuracy (Diehl et al. 2010, Börjesson et al. 2009). Concurrently, integrated treatment strategies began receiving attention (Yang et al. 2013).

Phase III (2014–2024): Risk Management and Control Stage. Research hotspots further expanded to encompass "microbial community," "pharmaceutical," "environment," "tetracyclines," "removal," and "degradation." This phase focused on developing and evaluating novel wastewater treatment technologies, driving the paradigm shift from "single-pollutant removal" toward "comprehensive resistance prevention and control" (Zarei-Baygi et al. 2020, Li et al. 2021). Multimedium transmission pathways and host evolutionary characteristics of ARG environmental dissemination were systematically elucidated, with ecological risks associated with pharmaceutical wastewater and sludge reuse attracting increasing attention (Qiao et al. 2025, Cachetas et al. 2024).

The important conclusions, core viewpoints, and breakthrough progress of the above literature have been summarized in Table 4.

3.3. Keyword Cluster Analysis

Keyword cluster analysis further reveals the internal structure and associative characteristics of research themes. This study identified three major clusters (Figure 4), corresponding to the three core dimensions of ARG research. By correlating cluster themes with the current research status across different wastewater types, the "imbalance landscape" of the contemporary research landscape can be clearly delineated.

Cluster 1 (Red) encompasses keywords including "mechanisms," "bacteria," "bacterial community," *Escherichia coli*, "genes," "diversity," "tetracycline resistance," "metagenomic analysis," "antimicrobial resistance," "disinfection," and "prevalence." This cluster focuses on fundamental research into ARG transmission mechanisms and microbial community evolution. Within wastewater treatment plants, plasmid-mediated horizontal gene transfer constitutes a crucial mechanism for ARG dissemination, with mobile genetic elements such as integrons and transposons playing pivotal roles (Yin et al. 2022, Gillings et al. 2015). Reductions in bacterial community diversity may potentiate horizontal gene transfer of ARGs by intensifying niche competition (Ju et al. 2019). Correlation analysis with wastewater types: The fundamental mechanism research encompassed in Cluster 1 is closely associated with the complex and diverse resistance mechanisms present in hospital wastewater, which harbors clinically relevant resistant bacteria, multidrug resistance plasmids, and high abundances of MGEs. However, hospital wastewater research accounts for merely 25.47% of global ARG literature (Figure 1b). This reveals a critical imbalance: the application scenario most requiring mechanistic elucidation (hospital wastewater) receives relatively insufficient research investment, creating a disconnect between fundamental research and application contexts.

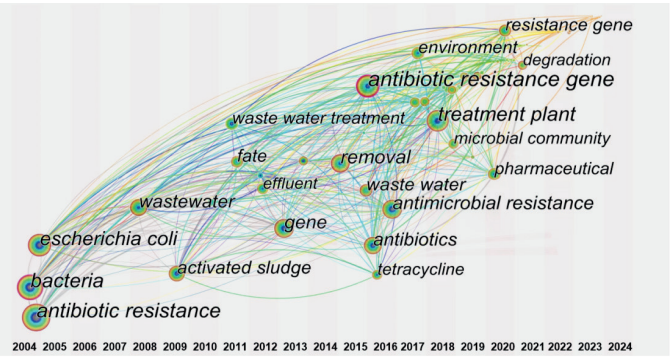


Fig 3. Time zone map of keywords in English literature during 2004~ 2024

Cluster 2 (Green) encompasses keywords including "removal of tetracycline," "degradation," "microbial community," "performance," "activated sludge," "biodegradation," "extracellular polymeric substances," and "sulfamethoxazole." This cluster emphasizes treatment process efficacy evaluation and biodegradation mechanism research. Membrane-aerated biofilm reactors exhibit strong degradation capacity for sulfamethoxazole (Li et al. 2024), while disinfection processes have been systematically evaluated for their ARG removal efficiency and effects on conjugative transfer (Lin et al. 2016, Guo et al. 2015, Michael-Kordatou et al. 2017). Correlation analysis with wastewater types: The process efficacy research represented by Cluster 2 primarily serves municipal wastewater treatment needs—municipal wastewater is characterized by large volumes, well-established collection systems, and mature treatment processes. Municipal wastewater research constitutes as much as 68.98% of global ARG literature (Figure 1b). This indicates that in the municipal wastewater domain, a virtuous cycle of "process needs driving technological development" has formed, with relatively mature technologies.

Cluster 3 (Blue) encompasses keywords including "resistance genes," "fate," "wastewater treatment plants," "veterinary antibiotics," "pharmaceuticals," "personal care products," and "soil." This cluster focuses on environmental fate and cross-media migration of ARGs. ARGs can disseminate across environmental compartments through pathways including bioaerosols, groundwater infiltration, and sludge migration (Chen et al. 2025), with specific bacterial genera serving as critical vectors for ARG transmission (Talat et al. 2025). Correlation analysis with wastewater types: The environmental fate concerns addressed by Cluster 3 closely align with the core risks associated with livestock wastewater—the cross-media transmission of antibiotics from livestock wastewater into soil, crops, and ultimately the food chain through manure land application represents a key proposition in ARG environmental fate research. However, livestock wastewater research accounts for merely 5.55% of global ARG

Table 5: Important conclusions, core viewpoints, and breakthrough progress of literature published from 2004-2024

year	Research Focus	Key Findings	reference
2004	Isolation of erythromycin-resistant plasmids from activated sludge, characterization of plasmid pRSB101	Environmental plasmids like pRSB101 achieve cross-host spread via "functional superposition" (resistance + adaptability), likely evolving from non-resistant plant pathogens through gene capture	(Szczepanowski et al. 2004)
2005	Complete sequencing of IncP-1α plasmid pTB11 from sewage, comparison with historic plasmid RK2	First revelation of high genetic stability and functional module conservation of IncP-1α plasmids in WWTPs. The skeleton (Rep, Trb, Tra) is 99.9% identical to RK2, while Tn402-like integrons carry diverse resistance gene cassettes	**(Tennstedt et al. 2005)**
2006	Analysis of ciprofloxacin resistance mechanisms (gyrA, gyrB, parC mutations) in *P. aeruginosa* from wastewater	Environmental ciprofloxacin resistance is primarily determined by specific co-mutation patterns (e.g., gyrA Thr83Ile and parC Ser87Leu)	(Schwartz et al. 2006)
2006	Assessment of coliform antibiotic resistance and horizontal gene transfer potential in influent vs. treated water	First demonstration that treated wastewater effluent contains strains capable of horizontally transferring plasmid-mediated resistance to *E. coli K-12*. Treatment reduces total coliforms but enriches the proportion of multi-drug resistant (MDR) bacteria.	(Silva et al. 2006)
2007	Comparison of *E. coli* and *Enterococcus* resistance in two WWTPs (with/without hospital input), effect of anaerobic digestion	Hospital wastewater significantly increases initial resistance ratios in *Enterococcus*. Anaerobic digestion is confirmed to significantly reduce MDR *Enterococcus* and 2-antibiotic resistant *E. coli*	(Garcia et al. 2007)
2007	Large-scale analysis of *Enterococcus* resistance (983 strains, 42 samples), risk assessment of sludge agricultural reuse	Revealed a 49.4% MDR rate in *Enterococcus* across 14 WWTPs and quantified the reduction effect of treatment. Highlights that agricultural sludge application is a potential pathway for spreading resistant bacteria	(da Costa et al. 2007)
2010	Monitoring of 11 ARG subtypes across treatment stages in a N. China WWTP, correlation with antibiotic conc	Identified biological treatment units (e.g., anoxic ponds, aeration tanks) as key hotspots for ARG proliferation, with activated sludge processes showing a stronger effect than SBR or bio-contact oxidation	(Zhai et al. 2016)
2011	Capture of novel plasmids from activated sludge using TRACA system, metagenomic analysis of ARGs and MGEs	MGEs (e.g., Class 1 integrons, Tn3 transposons) are found to highly co-exist with ARGs, playing a key role in their capture and spread by promoting HGT	(Zhang et al. 2011)
2012	Investigation of integron-positive Enterobacteriaceae (1832 strains) prevalence, MDR phenotypes, and gene cassette diversity	Revealed a gradient distribution of integron-positive bacteria across WWTP stages. Integron-positive strains were 100% MDR, harboring 24 distinct resistance-related gene cassette arrays	(Mokracka et al. 2012)
2012	Effect of temperature (22-55°C) on tetracycline resistance genes (tet) and intI1 removal during anaerobic/aerobic digestion	High-temperature anaerobic digestion (55°C) is identified as a promising technology for eliminating resistance genes, with temperature being a critical control factor	(Diehl et al. 2010)
2012	Development of a real-time PCR (LUX™) system for quantitative detection of four ARGs (tetA, tetB, mecA, aac(6'))	First application of LUX™ fluorogenic technology for rapid, highly reproducible quantification of ARGs in wastewater environments, revealing the prevalence of tetA and aac(6')-Ie+aph(2")	(Börjesson et al. 2009)

year	Research Focus	Key Findings	reference
2012	PCR-DGGE analysis of antibiotic-resistant bacteria diversity after primary and secondary treatment	Demonstrates that oxidative stress in aeration tanks and chlorination during secondary treatment exerts a strong selective pressure, enriching for specific resistant bacterial populations	(Sigala et al. 2012)
2013	Development of a structured ARG database and high-throughput pipeline for metagenomic data analysis	Established a standardized workflow for ARG detection, revealing subtypes missed by conventional PCR and eliminating amplification bias, enabling more accurate quantification and classification	(Yang et al. 2013)
2018	Lab-scale Anaerobic/Aerobic System (AAS) study on tetracycline selection pressure and intI1's role in ARG fate	Tetracycline and intI1 are the main factors controlling tet gene distribution. IntI1 plays a crucial role in HGT, while the tetX gene shows high environmental persistence, unaffected by AAS treatment	(Gao et al. 2018)
2020	Lab-scale Anaerobic Membrane Bioreactor (AnMBR) study on the impact of antibiotics on microbial community and ARGs	Provides insights into the correlation between microbial community dynamics and ARGs in AnMBRs. Antibiotic exposure caused a transient 167x increase in effluent ARGs, correlating with shifts in the effluent microbial community, suggesting pathogen involvement	(Zarei-Baygi et al. 2020)
2021	Development of a novel magnetic anion exchange resin (MAER)-mediated UV-Fenton system for antibiotic/ARG removal	Achieves >99% degradation of three antibiotics in 30 min. The cyclic Fe^{3+}/Fe^{2+} redox cycle on the MAER interface enhances electron transfer, with hydroxyl radicals (·OH) as the primary reactive species	(Li et al. 2021)
2024	Multi-media (water, sediment, soil) sampling downstream of a sulfonamide production plant to track ARGs and hosts	A Soil depth (20 cm) effectively reduces ARG presence, but 17 high-risk ARGs can still migrate to rivers and deep soil. First report on the host diversity of the sadABC antibiotic degradation gene, suggesting environmental evolution and cross-host transmission	(Qiao et al. 2025)
2024	Global meta-analysis of 163 metagenomes (29 countries) to define a core resistome across wastewater, freshwater, and soil	Established a cross-database annotation pipeline to resolve naming ambiguities. Proposed 27 wastewater-specific ARGs as "fingerprint" biomarkers to trace wastewater discharge impacts on downstream environments	**(Cachetas et al. 2024)**
2024	Two-year study on Zero-Valent Iron (ZVI) enhancement of antibiotic and ARG removal in integrated anoxic-aerobic biofilm reactors (IAOBRs)	ZVI supplementation significantly reduces ARGs/MGEs by enhancing microbial metabolic activity (dehydrogenase +44.8%, ATP +45.7%) and enriching for functional bacteria that are not potential ARG hosts	(Tang et al. 2024)

literature (Figure 1b), presenting an extreme contrast with its contribution of over 50% of global antibiotic usage. This reveals the most prominent deficiency in the current research landscape: the domain with the highest risk receives the lowest research investment.

In summary, the three clusters clearly delineate the "imbalance landscape" of ARG research: Cluster 2 (municipal wastewater) demonstrates technological maturity and sufficient investment, Cluster 1 (hospital wastewater) exhibits complex mechanisms yet insufficient investment, and Cluster 3 (livestock wastewater) presents the highest risk yet receives the lowest investment. This configuration provides unequivocal directional guidance for subsequent research resource allocation and policy formulation.

Conclusions

Based on a systematic analysis of 2,894 publications indexed in the Web of Science Core Collection from 2004 to 2024, this study elucidates the developmental trajectory and structural imbalances in global research on antibiotic resistance genes (ARGs) within wastewater treatment systems. The core conclusions are as follows:

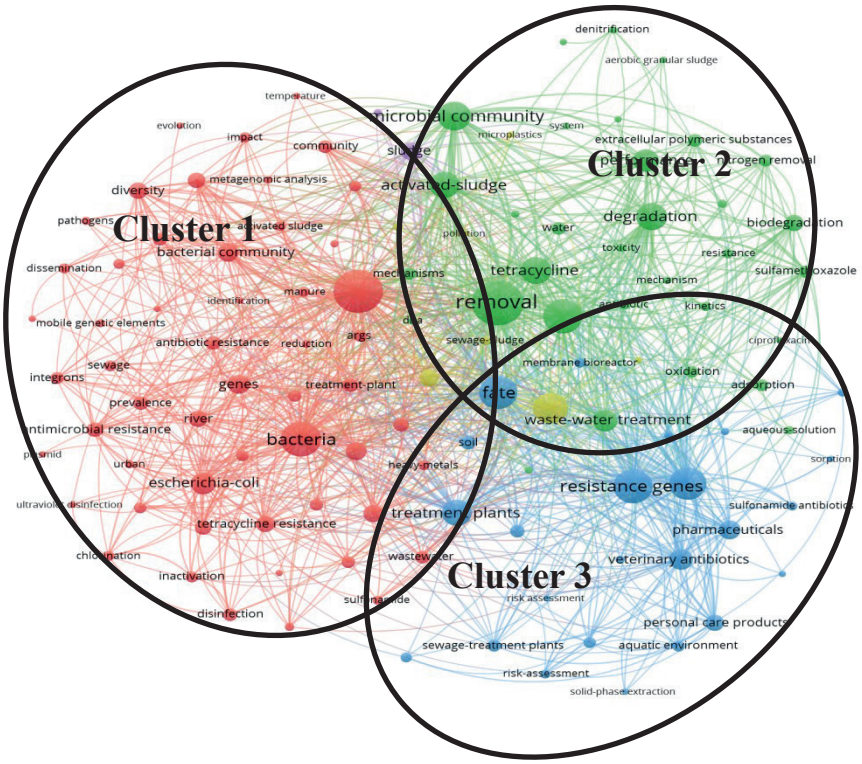


Fig 4. Cluster network view of keywords

(1) Research Output and Hotspot Evolution: Over the past two decades, global annual publications have exhibited exponential growth, undergoing three paradigm shifts from "mechanism cognition" and "technical standardization" to "risk management and control." China emerges as the core contributor, however, its average citation impact per publication requires further enhancement.

(2) Structural Imbalance in the Research Landscape: A pronounced misalignment exists between research investment and pollution source contributions. Livestock wastewater research, despite accounting for over half of global antibiotic usage, constitutes less than 6% of publications, whereas municipal wastewater research represents nearly 70%. This "municipal-heavy, livestock-light" configuration represents the most significant blind spot in current environmental regulation and risk prevention.

(3) Migration of High-Risk Genes: Research focus has shifted from traditional tetracycline resistance genes (tet) toward "super resistance genes" (e.g., mcr-1, blaNDM), characterized by higher clinical risk and enhanced transmission capacity, reflecting a "risk-oriented escalation" trajectory.

Based on these findings, the following recommendations for future research are proposed:

First, establish a comprehensive surveillance chain to address the "structural imbalance." Drawing upon the WHO's "Source-Tracing Initiative for Antibiotic Resistance Genes" three-tier technical framework (metagenomic census—culturomics-based host resolution—mobile genetic element risk assessment), develop a standardized monitoring network encompassing the three major wastewater categories (municipal, hospital, and livestock). For livestock wastewater, the most critical gap in surveillance should prioritize key transmission nodes, including anaerobic storage lagoons, manure-applied agricultural soils, and subsequently contaminated crops and groundwater. Furthermore, establish data-sharing protocols and risk assessment frameworks that enable integrated analysis across municipal, hospital, and livestock monitoring systems, facilitating coordinated interventions and early warning of resistance threats originating from agricultural sources.

Second, develop targeted control technologies to address "high-risk gene escalation." Focus on high-risk genes such as tet, mcr-1, and blaNDM by prioritizing research on coupled "anaerobic digestion + advanced oxidation" processes. Explore the feasibility of CRISPR-based gene-editing technologies and mobile genetic element-targeted inhibitors to overcome challenges in ARG removal from sludge and high-strength wastewater matrices.

Third, we call for deepening the integration of mechanistic understanding and practical applications to facilitate the transition from reactive monitoring to proactive resistance control. Priority should be given to cross-media (water, air, soil, and biota) transport dynamics and host succession patterns of ARGs, which underpin the environmental fate and dissemination of resistance. Building upon such mechanistic insights, targeted intervention technologies should be developed to eliminate high-risk genes. Emerging antibiotic removal technologies using waste-derived adsorbents (Slomkiewicz et al., 2025) represent a promising approach in this direction, yet their efficacy against ARG-hosting bacteria and mobile genetic elements requires further validation. Meanwhile, to translate technological advances into effective risk prevention, parallel efforts should be directed toward surveillance capacity. Recent advancements in watershed-scale water quality monitoring have demonstrated the value

of integrating real-time sensor systems with spatial modeling for early warning and source tracking (Syafrudin et al., 2025), providing a methodological framework that can be adapted to ARG surveillance across municipal, hospital, and livestock wastewater systems. Ultimately, the integration of ARGs into environmental quality standards should be promoted, thereby providing a scientific foundation for intersectoral governance of antimicrobial resistance.

Disclaimer/Publisher's Note: The statements, opinions and data contained in all publications are solely those of the individual author(s) and contributor(s), and not of MDPI and/or the editor(s). MDPI and/or the editor(s) disclaim responsibility for any injury to people or property resulting from any ideas, methods, instructions, or products referred to in the content.

Author Contributions: writing—original draft preparation, Z.Y., data curation, Q.H., software, F.H., supervision, all authors have read and agreed to the published version of the manuscript.

Funding: This work was supported by the Research Project of Yili Normal University, Yili, Xinjiang, China (Grant Nos. 2022YSYB025 and 2022HJZD02).

Institutional Review Board Statement: Not applicable.

Informed Consent Statement: Not applicable.

Data Availability Statement: Data will be made available on request.

Conflicts of Interest: The authors declare no conflicts of interest.

References

Baquero, F., Martínez, J.-L. & Cantón, R. (2008). Antibiotics and antibiotic resistance in water environments. *Curr. Opin. Biotechnol*. 19(3), pp. 260-265.

Ben, W.-W., Wang, J., Cao, R.-K., Yang, M., Zhang, Y. & Qiang, Z.-M. (2017). Distribution of antibiotic resistance in the effluents of ten municipal wastewater treatment plants in China and the effect of treatment processes. *Chemosphere,* 172, pp. 392–398.

Bengtsson-Palme, J., Jonsson, V., Heß, S. (2021). What Is the Role of the Environment in the Emergence of Novel Antibiotic Resistance Genes? A Modeling Approach. Environ. Sci. Technol., 55(23), 15734–15743. DOI: 10.1021/acs.est.1c02977.

Börjesson, S., Dienues, O., Jarnheimer, P.-Å., Olsen, B., Matussek, A. & Lindgren, P.-E. (2009). Quantification of genes encoding resistance to aminoglycosides, β-lactams and tetracyclines in wastewater environments by real-time PCR. *Int. J. Environ. Health Res*. 19(3), pp. 219-230.

Brown, C.-L., Maile-Moskowitz, A., Lopatkin, A.-J., Xia, K., Logan, L.-K., Davis, B.-C., Zhang, L.-Q., Vikesland, P.-J. & Pruden, A. (2024). Selection and horizontal gene transfer underlie microdiversity-level heterogeneity in resistance gene fate during wastewater treatment. *Nat. Commun*. 15(1), pp. 5412.

Cacace, D., Fatta-Kassinos, D., Manaia, C.-M., Cytryn, E., Kreuzinger, N., Rizzo, L., Karaolia, P., Schwartz, T., Alexander, J., Merlin, C., Garelick, H., Schmitt, H., de Vries, D., Schwermer, C.-U., Meric, S., Ozkal, C.-B., Pons, M.-N., Kneis, D. & Berendonk, T.-U. (2019). Antibiotic resistance genes in treated wastewater and in the receiving water bodies: A pan-European survey of urban settings. *Water Res*. 162,pp. 320-330.

Cachetas, D., Vaz-Moreira, I., Pereira, V. & Manaia, C.-M. (2024). Towards the definition of an antibiotic resistome signature in wastewater and downstream environments. *Environ. Pollut*. 357, pp. 124424.

Cadore, J.-S., Fabro, L.-F., Maraschin, T.-G., Souza Basso, N.-R., Pires, M.-J.R. & Briao, V.-B. (2020). Bibliometric approach to the perspectives and challenges of membrane separation processes to remove emerging contaminants from water. *Water Sci. Techno*l. 82(9), pp. 1721–1741.

Chen, H. & Zhang, M.-M. (2013). Effects of advanced treatment systems on the removal of antibiotic resistance genes in wastewater treatment plants from Hangzhou, China. *Environ. Sci. Technol*. 47(15), pp. 8157–8163.

Chen, X., Yin, X.-L., Xu, X.-Q. & Zhang, T. (2025). Species-resolved profiling of antibiotic resistance genes in complex metagenomes through long-read overlapping with Argo. *Nat. Commun*. 16, pp. 1744.

Chen, Y.-X., Lin, M.-W. & Zhuang, D. (2022). Wastewater treatment and emerging contaminants: Bibliometric analysis. *Chemosphere*. 297, pp. 133932.

da Costa, P.-M., Vaz-Pires, P. & Bernardo, F. (2007). Antimicrobial resistance in Enterococcus spp. isolated in inflow, effluent and sludge from municipal sewage water treatment plants. *Water Res*. 41(8), pp. 1735-1740.

Diehl, D.-L. & LaPara, T.-M. (2010). Effect of Temperature on the Fate of Genes Encoding Tetracycline Resistance and the Integrase of Class 1 Integrons within Anaerobic and Aerobic Digesters Treating Municipal Wastewater Solids. *Environ. Sci. Technol*. 44(23), pp. 9128-9133.

Dong, Q., Sun, B., Liu, Y.-C. & Huang, X. (2024). Sewerage surveillance tracking characteristics of human antibiotic resistance genes in sewer system. *Sci. Total Environ*. 952, pp. 175850.

Gao, P., Xu, W.-L., Ruan, X.-H., Qian, Y.-J., Xue, G. & Jia, H.-Z. (2018). Long-term impact of a tetracycline concentration gradient on the bacterial resistance in anaerobic-aerobic sequential bioreactors. *Chemosphere*. 205, pp. 308-316.

Garcia, S., Wade, B., Bauer, C., Craig, C., Nakaoka, K. & Lorowitz, W. (2007). The effect of wastewater treatment on antibiotic resistance in Escherichia coli and Enterococcus sp. *Water Environ. Res*. 79(12), pp. 2387-2395.

Garner, E., Maile-Moskowitz, A., Angeles, L.-F., Flach, C.-F., Aga, D.-S., Nambi, I., Larsson, D.-G.J., Burgmann, H., Zhang, T., Vikesland, P.-J. & Pruden, A. (2024). Metagenomic Profiling of Internationally Sourced Sewage Influents and Effluents Yields Insight into Selecting Targets for Antibiotic Resistance Monitoring. *Environ. Sci. Technol*. 58(37), pp. 16547-16559.

Gholipour, S., Shamsizadeh, Z., Halabowski, D., Gwenzi, W. & Nikaeen, M. (2023). Combating antibiotic resistance using wastewater surveillance: Significance, applications, challenges, and future directions. *Sci. Total Environ*. 908, pp. 168056.

Gillings, M.-R., Paulsen, I.-T. & Tetu, S.-G. (2015). Genomics and the evolution of antibiotic resistance. Ann. N.Y. *Acad. Sci*. 1347(1), pp. 1-17.

Grimbs, A., Shrestha, A., Rezk, A.-S.D., Grimbs, S., Said, I.-H., Schepker, H., Hütt, M.-T., Albach, D.-C., Brix, K., Kuhnert, N. & Ullrich, M.-S. (2017). Bioactivity in Rhododendron: A Systemic Analysis of Antimicrobial and Cytotoxic Activities and Their Phylogenetic and Phytochemical Origins. *Front. Plant Sci*. 8, pp. 551.

Guo, J.-H., Li, J., Chen, H., Bond, P.-L. & Yuan, Z.-G. (2017). Metagenomic analysis reveals wastewater treatment plants as hotspots of antibiotic resistance genes and mobile genetic elements. *Water Res*. 123, pp. 468-478.

Guo, M.-T., Yuan, Q.-B. & Yang, J. (2015). Distinguishing effects of ultraviolet exposure and chlorination on the horizontal transfer of antibiotic resistance genes in municipal wastewater. *Environ. Sci. Technol*. 49(9), pp. 5771-5778.

Jian, Z.-H., Zeng, L., Xu, T.-J., Sun, S., Yan, S.-X., Yang, L., Huang, Y., Jia, J.-J. & Dou, T.-F. (2021). Antibiotic resistance genes in bacteria: Occurrence, spread, and control. *J. Basic Microbiol*. 61(12), pp. 1049-1070.

Jiang, R.-Q., Cao, M.-N., Mei, S.-H., Guo, S.-S., Zhang, W., Ji, N. & Zhao, Z.-G. (2022). Trends in metabolic signaling pathways of tumor drug resistance: A scientometric analysis. *Front. Oncol*. 12, pp. 981406.

Ju, F., Beck, K., Yin, X.-L., Maccagnan, A., McArdell, C.-S., Singer, H.-P., Johnson, D.-R., Zhang, T. & Bürgmann, H. (2019). Wastewater treatment plant resistomes are shaped by bacterial composition, genetic exchange, and upregulated expression in the effluent microbiomes. *ISME J*. 13(2), pp. 346-360.

Karkman, A., Do, T.-T., Walsh, F. & Virta, M.-P.J. (2018). Antibiotic-Resistance Genes in Waste Water. *Trends Microbiol*. 26(3), pp. 220-228.

Korzeniewska, E., Korzeniewska, A. & Harnisz, M. (2013). Antibiotic resistant Escherichia coli in hospital and municipal sewage and their emission to the environment. *Ecotoxicol. Environ. Saf*. 91(5), pp. 96-102.

Kümmerer, K. (2009). Antibiotics in the aquatic environment-A review-Part I. *Chemosphere*. 75(4), pp. 417-434.

Li, T., Cao, X.-W., Gu, L.-J., Cui, Y., Li, X.-L., Li, Y., Khan, S.-J., Li, B.-A. & Zhang, S. (2024). Metabolism of nitrogen and sulfamethoxazole, performance recovery mechanism, and antibiotic resistance genes (ARGs) behaviors in membrane aerated biofilm reactor (MABR). *J. Clean. Prod*. 481, pp. 144172.

Li, Y., Zhang, J.-N. & Ying, G.-G. (2021). Performance and mechanism in degradation of typical antibiotics and antibiotic resistance genes by magnetic resin-mediated UV-Fenton process. *Environ. Sci*. 227, pp. 112908.

Liang, C.-Y., Wei, D., Yan, W.-Z., Zhang, S.-Y., Shi, J.-P. & Liu, L. (2022). Fates of intracellular and extracellular antibiotic resistance genes during the cattle farm wastewater treatment process. *Bioresour. Technol*. 344, pp. 126272.

Lin, W.-F., Li, S., Zhang, S.-T. & Yu, X. (2016). Reduction in horizontal transfer of conjugative Plasmid by UV irradiation and low-level chlorination. *Water Res*. 91, pp. 331-338.

Liu, T.-T., Yang, L.-P., Mao, H.-M., Ma, F., Wang, Y.-Y. & Zhan, Y.-L. (2021). Knowledge Domain and Emerging Trends in Podocyte Injury Research From 1994 to 2021: A Bibliometric and Visualized Analysis. *Front. Pharmacol*. 12, pp. 772386.

Liu, Y., Gao, J.-F., Zhao, M.-Y., Fu, X.-Y., Zhang, Y. & Zhang, H.-R. (2023). Removal of antibiotic resistant bacteria, genes and inhibition of plasmid-mediated horizontal transfer by peroxymonosulfate: Efficiency and mechanisms. *Chem. Eng. J*. 453, pp. 139728.

Ma, N.-J., Tong, L., Li, Y.-Q., Yang, C., Tan, Q. & He, J. (2021). Distribution of antibiotics in lake water-groundwater-sediment system in Chenhu Lake area. *Environ. Res*. 204, pp. 112343.

Madhogaria, B., Banerjee, S., Kundu, A. & Dhak, P. (2024). Efficacy of new generation biosorbents for the sustainable treatment of antibiotic residues and antibiotic resistance genes from polluted waste effluent. *Ind. Microbiol. J*. 3(1), pp. 100092.

Madhogaria, B., Banerjee, S., Kundu, A. & Dhak, P. (2024). Efficacy of new generation biosorbents for the sustainable treatment of antibiotic residues and antibiotic resistance genes from polluted waste effluent. *Ind. Microbiol. J*. 3(1), pp. 100092.

Magro, C., Mateus, E.-P., Paz-Garcia, J.-M. & Ribeiro, A.-B. (2020). Emerging organic contaminants in wastewater: understanding electrochemical reactors for triclosan and its by-products degradation. *Chemosphere.* 247, pp. 125758.

Malayil, L., Ramachandran, P., Chattopadhyay, S., Allard, S.M., Bui, A., Butron, J., Callahan, M.T., Craddock, H.A., Murray, R., East, C., Sharma, M., Kniel, K., Micallef, S., Hashem, F., Gerba, C.P., Ravishankar, S., Parveen, S., May, E., Handy, E., Kulkarni, P., Anderson-Coughlin, B., Craighead, S., Gartley, S., Vanore, A., Duncan, R., Foust, D., Betancourt, W., Zhu, L.B., Mongodin, E.F., Sapkota, A., Pop, M., Haymaker, J. & Sapkota, A.R. (2022) Variations in bacterial communities and antibiotic resistance genes across diverse recycled and surface water irrigation sources in the mid-atlantic and southwest united states: a conserve two-year field study. *Environ. Sci. Technol*. 56(21), pp. 15019–15033.

Manaia, C.-M., Rocha, J., Scaccia, N., Marano, R., Radu, E., Biancullo, F., Cerqueira, F., Fortunato, G., Iakovides, I.C. & Zammit, I. (2018). Antibiotic resistance in wastewater treatment plants: Tackling the black box. *Environ. Int*. 115, pp. 312-324.

Mao, D.-Q., Yu, S., Rysz, M., Luo, Y., Yang, F.X., Li, F.X., Hou, J., Mu, Q.H. & Alvarez, P.-J.J. (2015). Prevalence and proliferation of antibiotic resistance genes in two municipal wastewater treatment plants. *Water Res*. 85, pp. 458-466.

Michael, I., Rizzo, L., McArdell, C.-S., Manaia, C.-M., Merlin, C., Schwartz, T., Dagot, C. & Fatta-Kassinos, D. (2013). Urban wastewater treatment plants as hotspots for the release of antibiotics in the environment: A review. *Water Re*s. 47(3), pp. 957-995.

Michael-Kordatou, I., Andreou, R., Iacovou, M., Frontistis, Z., Hapeshi, E., Michael, C. & Fatta-Kassinos, D. (2017). On the capacity of ozonation to remove antimicrobial compounds, resistant bacteria and toxicity from urban wastewater effluents. *J. Hazard. Mater*. 323, pp. 414-425.

Michael-Kordatou, I., Karaolia, P. & Fatta-Kassinos, D. (2018). The role of operating parameters and oxidative damage mechanisms of advanced chemical oxidation processes in the combat against antibiotic-resistant bacteria and resistance genes present in urban wastewater. *Water Res*. 129, pp. 208-230.

Millet, S. & Maertens, L. (2011). The European ban on antibiotic growth promoters in animal feed: from challenges to opportunities. *Vet. J*. 187(2), pp. 143-144.

Mokracka, J., Koczura, R. & Kaznowski, A. (2012). Multiresistant Enterobacteriaceae with class 1 and class 2 integrons in a municipal wastewater treatment plant. *Water Res*. 46(10), pp. 3353-3363.

Murray, C.-J.L., Ikuta, K.-S., Sharara, F., Swetschinski, L., Aguilar, G.-R., Gray, A., Han, C., Bisignano, C., Rao, P. & Wool, E. (2022). Global burden of bacterial antimicrobial resistance in 2019: a systematic analysis. *Lancet,* 399(10325), pp. 629–655.

Parida, V.K., Saidulu, D., Majumder, A., Srivastava, A., Gupta, B. & Gupta, A.-K. (2021). Emerging contaminants in wastewater: a critical review on occurrence, existing legislations, risk assessment, and sustainable treatment alternatives. *J. Environ. Chem. Eng*. 9(5), pp. 105966.

Pruden, A., Pei, R.-T., Storteboom, H. & Carlson, K.-H. (2006). Antibiotic resistance genes as emerging contaminants: Studies in northern Colorado. *Environ. Sci. Technol*. 40(23), pp. 7445-7450.

Qian, F., He, M., Song, Y., Tysklind, M. & Wu, J. (2015). A bibliometric analysis of global research progress on pharmaceutical wastewater treatment during 1994-2013. *Environ. Earth Sci*.73, pp. 4995–5005.

Ren, H., Pan, Y.-W., Zhong, J.-H., Wang, J.-Y., Lu, Z.-X., He, Q., Zhou, S.-Y., Liao, X.-P., Liu, Y.-H., An, T.-C. & Sun, J. (2023). An antibiotic-destructase-activated Fenton-like catalyst for synergistic removal of tetracycline residues from aquatic environment. *Chem. Eng. J*. 459, pp. 141576.

Ren, H., Pan, Y.-W., Zhong, J.-H., Wang, J.-Y., Lu, Z.-X., He, Q., Zhou, S.-Y., Liao, X.-P., Liu, Y.-H., An, T.-C. & Sun, J. (2023). An antibiotic-destructase-activated Fenton-like catalyst for synergistic removal of tetracycline residues from aquatic environment. *Chem. Eng. J*. 459, pp. 141576.

Rizzo, L., Della Sala, A., Fiorentino, A. & Puma, G.-L. (2014). Disinfection of urban wastewater by solar driven and UV lamp-TiO_2 photocatalysis: effect on a multi drug resistant Escherichia coli strain. *Water Res*. 53, pp. 145–152.

Rizzo, L., Manaia, C., Merlin, C., Schwartz, T., Dagot, C., Ploy, M.C., Michael, I. & Fatta-Kassinos, D. (2013). Urban wastewater treatment plants as hotspots for antibiotic resistant bacteria and genes spread into the environment: A review. *Sci. Total Environ*. 447, pp. 345-360.

Rodriguez-Mozaz, S., Chamorro, S., Marti, E., Huerta, B., Gros, M., Sànchez-Melsió, A., Borrego, C.M., Barceló, D. & Balcázar, J.L. (2015). Occurrence of antibiotics and antibiotic resistance genes in hospital and urban wastewaters and their impact on the receiving river. *Water Res*. 69, pp. 234-242.

Schwartz, T., Volkmann, H., Kirchen, S., Kohnen, W., Schön-Hölz, K., Jansen, B. & Obst, U. (2006). Real-time PCR detection of Pseudomonas aeruginosa in clinical and municipal wastewater and genotyping of the ciprofloxacin-resistant isolates. *FEMS Microbiol. Ecol*. 57(1), pp. 158-167.

Sigala, J. & Unc, A. A (2012). PCR-DGGE approach to evaluate the impact of wastewater source on the antibiotic resistance diversity in treated wastewater effluent. *Water Sci. Technol*. 65(7), pp. 1323-1331.

Silva, J., Castillo, G., Callejas, L., Lopez, H. & Olmos, J. (2006). Frequency of transferable multiple antibiotic resistance amongst coliform bacteria isolated from a treated sewage effluent in Antofagasta, Chile. *Electron. J. Biotechnol*. 9(5), pp. 533-540.

Slomkiewicz, P., Szczepanik, B., Piekacz, K., Golombek, K. & Wlodarczyk-Makula, M. (2025) Adsorptive removal of sulfamethoxazole from water using carbon-mineral composites. Arch. Environ. Prot. 51(3), pp. 40-53.

Soni, K., Jyoti, K., Kumar, A. & Chandra, R. (2024). Coexistence of multidrug resistance and ESBL encoding genes - blaTEM, blaSHV, and blaCTX-M, its amplification and dispersion in the environment via municipal wastewater treatment plant. *Chemosphere*. 362, pp. 142829.

Su, J.-Q., An, X.-L., Li, B., Chen, Q.-L., Gillings, M.R., Chen, H., Zhang, T., Zhu, Y.-G. (2017). Metagenomics of urban sewage identifies an extensively shared antibiotic resistome in China. Microbiome, 5, 84. DOI: 10.1186/s40168-017-0298-7.

Syafrudin, S., Sarminingsih, A., Juliani, H., Budihardjo, M.A., Sani, M.T. & Wati, H.R. (2025) A review of watershed-scale water quality monitoring: integrating real-time systems and spatial modeling for sustainable water resource management. Arch. Environ. Prot. 51(1), pp. 12-31.

Szczepanowski, R., Krahn, I., Linke, B., Goesmann, A., Pühler, A. & Schlüter, A. (2004). Antibiotic multiresistance plasmid pRSB101 isolated from a wastewater treatment plant is related to plasmids residing in phytopathogenic bacteria and carries eight different resistance determinants including a multidrug transport system. *Microbiology*. 150, pp. 3613-3630.

Talat, A., Bashir, Y., Khalil, N., Brown, C.-L., Gupta, D. & Khan, A.-U. (2025). Antimicrobial resistance transmission in the environmental settings through traditional and UV-enabled advanced wastewater treatment plants: a metagenomic insight. *Environ. Microbiome*. 20(1), pp. 27.

Tang, L.-G., Li, J.-Z., Yu, Z.-L., Meng, J. & Li, J.-L. (2024). Improving antibiotic resistance removal from piggery wastewater by involving zero-valent iron within an integrated anoxic-aerobic biofilm reactor. *Chem. Eng. J*. 493, pp. 152688.

Tennstedt, T., Szczepanowski, R., Krahn, I., Pühler, A. & Schlüter, A. (2005). Sequence of the 68,869 bp IncP-1α plasmid pTB11 from a waste-water treatment plant reveals a highly conserved backbone, a Tn402-like integron and other transposable elements. *Plasmid*. 53(3), pp. 218-238.

Tian, Y., Tian, Z., Feng, H.-D., Luan, X., Han, Z.-M., Zhang, Y. & Yang, M. (2023). Unveiling the threshold values of organic and oxytetracycline loadings for nitrification recovery of a full-scale pharmaceutical wastewater treatment system. *Chem. Eng. J*. 463, pp. 142487.

Wang, C.-X., Yin, X.-L., Xu, X.-Q., Wang, D., Wang, Y.-B. & Zhang, T. (2025). Antibiotic resistance genes in anaerobic digestion: Unresolved challenges and potential solutions. *Bioresour. Technol*. 419, pp. 132075.

Wang, J.-L., Chu, L.-B., Wojnárovits, L. & Takács, E. (2020). Occurrence and fate of antibiotics, antibiotic resistant genes (ARGs) and antibiotic resistant bacteria (ARB) in municipal wastewater treatment plant: An overview. *Sci. Total Environ*. 744, pp. 140997.

Wen, G., Wu, H.-H., Guo, X.-Y., Gao, Y.-F., Zhang, C.-F. & Zhang, W.-J. (2024). Global research trends in pharmaceutical wastewater from 1990 to 2023 using bibliometric analysis. *Desalin. Water Treat*. 318, pp. 100386.

Xu, Z.-S., Ge, Z.-J., Wang, X.-X. & Kou, G. (2022). A Look at the Focus on Big Data for Information Technology and Decision Making During 1994 to 2020. *Int. J. Inf. Tech. Decis*. 22(01), pp. 7-35.

Yan, Q., Zhong, Z.-Z., Li, X.-Y., Cao, Z.-Y., Zheng, X.-L. & Feng, G.-Z. (2024). Characterization of heavy metal, antibiotic pollution, and their resistance genes in paddy with secondary municipal-treated wastewater irrigation. *Water Res*. 252, pp. 121208.

Yang, H.-Y., Li, X.-L., Li, X.-L., Wang, X.-L., Ma, H. & Zheng, X. (2024). The fate of antibiotic resistance genes and their correlation with microbial communities and wastewater quality/parameters in a wastewater treatment plant under different seasons. *J. Water Process Eng*. 60, pp. 105156.

Yang, Y., Li, B. & Zhang, T. (2013).Exploring Variation of Antibiotic Resistance Genes in Activated Sludge over a Four-Year Period through a Metagenomic Approach. *Environ. Sci. Technol*. 47(18), pp. 10197-10205.

Yang, Y.-Y., Liu, G.-H., Ye, C. & Liu, W.-Z. (2019). Bacterial community and climate change implication affected the diversity and abundance of antibiotic resistance genes in wetlands on the Qinghai-Tibetan Plateau. *J. Hazard. Mater*. 361, pp. 283-293.

Yin, Q., da Silva, A.-C., Zorrilla, F., Almeida, A.-S., Patil, K.-R. & Almeida, A. (2025). Ecological dynamics of Enterobacteriaceae

in the human gut microbiome across global populations. *Nat. Microbiol*. 10(2), pp. 69-70.

Yin, X.-L., Yang, Y., Deng, Y., Huang, Y., Li, L.-G., Chan, L.-Y.L. & Zhang, T. (2022). An assessment of resistome and mobilome in wastewater treatment plants through temporal and spatial metagenomic analysis. *Water Res*. 2022, 209, 117885.

Zare, P., Pettit, C., Leao, S. & Gudes, O. (2022). Digital Bicycling Planning: A Systematic Literature Review of Data-Driven Approaches. *Sustainability*. 14(23), pp. 16319.

Zarei-Baygi, A., Harb, M., Wang, P., Stadler, L.-B. & Smith, A.L. (2020). Microbial community and antibiotic resistance profiles of biomass and effluent are distinctly affected by antibiotic addition to an anaerobic membrane bioreactor. *Environ. Sci.: Water Res. Technol*. 6(3), pp. 724-736.

Zhai, W.-C., Yang, F.-X., Mao, D.-Q. & Luo, Y. (2016). Fate and removal of various antibiotic resistance genes in typical pharmaceutical wastewater treatment systems. *Environ. Sci. Pollut. Res*. 23(12), pp. 12030-12038.

Zhang, M.-L., Liu, J.-C., Zhang, W.-F., Feng, M.-B., Yu, X. & Ye, C.-S. (2024). Neglected contributors to the transmission of bacterial antibiotic resistance in drinking Water: Extracellular antibiotic resistance genes and the natural transformation. *Sci. Total Environ*. 953, pp. 175970.

Zhang, Q.-Q., Ying, G.-G., Pan, C.-G., Liu, Y.-S. & Zhao, J.-L. (2015). Comprehensive Evaluation of Antibiotics Emission and Fate in the River Basins of China: Source Analysis, Multimedia Modeling, and Linkage to Bacterial Resistance. *Environ. Sci. Technol*. 49(11), pp. 6772-6782.

Zhang, Q.-R., Zhou, H.-X., Jiang, P., Wu, L.-J. & Xiao, X. (2024). Silver nanoparticles facilitate phage-borne resistance gene transfer in planktonic and microplastic-attached bacteria. *J. Hazard. Mater*. 469, pp. 133942.

Zhang, T., Zhang, X.-X. & Ye, L. (2011). Plasmid Metagenome Reveals High Levels of Antibiotic Resistance Genes and Mobile Genetic Elements in Activated Sludge. *PLoS One*. 6(10),pp. e26041.

Zhang, Y., Wang, C., Han, Z.M., Feng, H.D., Tian, Y. & Tian, Z. (2024). Research progress and prospect of anaerobic membrane bioreactor for treatment of antibiotic wastewater. *Chin. J. Environ. Eng*. 18(3), pp. 623-633.

Zhang, Y.-L., Zhao, D.-H., Liu, H.-C., Huang, X.-R., Deng, J.-Z., Jia, R.-C., He, X.-P., Tahir, M.N. & Lan, Y.B. (2022). Research hotspots and frontiers in agricultural multispectral technology: Bibliometrics and scientometrics analysis of the Web of Science. *Front. Plant Sci*. 13, pp. 955340.

Zhao, J., Yue, P., Li, Z.-J., Xu, T., Xing, G.-Z., Shao, Y. & Yu, H.-Y. (2025). Distribution and Antibiotic Resistance Analysis of Clinically Common Isolates. *Infect. Drug Resist*. 18, pp. 1071-1081.

Zhao, Y.-T., Zhang, X.-X., Zhao, Z.-H., Duan, C.-L., Chen, H.-G., Wang, M.-M., Ren, H.-Q., Yin, Y. & Ye, L. (2018). Metagenomic analysis revealed the prevalence of antibiotic resistance genes in the gut and living environment of freshwater shrimp. *J. Hazard. Mater*. 350, pp. 10-18.

Zheng, C.-L., Cotner, J.-B., Sato, C., Li, G. & Xu, Y.-Y. (2018). Global development of the studies focused on antibiotics in aquatic systems from 1945 to 2017. *Environ. Sci. Pollut. Res*. 25(22), pp. 22023–22034.

Zheng, C.-L., Wang, Y.-F., Qiu, Q.-L.L., Li, G. & Xu, Y.-Y. (2019). Bibliometric profile of research on antibiotics in sediments during 1958–2016. *Curr. Sci*. 117(1), pp. 37–45.

Zheng, J., Su, C., Zhou, J.-W., Xu, L.-K., Qian, Y.-Y. & Chen, H. (2017). Effects and mechanisms of ultraviolet, chlorination, and ozone disinfection on antibiotic resistance genes in secondary effluents of municipal wastewater treatment plants. *Chem. Eng. J.* 317, pp. 309-316.

Zhong, L., Ding, J., Wu, T., Zhao, Y.-L., Pang, J.-W., Jiang, J.-P., Jiang, J.-Q., Li, Y., Ren, N.-Q. & Yang, S.-S. (2023). Bibliometric overview of research progress, challenges, and prospects of rural domestic sewage: Treatment techniques, resource recovery, and ecological risk. *J. Water Process Eng*. 51, pp. 103389.

Zhu, X.-H., Li, Y.-L., Wang, Z.-W., Pang, Z.-Y., Si, Z.-S., Liu, C., Lu, J.-B., Cao, S.-L., Pei, L.-Y. & Li, Y.-B. (2023). Antibiotic resistance of Riemerella anatipestifer and comparative analysis of antibiotic-resistance gene detection methods. *Poultry Sci*. 102(3), pp. 102405.

Archives of Environmental Protection
Vol. 52 no. 3 pp. 76–87

PL ISSN 2083-4772
DOI: 10.24425/aep.2026.3679



© 2026. The Author(s). This is an open-access article distributed under the terms of the Creative Commons Attribution-ShareAlike 4.0 International Public License (CC BY SA 4.0, https:// creativecommons.org/licenses/by-sa/4.0/legalcode), which permits use, distribution, and reproduction in any medium, provided that the article is properly cited.

Biomass-derived activated carbons from date pits and spirulina for CO_2 and water vapor adsorption: A comparative uptake ratio study

Janaen Y. Al-Saeedi[1], Shaima Al-Bazzaz[2]*, Anwar A. Abbood[2], Harith Y. Mahmood[3]

[1]Department of Biology, College of Science, University of Basrah, Iraq
[2]Department of Chemical Engineering, College of Engineering, University of Basrah, Iraq
[3]Department of Physiology and Chemistry, College of Veterinary, University of Basrah, Iraq

*Corresponding author's e-mails: shaima.shueayb@uobasrah.edu.iq

Keywords: activated carbon, adsorption, isotherm, water vapor

Abstract: Increasing emissions of greenhouse gases, such as CO_2, cause a rise in the average temperature of the Earth's climate system. It is well established that $ZnCl_2$ activation or treatment is one of the most widely used methods for maximizing CO_2 adsorption capacity. However, water vapor co-adsorption during CO_2 capture processes can result in higher regeneration energies. This study aims to evaluate the effectiveness of $ZnCl_2$-activated carbons coated with a thin layer of vinyltrimethoxysilanein to increase the CO_2/H_2O uptake ratio. Date pits and Spirulina were used separately to produce activated carbons. The CO_2 adsorption capacities of the samples were investigated using thermogravimetric analysis with 15% CO_2 in nitrogen, while the water vapor uptake at 10, 50, and 95% relative humidity (RH) was investigated using Dynamic Vapor Sorption. Partial reductions in specific surface area and pore volume occurred after silane modification. However, heat treatment of the coated samples at 450 °C, which moderated the coating layer on the surface and reopened some of the blocked pores, increased the CO_2/H_2O uptake ratio, especially for the activated carbon derived from date pits (DPZHC), to 3.01 at 10% RH. Therefore, this sample is a promising candidate for co-adsorption processes. Although the study was conducted under controlled conditions, the adsorbent's stability and its ability to regenerate and be reused still need to be determined.

Introduction

Human activities, especially over the last few decades, have significantly increased atmospheric pollutant concentrations, leading to an increase in the Earth's average surface temperature. Greenhouse gases, particularly carbon dioxide (CO_2), are emitted from industrial processes and contribute significantly to global warming (Mashkhool et al. 2021). However, CO_2 can be captured using various technologies. Among the wide variety of adsorbents, including silica, zeolites, polymers, metal-organic frameworks (MOFs), and activated carbons that have been extensively investigated for CO_2 capture, carbon-based materials derived from different precursors exhibit high CO_2 uptake capacities and stability during adsorption–desorption cycling (Reddy et al. 2021). Limited CO_2 adsorption selectivity in the presence of water vapor is one of the main obstacles to the widespread use of conventional activated carbon in CO_2 capture technologies. Therefore, the development of well-designed carbon-based materials with controlled properties has become essential for efficient environmental applications. Chemical and physical treatments have been used to modify the surface chemistry of carbon materials and tailor their adsorption properties. For instance, enlarged micropores with small amounts of mesopores can be obtained using potassium hydroxide (KOH) (Oumabady et al. 2021), sodium hydroxide (NaOH) (Borisut et al. 2025), and zinc chloride ($ZnCl_2$) (Möller et al. 2023). Due to its acidifying properties, zinc chloride plays an important role in activating carbonaceous precursors and improving the adsorption capacity of the resulting carbon materials by promoting dehydration and bond cleavage in biomass, facilitating aromatization and crosslinking of the carbon matrix. Furthermore, subsequent acid washing dissolves zinc species and removes them from the carbon matrix, creating voids that develop into micropores and mesopores (Li et al. 2020). These processes strengthen the internal pore network and increase surface accessibility for adsorption, making the activated carbon more effective.

Two biomass precursors were selected in this study: date pits and *Spirulina*. Their selection was based on carbon



Fig 1. Spirulina powder and Date pits powder

density, cost, abundance, CO_2 adsorption potential, and their fundamentally different biochemical compositions. Date pits are lignocellulosic materials rich in cellulose, hemicellulose, and lignin, whereas *Spirulina* is a protein-rich microalga containing nitrogenous functional groups that may lead to differences in the surface chemistry and adsorption behavior of the resulting carbons. Water vapor is the third most abundant component of flue gas after nitrogen and carbon dioxide. The presence of water is generally detrimental to CO_2 capture using activated carbons, especially at low relative pressures, where water and gas molecules compete for active sites. In general, for most CO_2 capture processes, water vapor in a gas stream increases the energy demand. Water molecules (diameter ≈ of 0.275 nm) adsorb first onto the functional groups, which represent the primary active sites. These sites typically occur at the edges and corners of basal planes and interact with water molecules through hydrogen bonding, forming a water layer on the activated carbon surface. Subsequently, as the relative humidity (RH) increases, water clusters form around the initially adsorbed water molecules, which themselves become secondary adsorption sites.

Once a critical cluster size is reached, the clusters possess sufficient dispersive interaction energy to fill the carbon pores (Duan et al. 2023). At equilibrium, water isotherms on the pore surface typically exhibit a V-type topology, which is relatively rare. This is due to the hydrophobic nature of activated carbons, which has been shown to be strongly dependent on relative humidity (Zheng et al. 2023). Therefore, studying water adsorption is important for evaluating sorbent performance in CO_2 capture. Querejeta et al. (2016) reported that moisture strongly influenced the adsorption performance of activated carbons derived from biomass under post-combustion CO_2 capture conditions. Surface post-treatments can increase water vapor adsorption capacity by altering pore accessibility and surface chemistry. Liu et al. (2018) confirmed that adsorption processes are strongly affected by moisture. They investigated the sorption equilibria and kinetics of CO_2 and H_2O on KOH-treated activated carbon and reported that the adsorption capacity for H_2O was higher than that for CO_2. The main objective of this study was to evaluate the adsorption performance of modified activated carbons toward CO_2 and water vapor separately and to assess their relative affinity using a CO_2/H_2O uptake ratio. Laboratory-scale adsorption experiments were conducted using thermogravimetric analysis and a dynamic vapor sorption instrument.

Materials and methods

Materials

Spirulina powder (*Spirulina Hawaiiana*) was purchased from Cyanotech, USA, and used as the algal raw material for the preparation of activated carbon. The powder was dried at 105 °C for 5 h to remove moisture and then cooled to room temperature. Dates were collected from local markets in Basra, Iraq, and the pits were manually separated from the fruit. The pits were first washed several times with potable water followed by distilled water, and then dried and cooled using the same procedure as that applied to the *Spirulina* powder. The dried pits were subsequently crushed and sieved to obtain particles with diameters in the range of 1.0-1.4 mm.

Methods

Carbonization

The carbonization process was conducted separately for each dried powder by heating it to 550 °C at 5 °C/min under nitrogen (N_2), maintaining this temperature for 60 min and then cooling to room temperature. The resulting carbonized samples derived from date pits and *Spirulina* were designated DP and SP, respectively. $ZnCl_2$ (purity ≥ 98%) was purchased from Sigma-Aldrich (UK).

Activation of Materials

The following steps were carried out for chemical activation:

1- The SP carbon was mixed with ground $ZnCl_2$ at a mass ratio of 1:1 (m/m).

2- Approximately 5 g of the mixture was placed in a ceramic pot and loaded into a quartz tube of a horizontal tube furnace (Elite Thermal Systems Ltd., UK). The system was purged with nitrogen (N_2 gas (1 bar, 1 L/min) for 30 min to remove residual air and moisture. The samples were then heated to 650 °C at 5 °C/min for over 60 min under continuous nitrogen flow, followed by cooling to room temperature.

3- To remove residual $ZnCl_2$ and achieve neutral pH, the resulting activated carbon was treated with 1 M hydrochloric acid and subsequently washed repeatedly with distilled water. The washed samples were then dried in an oven at 110 °C for 6 hours. The final activated carbon derived from *Spirulina* was labelled SPZ. The same procedure was applied to the date pit-derived carbon, yielding DPZ.

Modification of Activated Carbon

The surface modification was performed according to the experimental protocol described by Albazzaz (2020) and consisted of three stages: oxidation, reduction, and hydrophobization. First, the oxidation step was conducted by adding 2.5 g of DPZ to 250 mL of 15% w/w H_2O_2 solution. The mixture was subsequently washed with distilled water, dried at 100 °C for 24 hours, and then heated at 450 °C for 3 hours under N_2 gas. The second stage, reduction, was performed by dissolving 2.5 g of the $NaBH_4$ in 250 mL of anhydrous methanol. The sample was submerged in the mixture for 12 hours, then diluted with 250 mL of water and boiled for 3 hours. The sample was then removed from the solution, washed with water, and dried in a vacuum oven at 100 °C for 24 hours. Finally, the hydrophobization step was conducted by partially dissolving vinyltrimethoxysilane (VTMOS) in toluene at a volume ratio of 1:10 (VTMOS:toluene:v/v), followed by the addition of a few drops of water to induce the hydrolysis of the alkoxysilane molecules. The sample was placed in an extraction thimble and loaded into the main chamber of a Soxhlet extractor connected to a distillation flask and a reflux condenser. The distillation flask was heated to the boiling point of toluene (110.6 °C), and the condensation reaction was allowed to procees via Soxhlet extraction for 3 hours to achieve hydrophobization. The resulting coated activated carbon derived from date pits was labelled DPZH. The same procedure was applied to SPZ, producing the hydrophobized sample SPZH.

Calcination

To moderate the thickness of the coating layer, the two samples, DPZH and SPZH, were separately subjected to thermal treatment under N_2 (1 bar, 100 mL/min). The process was conducted using thermogravimetric analysis (TGA) (Q500, TA Instruments Incorporated) at 450 °C for 1 hour, a temperature identified by the referenced study as optimal for CO_2 adsorption. TGA is an integrated thermal weight-change analysis instrument. It is equipped with standard mass flow controllers to measure the amount and rate of change in the weight of a material as a function of temperature or time, and operates in the temperature range from ambient to 1000°C. It has an isothermal temperature accuracy of ±1 °C, an isothermal temperature precision of ±0.1 °C, a weighing capacity of 100 mg, a sensitivity of 0.1 µg and a precision of ± 0.01%. The resulting samples were labelled DPZHC and SPZHC.

Textural Characterization of the Samples

The textural properties of the samples, including the specific surface area and pore volume, were characterized using N_2 and CO_2 sorption isotherms. Surface area and porosity data were measured using both experimental techniques and models applied to the isotherms, such as the BET and Non-Local Density Functional Theory (NLDFT) models.

Experimental Procedure

The textural properties of the samples (DP, DPZ, DPZH, DPZHC SP, SPZ, SPZH, and SPZHC) were characterized using a Micromeritics Accelerated Surface Area and Porosimetry Analyzer (ASAP 2420, Micromeritics Corporation) with N_2 (at -196 °C) and CO_2 (at 0 °C) as adsorbates. Before the measurements, approximately 0.2 g of each sample was weighed into a sample tube and degassed under high vacuum (<0.013 mbar) at 120 °C for 6 hours to remove adsorbed moisture and gases. The surface area was calculated using the BET model from N_2 adsorption isotherm data over the relative pressure range of 0.01-0.10, yielding positive BET 'C' parameters. The cumulative pore volumes (Vtotal) were calculated using a non-local density functional theory (NLDFT) carbon slit pore model through a combined analysis of N_2 adsorption isotherms at -196 °C (over a relative pressure range of 0.00001 to 0.99850) and CO_2 adsorption isotherms at 0 °C (over a relative pressure of 0.00006 to 0.03498) using Microactive Software V5.0.

Fourier Transform Infrared (FTIR) Spectroscopy analysis

Fourier transform infrared spectroscopy (FTIR) analysis was performed using a Perkin Elmer Spectrum 100 instrument in the mid-infrared range (4000–400 cm^{-1}) at a resolution of 2 cm^{-1}. Each spectrum represents the average of 16 scans acquired in transmittance mode. Using a mortar, 0.0015 g of the sample was mixed and ground with 0.25 g of potassium bromide (KBr). The obtained powder was loaded into a circular die and subjected to high pressure (100 MPa) for 10 seconds. The sample was then dried in a drying oven at 100 °C overnight under vacuum and left to cool to ambient temperature under vacuum. After that, the sample was analyzed using an FTIR spectrophotometer.

CO_2 and H_2O Adsorption Measurement

CO_2 Adsorption Measurement

The samples were analyzed using a TGA to determine the amount of CO_2 adsorbed. Approximately 20 mg of a sample was placed in a platinum pan and heated to 150 °C at a rate of 20 °C/min under a flow of N_2 (1 bar, 100 mL/min) for 30 minutes to remove any moisture and/or pre-adsorbed CO_2. After drying, the sample was cooled to the adsorption temperature of 25 °C under the same N_2 flow rate. The gas was then switched to simulated flue gas (15:85 v/v CO_2: N_2, 1 bar, 100 mL/min), and the sample was held isothermally for 1 hour. The sample's weight change at the point of gas switch-over was taken as the baseline, and the subsequent increase in mass during exposure to the simulated flue gas was used to calculate CO_2 uptake. From this, the adsorption kinetics at t60, t80, and t90 were calculated for the samples by determining the time taken to reach 60, 80, and 90% of the CO_2 equilibrium capacity, based on the net weight gain recorded during the adsorption period. The experiment was repeated for all other samples. Since N_2 is assumed to be non-adsorbing under the experimental conditions, the observed mass increase after gas switching was attributed solely to CO_2 adsorption.

H_2O Adsorption Measurements

Dynamic vapor sorption (DVS) measurements were carried out using a DVS Adventure analyzer (Surface Measurement Systems Ltd., London, UK). The balance head and reaction chamber were purged with dry nitrogen before sample loading. The flow of nitrogen is automatically controlled to keep the head of the sensitive recording microbalance dry inside the controlled temperature chamber, thereby preventing the condensation of vapor in connections and ensuring accurate

uptake measurements. The uptake was calculated by dividing the difference between the temporal mass measured and the mass of adsorbent after the drying process (before the start of adsorption process) by the mass of the adsorbent after the drying process. An optical vapor pressure sensor and an RTD temperature probe fixed beside the sample pan (which contained 10 mg of the sample) were used to measure the test conditions in DVS. The weights of samples measured by the microbalance were transmitted directly to a PC microcomputer for recording and analysis. The six samples were dried at 150 °C for 12 hours, and the adsorption process was then conducted at 25 °C.

Results and discussion

Characterization of Activated Carbon

Table 1 summarizes the specific BET surface areas (SBET) and pore volumes, including micropore volumes, for all samples. The SP sample exhibited the lowest SBET value, 198 m^2/g, which is typical for carbonized *Spirulina platensis* (Yu et al. 2022). SPZ showed a well-developed porous structure, where the intercalation of $ZnCl_2$ led to an increase in specific surface area to 796 m^2/g, the total pore volume to 0.59 cm^3/g, and a micropore volume to 0.34 cm^3/g, increasing from 0.26 cm^3/g for SP. In addition, the textural properties of carbonized date pits (DP) developed after the activation process. The SBET values for DP and DPZ were 613 and 1,214 m^2/g, respectively, while the micropore volume and total pore volume increased from 0.31 to 0.54 and from 0.48 to 0.87 cm^3/g, respectively. These results suggest that the modification treatments drastically altered the pore texture of the activated carbon, driven by the chemical activation ($ZnCl_2$) of the carbon network, and are consistent with those previously reported by Bouchemal and Addoun (2009), where the specific surface area and total pore volume of the activated carbon prepared from date pits increased to 1,322 m^2/g and 0.81 cm^3/g, respectively, after activation by $ZnCl_2$ at 600 °C. After VTMOS modification, a significant decrease in the BET surface area and pore volume of the coated samples (DPZH and SPZH) was observed.

This trend is consistent with reports in the literature, which indicate that chemical treatments may partially reduce porosity without drastically altering the pore structure, as silane modification can create a thin layer on the external surface, leading to partial blockage of pore entrances while preserving the overall pore architecture of the activated carbon (Pustahija et al. 2024). On the other hand, the effect of heat treatment was very clear on the two coated samples. The surface area increased and approached its pre-modification value, accompanied by increases in micropore and total pore volume. This trend is consistent with results reported in the literature, which indicate that heat treatment of coated activated carbons increases specific surface area and pore volume (Albazzaz, 2020).

SBET is the specific surface area obtained using the BET model from the N_2 isotherm in the relative pressure range of 0.01 - 0.10 P/Po. Vmicro, Vmeso, and Vtotal are pore volumes corresponding micropores, mesopores, and total pores up to 100 nm, respectively, determined using NLDFT with a carbon slit-pore model applied to combined N_2 and CO_2 isotherms.

Scanning Electron Microscopy of Samples

The morphologies of the six samples were examined using a Quanta 600 scanning electron microscope (SEM) on the micrometer scale. The SEM images in Fig. 2 (a-f) were acquired at magnifications ranging from 1000× to 1500×, with a constant scale bar of 50 µm. The SEM image of DP shows a relatively smooth surface with limited pore development. Most of the visible pores are shallow and spherical, reflecting the natural structure of the biomass, which has not yet been significantly altered. The hemicellulose and lignin in the date pits were partially decomposed during the carbonization process, but this did not yield a well-developed porous network.

Table 1: Texture properties of activated carbon samples.

	SBET (m^2/g)	Vmicro (cm^3/g)	Vmeso (cm^3/g)	Vmacro (cm^3/g)	Vtotal (cm^3/g)
DP	613	0.31 (65%)	0.13	0.04	0.48
DPZ	1214	0.54 (62%)	0.23	0.09	0.87
DPZH	789	0.34(63%)	0.12	0.08	0.53
DPZHC	1177	0.46 (64%)	0.19	0.07	0.72
SP	198	0.26 (40%)	0.07	0.02	0.35
SPZ	796	0.34 (58%)	0.20	0.05	0.59
SPZH	423	0.28(72%)	0.07	0.04	0.39
SPZHC	752	0.31 (70%)	0.09	0.04	0.44

The DPZ sample reveals a highly porous structure characterized by rough, irregular, and heterogeneous pores of varying sizes, including micro-, meso-, and macropores. Additionally, some $ZnCl_2$ residue, which may not have been removed during repeated washing, appears as light or white particles due to its higher electron density than carbon. After the VTMOS coating, many small pores disappeared from the surface of the DPZH sample, while others were partially closed by the coating material, which covered the remaining residue of the chemical activating agent. Despite this, the overall pore structure remained clear, indicating the coating layer did not have a major effect on the underlying pore structure. Calcination of the DPZH sample removed a large portion of the VTMOS and reopened many pores. On the other hand, the SEM image of SP shows a compact and weakly porous structure with a rough surface. This morphology is consistent with the recent literature, which reports that low porosity typically forms on the *Spirulina* surface after carbonization due to its high protein content (Mushtaq and Alzurfi, 2023). Conversely, the SPZ sample exhibits a highly porous structure with irregularly shaped pores. Distinct crevices are apparent on the porous surface, indicating pores of various sizes, including mesopores and macropores. Some $ZnCl_2$ residues are more clearly visible on the carbon surface. The image of SPZH shows changes in the surface structure after VTMOS-coating. The large cavities disappeared from the SPZH sample, resulting in a low-level pore network. The bright, light-colored edges indicate the presence of a coating or surface effects caused by VTMOS that were not present in the DPZH sample. A notable reduction in the number and size of pores was observed, resulting in a smoother, more uniform surface. Some pores remained scattered across the surface, indicating that the coating process successfully reduced porosity.

The effect of heat treatment was very clear in the coated sample, where many pores reopened, and the surface morphology of SPZHC was similar to that observed before modification. The same effects of coating materials and calcination on pore size were observed by Albazzaz (2020), who found that VTMOS coated most pores in the activated carbon, especially the large cavities, and that calcination at 450 °C reopened most of them, suggesting that the VTMOS coating collapsed on the surface.

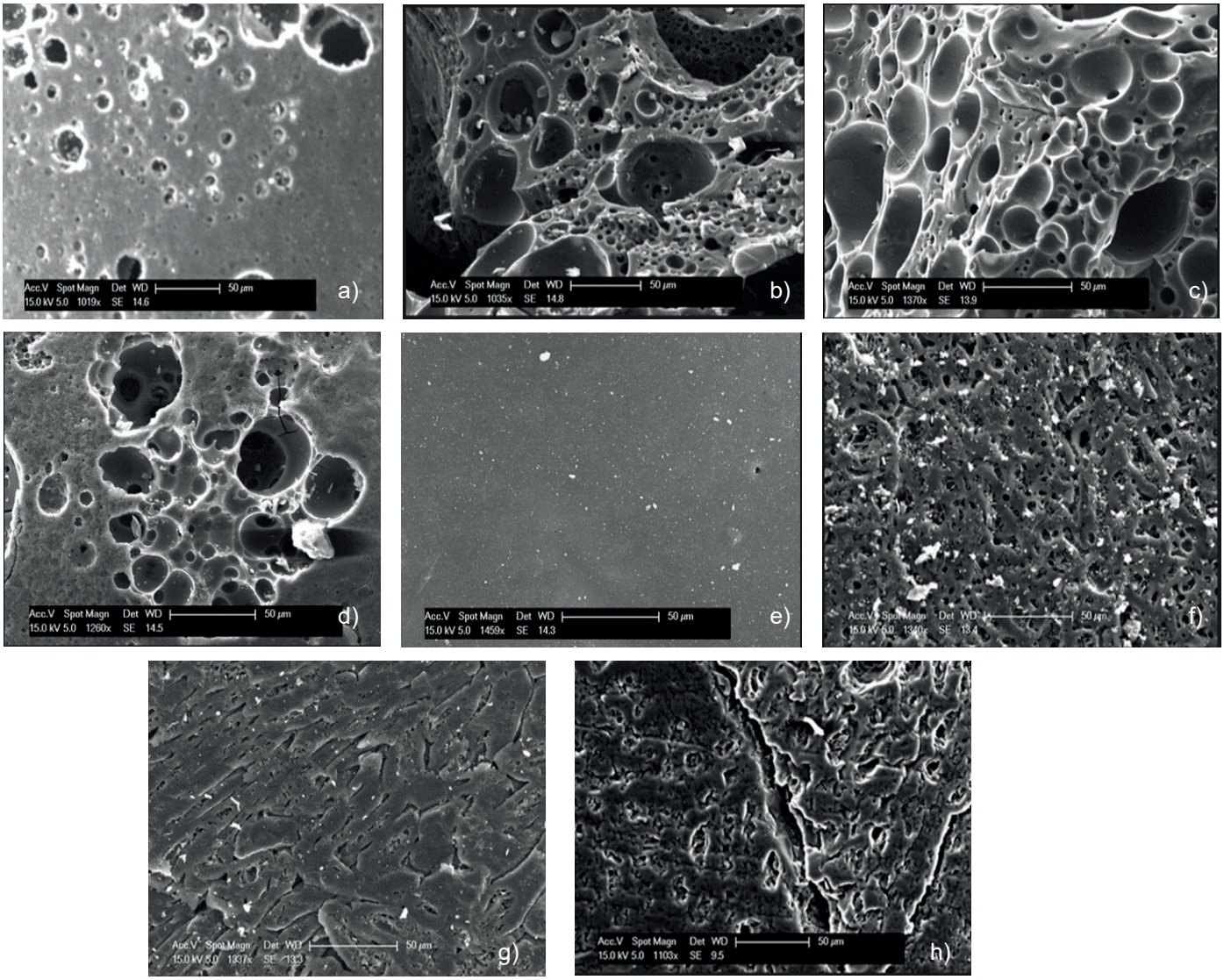


Fig 2. SEM images of carbon (a) DP, (b) DPZ, (c) DPZH, (d) DPZHC, (e) SP, (f) SPZ, (g) SPZH, and (h) SPZHC

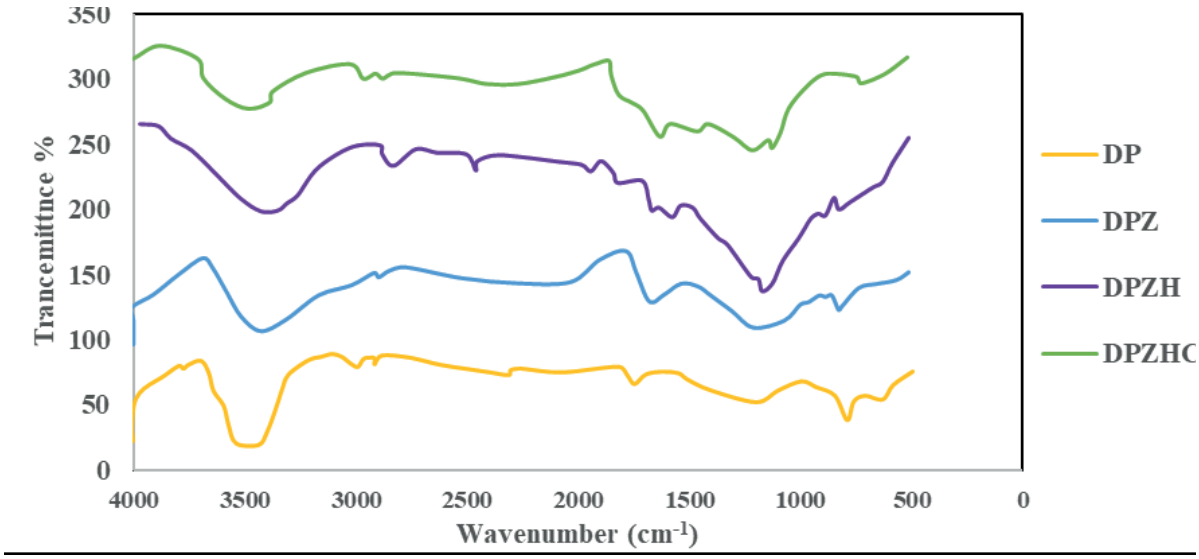


Fig 3. FTIR spectra of DP, DPZ, DPZH and DPZHC.

Fourier Transform Infrared Spectroscopy (FTIR)

In this work, FTIR spectroscopy was performed on samples derived from date pits, which exhibited higher specific surface area and pore volume, to evaluate the effects of carbonization, activation, and VTMOS grafting on the carbon surface, as well as the effect of heat treatment on the chemical structure of VTMOS. As shown in Figure 3, DP and DPZ exhibited a broad band in the 3,650–3,200 cm−1 wavelength range; the broader band with a gradual decrease was observed in the coated sample DPZH. This is possibly due to the O-H stretching vibration of surface hydroxyl groups (Yang and Yuan, 2025). However, the broad band decreased considerably after heat treatment, possibly indicating the removal of some hydroxyl groups from the DPZHC sample. Another large absorption band was observed in the DPZH spectrum in the 1,450-900 cm^{-1} region, with a maximum at about 1,170 cm^{-1}, possibly due to the stretching vibrations of Si–O–Si and Si–O–CH3 groups, confirming the successful incorporation of silane-based coating species onto the carbon surface (Albazzaz, 2020). As a result of heat treatment, the intensity of this band decreased to a weak shoulder, reflecting a reduction in the characteristic absorption features in DPZHC, and a new band appeared at 1,126 cm-1. Finally, the bands appearing below 800 cm^{-1} in DP and DPZ may be attributed to out-of-plane bending vibrations of aromatic C–H bonds. In conclusion, the effectiveness of the activation and coating processes was confirmed by FTIR analysis. The DPZH sample exhibited the most pronounced chemical modification, indicating a successful transformation from hydrophilic to hydrophobic surface characteristics. Heat treatment significantly altered the chemistry of the coated sample by removing some hydroxyl groups.

Measurement of the Kinetic Adsorption of CO2

Dry simulated flue gas (15% CO_2) at a flow rate of 100 mL/min was used to evaluate the kinetics of CO_2 adsorption for all samples using TGA. Overall, the kinetics were relatively fast, with most samples approaching equilibrium within 10 minutes (Fig. 4).

Detailed adsorption kinetics at t_{60}, t_{80}, and t_{90} are further reported in Table 2. As expected, and because they contain high proportions (40% and 72%) of the total pore volumes, the microspores offer sufficient active sites for adsorbate molecules (CO_2). Therefore, less than 2.5 minutes was sufficient to attain 60% of equilibrium uptake for all samples. For instance, DP

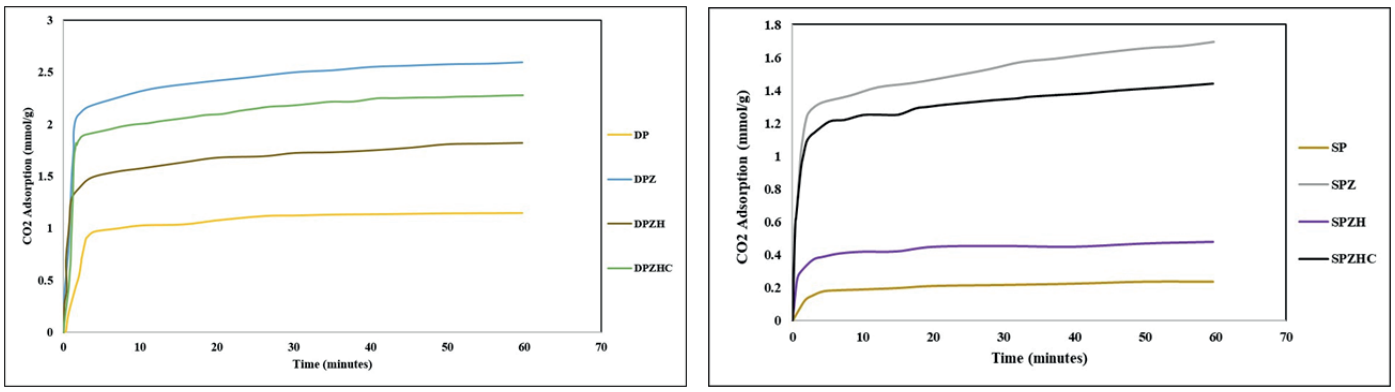


Fig 4. SCO_2 adsorption (a) for the DP, DPZ, DPZH, and DPZHC samples (b) for the SP, SPZ, SPZH, and SPZHC using TGA in 15% CO_2 and 85% N_2 at 25 °C

and SP attained 60% of equilibrium at 2.3 and 2.42 minutes, respectively. These outcomes confirm the results obtained by Kretzschmar et al (2021), which showed that a short contact time (~3 minutes) is sufficient to achieve high adsorption capacity for carbonized materials. After activation, the CO_2 adsorption performance of $ZnCl_2$-activated carbons (DPZ and SPZ) was markedly enhanced, and the adsorption kinetics were faster in reaching 60% of equilibrium. This can be attributed, first, to the activation process, which led to significant mesopore development, facilitating rapid diffusion into the microspores and increasing their volume (see Table 1). This effect not only improved accessibility but also provided abundant high-energy adsorption sites that are rapidly saturated with CO_2 molecules (Meng and Park 2014). Second, oxygen-containing functional groups (such as carboxyl and hydroxyl groups) were formed due to changes in surface chemistry. These groups interact strongly with CO_2 molecules, thereby accelerating adsorption (Liu et al. 2018).

In the first stage of adsorption, which accounts for 60-80% of the total adsorption within the micropores, uptake is driven by van der Waals forces between carbon dioxide molecules and the pore walls. These interactions occur more rapidly than those in the second stage, when adsorption approaches equilibrium. This explains the longer time required to reach 90% of total adsorption for all samples. On the other hand, except for the DPZH sample, which required a relatively long time to achieve 90% of the equilibrium (15.6 minutes), the two coated samples attained 60, 80, and 90% of equilibrium in shorter times compared to DPZ and SPZ. The effect of heat treatment was very clear in the time required to reach equilibrium for the two calcined samples. These results are superior to those reported in a previous study using zeolite calcined at 600 °C and a syngas flow rate of 0.5 L/min containing 15% of CO_2, where the adsorbent required 30, 32.5 and 38 minutes to reach 60%, 80%, and 90% of the total adsorption capacity (1.9452 mg CO_2 / kg adsorbent ≈ 4.42×10^{-5} mmol CO_2/g adsorbent), respectively (Maceiras et al. 2025).

Gravimetric Measurement of Water Vapor Adsorption

DVS was used to determine the adsorption isotherm data for H2O on all samples. As shown in Fig. 5, the samples exhibited a type IV isotherm according to the IUPAC classification (Thommes et al. 2015).

Water molecules showed preferential adsorption on the DPZ and SPZ (<20% RH). The high adsorption of H2O on the DPZ can be attributed to the abundance of high-density hydrophilic surface functional group, which increased during the washing process, and to the greater volume of micropores after ZnCl2 activation, where residual Zn^{2+} and Cl^{1-} species are removed and oxygen-containing functionalities such as –OH and –COOH are formed or increased (Möller et al. 2023; Li et al. 2020; Li et al. 2023). In addition, the precursor material (date pits) is rich in lignin and cellulose, which promotes the development of oxygen-containing functional groups on the activated carbon surface (Al-Harrasi et al. 2025). On the other hand, as reported in the literature, *Spirulina platensis* contains nitrogen and sulphur. Therefore, after activation, the surface may remain more heterogeneous, with the presence of –N and –S groups in addition to oxygen-containing groups (–O), which promote the hydrophilicity of the SPZ surface (Xie et al. 2022). In general, the adsorption in this range for both samples can be considered minor or initial water uptake. By increasing the relative humidity to 60%, the adsorbed water molecules may serve as secondary adsorption sites for cluster formation. The critical size of these clusters may enable them to possess sufficient dispersive energy to fill the carbon pores (Jia et al. 2022). Consequently, this region exhibited the highest water uptake rate, characterized by a gradual yet more pronounced increase in adsorption compared with other regions.

Table 2: Comparison of CO_2 equilibrium capacity and adsorption times (or kinetics) of CO_2 under dry conditions for all samples using TGA in 15% CO_2 and 85% N_2 at 25 °C

Sample	Adsorption time of CO_2 (minutes)			CO_2 equilibrium capacity(mmol/g)
	t_{60}	t_{80}	t_{90}	
DP	2.30	7.25	21.09	1.62
DPZ	1.61	2.87	11.41	2.56
DPZH	1.09	2.1	15.6	1.81
DPZHC	1.51	2.82	12.51	2.52
SP	2.42	10.01	23.42	0.24
SPZ	1.42	9.87	21.51	1.71
SPZH	0.85	3.24	15.12	0.48
SPZHC	1.21	5.02	21.09	1.60

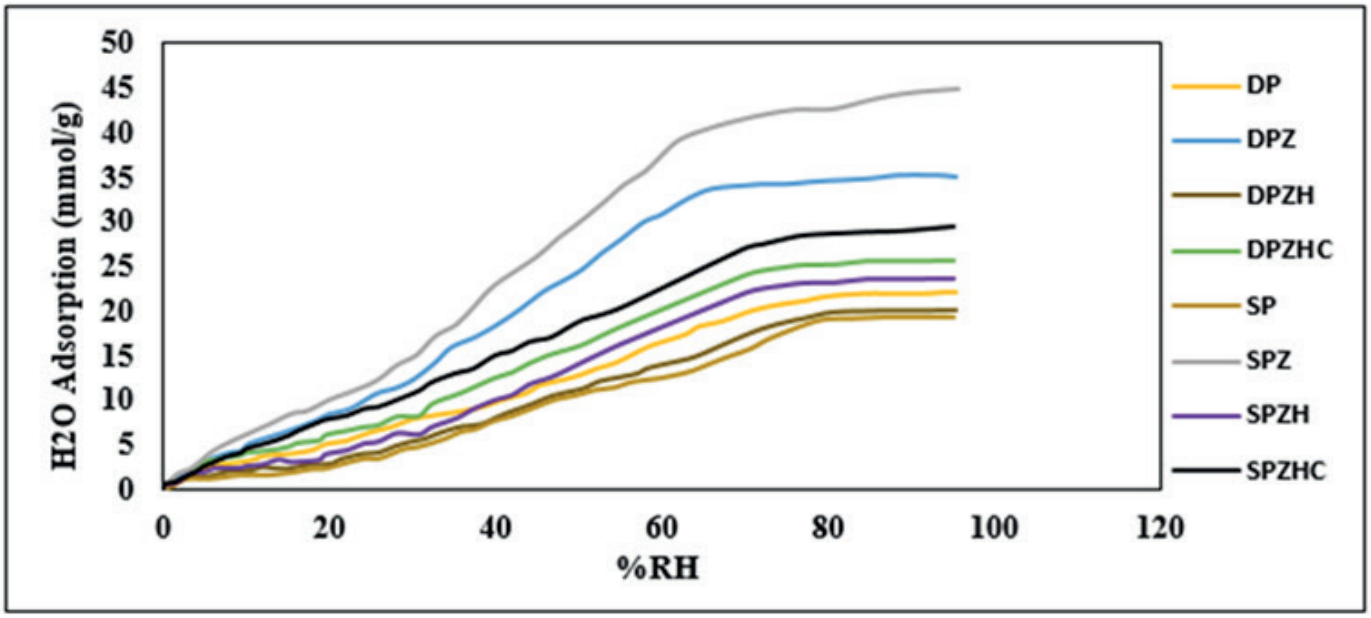


Fig 5. Water vapor adsorption isotherms of the samples using DVS in 100% N_2 at 25 °C (desorption omitted for clarity).

At higher relative humidity (RH >60%), both DPZ and SPZ exhibited higher water adsorption capacities owing to their advanced microporous structures. There was a clear difference in adsorption capacity between the two isotherms, with SPZ sample showing higher performance. This can be attributed to the nitrogen- and oxygen-containing functional groups in Spirulina platensis, which increase surface polarity and promote stronger interactions with water molecules. These observations are consistent with a previous study reporting that heteroatom co-doping (N, S, and O) enhances surface polarity, increases the density of active sites, and promotes hydrogen-bonding interactions with water molecules (Zhang et al., 2019). At high relative humidity (95% RH), the H_2O uptakes for DPZ and SPZ were 42.61 and 33.38 mmol/g, respectively, indicating that *Spirulina platensis* is more affected by $ZnCl_2$ activation than date pits, and that water uptake depends more on the surface chemistry than on its porosity. These results are consistent with those previously reported by Bai et al. (2020). As expected, water vapor adsorption declined markedly due to effectiveness of the coating on the DPZH and SPZH surfaces. In contrast, the calcination process increased the amount of water vapor adsorbed on the DPZHC and SPZHC samples.

The kinetic H_2O sorption profiles of the samples at 10%, 50%, and 95% RH were obtained using DVS. At less than 10% RH, both carbonized samples (DP and SP) showed low adsorption capacities (<1.5 mmol/g) and required less than 60 minutes to reach equilibrium (Figs. 5(a) and 6(a)). This is likely due to their low surface area (613 and 198 m^2/g) and limited micropore volumes (0.31 and 0.26 cm^3/g). The DPZ sample reached equilibrium after 60 minutes. In contrast, the SPZ sample showed a higher affinity for water molecules and required approximately 120 minutes to reach equilibrium despite having a lower total pore volume and surface area. On the other hand, the water absorption of the coated samples (DPZH and SPZH) ranged from 1.4 to 2 mmol/g. This may be due to the closure of some pores during the coating process. A decrease in the BET surface area and pore volume of the coated samples was shown in Table 1. The samples submitted to heat treatment after coating with VTMOS showed higher values.

At moderate humidity (50% RH) and high relative humidity (95% RH), DPZ surpassed SPZ in water uptake (Figs. 6(b, c) and 7(b, c)) because of its larger surface area (1,214 m^2/g) and higher micropore volume (0.33 cm^3/g), which provide more accessible microporous sites and more substantial capillary condensation effects within these pores. Except for DPZH, which showed high water adsorption, the other samples maintained the expected relative values during adsorption and desorption. The heat-treated samples recorded intermediate values between those of the activated and carbonized samples across all relative humidities.

These differences in the time required to reach equilibrium for activated carbons derived from date pits and *Spirulina* can be principally attributed to their different textural properties, particularly the abundance of narrow micropores. In general, the presence of small pores can retard diffusion and lead to much longer equilibration times, although the adsorption rate is fast at low relative humidity. It is important to note that the absence of a large difference in the time required to reach equilibrium at 60%, 80%, and 95% RH for each sample (Figs. 6 and 7) is consistent with literature reports (Martins et al., 2015, Jia et al., 2017). Previous studies have shown that, with increasing relative humidity, an increase in the adsorption capacity of an adsorbent may not always lead to an increase in the adsorption rate, as diffusion limitations may occur within micropores. Therefore, the adsorption capacity increases as the pores are filled at elevated RH.

Table 3. demonstrates the differences in H_2O adsorption of the samples at 10%, 50%, and 95% RH for 10 minutes (typical residence time in fluidized bed sorbents). All values were obtained from the two figures above.

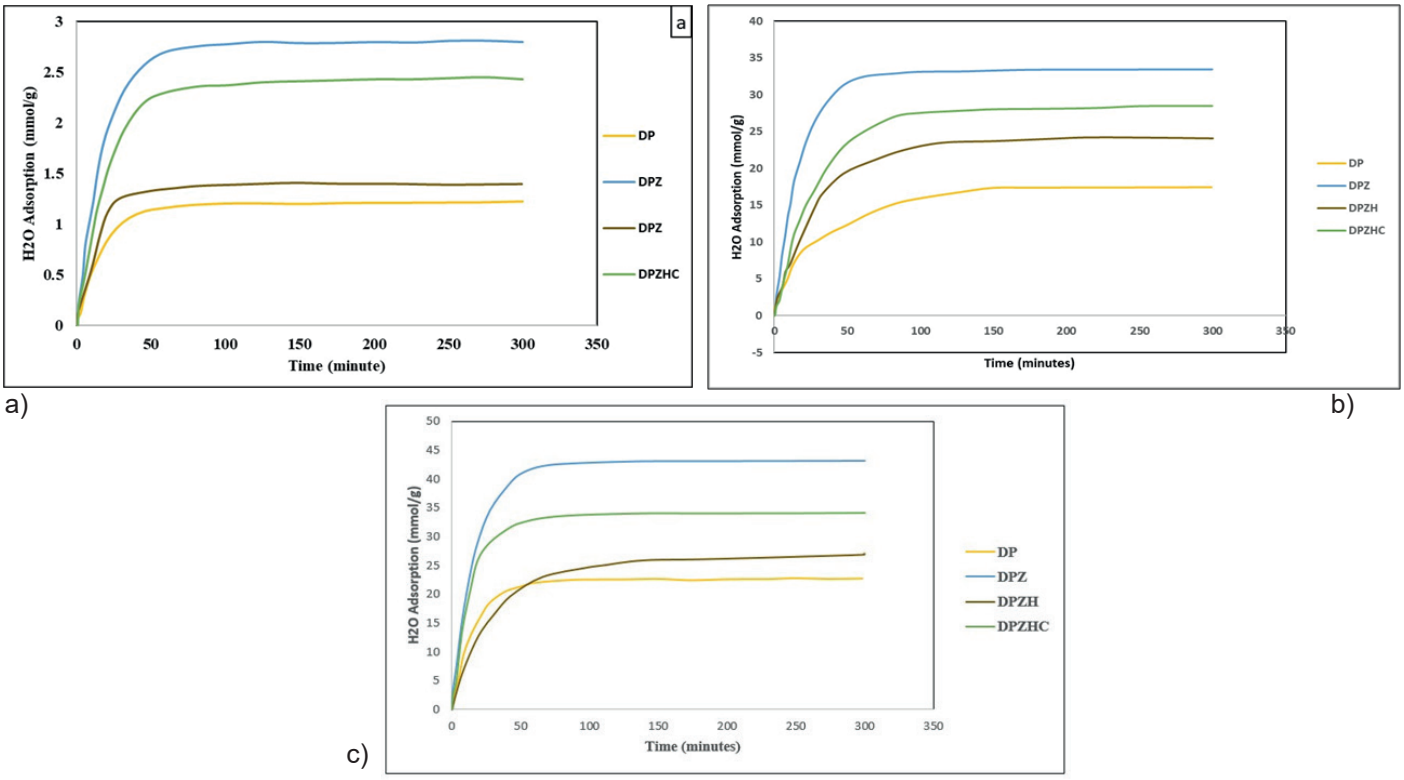


Fig 6. H_2O uptake DP, DPZ, DPZH, and DPZHC samples using DVS in 100% N_2, (a) 10% RH, (b) 50% RH, and (c) 95% RH at 25 °C.

CO_2/H_2O uptake ratio

The adsorption performance ratio of the CO_2 to H_2O is calculated as follows:

S (CO_2/ H_2O) = Adsorption CO_2 (mmol/g) / Adsorption H_2O (mmol/g)

In this work, the uptake ratio of the samples was evaluated after 10 minutes under typical post-combustion flue gas conditions. At 10% RH, the $S_{CO2/H2O}$ ratios of DPZ and SPZ were 1.9 and 2.09, respectively, compared with 1.84 and 0.57 for DP and SP, as shown in Table 4. The CO_2/ H_2O uptake ratios of the coated samples were lower than those recorded for the modified samples. The differences in CO_2 adsorption between DPZ and DPZHC were 13%, whereas those between SPZ and SPZHC were 5%. The differences in H_2O adsorption were higher than these values: 15% between DPZ and DPZHC and 37% between SPZ and SPZHC, as shown in Table 4.

The highest CO_2/H_2O values were observed for the heat-treated samples (DPZHC: 3.01; SPZHC: 2.46), indicating that the thickness of the coating layer played a significant role in determining CO_2 and H_2O adsorption.

Table 3: H_2O uptake of the samples at different RHs after 10 minutes

Sample	H_2O adsorption (mmol/g)		
	10% RH	50% RH	95% RH
DP	0.50	5.4	10.2
DPZ	1.12	14.6	20.3
DPZH	0.61	7.5	10.1
DPZHC	0.83	11.9	16.3
SP	0.28	4.2	10.2
SPZ	0.62	9.0	26.6
SPZH	0.34	5.1	7.2
SPZHC	0.49	6.5	18.1

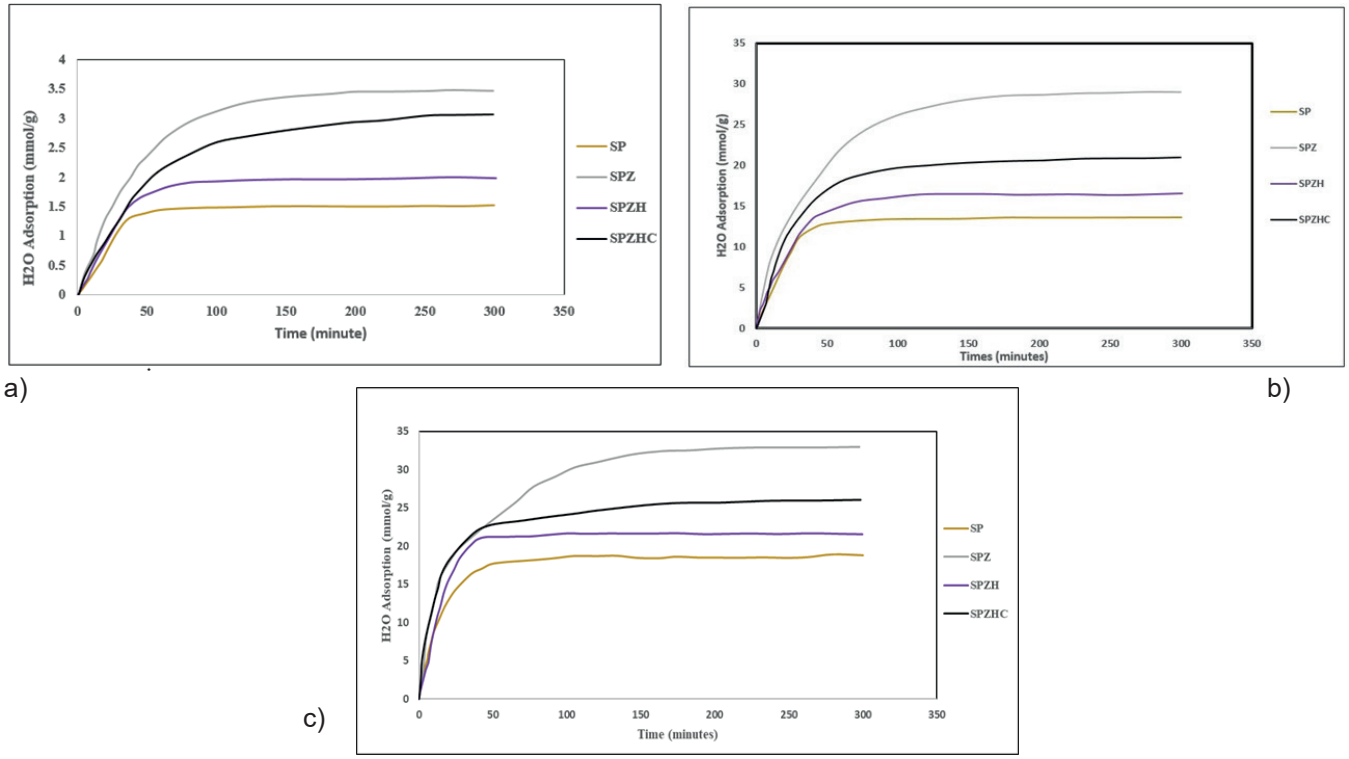


Fig 7. H_2O uptake SP, SPZ, SPZH, and SPZHC samples using DVS in 100% N_2, (a) 10% RH, (b) 50% RH, and (c) 95% RH at 25 °C.

The differences in CO_2/H_2O uptake were not significant among all samples at 50% and 95% RH (Table 4). Based on the previous results, the highest CO_2/H_2O ratio was observed for DPZHC, suggesting that it is a promising adsorbent for co-adsorption processes.

CO_2 adsorption capacities were collected from the literature and measured under different experimental conditions. H_2O adsorption is expressed qualitatively (e.g., low, moderate, high) because it strongly depends on relative humidity and temperature, making direct numerical comparison difficult. Additionally, most literature values are based on equilibrium measurements, whereas the present study reports kinetic adsorption (t = 10 min); therefore, direct comparison should be made with caution.

Table 4: CO_2 and H_2O adsorption capacities at 10% RH, 50% RH, and 95% RH, and the CO_2/H_2O ratio of the samples after 10 minutes.

Samples	CO_2 adsorption (mmol/g)	At 10% RH		At 50% RH		At 95% RH	
		H_2O uptake (mmol/g)	$S_{CO2/H2O}$	H_2O uptake (mmol/g)	$S_{CO2/H2O}$	H_2O uptake (mmol/g)	$S_{CO2/H2O}$
DP	1.03	0.56	1.84	6.72	0.15	10.61	0.1
DPZ	2.31	1.21	1.9	14.31	0.16	19.89	0.12
DPZH	1.57	0.52	1.23	6.95	0.23	8.49	0.18
DPZHC	2.01	0.93	3.01	11.23	0.18	16.31	0.12
SP	0.19	0.33	0.57	4.51	0.04	8.21	0.02
SPZ	1.32	0.63	2.09	8.33	0.16	13.92	0.09
SPZH	0.42	0.40	1.67	4.92	0.09	6.82	0.06
SPZHC	1.26	0.52	2.46	6.57	0.19	10.42	0.12

Table 5: Comparison of the CO^2 and H_2O adsorption performance of this study with that of previously reported adsorbents. CO_2 uptake is reported in mmol/g, while H_2O adsorption is presented qualitatively due to its dependence on relative humidity (RH).

Adsorbent	CO_2 uptake (mmol/g)	H_2O uptake	Selectivity/ uptake ratio (basis -dependent)	Basis of measurement
Activated carbon	1-3 (reported range)	moderate	moderate	equilibrium isotherm (batch)
Zeolite 13X	3-5 (equilibrium)	Very high	high	equilibrium adsorption
KOH-activated carbon	2-5	moderate	moderate-high	equilibrium adsorption
activated alumina	0.2-1	Very high	low	equilibrium adsorption
amine-functionalized carbon	2-4	low-moderate	high	equilibrium adsorption
Biomass-based carbon	0.5-2.5	moderate-high	low-moderate	equilibrium adsorption
DPZHC	2.01	0.93 mmol/g, at 10%RH	3.1 (Moderate to moderately high)	kinetic of adsorption (non equilibrium, t = 10 min)

Conclusions

One of the main challenges that CO_2 capture technology faces today is the efficiency of adsorbents, such as activated carbons, for CO_2 adsorption in the presence of water vapor. Water molecules strongly compete with CO_2 for the adsorbent's active sites because of their higher polarity and smaller size. Therefore, the CO_2/H_2O uptake ratio is an important parameter for evaluating the relative adsorption affinities of the prepared adsorbents toward CO_2 and water vapor under independent adsorption conditions, and for identifying promising materials for applications in humid environments.

The results of this study establish that both VTMOS-activated carbon produced from date pits and *Spirulina platensis*, synthesized through thermal treatment at 450 °C and designated as DPZHC and SPZHC, respectively, exhibit high CO_2/H_2O selectivity. The DPZHC sample exhibited higher CO_2 adsorption performance and hydrophobic properties, with CO_2/H_2O selectivity exceeding 3 at 10% RH. It is important to note that, as relative humidity increases to 50% and 95%, the CO_2/H_2O values become very low and approach zero, indicating that water vapor adsorption increases significantly with increasing relative humidity across all samples, and that the coating layers are not sufficiently thick. This study indicates that activated carbons, with their distinct structural characteristics, including high specific surface area, micro- and mesoporosity, and a thin VTMOS coating, can be used as hydrophobic adsorbents in CO_2 capture technology.

The CO_2/H_2O uptake ratio at higher relative humidities (50% and 95%) did not vary significantly across all samples, indicating that the adsorption sites on the adsorbents are mainly occupied by water molecules. Multilayer adsorption of water dominates the surface, blocking most of the active sites that would otherwise adsorb CO_2. Under the studied conditions, the relative CO_2/H_2O uptake is highly sensitive to surface modification and differences in porosity. This study also demonstrates that date pits and *Spirulina platensis* byproducts can serve as cost-effective sorbents for CO_2 removal from flue gas. Further investigations are needed to develop applications for these adsorbents and to address operational challenges at the pilot scale.

Acknowledgement

The authors would like to thank the Department of Chemical Engineering at the University of Basra, Iraq, for their technical support throughout this work.

References

Albazzaz, S. (2020). Understanding and minimising water vapour co-adsorption for activated carbons in post-combustion CO2 capture. Doctoral dissertation, The University of Nottingham, United Kingdom.

Albazzaz, S., Al-Saeedi, J.Y., Abbood, A.A., Mahmood, H.Y. & Mohammed, R.N. (2025). Application of activated carbon from jojoba seed residue in refinery wastewater treatment. *Environmental Research, Engineering and Management*, 81(4), pp. 79-92. DOI:10.5755/j01.erem.81.4.40346

Al-Harrasi, K., Al-Habsi, N., Al-Kindi, M.A., Shi, L., Suleria, H.A., Ashokkumar, M. & Rahman, M. S. (2025). Structural characterization of micronized lignocellulose date pits as affected by water sonication followed by alcoholic fractionations. *International Journal of Molecular Sciences*, 26(14), 6644. DOI:10.3390/ijms26146644

Bai, J., Kang, Y., Chen, M., Chen, Z., You, L., Li, X. & Chen, G. (2020). Impact of surface chemistry and pore structure on water vapor adsorption behavior in gas shale. *Chemical Engineering Journal*, 402, 126238. DOI: 10.1016/j.cej.2020.126238

Borisut, P., Tangsathitkulchai, C., Wongkoblap, A., Nuchitprasittichai, A. & Phothong, K. (2025). Carbon dioxide capture in NaOH impregnated activated carbon: simulation and experimental studies. *Adsorption*, 31(5), 82. DOI:10.1007/s10450-025-00633-4

Bouchemal, N. & Addoun, F. (2009). Adsorption of dyes from aqueous solution onto activated carbons prepared from date pits: The effect of adsorbents pore size distribution. *Desalination and Water Treatment*, 7(1-3), pp. 242-250. DOI:10.5004/dwt.2009.731

Duan, X.Y., Qian, Z. H., Tuo, Y. X., Gong, L. & Zhu, C.Y. (2023). Atomistic insights into the effect of functional groups on the adsorption of water by activated carbon for heat energy storage. *Molecules*, 29(1), 11. DOI:10.3390/molecules29010011

Jia, L., Niu, B., Jing, X. & Wu, Y. (2022). Equilibrium and hysteresis formation of water vapor adsorption on microporous adsorbents: Effect of adsorbent properties and temperature. *Journal of the Air & Waste Management Association*, 72(2), pp. 176-186. DOI:10.1080/10962247.2021.2011477

Kretzschmar, A., Selmert, V., Weinrich, H., Kungl, H., Tempel, H. & Eichel, R. A. (2021). Study of CO2 sorption kinetics on electrospun polyacrylonitrile-based carbon nanofibers. *Chemical Engineering & Technology*, 44(7), pp. 1168-1177. DOI:10.1002/ceat.202000463

Li, B., Hu, J., Xiong, H. & Xiao, Y. (2020). Application and properties of microporous carbons activated by ZnCl2: adsorption behavior and activation mechanism. *ACS Omega*, 5(16), pp. 9398-9407. DOI:10.1021/acsomega.0c00461

Li, B., Li, C., Li, D., Zhang, L., Zhang, S., Cui, Z. & Hu, X. (2023). Activation of pine needles with zinc chloride: Evolution of functionalities and structures of activated carbon versus increasing temperature. *Fuel Processing Technology*, 252, 107987. DOI:10.1016/j.fuproc.2023.107987

Liu, L., Jin, S., Park, Y., Park, Y.C. & Lee, C.H. (2018). Sorption equilibria and kinetics of CO2, N2 and H2O on KOH-treated activated carbon. *Industrial & Engineering Chemistry Research*, 57(50), pp. 17218-17225. DOI: 10.1021/acs.iecr.8b03862

Maceiras, R., Feijoo, J., Alfonsin, V., Alvarez-Feijoo, M.A. & Azofra, L. (2025). Enhanced CO2 adsorption for hydrogen purification using calcined zeolite: process analysis and kinetic study. *Microporous and Mesoporous Materials*, 113869. DOI:10.2139/ssrn.5309354

Martins, F.C.B., Chebbi, M., Monsanglant-Louvet, C., Marcillaud, B. & Roynette, A. (2025). Simulation of water vapor sorption profiles on activated carbons in the context of the nuclear industry. *Separations*, 12(5), 126. DOI:10.3390/separations12050126

Mashkhool, M. ., Azeez, N.M. & Abduljaleel, S.A. (2021). Monitoring of total hydrocarbons and particulate matters in AL Nasiriya City, South of Iraq. *University of Thi-Qar Journal of Science*, 8(2), pp. 6-10. DOI:10.32792/utq/utjsci/v8i2.805

Meng, L.Y. & Park, S.J. (2014). Effect of ZnCl2 activation on CO2 adsorption of N-doped nanoporous carbons from polypyrrole. *Journal of Solid State Chemistry*, 218, pp. 90-94. DOI: 10.1016/j.jssc.2014.06.005

Möller, E., Palm, R., Tuul, K., Härmas, M., Koppel, M., Aruväli, J. & Lust, E. (2023). Peat-derived ZnCl2-activated ultramicroporous carbon materials for hydrogen adsorption. *Nanomaterials*, 13(21), pp. 2883. DOI:10.3390/nano13212883

Mushtaq, K.J. & Alzurfi, S.K. (2023). Biochar and biochar magnetite of *Spirulina platensis* to remove cadmium ions from aqueous solutions. *Egyptian Academic Journal of Biological Sciences. C, Physiology and Molecular Biology*, 15(2), pp. 471-485. DOI:10.21608/eajbsc.2023.321788

Oumabady, S., Selvaraj, P.S., Kamaludeen, S.P., Ettiyagounder, P. & Suganya, K. (2021). Application of sludge-derived KOH-activated hydrochar in the adsorptive removal of orthophosphate. *RSC Advances*, 11(12), pp. 6535-6543. DOI:10.1039/d0ra10943f

Pustahija, L., Bandl, C., Alem, S.A.A. & Kern, W. (2024). Surface functionalization of activated carbon: Coupling of 3-(aminopropyl)trimethoxysilane and (3-glycidyloxypropyl) trimethoxysilane. *C – Journal of Carbon Research*, 10(4), 104. DOI:10.3390/c10040104

Querejeta, N., Plaza, M.G., Rubiera, F. & Pevida, C. (2016). Water vapor adsorption on biomass based carbons under post-combustion CO2 capture conditions: Effect of post-treatment. *Materials*, 9(5), 359. DOI:10.3390/ma9050359

Reddy, M.S.B., Ponnamma, D., Sadasivuni, K.K., Kumar, B. & Abdullah, A.M. (2021). Carbon dioxide adsorption based on porous materials. *RSC Advances*, 11, pp. 12658-12681. DOI:10.1039/D0RA10902A

Thommes, M., Kaneko, K., Neimark, A.V., Olivier, J.P., Rodriguez-Reinoso, F., Rouquerol, J. & Sing, K.S.W. (2015). Physisorption of gases, with special reference to the evaluation of surface area and pore size distribution (IUPAC Technical Report). *Pure and Applied Chemistry*, 87, pp. 1051-1069. DOI:10.1515/pac-2014-1117

Xie, K., Hu, Y., Afonaa-Mensah, S., Yuan, C., Cao, B., Wang, S. & Wang, Q. (2022). Study on preparation of nitrogen-doped hierarchically porous and high-performance carbon materials from seaweed biomass. *Journal of Renewable Materials*, 10(2), pp. 541. DOI:10.32604/jrm.2022.017911

Yang, L. & Yuan, Y. (2025). Functional group characteristics of coal treated with clean biomass surfactant via FTIR spectroscopy. *Scientific Reports*, 15(1), pp. 18676. DOI:10.1038/s41598-025-03769-z

Yu, Z., Liu, B., Li, Z., Liu, T. & Su, G. (2022). Biochar by *Spirulina platensis* promotes the antifouling effect of Cu2O in styrene-acrylic resin coating. *Progress in Organic Coatings*, 168, 106891. DOI: 10.1016/j.porgcoat.2022.106891

Zhang, Q., Huang, Y., Xia, D., Hu, L., Li, P., Tan, L. & Xie, X. (2019). High-performance water desalination of heteroatom nitrogen- and sulfur-codoped open hollow tubular porous carbon electrodes via capacitive deionization. *Environmental Science: Nano*, 6(11), pp. 3359-3373. DOI:10.1039/C9EN00794F

Zheng, C., Song, H., Xie, Y., Yang, X., Lan, L., Kang, K. & Bai, S. (2023). Modeling of multi-temperature IV and V-type water vapor adsorption isotherms on activated carbons for chemical protection. *Colloids and Surfaces A: Physicochemical and Engineering Aspects*, 670, 131486. DOI: 10.1016/j.colsurfa.2023.131486

Archives of Environmental Protection
Vol. 52 no. 3 pp. 88–99

PL ISSN 2083-4772
DOI: 10.24425/aep.2026.3686



© 2026. The Author(s). This is an open-access article distributed under the terms of the Creative Commons Attribution-ShareAlike 4.0 International Public License (CC BY SA 4.0, https:// creativecommons.org/licenses/by-sa/4.0/legalcode), which permits use, distribution, and reproduction in any medium, provided that the article is properly cited.

Development of a low-cost dissolved oxygen estimation model using calibrated Arduino-based sensors

Merve Sürmen[1]*, Mehmet Kazım Yetik[2]

[1] Institute of Science, Karabük University, Karabük, Turkey
[2] Department of Environmental Engineering, Karabük University, Karabük, Turkey

*Corresponding author's e-mails: mervesurmenn@gmail.com

Keywords: water quality; environmental monitoring; dissolved oxygen; sensor technology

Abstract: Conventional river water quality monitoring is often constrained by high operational costs and maintenance-intensive sensors. To address these limitations, this study proposes a low-cost framework for estimating dissolved oxygen (DO) concentrations without direct DO probes by deploying an Arduino-based multi-sensor array (pH, temperature, and turbidity) coupled with multivariate regression modeling. The baseline model was calibrated using laboratory experimental data and subsequently validated under field conditions in the Kızılırmak River, Turkey (N=19). The proposed framework demonstrated high predictive accuracy, yielding a coefficient of determination (R^2) of 0.842, a Leave-One-Out Cross-Validation (LOOCV,Q^2) score of 0.798, a Mean Absolute Percentage Error (MAPE) of 4.91%, and a Mean Squared Error (MSE) of 1.64. The primary novelty lies in substituting expensive optical DO probes with robust proxy sensors integrated into a computationally lightweight model suitable for edge-computing IoT nodes. Serving as a foundational proof-of-concept, the developed regression coefficients are site-specific and require localized re-calibration (15–20 paired samples) prior to deployment in distinct catchment basins. Overall, this framework offers a scalable, cost-effective solution for continuous environmental impact assessment and sustainable water resource management.

Introduction

Effective water resource management increasingly depends on timely, accurate, and spatially distributed water quality data. Conventional monitoring approaches based on periodic sampling and laboratory analysis often fail to capture short-term variations and localized pollution events, limiting their usefulness for real-time decision-making and adaptive water management (Hart & Martinez, 2006; Loucks et al., 2005). In addition, the high operational costs, labor requirements, and limited temporal resolution of traditional monitoring programs restrict their applicability, particularly in long-term and large-scale river monitoring studies.

In response to these limitations, hydroinformatics has emerged as a multidisciplinary field that integrates sensing technologies, data acquisition systems, information processing tools, and analytical models to support data-driven water resources management (Abbott, 1999; Abrahart et al., 2008; Solomatine and Ostfeld, 2008). Recent advances in Internet of Things (IoT) Technologies have enabled the deployment of distributed sensor networks for continuous and real-time monitoring, offering improved temporal resolution, enhanced spatial coverage, and reduced operational costs. Key physicochemical parameters such as temperature, pH, and turbidity are fundamental indicators of aquatic ecosystem health and are widely used to evaluate freshwater quality. Temperature directly influences dissolved oxygen solubility according to Henry's law, whereas pH and turbidity reflect the biological and optical characteristics of aquatic environments. These parameters exhibit well-established relationships with dissolved oxygen (DO), a critical indicator of river water quality that influences aquatic life and biogeochemical processes. Recent developments in hydroinformatics have further enhanced the integration of environmental sensing, statistical modelling, and intelligent decision-support systems, enabling continuous and data-driven water quality assessment (Abrahart et al., 2008; Solomatine and Ostfeld, 2008). These technological developments have significantly improved the feasibility of low-cost and continuous environmental monitoring, providing practical alternatives to conventional laboratory-based approaches.

Despite the importance of DO, continuous monitoring is often constrained by the high cost and maintenance requirements of specialized electrochemical sensors, which are highly sensitive to environmental factors and biofouling. Accordingly, alternative approaches that estimate DO using more easily measurable parameters have gained increasing attention. Environmental Impact Assessment (EIA) processes rely heavily on accurate data to evaluate anthropogenic impacts; however, insufficient monitoring frequency often leads to incomplete assessments, increasing the risk of undetected

environmental degradation (Glasson et al., 2013; Noble, 2015). Previous studies have demonstrated that parameters such as temperature, pH, and turbidity can be utilized within multivariate statistical models to predict DO concentrations, effectively bridging the gap between low-cost sensing and robust analytical requirements (Abyaneh, 2014; Tripathi & Singal, 2019). Therefore, the development of reliable and low-cost approaches for indirect DO estimation has become an important research topic in hydroinformatics and smart water quality monitoring.

To address these challenges, this study presents the design and field validation of an integrated, low-cost, multi-sensor empirical framework for continuous dissolved oxygen (DO) estimation without direct DO instrumentation. The main contribution and novelty of this work lies in bypassing expensive and maintenance-intensive optical or galvanic DO probes by utilizing calibrated, highly robust, and low-cost proxy sensors, specifically pH, water temperature, and turbidity. Furthermore, this study provides a fully validated methodology that seamlessly couples controlled laboratory calibration with real-world field verification in the Kızılırmak River, demonstrating high predictive stability across different conditions. Finally, the proposed framework provides a computationally lightweight and transparent multivariate regression approach that is inherently suitable for direct deployment on low-cost IoT nodes and microcontroller-based edge computing systems, bridging the gap between hardware limitations and continuous environmental decision support.

Materials and methods

The assessment of river water quality is commonly conducted through the monitoring of physicochemical parameters that reflect the overall condition of aquatic environments. In this study, a low-cost Arduino-based monitoring system was developed to measure selected water quality parameters and estimate dissolved oxygen (DO) concentrations through statistical modeling. The methodological framework consists of sensor-based data acquisition, laboratory calibration of sensor outputs, and the development of a multivariate regression model using calibrated measurements. The monitoring system was constructed using an Arduino Mega 2560 microcontroller board, selected for its compatibility with multiple analog and digital sensors and its suitability for real-time data acquisition applications. Three water quality parameters, i.e., pH, temperature, and turbidity, were measured using cost-effective sensors integrated into the Arduino platform. These parameters were selected due to their widespread use in water quality assessment and their established relationships with dissolved oxygen concentrations. The complete hardware architecture, sensor connection scheme, and power supply configuration are illustrated in the schematic diagram (Fig. 1), which also includes the system workflow diagram.

pH measurements were obtained using an analog pH sensor (DFRobot SEN0161) connected via a Bayonet Neill-Concelman (BNC) interface. Laboratory calibration was performed using buffer solutions prepared with hydrochloric acid (HCl) and sodium hydroxide (NaOH) to cover a wide pH range. Reference measurements were obtained using a SevenCompact S220 pH meter, and a linear calibration equation was derived by comparing the sensor outputs with reference values.

Water temperature was measured using a DS18B20 digital temperature sensor operating within a range of −10 °C to +85 °C, with an accuracy of ±0.5 °C. Data acquisition was carried out using the OneWire and DallasTemperature libraries in the Arduino environment. Calibration experiments were conducted using a WTW Cond 3110 conductivity meter as a reference instrument, and a linear calibration relationship was established.

Turbidity measurements were carried out using a DFRobot SEN0189 turbidity sensor, which determines turbidity based on light transmittance through the water sample. Sensor output voltages were recorded and converted to nephelometric turbidity units (NTU). Laboratory calibration was conducted using a VELP TB1 turbidimeter, and a voltage–NTU calibration equation was obtained.

To ensure strict experimental reproducibility of the data acquisition protocol, calibration for each sensor was performed using five distinct calibration points covering the operational environmental range of the river system. At each calibration point, measurements were conducted in triplicate to minimize random environmental errors. The data acquisition frequency of the Arduino Mega 2560 microcontroller was set to 1 Hz (one reading per second). A stabilization time of 3 minutes was observed before recording the final measurement at each reference point. Data points falling outside three standard deviations from the dataset mean were considered outliers caused by electrical noise and were excluded from the calibration criteria.

Linear regression analysis was applied to establish calibration equations for each parameter. Calibration performance was evaluated using mean absolute percentage error (MAPE) and mean squared error (MSE).

To rigorously assess model generalization and prevent overfitting or optimistic accuracy estimation, data partitioning was strictly enforced between model training and validation phases. The training dataset comprised laboratory-controlled experimental observations (N = 19), summarized in Table 3, which were utilized exclusively to derive the multivariate linear regression coefficients via ordinary least squares (OLS). Conversely, an entirely independent validation dataset, collected from real-world field monitoring at the Kızılırmak River (Supplementary Table S2), was reserved solely for evaluating the predictive capability and robustness of the pre-trained model under actual field conditions. Furthermore, given the compact sample size, a Leave-One-Out Cross-Validation (LOOCV) procedure was performed on the training set to evaluate structural stability. The resulting cross-validation Root Mean Squared Error ($RMSE_{CV}$ = 1.31 mg/L) and Cross-Validated Coefficient of Determination (Q^2 = 0.798) closely aligned with the primary model statistics, confirming that the regression model is robust and not subject to overfitting.

Following sensor calibration, a multivariate linear regression model was developed to estimate dissolved oxygen (DO) concentrations using calibrated pH, temperature, and turbidity values as independent variables. The laboratory dataset summarized in Table 3 was used as the training dataset, with experimentally measured DO concentrations serving as the dependent variable. Regression coefficients were estimated using the ordinary

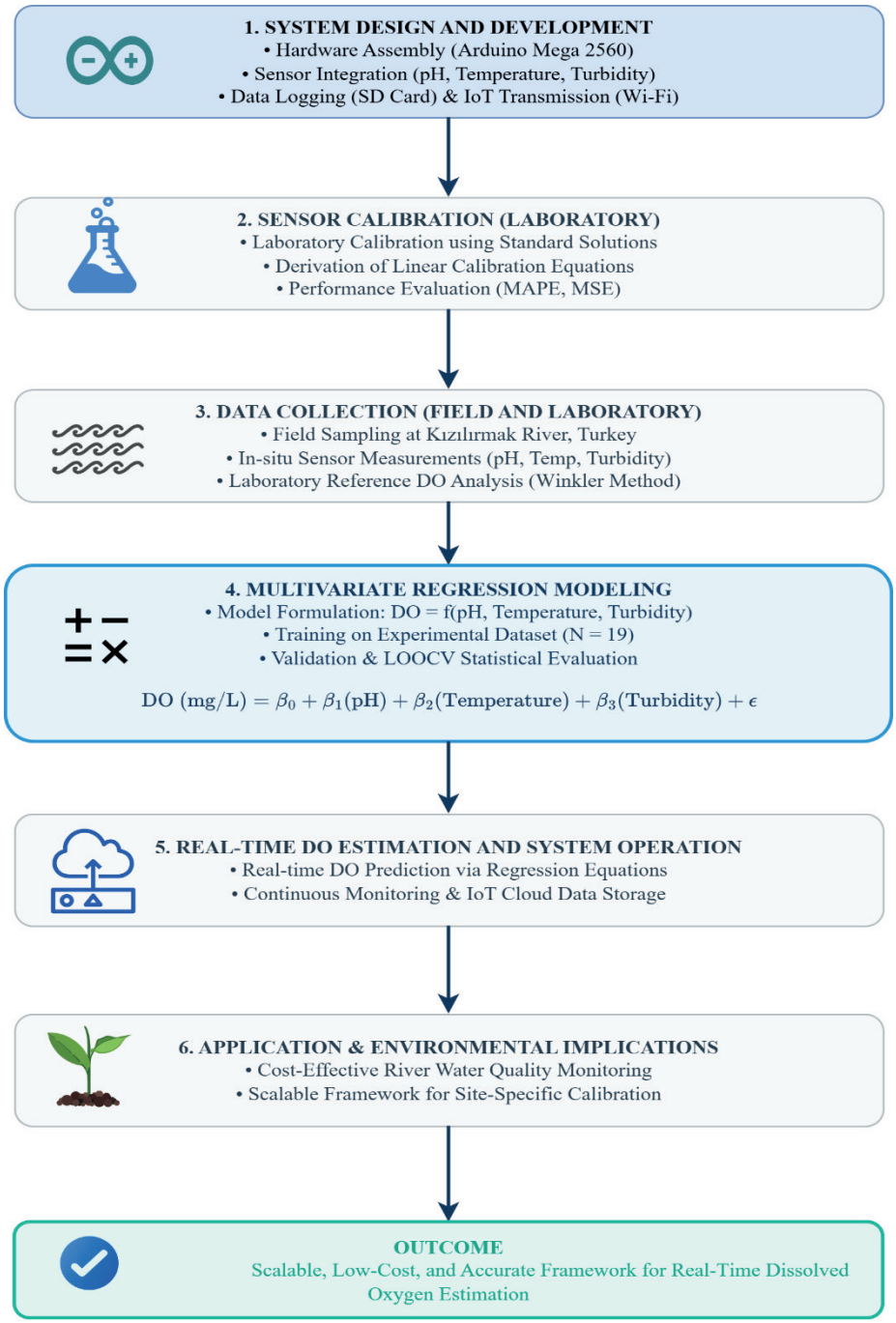


Fig 1. Overall workflow of the proposed Arduino-based water quality monitoring framework, illustrating field sampling at the Kızılırmak River, laboratory reference DO analysis via the Winkler method, multivariate regression modeling with LOOCV validation, real-time IoT cloud-based DO estimation, and its practical environmental applications.

least squares (OLS) method, and the resulting model was subsequently validated using an independent field dataset collected from the Kızılırmak River. Statistical analyses and model development were conducted using Minitab, MATLAB, and Microsoft Excel software.

Since dissolved oxygen concentration was estimated indirectly from multiple independent sensor inputs (pH, temperature, and turbidity), the propagation of measurement uncertainties to the final DO prediction was systematically evaluated. Assuming that the input variables were uncorrelated, the combined standard uncertainty of the DO prediction (u_{DO}) was calculated using the root-sum-square (RSS) error propagation method. The uncertainty propagation equation based on the regression coefficients is presented in Equation

$$u_{DO} = \sqrt{(1.414 \cdot u_{pH})^2 + (0.303 \cdot u_T)^2 + (0.028 \cdot u_{Turb})^2} \quad (1):$$

where u_{pH}, uT and u_{Turb}, denote the standard uncertainties associated with the calibrated pH, temperature, and turbidity measurements, respectively. These uncertainties were derived from the individual sensor calibration Mean Squared Errors presented in Table 8.

Results

The pH calibration results were obtained by comparing the raw voltage outputs of the developed sensor with laboratory reference measurements obtained from a SevenCompact S220 pH meter. The statistical summary and error metrics of this calibration dataset are summarized in Table 1. Based on linear regression analysis, the empirical calibration equation used to convert the raw analog sensor voltage into the corrected pH value was derived as follows:

$$p_H = 3.56 \cdot V_{pH} + 0.24 \quad (2)$$

where V_{pH} represents the raw analog output voltage obtained from the DFRobot SEN0161 sensor.

The predictive performance of this calibration model was evaluated using relative error analysis. The relative error ranged from −13.03% to −0.22%, with a variance of 8.12, indicating good agreement between the calibrated sensor outputs and the reference measurements (Table 1). Furthermore, to validate the practical field performance of the calibrated model, the sensor outputs were compared with real-world environmental measurement data obtained from the State Hydraulic Works (DSİ). The high degree of linearity and agreement, as well as the distribution of relative errors between the DSİ reference values and the calibrated sensor outputs, are clearly illustrated in Fig. 2.

Water temperature was selected as a primary predictor because it exerts a fundamental physical control on dissolved oxygen (DO) dynamics; specifically, gas solubility in water decreases nonlinearly as temperature increases, following Henry's law. The calibration results for water temperature measurements were obtained by comparing the raw outputs of the digital temperature sensor with laboratory reference values obtained using a WTW Cond 3110 conductivity meter. To ensure reproducibility, calibration experiments were carried out across 19 independent temperature points, with three distinct replicates per point with a fixed stabilization time of 5 minutes before recording each data acquisition sequence.

The detailed statistical properties and error metrics of this temperature calibration dataset are presented in Table 2. A linear calibration relationship was established using regression analysis and is given as Equation (3):

$$\text{Temperature (°C)} = 0.984 \cdot \text{sensor}_T + 0.686 \quad (3)$$

where sensor_T represents the raw digital output obtained from the DS18B20 temperature sensor. The predictive performance of this model was systematically evaluated using relative error analysis to assess the error distribution. The relative error varied between −0.96% and 3.85%, with a variance of 2.47, confirming the reliability of the calibration model and its close agreement with the reference measurements (Table 2).

Furthermore, to validate the practical field performance of the calibrated temperature model under real environmental conditions, the sensor outputs were compared with independent reference data obtained from the State Hydraulic Works (DSİ). The high accuracy and thermal stability, as well as the distribution of relative errors between the DSİ reference values and the calibrated sensor outputs, are clearly illustrated in Fig. 3. While the model shows excellent linear agreement, practical field limitations during continuous monitoring include potential sensor drift and biofouling, which necessitate regular maintenance and biweekly local calibration intervals.

Turbidity measurements were carried out using a DFRobot SEN0189 turbidity sensor, which determines turbidity based on light transmittance through the water sample. The laboratory calibration was performed using a VELP TB1 turbidimeter to measure turbidity in Nephelometric Turbidity Units (NTU). The detailed statistical properties and error metrics of this calibration dataset are presented in Table 3. A linear calibration relationship was established using regression analysis and is expressed as Equation (4):

$$\text{NTU} = -652.747 \cdot \text{sensor}_{\text{NTU}} + 2145 \quad (4)$$

where Turb_{raw} represents the raw voltage output of the DFRobot SEN0189 turbidity sensor, and Turb denotes the calibrated turbidity value expressed in Nephelometric Turbidity Units (NTU).

The statistical consistency between the reference measurements and the calibrated sensor outputs is presented in Fig. 4, while a summary of these measurements is provided in Table 3. Furthermore, the distribution of calibration errors is detailed in Table 4, demonstrating the performance variations across the tested turbidity range.

The correlation coefficients between dissolved oxygen (DO) and the independent water quality parameters, pH, temperature, and turbidity, are summarized in Table 5. These statistical values, derived from the experimental dataset, reveal positive correlations between DO and both pH (r = 0.417) and turbidity (r = 0.362), while a significant negative correlation is observed between DO and temperature (r = 0.599). These findings are consistent with established limnological processes: the negative correlation with temperature is driven by the physical reduction in gas solubility in warmer waters, while the positive correlation with pH and turbidity reflects the interplay between photosynthetic oxygen production and the light-attenuation characteristics of the water column. Specifically, the inclusion of turbidity as a covariate in the regression model is important, as it accounts for the optical conditions that influence the depth of the euphotic zone and, consequently, the oxygen dynamics of the river system.

Following the individual sensor calibrations, a multivariate linear regression model was developed using the ordinary least squares (OLS) method to estimate dissolved oxygen (DO) concentrations based on calibrated pH, temperature, and turbidity values. The derived multivariate regression model is expressed in Equation (5):

Table 1: Comparison of reference pH measurements and calibrated pH sensor outputs with relative error distribution.

Parameter / Source	MAX	MIN	VAR
Seven Compact S220 pH meter	13.59	4.22	8.91
DF Robot SEN0161 pH sensor	13.98	4.77	9.05
Model	13.59	4.46	8.89
Relative Error Distribution (%)	28.5	-13.03	8.12

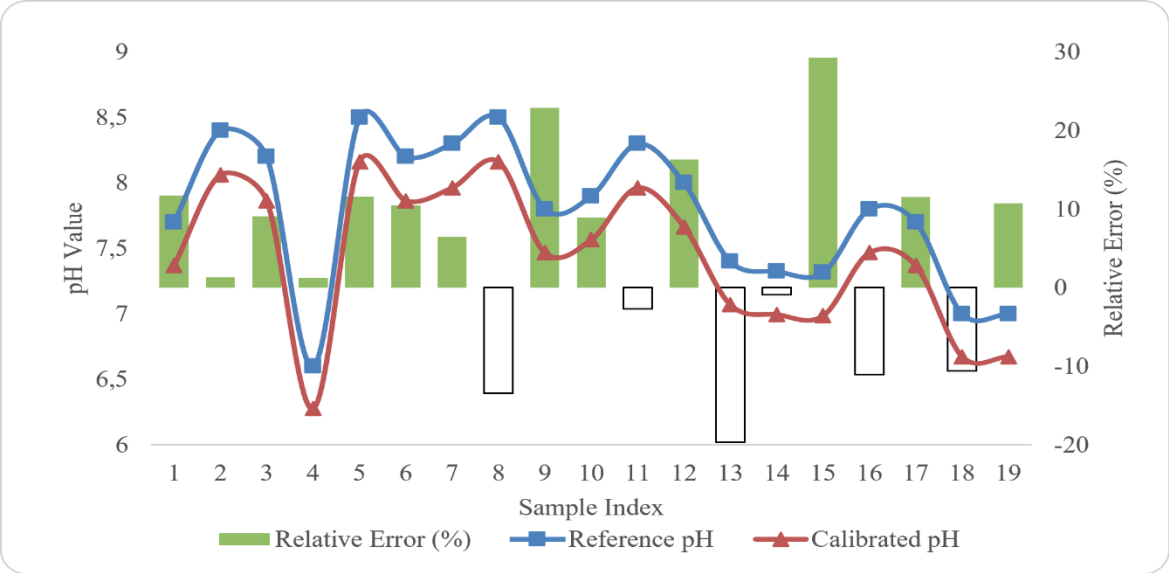


Fig 2. Comparison of reference pH measurements and calibrated pH sensor outputs with relative error distribution.

$$DO = 2.499 + 1.414 \cdot pH - 0.303 \cdot T + 0.028 \cdot Turbidity \quad (5)$$

A comprehensive statistical evaluation of the regression model parameters, including regression coefficients, standard errors, *t*-statistics, *p*-values, 95% confidence intervals, coefficient of determination (R^2), adjusted R^2, and *F*-statistic, is summarized in Table 9.

Model Overall Statistics:

Sample size (N): 19

Coefficient of determination (R^2): 0.842 (or 84.2%)

Adjusted R^2 (R^2_{adj}): 0.810 (or 81.0%)

Standard error of the estimate (*S*): 0.621 mg/L

F-Statistic: 26.65 ($p < 0.001$)

The model demonstrated a high overall goodness of fit, explaining 84.2 % of the variance in dissolved oxygen concentrations (R^2 = 0.842, R^2_{adj} = 0.810) with a statistically significant overall regression relationship (F = 26,64, p < 0.001). All three independent variables contributed significantly to the prediction model at the 95% confidence level ($p < 0.05$). Specifically, water temperature exhibited a strong negative relationship with β = –0.303, $p < 0.001$, strictly adhering to thermodynamic oxygen solubility laws. Conversely, pH (β = 1.414, p = 0.001) and turbidity (β =0.028, p = 0.034) yielded positive regression coefficients, reflecting the biochemical and optical influences on dissolved oxygen dynamics within the aquatic system. To rigorously assess model stability and rule out overfitting resulting from sample size constraints, a Leave-One-Out Cross-Validation (LOOCV) procedure was implemented. The cross-validated coefficient of determination (Q^2) was computed using the Prediction Residual Sum of Squares (PRESS) metric according to Equation (6):

$$Q^2 = 1 - \frac{PRESS}{TSS} = 1 - \frac{\sum_{i=1}^{N} (y_i - y_{i,(-i)})^2}{\sum_{i=1}^{N} (y_i - y)^2} = 0.798$$

where y_i represents the observed dissolved oxygen concentration, $y_{i,(-i)}$ is the predicted value obtained from the model calibrated excluding the *i*-th observation, y is the sample mean, and N = 19 denotes the sample size. The high agreement between the cross-validated goodness-of-fit (Q^2 = 0.798) and the primary coefficient of determination (R^2 = 0.842) confirms that the regression model is structurally robust and maintains high generalization performance without overfitting.

The predictive performance of the developed regression model was evaluated using an independent validation dataset collected from the Kızılırmak River. The out-of-sample evaluation was conducted using field data that were not involved in the coefficient estimation process. Predicted DO concentrations were compared with experimentally measured values, and the resulting error distribution is summarized in Table 10.

The model achieved a Mean Absolute Percentage Error (MAPE) of 4.91% and a Mean Squared Error (MSE) of 1.64 mg^2/L^2 on this independent validation set. The strong agreement between the predicted and observed DO values (Q^2_{Loo} = 0.798)

Table 2: Comparison of reference temperature measurements and calibrated temperature sensor outputs with relative error distribution.

Parameter / Source	MAX	MIN	VAR
WTW Cond 3110 Conductivity Meter	77.5	10.2	408.28
DS18B20 Temperature sensor	77.90	9.9	412.99
Model	77.3	10.42	408.23
Relative Error Distribution (%)	3.85	-0.96	2.47

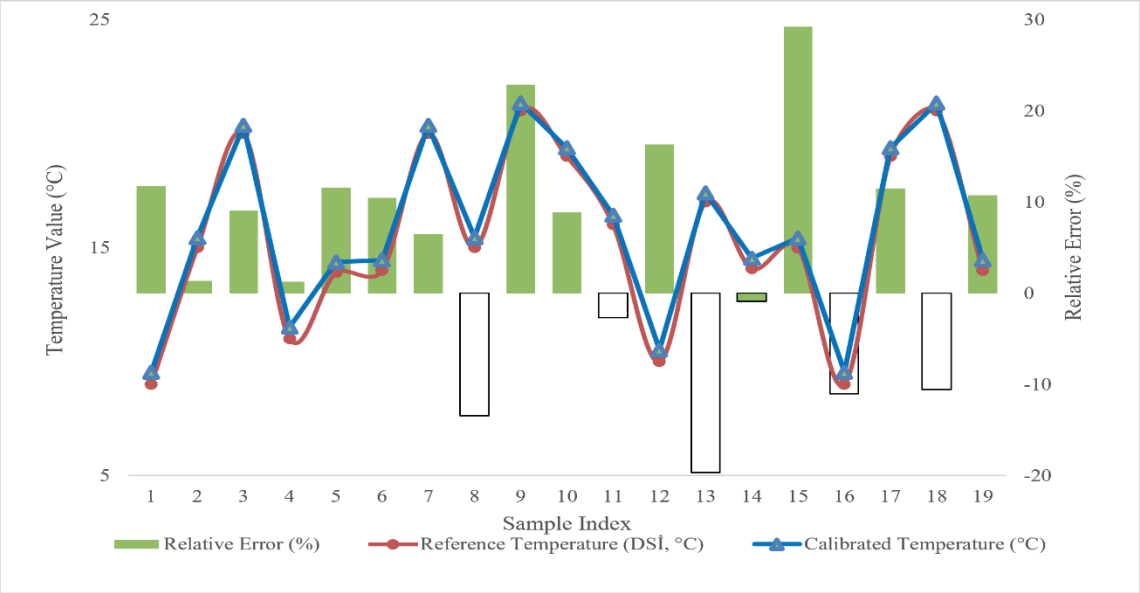


Fig 3. Comparison of reference temperature measurements and calibrated temperature sensor outputs with relative error distribution.

demonstrates that the low-cost sensor framework maintains high predictive performance when applied to external environmental datasets. A summary of the model performance metrics is presented in Table 10, while the full point-by-point error analysis for all field samples is detailed in Supplementary Table S1. The graphical agreement between the measured and predicted DO concentrations is illustrated in Fig. 5.

To assess the operational robustness of the proposed framework, two distinct prediction scenarios were evaluated against the measured reference DO values: (i) model predictions using State Hydraulic Works (DSİ) reference instrumentation inputs, and (ii) model predictions using input values directly measured by the calibrated Arduino sensor array. Table 11 presents the comparative statistical summary of these estimation scenarios, whereas the complete sample-by-sample data matrix of sensor readings and model outputs is documented in Supplementary Table S2. The mean predicted DO value using Arduino sensor inputs (8.64 mg/L) closely matched the measured DO concentration (9.18 mg/L) and the prediction based on DSİ reference inputs (9.24 mg/L). Table 11. Statistical summary comparing measured dissolved oxygen (DO) concentrations with model predictions derived from reference inputs (DSİ) and calibrated Arduino sensor inputs. Complete sample-by-sample observation data are available in Supplementary Table S2.

Discussion

The performance analysis of the developed sensor system demonstrates high accuracy for pH and temperature measurements, characterized by strong correlation coefficients and minimal error metrics. However, the turbidity sensor exhibited a higher MAPE (21.82%). This discrepancy is primarily attributed to the inherent sensitivity of the DFRobot SEN0189 sensor to optical threshold effects. In low-particle environments, light-scattering effects become non-linear, which complicates calibration consistency. Furthermore, this optical performance is susceptible to environmental factors such as biofilm accumulation (biofouling) on the sensor lens, which acts as a secondary scattering source and causes signal attenuation over time.

The integration of the multivariate regression model (Equation 5) played an important role in accounting for individual sensor errors. By incorporating pH, temperature, and turbidity as independent variables, the model effectively mitigated the cross-correlation errors between parameters. The positive contribution of turbidity suggests that suspended solids provide complementary information associated with light attenuation and aquatic environmental dynamics, thereby improving the predictive capability of the multivariate model. As a result, the proposed framework achieved an overall MAPE of 4.91% and an MSE of 1.64, indicating satisfactory predictive performance for continuous river water quality monitoring.

Table 3: Statistical summary of the training dataset used for dissolved oxygen prediction.

Parameter	DO (mg/L)	pH	T (°)	Turb (NTU)
Max	12.8	8.5	21	19.6
Min	5.1	6.6	9	0.4
Mean	9.081984	7.786304064	15.42001	8.905514456
Var	3.37138	0.309305032	15.14886	30.00486022

Table 4: Statistical summary of turbidity sensor calibration error distribution.

Metric	Relative Error (%)
Maximum Relative Error	8.24
Minimum Relative Error	-1.15
Variance of Errors	5.82

Table 5: Correlation coefficients between dissolved oxygen and independent water quality parameters.

Correlation	pH	Temperature (°C)	Turbidity (NTU)
DO	0.416922	-0.599055524	0.361526

The predictive performance obtained in this study is consistent with previous studies demonstrating the effectiveness of multivariate statistical approaches for water quality prediction. Similar findings were reported by Abyaneh (2014), who demonstrated that multivariate linear regression can successfully estimate water quality parameters using multiple physicochemical variables. Likewise, multivariate statistical techniques have been shown to improve the interpretation and prediction of water quality compared with conventional single-parameter approaches (Maiolo and Pantusa, 2021; Isaac and Siddiqui, 2022). The obtained MAPE value of 4.91% indicates that the proposed regression model provides competitive predictive performance while using only low-cost sensors and an Arduino-based monitoring platform. Compared with previously reported hydroinformatic monitoring frameworks, the proposed methodology offers a practical and economically attractive alternative for continuous environmental monitoring without requiring dedicated dissolved oxygen instrumentation (Abbott, 1999; Solomatine and Ostfeld, 2008). These findings indicate that the proposed multivariate regression model provides reliable dissolved oxygen estimation while maintaining the economic advantages of a low-cost sensing platform, demonstrating that reliable dissolved oxygen prediction can be achieved without direct dissolved oxygen measurements.

Despite these promising results, the practical deployment of this low-cost system under field conditions entails several limitations. Sensor drift, particularly in the pH and turbidity sensors, is an inevitable challenge in long-term environmental monitoring. Consequently, periodic recalibration and regular maintenance, including cleaning of optical sensor surfaces to minimize biofouling, are necessary to maintain measurement reliability. Similar operational challenges have also been reported for low-cost Arduino-based water quality monitoring systems (Alimorong et al., 2020; Kamboj et al., 2021).

Another important limitation of this study is that the developed regression coefficients are specific to the Kızılırmak River dataset used for model training. Since physicochemical characteristics vary among aquatic ecosystems depending on geological, climatic, and anthropogenic conditions, the proposed regression equation should be recalibrated before being applied to different rivers or reservoirs. Nevertheless, the methodological framework remains transferable to other freshwater environments, provided that representative, site-specific calibration and training datasets are collected (Tripathi and Singal, 2019; Liu et al., 2021).

A primary limitation of the present study is the relatively compact sample size (N = 19) utilized for model calibration and field evaluation. While the statistical diagnostics (R^2 = 0.842, Q^2 = 0.798) and Leave-One-Out Cross-Validation (LOOCV) confirm the structural stability of the regression model, an N = 19 dataset inherently captures a snapshot of localized hydrological and meteorological conditions. Consequently, extreme environmental events such as rapid thermal stratification, flash flood turbidity spikes, or seasonal algal blooms may introduce non-linear response dynamics that are not fully encompassed by the current linear formulation. Therefore, this work should be interpreted as a foundational

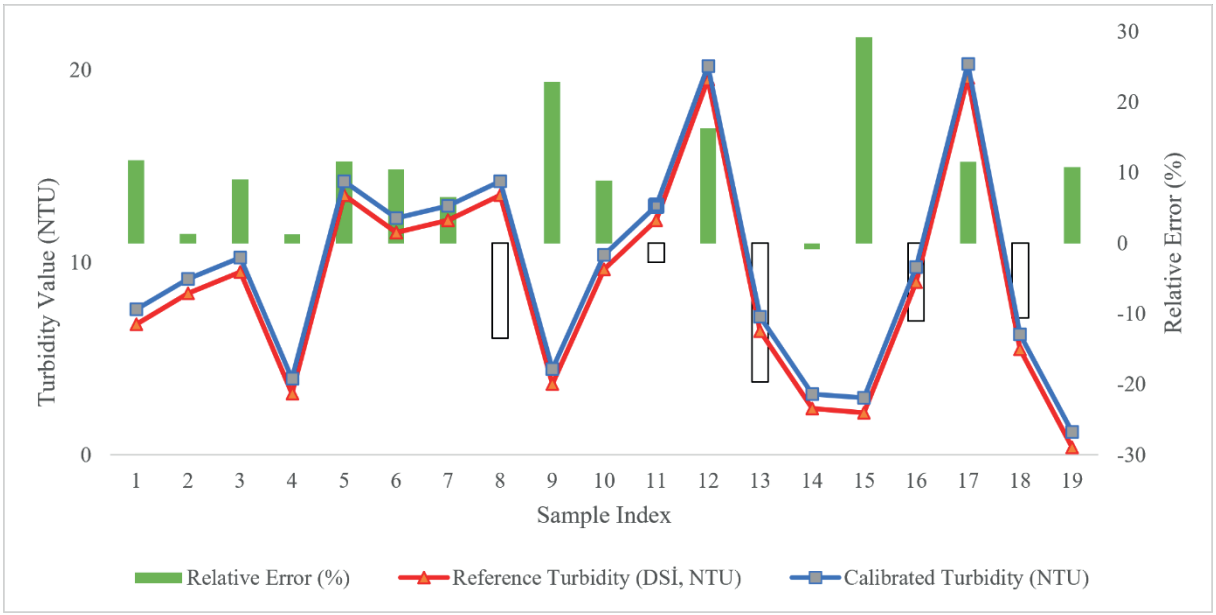


Fig 4. Comparison of reference turbidity measurements and calibrated sensor outputs with relative error distribution.

Table 6: Linear calibration equations and sensor coefficients.

Parameter	Slope	Intercept	Equation
pH	0.99	-0.263	$ph = 0.991 \cdot pH_{raw} - 0.263$
T(°C)	0.98	0.686	$T = 0.984 \cdot T_{raw} + 0.686$
Turb (NTU)	-652.747	2145	$T_{urb} = 652.747 \cdot Turb_{raw} + 2145$

initial validation study demonstrating the viability of replacing direct, high-maintenance dissolved oxygen (DO) probes with calibrated multi-sensor arrays (pH, temperature, and turbidity) and empirical modeling. To reduce parameter uncertainty and broaden regional applicability, future iterations of this monitoring framework will incorporate continuous multi-seasonal data collection across varying flow regimes and extended geographical river cross-sections.

Furthermore, empirical regression coefficients derived in environmental modeling are inherently site-specific, reflecting the distinct biochemical composition, reaeration rates, and thermal regimes of the target water body. Consequently, the specific coefficient magnitudes reported in Equation (5)

($DO = 2.499 + 1.414 \cdot \text{pH} - 0.303 \cdot T + 0.028 \cdot Turbidity$)

are tailored to the hydrodynamic conditions of the Kızılırmak River basin and should not be directly applied to disparate aquatic systems without re-calibration. However, the core contribution of this work lies in the reproducible methodological calibration framework rather than static equation parameters. To transfer this low-cost DO estimation framework to alternative river systems or distinct catchment basins, a standardized local calibration protocol should be adopted. Specifically, a local sampling campaign consisting of a minimum of 15–20 paired observations covering typical diurnal thermal variations and turbidity fluctuations should be conducted, followed by the re-execution of Ordinary Least Squares (OLS) regression to adjust the baseline intercept (β_0) and partial slopes (β_{pH}, β_T, βT_{urb}). In regions experiencing pronounced seasonal shifts, such as severe winter ice cover or summer eutrophication, semi-annual coefficient re-estimation is advisable to properly account for changes in biological oxygen demand (BOD) dynamics.

Future studies should focus on implementing autonomous drift-compensation algorithms, expanding the training dataset under different seasonal conditions, integrating IoT-based real-time monitoring systems, and evaluating advanced machine-learning algorithms to further improve predictive accuracy. Such developments would enhance the applicability of the proposed framework for long-term environmental monitoring and environmental impact assessment.

Conclusions

This study demonstrated that reliable river water quality monitoring can be achieved using a low-cost Arduino-based sensor framework combined with multivariate regression modeling. The proposed system effectively estimated dissolved oxygen (DO) concentrations without direct DO measurement, yielding strong predictive accuracy defined by a coefficient of determination (R^2) of 0.842, a Leave-One-Out Cross-Validation (Q^2) score of 0.798, a Mean Absolute Percentage Error (MAPE) of 4.91%, and a Mean Squared Error (MSE) of 1.64. Experimental validation confirmed that these performance metrics indicate the potential suitability of the proposed framework for continuous environmental monitoring while reducing operational costs compared with conventional monitoring approaches.

Individual sensor calibration performance was rigorously quantified, with the pH and temperature sensors exhibiting high accuracy (MAPE < 5%). While the turbidity sensor showed a higher calibration error (MAPE of 21.82%) due to optical sensitivity constraints, its integration into the multivariate model proved essential for capturing the complex environmental dynamics of the river. The results confirm that unmeasured water quality parameters can be successfully estimated using statistically robust models based on easily measurable, low-cost variables.

As a proof-of-concept study based on a localized dataset (N = 19), the developed regression coefficients are inherently specific to the Kızılırmak River. Nevertheless, the methodological framework is fully transferable to other aquatic systems, provided that localized re-calibration protocols utilizing representative baseline datasets of 15–20 paired observations are implemented. Future research should prioritize enhancing sensor longevity through automated drift compensation, improving field-based maintenance protocols to mitigate biofouling, and integrating real-time IoT data transmission modules. Ultimately, this framework provides a practical and scalable solution for environmental impact assessment, supporting proactive decision-making for sustainable water resource management.

Table 7: Correlation coefficients between calibrated sensor outputs and reference measurements.

Parameter and Calibration Model	Correlation
pH meter and sensor value	0.998748403
Correlation T and T sensor	0.999937548
Correlation turbidity sensor	-0.998253773

Table 8: Calibration performance metrics (MAPE and MSE) for pH, temperature, and turbidity sensors.

Parameter	MAPE **(%)**	MSE
pH	4.293792	0.110908
T(°C)	3.12254	0.190662
Turb (NTU)	21.821	0.565946

Table 9: Summary of multivariate linear regression analysis for dissolved oxygen (DO) prediction.

Predictor/Term	Coefficient (β)	Standard Error (SE)	t-Statistic	pH Value	95% Confidence Interval (CI)
Constant (Intercept)	2.499	0.812	3.078	0.007*	[0.768, 4.230]
pH	1.414	0.345	4.099	0.001*	[0.678, 2.150]
Temperature (°C)	-0.303	0.062	-4.887	< 0.001*	[-0.435, -0.171]
Turbidity (NTU)	0.028	0.012	2.333	0.034*	[0.002, 0.054]

* Denotes statistical significance at $p<0.05$.

Table 10: Overall predictive performance metrics and cross-validation statistics of the multivariate regression model on the field validation dataset (*N*=19). Detailed point-by-point calculation residuals are provided in Supplementary Table S1

Metric	Value
Sample Size (*N*)	19
Mean Absolute Percentage Error (MAPE)	4.91%
Mean Squared Error (MSE)	1.64 mg/L^2
Root Mean Squared Error (RMSE)	1.28 mg/L
Leave-One-Out Cross-Validation (Q^2)	0.798

Supplementary material

The supplementary material associated with this article can be found in the online version. It includes:

Table S1: Point-by-point comparison between measured and predicted dissolved oxygen concentrations for the independent field validation dataset.

Table S2: Complete sample-by-sample observation dataset comparing DSİ reference measurements, calibrated Arduino sensor outputs, and model-predicted DO concentrations.

Acknowledgements

The authors would like to thank Karabük University for providing laboratory facilities and technical support during the experimental studies.

Fundıng

This research did not receive any specific grant from funding agencies in the public, commercial, or not-for-profit sectors.

Ethical approval

This study does not involve human participants or animals, and therefore ethical approval was not required.

Consent to partıcıpate

Not applicable.

Consent for publıcatıon

Not applicable.

Competıng ınterests

The authors declare that they have no competing interests.

Data avaılabılıty

The datasets generated and/or analyzed during the current study are available from the corresponding author upon reasonable request.

References

Abyaneh, H.Z. (2014), Evaluation of multivariate linear regression and artificial neural networks in prediction of water quality parameters, *Journal of Environmental Health Science and Engineering*, 12(1), 40, DOI:10.1186/2052-336X-12-40.

Abbott, M. B. (1999), *Introducing hydroinformatics*, *Journal of Hydroinformatics*, 1(1), 3–19, DOI:10.2166/hydro.1999.0002.

Abrahart, R.J., See, L.M. & Solomatine, D.P. (2008), *Practical Hydroinformatics: Computational Intelligence and Technological Developments in Water Applications*, Springer.

Alimorong, F.M.L.S., Apacionado, H.A. D. & Villaverde, J.F. (2020), Arduino-based multiple aquatic parameter sensor device for evaluating pH, turbidity, conductivity, and temperature, *2020 IEEE 12th International Conference on HNICEM*, DOI:10.1109/HNICEM51456.2020.9400145.

Glasson, J., Therivel, R. & Chadwick, A. (2013), *Introduction to Environmental Impact Assessment* (4th ed.), Routledge.

Hart, J.K. & Martinez, K. (2006), *Environmental Sensor Networks: A Revolution in the Earth System Science?*, *Earth-Science Reviews*, **78**(3–4), pp. 177–191, DOI:10.1016/j.earscirev.2006.05.001.

Isaac, R. & Siddiqui, S. (2022), Application of water quality index and multivariate statistical techniques for assessment of water quality

Table 11: Comparative statistical summary of measured dissolved oxygen (DO) concentrations and model predictions derived from DSİ reference inputs and calibrated Arduino sensor inputs (*N*=19).

Parameter / Scenario	Measured DO	DO Prediction (DSİ Inputs)	DO Prediction (Arduino Inputs)
Mean (mg/L)	9.18	9.24	8.64
Min (mg/L)	5.10	6.18	5.64
Max (mg/L)	12.80	11.32	10.71
Standard Deviation	1.83	1.45	1.39
Mean Absolute Percentage Error - MAPE (%)	-	-	4.91%

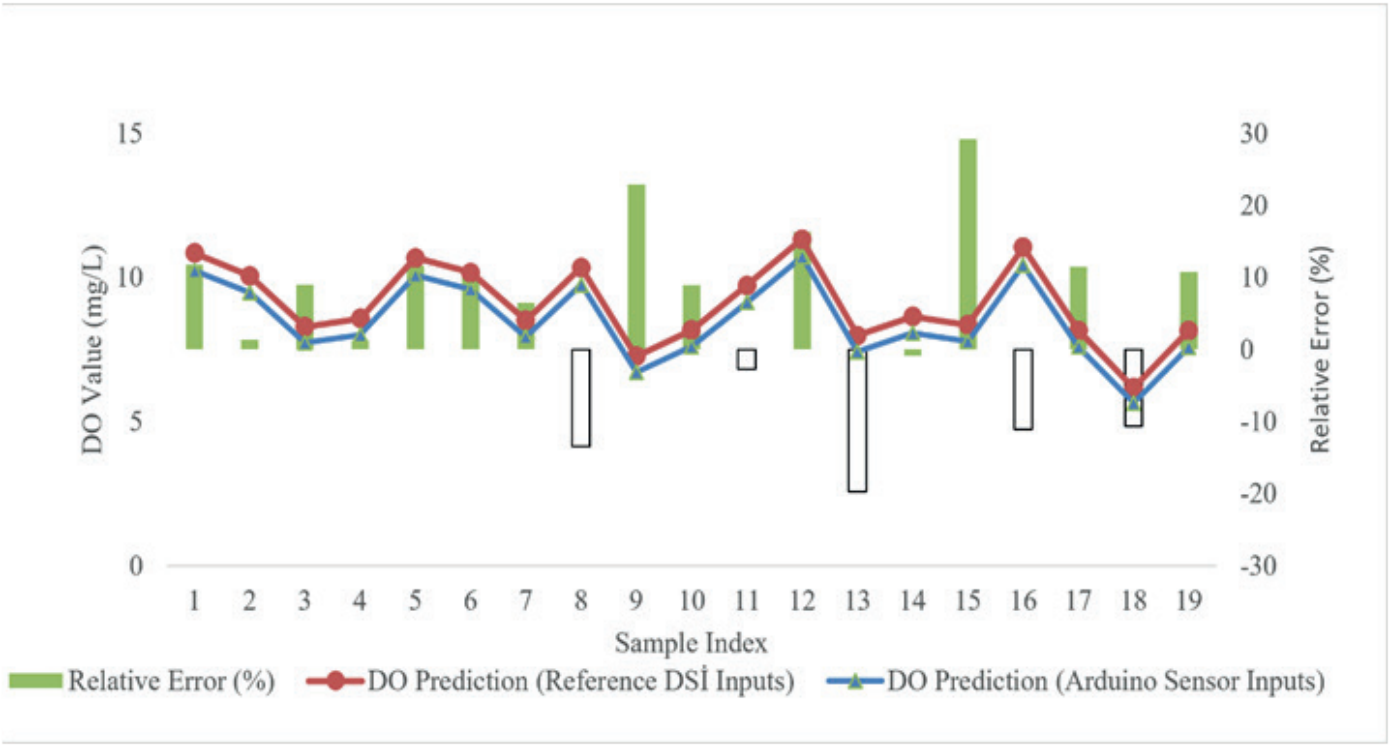


Fig 5. Comparison of experimentally measured and model-predicted dissolved oxygen values.

around Yamuna River in Agra region, Uttar Pradesh, India, *Water Supply*, 22(3), pp. 3399–3418, DOI:10.2166/ws.2021.395.

Jiang, J., Tang, S., Han, D., Fu, G., Solomatine, D. & Zheng, Y. (2021), A comprehensive review of catchment water quality monitoring using a tiered framework of integrated sensing technologies, *Science of the Total Environment*, 765, 142766, DOI:10.1016/j.scitotenv.2020.142766.

Kamboj, A., Garg, P., Bansal, D., Sankar, A. & Bukya, M. (2021), Development of Android app-based portable water quality testing device using Arduino, *2021 9th International Conference on Reliability, Infocom Technologies and Optimization (ICRITO)*, DOI:10.1109/ICRITO51393.2021.9596398.

Liu, Z., Zhu, H., Cui, X., Wang, W., Luan, X., Chen, L., Cui, Z. & Zhang, L. (2021), Groundwater quality evaluation of the Dawu water source area based on water quality index (WQI): comparison between Delphi method and multivariate statistical analysis, *Water (Switzerland)*, 13(8), 1127, DOI:10.3390/w13081127.

Loucks, D.P., van Beek, E., Stedinger, J.R., Dijkman, J.P.M. & Villars, M.T. (2005), *Water Resources Systems Planning and Management: An Introduction to Methods, Models and Applications*, UNESCO Publishing, Paris.

Maiolo, M. & Pantusa, D. (2021), Multivariate analysis of water quality data for drinking water supply systems, *Water (Switzerland)*, 13(13), 1766, DOI:10.3390/w13131766.

Noble, B.F. (2015), *Introduction to Environmental Impact Assessment: A Guide to Principles and Practice* (3rd ed.), Oxford University Press.

Solomatine, D.P. & Ostfeld, A. (2008), Data-driven modelling: Some past experiences and new approaches, *Journal of Hydroinformatics*, 10(1), pp. 3–22, DOI:10.2166/hydro.2008.01.

Tripathi, M. & Singal, S.K. (2019), Use of principal component analysis for parameter selection for development of a novel water quality index: a case study of River Ganga, India, *Ecological Indicators*, 96, 430–436, DOI:10.1016/j.ecolind.2018.09.025.

Table S1: Point-by-point comparison between measured and predicted dissolved oxygen concentrations for the independent field validation dataset (N = 19).

Sample	Measured DO	Predicted DO (Arduino Model) (mg/L)	Residual (Measured Predicted) (mg/L)
1	11.60	10.2368	1.3632
2	9.60	9.4724	0.1276
3	8.50	7.7309	0.7691
4	8.10	7.9982	0.1018
5	11.40	10.0805	1.3195
6	10.70	9.5784	1.1216
7	8.50	7.9463	0.5537
8	8.60	9.7541	−1.1541
9	8.70	6.7106	1.9894
10	8.3577	7.6126	0.7451
11	8.90	9.1397	−0.2397
12	12.80	10.7123	2.0877
13	6.20	7.4191	−1.2191
14	8.00	8.0704	−0.0704
15	11.00	7.7834	3.2166
16	9.40	10.4380	−1.0380
17	8.60	7.6094	0.9906
18	5.10	5.6393	−0.5393
19	8.50	7.5859	0.9141

Note: Overall model performance statistics (MAPE, MSE, RMSE, and Leave-One-Out Cross-Validation (LOOCV)) are reported in Table 10 of the main manuscript.

Table S2: Complete dataset of reference DSİ measurements, calibrated Arduino sensor outputs, and corresponding DO model predictions (*N*=19).

Measured DO (mg/L)	DO Prediction (Reference DSİ Inputs)	Reference pH (DSİ)	Calibrated pH	Reference Temperature (DSİ, °C)	Calibrated Temperature (°C)	Reference Turbidity (DSİ, NTU)	Calibrated Turbidity (NTU)	DO Prediction (Arduino Sensor Inputs)	Relative Error Distribution (%)
11.6	10.84856	7.7	7.367775	9	9.537775	6.8	7.559411	10.2368	11.75172
9.6	10.06317	8.4	8.061544	15	15.43909	8.4	9.153828	9.472377	1.329405
8.5	8.294365	8.2	7.863324	20	20.35685	9.5	10.24999	7.730925	9.047947
8.1	8.585751	6.6	6.277568	11	11.50488	3.2	3.971973	7.998166	1.257214
11.4	10.67853	8.5	8.160653	13.90601	14.36309	13.48942	14.22549	10.08052	11.57443
10.7	10.17196	8.2	7.863324	14	14.45554	11.56259	12.30538	9.578381	10.48242
8.5	8.5113	8.3	7.962434	20	20.35685	12.20487	12.94542	7.946337	6.513683
8.6	10.34668	8.5	8.160653	15	15.43909	13.48942	14.22549	9.754128	-13.4201
8.7	7.263421	7.8	7.466885	21	21.3404	3.7	4.470228	6.710571	22.867
8.357701	8.177224	7.9	7.565995	19	19.3733	9.635758	10.38527	7.612559	8.915637
8.9	9.72464	8.3	7.962434	16	16.42264	12.20487	12.94542	9.13972	-2.69349
12.8	11.32405	8	7.665105	10	10.52133	19.5	20.2151	10.71226	16.31048
6.2	7.987132	7.4	7.070446	17	17.40619	6.424371	7.185093	7.419095	-19.6628
8	8.65158	7.324398	6.995518	14.08667	14.54078	2.4	3.174764	8.070353	-0.87941
11	8.360001	7.315379	6.986578	14.98745	15.42675	2.2	2.975462	7.783401	29.24181
9.4	11.05122	7.8	7.466885	9	9.537775	8.99348	9.745237	10.43799	-11.0424
8.6	8.172558	7.7	7.367775	19	19.3733	19.6	20.31475	7.609439	11.51815
5.1	6.182298	7	6.674007	21	21.3404	5.5	6.263947	5.639345	-10.5754
8.5	8.163264	7	6.674007	14	14.45554	0.4	1.181743	7.585883	10.75432

Archives of Environmental Protection
Vol. 52 no. 3 pp. 100–107

PL ISSN 2083-4772
DOI: 10.24425/aep.2026.555



© 2026. The Author(s). This is an open-access article distributed under the terms of the Creative Commons Attribution-ShareAlike 4.0 International Public License (CC BY SA 4.0, https:// creativecommons.org/licenses/by-sa/4.0/legalcode), which permits use, distribution, and reproduction in any medium, provided that the article is properly cited.

A feasibility assessment of remediating copper-contaminated soils with construction waste

Rixiu Zhou[1], Quan Zhou[2], Chaozhen Xie[1], Zhenzhou Zhang[3], Furong Wu[3], Qiming Li[1], Fangze Shang[3], Yifan Hu[3], Zhengjie Zhu[4], Dianpeng Li[5], Shuqing An[1,4]

[1] School of Life Science, Nanjing University, Nanjing, P R China
[2] Powerchina Real Estate Group Ltd., Beijing, P R China
[3] Powerchina Eco-Environmental Group Co., Ltd., Shenzhen, P R China
[4] Nanjing University Ecological Research Institute of Changshu, Suzhou, P R China
[5] Xiangyang Institute of History and Culture & Hanjiang Institute (Kongming Academy), Hubei University of Arts and Science, Xiangyang, P R China

*Corresponding author's e-mails: Dianpeng Li: lldp05120@126.com
Shuqing An: anshq@nju.edu.cn

Keywords: soil remediation; waste concrete; Langmuir equation; potentially toxic metal

Abstract: This study investigated the potential of waste concrete fines and carbonated waste concrete fines as soil amendments for the remediation of copper-contaminated soils through adsorption and solidification experiments. The Langmuir equation indicated that both waste concrete fines and carbonated waste concrete fines achieved high adsorption capacities of 27.71 mg/g and 27.60 mg/g, respectively. These construction wastes were as effective as steel slag and fly ash in stabilizing copper in soils, primarily by converting copper from weakly acid-extractable forms to reducible and oxidized states, while exhibiting no significant effect on the residual state of copper. The results suggest a promising application of construction wastes in soil remediation; however, further investigation is needed to understand their long-term effects and the migration of potentially toxic metals in plants.

Introduction

Potentially toxic metal (PTM) pollution in soil is an increasingly serious environmental problem of global concern that jeopardizes soil health and food safety (Ma et al., 2023). In addition to natural releases, PTMs enter and accumulate in soil systems through human activities, such as mine drainage, smelting, and battery manufacturing, adversely affecting ecosystems (Liu et al., 2018). These PTMs include cadmium, lead, mercury, arsenic, chromium, copper, zinc, nickel, manganese, cobalt, etc. (Zhang et al., 2024). Beyond conventional industrial sources, recent studies have highlighted that military conflicts can also cause significant heavy metal contamination in soils, with copper being one of the predominant pollutants, alongside concomitant declines in soil microbial communities (Moliszewska et al., 2025).

Copper (Cu) is an essential trace element for the growth and development of living organisms; however, excess Cu can be toxic to plants and pose a threat to human health through the food chain (Rehman et al., 2019). In plants, elevated Cu levels can cause physiological disorders in the root system, inhibit growth, and even lead to chlorosis. In animals, excessive Cu exposure can cause damage to organs such as the liver and gallbladder, thereby disrupting normal metabolism. In addition, Cu pollution can negatively affect the growth of soil microorganisms and the activity of soil enzymes, thereby disrupting the soil ecological balance. Anthropogenic activities, including copper mining, industrial wastewater discharges, and the use of copper-containing pesticides, can result in Cu concentrations in soils that exceed natural background levels, posing a threat to ecosystems (Zhou et al., 2005a; Zhou et al., 2005b).

In recent years, using various amendments to stabilize PTMs in soil and reduce their mobility has gained attention due to the simplicity, efficiency, in situ applicability, and cost-effectiveness of this approach (Rinklebe and Shaheen, 2015). The mechanisms by which amendments reduce PTM mobility are complex; most amendments achieve this by lowering the concentration of soluble and exchangeable PTMs through chelation, adsorption of metal ions, or by altering soil pH (Lu et al., 2015). Industrial and agricultural by-products, such as steel slag (Kong et al., 2023), fly ash (Cui et al., 2016), and biochar (Nguyen et al., 2023), are commonly used materials for green soil remediation. In a study by Meier et al. (2017), it was revealed that biochar originating from chicken manure resulted in a decrease in Cu uptake in Cu-contaminated soil by Oenothera picensis. Specifically, Cu uptake decreased from

66.9 mg kg $^{-1}$ to 36.6 mg kg $^{-1}$. In addition, biochar application increased soil pH and key soil nutrients, resulting in a significant 3.5-fold increase in shoot biomass and a 3.1-fold increase in root biomass. Kong et al. (2023) used sulphur slag, a by-product of wet fuming sulphur, as a stabilizer and found that the application of sulphur slag reduced the levels of Cd, Cu, Zn, and Pb in the soil, but significantly increased the levels of Cr in the soil due to the presence of Cr. The sulphur slag changed the chemical composition of potentially toxic metals (Cu, Zn, and Pb) in the soil from exchangeable and reducible to oxidizable and residual states.

Construction waste, especially waste concrete that contains a large amount of cement constitutes the largest proportion of solid waste in the city (Li et al., 2023). Its resource utilization has attracted much attention and is commonly used in road paving, recycled brick production, artificial wetlands, soil improvement, etc.; however, research on its use as a soil stabilizer is still relatively limited. The alkali-activated mixture contained in construction waste improves and stabilizes soil through cation exchange, hydration reactions, and enhanced pozzolanic reactions (Ho et al., 2021).

Certain components in waste concrete share similarities with the primary constituents of common inorganic passivators, such as Ca $(OH)_2$ and silicates, demonstrating potential as a passivator for soil contaminated with potentially hazardous metals. The application of waste concrete in soil remediation remains limited but holds significant potential. The application of waste concrete in soils contaminated with PTMs could significantly reduce the cost and difficulty of remediation. The objective of this study was to assess the feasibility of waste concrete fines and carbonated waste concrete fines as amendments to copper-contaminated soils and to investigate the stabilization performance of construction waste compared to other amendments, such as steel slag and fly ash. The results of this research can provide technological support for broader applications of construction waste.

Materials and methods

Material acquisition

Modifier preparation

The amendments used in this study included fly ash (FF), steel slag (SS), waste concrete fines (WW), and carbonated waste concrete fines (CC). Fly ash and steel slag were procured online, while waste concrete fines were sourced from Jiangsu Shunjia Construction Co., Ltd. Carbonated waste concrete fines were obtained by leaving the waste concrete fines indoors to naturally air-dry and carbonate for six months. During this period, the carbon dioxide concentration was approximately 0.10%, the temperature fluctuated between 20 and 26°C, and humidity ranged from 30 to 60%.). All samples were dried and passed through a 100-mesh sieve.

Soil samples

Surface soil samples (0-20 cm) were collected in the winter of 2023 from roadside farmland in Lingkun Island, Wenzhou City, Zhejiang Province, China. The physicochemical parameters of the soil are shown in Table 1, and the concentrations of PTMs are shown in Table 2. According to the "Risk Control Standards for Soil Pollution in Agricultural Land" (GB 15618-2018), the risk screening value for copper contamination in agricultural land soil is 200 mg/kg. Therefore, the soil was air-dried, pulverized, and mixed with a copper sulfate solution (700 mg $CuSO_4$/kg soil) and kept at 70% of its maximum water holding capacity for two weeks to reach a Cu concentration of 221.35 mg/kg, thereby creating contaminated soil. The treated soil was then air-dried and pulverized again, and subsequently passed through a 100-mesh sieve.

Adsorption experiments

A copper standard solution at a concentration of 1000 mg/L was prepared using 3.929 g of $CuSO_4$ and 1L of deionized water. A 0.01 mol/L $NaNO_3$ solution was used as the supporting electrolyte, and the pH of the solution was adjusted to 5.5 using either 1 mol/L HNO_3 or 1 mol/L NaOH. The gradient concentrations of Cu standard solutions required for the experiments were 10, 20, 40, 80, 160, and 220 mg/L, respectively. Accurately 0.5±0.01 g of each amendment was weighed and placed separately into 50 ml polyethylene centrifuge tubes. For each amendment, 18 portions were prepared. A 30 ml solution of copper (Cu) at different concentrations, prepared from the Cu standard solution, was added to each centrifuge tube, and each amendment was tested in triplicate at each concentration. The centrifuge tubes were then placed in an incubator at (25 ± 1) °C and shaken at 150 r/min for 24 hours. After equilibration, the tubes were centrifuged at 4000 r/min for 10 minutes. Subsequently, the supernatant was filtered through a 0.22 μm membrane and transferred to a plastic bottle, to which one drop of concentrated nitric acid was added. The samples were then stored in a refrigerator at 4 °C for further testing.

Stabilization experiments

Based on previous experiments, soil stabilization tests were designed to investigate the effectiveness of different amendments in stabilizing Cu in contaminated soil. Different types of amendments were added to each 300 g portion of contaminated soil prepared as described in Section 2.1.2 at 3%, 5% and 10% mass ratios, corresponding to 9 g, 15 g, and 30 g of amendments, respectively. Each amendment was tested in triplicate at each dosage. The soil and amendments are thoroughly mixed through a blender. Water was added to each portion of soil to achieve 70% of the maximum water-holding capacity, and the mixture was transferred to a beaker. The beaker was sealed with a film containing small holes to maintain air-water equilibrium. Incubation was conducted in an automatic incubator at a temperature of 25 ± 2 °C for 28 days. After this period, soil samples were collected, thoroughly pulverized, air-dried, and analyzed for pH and potentially toxic metal forms.

Analytical methods

Adsorption isotherm analysis

The Cu content in the supernatant from the adsorption experiments was determined using inductively coupled plasma mass spectrometry (ICP-MS, NexION 300X, PerkinElmer, USA).

The adsorption of Cu by different amendments was modeled using the Langmuir and Freundlich equations. The Langmuir equation is given as:

Table 1: Physical and chemical properties of soils

DOC mg/kg	OC g/kg	AOC g/kg	IOC g/kg	TN g/kg	ON mg/kg	AON g/kg	ION g/kg	NH_4-N mg/kg	NO_3-N mg/kg	NO_2-N mg/kg	STN mg/kg	SON mg/kg	SO_4-S g/kg	TS %	pH	HN mg/kg	TP %	AP mg/kg	TK g/kg	AK mg/kg	TDS g/kg
895.00	11.70	7.49	4.21	1.30	1290.00	0.97	0.32	0.33	7.48	0.26	16.00	7.91	0.07	0.004	7.32	114.00	0.08	14.00	10.70	132.00	0.12

* DOC: dissoluble organic carbon; OC: organic carbon; AOC: active organic carbon; IOC: inert organic carbon; TN: total nitrogen; ON: organic nitrogen; AON: active organic nitrogen; ION: inert organic nitrogen; NH4-N: ammonium nitrogen; NO_3-N: nitrate nitrogen; NO_2-N: nitrite nitrogen; STN: total soluble nitrogen; SON: soluble organic nitrogen; SO_4-S: sulfate; TS: total sulfur; HN: hydrolyzable nitrogen; TP: total phosphorus; AP: effective phosphorus; TK: total potassium; AK: quick-acting potassium; TDS: total salinity

Table 2: Concentration of potentially toxic metals in virgin soil

Pb (μg/kg)	Cr (μg/kg)	Cd (μg/kg)	Zn (μg/kg)	Cu (μg/kg)	Ni (μg/kg)	As (mg/kg)	Hg (mg/kg)
31980.68	82471.74	260.84	71134.37	18419.80	24312.92	6.52	0.86

* Pb: lead; Cr: chromium; Cd: cadmium Zn: zinc; Cu: copper; Ni: nickel; As: arsenic Hg: mercury.

Table 3: Copper species extraction by Improved BCR Extraction

Steps	Extracted copper form
(1) 40 m L 0.11 mol·L^{-1} HOAc solution, continuous shaking at (22±5) °C for 16 hand then centrifuging.	F1 (Weak acid extraction state)
(2) 40 mL 0.5 mol·L^{-1} NH_2OH·HCl, adjusted with HNO_3 to pH=2, continuously oscillate at (22±5) °C for 16 h and then centrifuging.	F2 (Reducible state)
(3) 10 mL 8.8 mol·L^{-1} H_2O_2(pH=2.0 ~ 3.0), digested at room temperature for 1 h, then heated to (85±2) °C, digested for 1 h and evaporated to dryness; then add 10 mL 8.8 mol·L^{-1} H_2O_2(pH=2.0), digested for 1 h at (85±2) °C, and evaporated to dryness; finally add 50 mL 1 mol·L^{-1} NH_4Ac (pH=2.0), at (22±5) °C, continuous shake for 16 h, then centrifuge for 20 min.	F3 (Oxidizable state)
(4) 20 m L aqua regia digestion.	F4 (Residual state)

$$Q_e = {}^{C_m K_L C_e} / (1 + K_L C_e) \quad (1)$$

(1) where Q_e represents the adsorption amount of potentially toxic metals by the amendment at adsorption equilibrium (mg/g); C_m is the maximum adsorption capacity of the amendment (mg/g), K_L is the constant related to the adsorption binding energy, and C_e is the concentration of potentially toxic metals in the solution at adsorption equilibrium (mg/L).

The Freundlich equation is as follows:

$$Q_e = K_F C_e^n \quad (2)$$

(2) where Q_e indicates the amount of potentially toxic metal adsorbed by the amendment at adsorption equilibrium (mg/g); K_F and n are the Freundlich adsorption constants, and C_e represents the concentration of potentially toxic metal in the solution at adsorption equilibrium (mg/L).

Analysis of potentially toxic metal forms

The chemical forms of potentially toxic metals were analyzed through sequential chemical extraction. The modified BCR sequential extraction method provides good reproducibility and high extraction accuracy, producing data comparable to standardized references; thus, it is widely recognized and used internationally (Zou et al., 2022). The procedure for the modified BCR sequential extraction method is presented in Table 3. The extract was filtered through a 0.22 μm filter membrane and subsequently analyzed using ICP-MS.

Analysis of the Valence State of Metals

X-ray photoelectron spectroscopy (XPS) (Thermo Scientific K-Alpha, USA) was employed to analyze the valence states of potentially hazardous metals. The parameters were as follows: Al Kα radiation (hv=1486.6 eV) was used as excitation source, with a 400 μm spot size. Under laboratory vacuum conditions exceeding 5.0×10^{-7} mbar, the instrument operated at a working voltage of 12 kV and a filament current of 6 mA. Full-spectrum scanning was performed over an energy range of 150 eV with 1 eV increments, while narrow-scan measurements were performed over an energy range of 50 eV with 0.1 eV increments. Final charge correction was performed using C1s = 284.80 eV as the binding-energy reference. The XPS results were further analyzed and fitted using Avantage software.

Statistical analysis

The experimental data were processed using Excel. Statistical analysis of the BCR data was performed using IBM SPSS Statistics 25, with the significance level set at 0.05. Visualization graphs were generated using Origin 2023b.

Discussion and analysis

Analysis of the adsorption capacity of amendments on Cu

As shown in Fig. 1, the adsorption of Cu by the four amendments gradually increased with the concentration of the Cu solution. As the Cu concentration rose from 10 mg/L to 220 mg/L, the adsorption capacity of steel slag (SS) increased from 0.62 mg/g to 12.99 mg/g, while those of carbonated waste concrete fines (CC) and waste concrete fines (WW) both increased from 0.62 mg/g to 13.07 mg/g. The adsorption capacity of Cu by fly ash (FF) increased from 0.62 mg/g to 8.41 mg/g.

At low Cu concentrations, the four amendments exhibited similar adsorption capacities; however, differences became apparent at higher concentrations, with the order of effectiveness being CC ≈ WW > SS > FF. Both carbonated waste concrete fines and waste concrete fines demonstrated the highest Cu immobilization capacities, with no significant difference between the two amendments ($p > 0.05$).

The Langmuir and Freundlich equations were used to fit the Cu adsorption isotherms for the different amendments, as presented in Table 4 and Fig. 1. As shown in Table 4, SS, WW, and CC were fitted with correlation coefficients (R^2) greater than 0.90, indicating that both Langmuir and Freundlich equations effectively describe the adsorption behavior of SS, WW, and CC toward Cu. However, the adsorption behavior of FF is better described by the Langmuir equation. The parameter C_m in the Langmuir equation represents the maximum monolayer adsorption capacity of the amendment for pollutants, which can be used to compare the potential adsorption capacities of different amendments (Dai et al., 2009). According to the Langmuir equation, the maximum adsorption capacities of Cu were 20.90 mg/g for SS, 27.60 mg/g for CC, and 27.71 mg/g for WW, while the maximum adsorption capacity for FF was only 7.89 mg/g.

The Freundlich equation is often applied to describe the adsorption behavior of solids with heterogenous surfaces, where K_F reflects the magnitude of the adsorption binding

energy of the amendment for the pollutant (Arias et al., 2005). In the Freundlich equation, the K_F value for SS in Cu adsorption is 4.21, which is higher than those of CC, WW, and FF, indicating that the adsorption binding energy of SS for Cu is greater than those of the other three amendments.

Characterization of Cu adsorption by various amendments

High-resolution XPS spectra of the Cu2p region for the different amendments were deconvoluted to identify the corresponding chemical species and fitted with component peaks. The different amendments showed distinct Cu2p peaks after Cu adsorption. It was observed that the $Cu2p^{3/2}$ peaks appeared at approximately 933.1, 935.1, and 943.30 eV for the different amendments, corresponding to $Cu(OH)_2$, CuO, and $CuCO_3$, respectively (Qian et al., 2023). These results indicate that the Cu adsorbed on the surface of the amendment existed as Cu (II) and that the amendment did not change the oxidation state of Cu. In SS, the relative proportions of Cu $(OH)_2$, CuO, and $CuCO_3$ were 64.69%, 5.25%, and 30.06%, respectively. The CC treatment had the highest proportion of CuO at 18.78% (Table 5), while the highest proportion of Cu $(OH)_2$ was 64.94% in the FF treatment. Cu $(OH)_2$ accounted for the largest proportion in each amendment, indicating that hydroxyl groups (-OH) on the amendment surfaces and hydroxide ions (OH-) in the solution play important roles in Cu (II) adsorption. Cu(II) was chemisorbed onto the amendment surfaces, promoting the formation of Cu $(OH)_2$.

Effect of amendments on soil pH

The four amendments used in this study have a large specific surface area and are alkaline, which can increase the pH of the system and promote the formation of potentially toxic metal precipitates (Cui et al., 2016). As shown in Fig. 3, compared to the original contaminated soil, the soil pH increased with increasing dosages of the different amendments. The highest pH of 8.52 was observed with the addition of 10% FF, followed by the addition of WW, which reached a pH of 8.30 at a 10% dosage. The pH for CC and SS varied less, reaching 8.17 and 8.07 at a 10% addition, respectively.

The addition of amendments, especially alkaline amendments, will enhance soil pH. Alkaline environments may cause soil compaction and inhibit microbial activity, as well as plant growth and development. Existing studies indicate that alkaline stress exerts a greater negative impact on soil crop yields than saline stress (Liu et al., 2024). The appropriate application of amendments can improve soil pH and physical conditions while providing essential nutrients such as calcium (Ca), potassium (K), and magnesium (Mg) to promote plant growth (Rinklebe and Shaheen, 2015). In practical applications, it is essential to balance the agronomic benefits with the potential impacts of amendments.

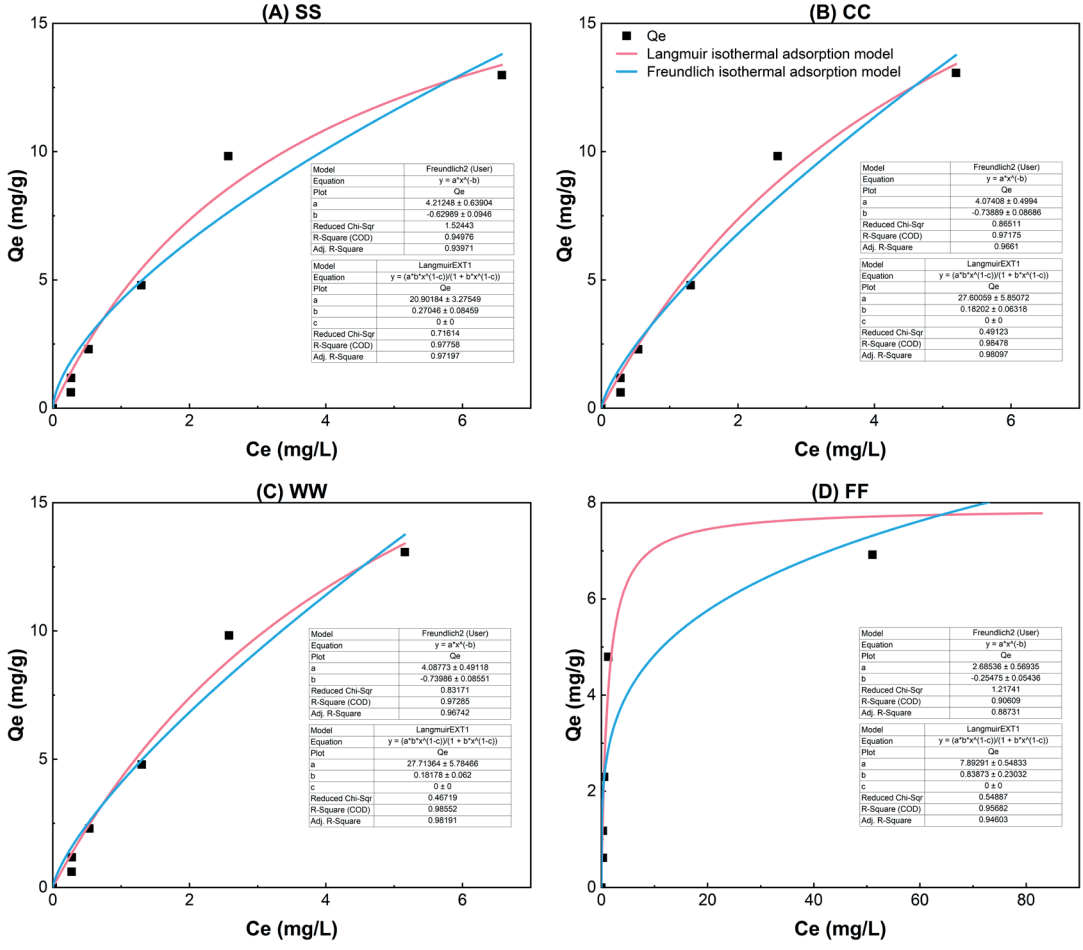


Fig 1. Adsorption isotherms of Cu by four amendments (SS: steel slag; CC: carbonated waste concrete fines; WW: waste concrete fines; FF: fly ash)

Table 4: Langmuir and Freundlich adsorption fitting parameters (R2: correlation coefficients of nonlinearly fitted curves)

	langmuir			Freundlich		
	C_m	K_L	R^2	K_F	n	R^2
SS	20.90	0.27	0.97	4.21	0.63	0.94
CC	27.60	0.18	0.98	4.07	0.74	0.97
WW	27.71	0.18	0.98	4.09	0.74	0.97
FF	7.89	0.84	0.95	2.69	0.25	0.89

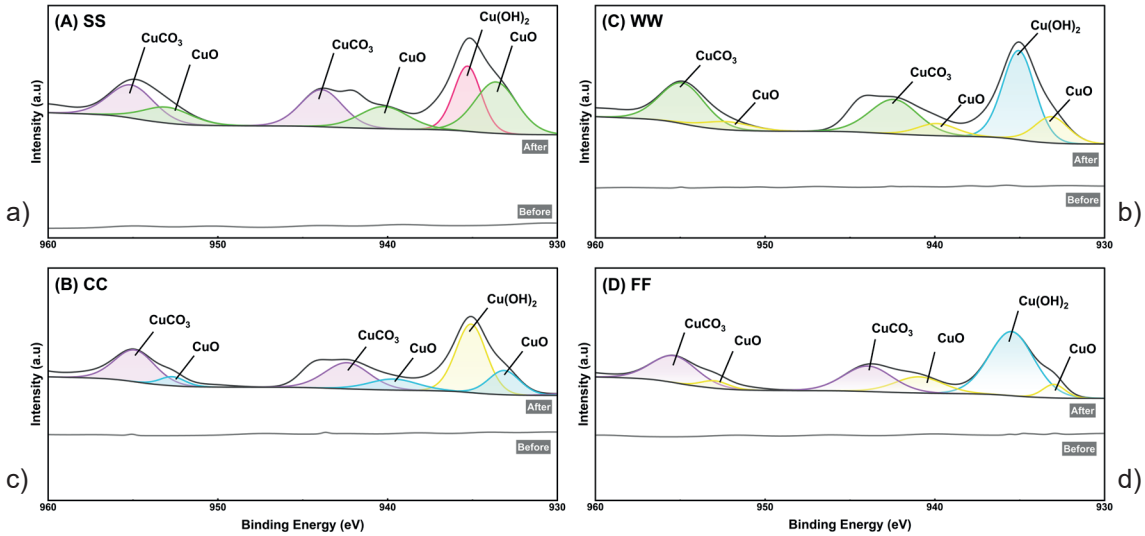


Fig 2. XPS curves of Cu2p after adsorption of Cu by different amendments ((A) SS: steel slag; (B) CC: carbonated waste concrete fines; (C) WW: waste concrete fines; (D) FF: fly ash).

Effect of amendments on the distribution of soil Cu chemical forms

The changes in the chemical forms of soil Cu after 28 days of treatment with different doses of different amendments are illustrated in Fig. 4. In the control treatment, Cu was predominantly found in the weak acid extractable state (46.76%), with the distribution pattern of the four Cu forms as follows: weak acid-extractable state (99.88 mg/kg) > oxidizable state (70.87 mg/kg) > reducible state (32.03 mg/kg) >residual state (10.79 mg/kg). The addition of amendments resulted in a significant ($p<0.05$) decrease in Cu content in the weak acid-extractable state and an increase in Cu content in the oxidizable state across all treatments. The treatment with 10% WW recorded the lowest Cu content in the weak acid-extractable state at 25.13 mg/kg (11.73%), while the treatment with 5% WW had the highest Cu content in the oxidizable state at 160.31 mg/kg (69.34%). Additionally, the treatment with 10% FF exhibited the highest Cu content in the reducible state at 39.34 mg/kg (20.41%). All four amendments are rich in calcium, iron and aluminum, which play important roles in the stabilization of PTMs (Rehman et al., 2019; Shu and Sasaki, 2022). The effects of different amendments vary with the amount added. At a 3% amendment addition, the best stabilization was achieved with FF, which showed the lowest Cu content of 27.90 mg/kg in the weak acid-extractable state. As the addition increased to 5% and 10%, WW provided the best stabilization, with Cu contents of 29.36 mg/kg and 25.13 mg/kg in the weak acid-extractable state, respectively.

Table 5: XPS quantitative results of surface elements after adsorption of Cu by the amendments

Amendment	$Cu(OH)_2$	$CuCO_3$	CuO
SS	64.69	30.06	5.25
WW	52.73	30.93	16.33
CC	51.76	29.45	18.78
FF	64.94	28.25	6.81

Overall, the changes in Cu forms 28 days after the addition of amendments primarily involved a transition from the weak acid-extractable state to the oxidizable state, with some treatments showing an increase in Cu content in the reducible state. This indicates a gradual transformation of Cu from active states to potentially active and inactive states. However, there was no significant difference in residual-state Cu among the treatments. Notably, with increasing amendment additions, the Cu content in the residual state did not show a significant increase across the different treatments, indicating that changes in the amount of amendment added had little effect on the transformation of Cu forms.

Conclusion

Waste concrete fines and carbonated waste concrete fines demonstrate effective stabilization of Cu in contaminated soil. Based on the Langmuir model, the maximum adsorption

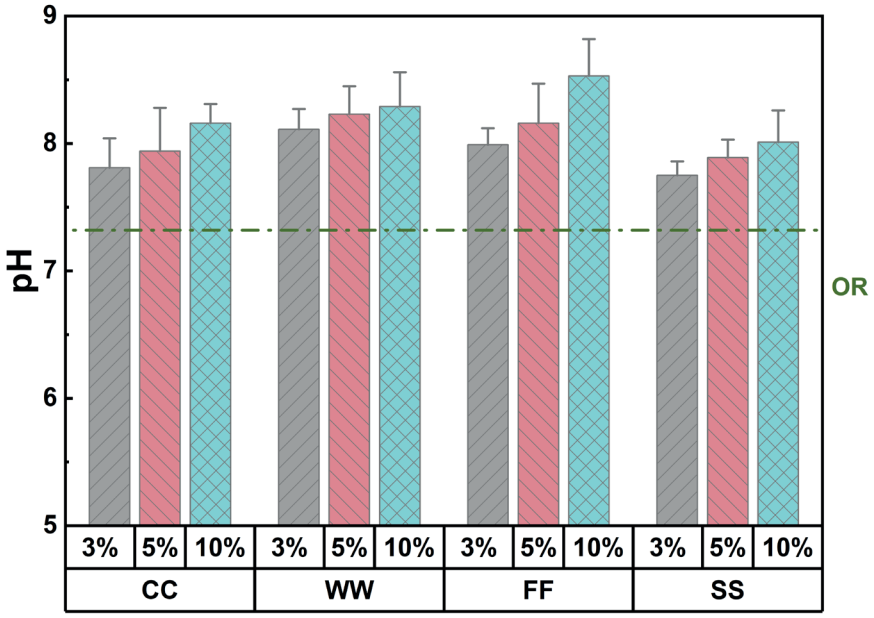


Fig 3. Effect of different amendments on soil pH (SS: steel slag; CC: carbonated waste concrete fines; WW: waste concrete fines; FF: fly ash) (legend: different passivator additions)

capacities for Cu were determined to be 20.90 mg/g for SS, 27.60 mg/g for CC, and 27.71 mg/g for WW, whereas FF exhibited a significantly lower capacity of only 7.89 mg/g. The stabilization efficiency follows the order: carbonated waste concrete ≈ waste concrete > steel slag > fly ash.

Cu adsorbed onto the surfaces of these four amendments predominantly exists in the form of Cu(II), with no alteration in its valence state observed. The hydroxyl groups (-OH) present on the amendment surfaces, along with hydroxide ions (OH^-) in the solution, play a critical role in the adsorption of Cu(II).

The addition of alkaline amendments elevates soil pH, although controlling their dosage can mitigate substantial impacts on pH levels. This process promotes the transformation of Cu from a weakly acid-leachable state to an oxidizable state, thereby gradually converting it from a mobile to a more stable form.

The secondary use of waste concrete as a soil amendment appears feasible for Cu stabilization. However, the

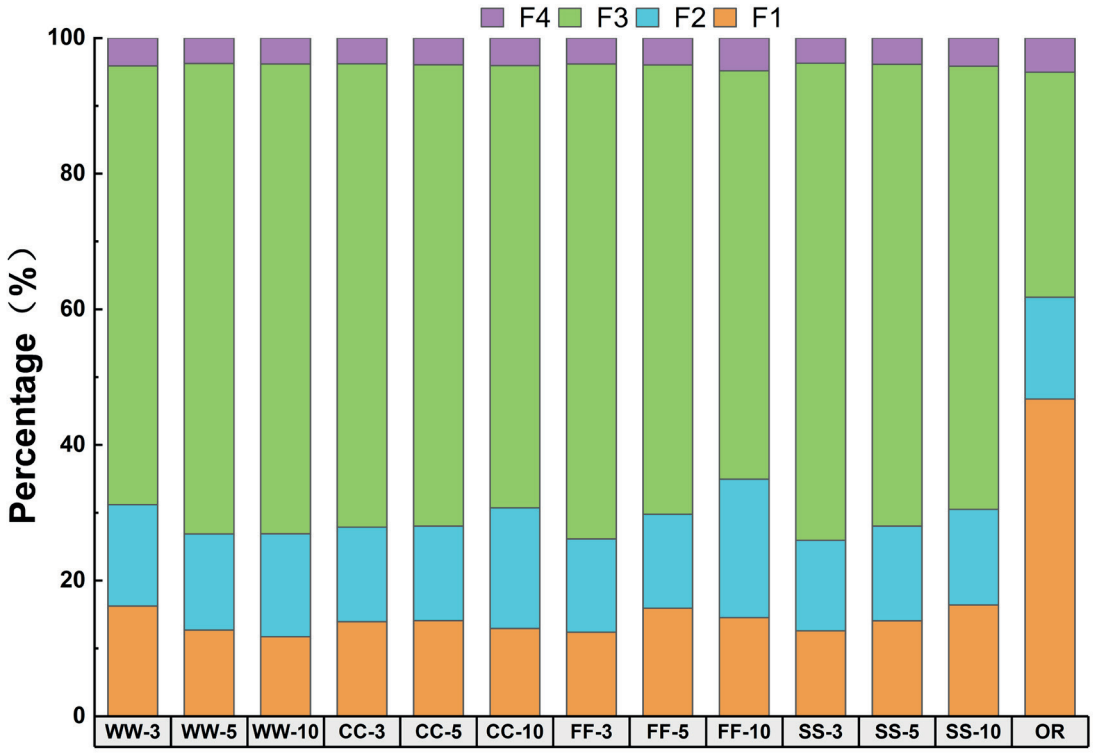


Fig 4. Effect of different amendments on the chemical form of soil Cu (SS: steel slag; CC: carbonated waste concrete fines; WW: waste concrete fines; FF: fly ash. 3: 3% addition; 5: 5% addition; 10: 10% addition)

contaminated soil used in this study was artificially prepared. In actual contaminated soils, the stabilization of Cu may be more complex, requiring further investigation into the behavior of waste concrete. Additionally, despite its short-term effectiveness, the long-term stability of immobilized Cu and the potential uptake of potentially toxic metals by plants require further experimental investigation.

Credit authorship contribution statement

Rixiu Zhou: Conceptualization, methodology, validation, formal analysis, data curation, investigation, writing - original draft, resources. **Quan Zhou:** Investigation, resources, project administration. **Chaozhen Xie:** Validation, data curation, investigation. **Zhenzhou Zhang:** Investigation, resources. **Furong Wu:** Investigation, resources. **Qiming Li:** Validation, investigation. **Fangze Shang:** Investigation. **Yifan Hu:** Investigation. **Zhengjie Zhu:** Project administration. **Dianpeng Li:** Project administration, funding acquisition. **Shuqing An:** Project administration, funding acquisition.

Acknowledgments

This work was supported by the Research and Application on Key Technologies of Engineering in Intelligent Ecological City, China (No. KYZB2022Z003).

Reference

Arias, M., Pérez-Novo, C., Osorio, F., López, E. & Soto, B. (2005). Adsorption and desorption of copper and zinc in the surface layer of acid soils. *Journal of Colloid and Interface Scienc*e 288(1), pp. 21-29. DOI:10.1016/j.jcis.2005.02.053

Cui, H., Wu, Q., Zhang, X., Su, B., Yi, Q., Zhang, S. & Zhou, J. (2016). Immobilization of Cu and Cd in Contaminated Soil by Coal Fly Ash. *Soils* 48(5), pp. 971-977. DOI:10.13758/j.cnki.tr.2016.05.019

Dai, J.L., Zhang, M., Hu, Q.H., Huang, Y.Z., Wang, R.Q. & Zhu, Y.G. (2009). Adsorption and desorption of iodine by various Chinese soils: II. Iodide and iodate. *GEODERMA* 153(1-2), pp. 130-135. DOI:10.1016/j.geoderma.2009.07.020.

Ho, H.-J., Iizuka, A. & Shibata, E. (2021). Chemical recycling and use of various types of concrete waste: A review. *Journal of Cleaner Production* 284, 124785. DOI:10.1016/j.jclepro.2020.124785.

Kong, F., Ying, Y. & Lu, S. (2023). Heavy metal pollution risk of desulfurized steel slag as a soil amendment in cycling use of solid wastes. J*OURNAL OF ENVIRONMENTAL SCIENCES* 127, pp. 349-360. DOI:10.1016/j.jes.2022.05.041

Li, Q., Ma, Y., Chen, J., Cai, Y., Lu, Q., Yu, Q., Duan, X., Zhao, D. & An, S. (2023). The negative effect of the high pH of waste concrete in constructed wetlands on COD and N removal. *Journal of Water Process Engineering* 51, 103356. DOI:10.1016/j.jwpe.2022.103356

Liu, B., Huang, L., Jiang, X., Liu, Y., Huang, G., Yang, C., Liang, Y., Cai, J., Zhu, G. & Kong, Q. (2024). Quantitative evaluation and mechanism analysis of soil chemical factors affecting rice yield in saline-sodic paddy fields. *Science of The Total Environment* 929, 172584. DOI:10.1016/j.scitotenv.2024.172584

Liu, L., Li, W., Song, W. & Guo, M. (2018). Remediation techniques for heavy metal-contaminated soils: Principles and applicability. *Science of The Total Environment* 633, 206-219. DOI: 10.1016/j.scitotenv.2018.03.161

Lu, X.-M., Lu, P.-Z., Chen, J.-J., Zhang, H. & Fu, J. (2015). Effect of passivator on Cu form transformation in pig manure aerobic composting and application in soil. *Environmental Science and Pollution Research* 22(19), pp. 14727-14737. DOI:10.1007/s11356-015-4680-7

Ma, M., Ha, Z., Xu, X., Lv, C., Li, C., Du, D. & Chi, R. (2023). Simultaneous immobilization of multiple heavy metals in polluted soils amended with mechanical activation waste slag. *Science Of The Total Environment* 894. DOI:10.1016/j.scitotenv.2023.164730

Meier, S., Curaqueo, G., Khan, N., Bolan, N., Cea, M., Eugenia, G.M., Cornejo, P., Ok, Y.S. & Borie, F. (2017). Chicken-manure-derived biochar reduced bioavailability of copper in a contaminated soil. *Journal of Soils and Sediments* 17(3), pp. 741-750. DOI:10.1007/s11368-015-1256-6

Moliszewska, E.B., Bida, I., Matik, K.R., Hovorukha, V. et al. (2025). Analysis of variations in heavy metal levels and soil microorganism counts resulting from shelling incidents in Ukraine. *Archives of Environmental Protection*, 51(1), pp. 83–91. DOI:10.24425/aep.2025.153752

Nguyen, T.-B., Sherpa, K., Bui, X.-T., Nguyen, V.-T., Vo, T.-D.-H., Ho, H.-T.-T., Chen, C.-W. & Dong, C.-D. (2023). Biochar for soil remediation: A comprehensive review of current research on pollutant removal. *Environmental Pollution* 337. DOI:10.1016/j.envpol.2023.1224571

Qian, Z., Zeng, J., Zhang, L., Lei, X. & Li, Y. (2023). Cu(II) adsorption characteristics by deep-sea sediment from the South China Sea. *Acta Scientiae Circumstantiae* 43(09), pp. 152-163. DOI:10.13671/j.hjkxxb.2023.0006

Rehman, M., Liu, L., Wang, Q., Saleem, M.H., Bashir, S., Ullah, S. & Peng, D. (2019). Copper environmental toxicology, recent advances, and future outlook: a review. *Environmental Science and Pollution Research* 26(18), pp. 18003-18016. DOI:10.1007/s11356-019-05073-6

Rinklebe, J. & Shaheen, S.M. (2015). Miscellaneous additives can enhance plant uptake and affect geochemical fractions of copper in a heavily polluted riparian grassland soil. *Ecotoxicology and Environmental Safety* 119, pp. 58-65. DOI:10.1016/j.ecoenv.2015.04.005

Shu, K. & Sasaki, K. (2022). Occurrence of steel converter slag and its high value-added conversion for environmental restoration in China: A review. *Journal Of Cleaner Production* 373. DOI:10.1016/j.jclepro.2022.133876

Zhang, Y., Lu, X., Deng, S., Zhu, T. & Yu, B. (2024). Bibliometric and visual analysis of heavy metal health risk assessment: Development, hotspots and trends. *Archives of Environmental Protection*, 50(1). DOI:10.24425/aep.2024.149432

Zhou, D.M., Deng, C.F., Alshawabkeh, A.N. & Cang, L. (2005a). Effects of catholyte conditioning on electrokinetic extraction of copper from mine tailings. *Environment International* 31(6), pp. 885-890. DOI:10.1016/j.envint.2005.05.034

Zhou, D.M., Hao, X.Z., Wang, Y.J., Dong, Y.H. & Cang, L. (2005b). Copper and Zn uptake by radish and pakchoi as affected by application of livestock and poultry manures. *Chemosphere* 59(2), pp. 167-175. DOI:10.1016/j.chemosphere.2004.11.008

Zou, C., Jiang, Y. & Huang, H. (2022). Distribution, Exposure and Health Risk Assessment of Heavy Metal Cadmium: A Review. *Asian Journal of Ecotoxicology* 17(6), pp. 225-243. DOI:10.7524/AJE.1673-5897.2021062300.

Archives of Environmental Protection
Vol. 52 no. 3 pp. 108–120

PL ISSN 2083-4772
DOI: 10.24425/aep.2026.3680



© 2026. The Author(s). This is an open-access article distributed under the terms of the Creative Commons Attribution-ShareAlike 4.0 International Public License (CC BY SA 4.0, https:// creativecommons.org/licenses/by-sa/4.0/legalcode), which permits use, distribution, and reproduction in any medium, provided that the article is properly cited.

Hydrodynamic cavitation as a pretreatment to enhance organic matter solubilization in orange waste prior to anaerobic digestion

Aleksandra Szaja*[1], Agnieszka Montusiewicz[1], Sylwia Pasieczna-Patkowska[2], Elżbieta Grządka[2], Jerzy Montusiewicz[3], Magdalena Lebiocka[1]

[1]Lublin University of Technology, Faculty of Environmental Engineering and Energy, Poland
[2]Maria Curie Skłodowska University, Faculty of Chemistry, Institute of Chemical Sciences, Plac Marii Skłodowskiej-Curie 3, 20-031 Lublin, Poland
[3]Lublin University of Technology, Faculty of Electrical Engineering and Computer Science, Poland

*Corresponding author's e-mails: a.szaja@pollub.pl

Keywords: multi-criteria analysis, hydrodynamic cavitation, pre-treatment prior anaerobic digestion, FT-IR/ATR, solubilization, d-limonene

Abstract: This study evaluated the effectiveness of using hydrodynamic cavitation (HC) as a pre-treatment strategy for orange wastes. Two pressures, 3 and 5 bar, were tested, and time intervals of 0, 5, 10, 20, 30, and 45 min were investigated. An orifice plate with one concentric conical hole (3/10 mm) was used as the cavitation inducer. Among all the examined cases, the results of the multi-stage author's Multi-Criteria Determination of Recommended Variants (MCDRV) analysis showed that the most advantageous variant, in terms of enhancing the solubilization of organic matter and energy consumption, was a pressure of 3 bar and a cavitation time 20 min. under these conditions, the DOC/TOC (dissolved to total organic carbon) ratio was enhanced 2.45-fold. Additionally, a two-fold increase in the sCOD/COD (soluble to total chemical oxygen demand) ratio was achieved with an energy consumption of 0.164 kWh. In turn, in the second step of the MCDRV method, the determined optimal sub-set contained variants with a pressure of 3 bar and cavitation times of 10 and 30 min, respectively. Importantly, in all analyzed cases, the releases of both d-limonene and phenols was observed, which might potentially inhibit subsequent anaerobic digestion

Introduction

In recent years, due to the growing energy demand and the depletion of conventional fuels, energy recovery from organic wastes through anaerobic digestion (AD) has gained great importance. Currently, AD is recognized as the leading treatment process for converting organic residues into renewable energy, i.e., biogas (Hovorukha, 2024; Ponzelli et al. 2024). Importantly, this technology is widely applied at many wastewater treatment and biogas plants (Dauknys et al., 2024). Despite significant progress in the development of AD, the energy potential of some wastes is still not being fully utilized. This is related to the presence of substrate components that are not readily biodegradable or that are toxic to AD microorganisms. AD is recognized as a highly complex process whose stability, and consequently biogas production, can be easily disturbed by those factors (Chen et al. 2024).

Oranges are among the most widely cultivated fruits in the world. During their processing into various products, a huge amount of residues is generated; it is estimated that approximately half of the fruit becomes waste, including peels, seeds, and pulp. Those by-products have considerable potential for various applications, such as in the pharmaceutical, cosmetic and food industries (Wang et al. 2026, Vasconcellos and Saavedra 2026). However, their utilization requires additional expenditures; therefore, most orange wastes (OW) remain unused. Moreover, their effective application in AD still constitutes a technological challenge due to the presence of lignin and essential oils.

Previous studies have indicated that the application of an appropriate pre-treatment method of lignocellulosic biomass has become a necessity for its efficient conversion into biogas through AD (Prasad et al. 2024). However, the section of a suitable pre-treatment method can be challenging and requires advanced technological research. An appropriate strategy should effectively disturb the recalcitrant structure of lignocellulosic biomass while minimizing the potential for generating toxic by-products. Moreover, the selected technology should take into account energy efficiency and technical scalability (Mankar et al. 2021).

Among the various pre-treatment strategies, hydrodynamic cavitation (HC) has demonstrated proven effectiveness in many fields of environmental engineering. It has been applied

for the degradation of dyes and other emerging contaminants, disinfection, sludge treatment, biodiesel production, and improving the biodegradability of side-streams such as landfill leachate (Roy et al. 2025). Additionally, numerous studies have investigated the application of this strategy for biomass pre-treatment (Muhandiram and Rudra 2025). Compared with other well-described pre-treatment methods, HC offers several advantages, including high effectiveness, scalability, cost- and energy efficiency, and low environmental impact (Galloni et al. 2025).

Although HC has previously been applied to the pre-treatment of various wastes, the complexity of the process and the transformations involved require that each residue be considered individually. It should be emphasized that there is an optimal range of cavitation intensity in which solubilization is maximized without excessive energy consumption or excessive release of inhibitors. In this context, time-consuming optimization studies are necessary. Such HC experiments frequently generate multiple results that are difficult to compare, making the selection of the most favorable variant challenging. Therefore, the application of multi-criteria analysis may provide a valuable tool for technologists and researchers (Montusiewicz et al. 2024).

This research concerns the use of hydrodynamic cavitation (HC) as a method for enhancing the solubilization of organic matter in orange waste. To ensure the technical and financial feasibility of the process, optimization studies involving multi-criteria analysis were conducted. To evaluate the changes occurring through HC, surface tension, particle size, and physiochemical properties of the tested samples were determined. Moreover, to provide a comprehensive assessment, the potential generation of toxic by-products, i.e., d-limonene, phenols, ammonia nitrogen, and volatile fatty acids, was also evaluated. In addition, the FT-IR/ATR method was employed to identify the functional groups present in the samples.

Materials and methods

Materials

The orange waste (OW) used in this experiment was obtained from a local market. First, it was thoroughly washed with water and crushed using a laboratory blender to obtain particles with a size of 2 mm. For each HC experiment, a fresh portion of OW was used. To conduct the HC experiments, 640 g of OW was suspended in 30 L of primarily-treated wastewater collected from the municipal wastewater treatment plant "Hajdów" in Lublin, Poland. The applied substrate dose was established based on the acceptable total solids (TS) content in the mixture subjected to HC, taking into account the technical capabilities of the device. The composition of the materials used in the experiment is presented in Table 1.

Table 1: Composition of orange wastes (OW) and wastewater after primary treatment (PW).

Parameter	Unit	PW	OW
TS	g/kg	1.11± 0.05	244.6±7.1
VS	g/kg	0.33± 0.04	229.2±5.9
VS/TS	-	0.30	0.94
COD	mg/L	544.7±9.3	-
sCOD	mg/L	462.3±5.4	-
pH	-	7.39±0.05	-
limonene	µg/g	nd	298
phenols	mg/L	3.2±0.05	-

HC experiments

The HC experiments were performed using a laboratory-scale device consisting of cavitation reactor, a circulation tank with the active volume of 30 L, a submersible pump with a flow rate of 0.65 L/s and a head of up to 80 m. The control and measurement system included manometers, an electromagnetic flow meter, piezoelectric pressure gauges, and a computer unit. All components were connected by pipes equipped with the necessary valves, allowing the treated medium to circulate in a closed loop and repeatedly pass through the cavitation zone. The laboratory setup did not include a cooling system. An orifice plate with a diameter of 64 mm and a thickness of 10 mm, made of stainless steel, was used as a cavitation device. This plate contained a single concentric conical hole with an inlet/outlet diameter of 3/10 mm located on its axis. The hole had an area of 7.0686 mm^2 and a total perimeter of 9.42 mm, while the geometric parameters α and β were 1.333 mm^{-1} and 0.0023, respectively. The laboratory setup and the applied orifice plate are shown in Figure 1.

To conduct the HC experiments, two inlet pressures, 3 and 5 bar, were selected. Under these conditions, the flow rates and velocities in the orifice were as follows: 0.268 L/s and 40.4 m/s at a pressure of 3 bar, and 0.361 L/s and 51.03 m/s at a pressure of 5 bar, respectively. The corresponding cavitation numbers were 0.114 and 0.068 for pressures of 3 and 5 bar, respectively. The influence of HC on the properties of the pre-treated waste was examined at treatment times (t) of 5, 10, 20, 30, and 45 min. The corresponding numbers of passes through the cavitation zone were 2.9, 5.7, 11.4, 17.1, and 25.7 at a pressure of 3 bar, and 3.6, 7.2, 14.4, 21.6, and 32.5 at a pressure of 5 bar, respectively.

The experiment was repeated five times for each pressure. For each replicate, a new, fresh portion of wastewater and OW was prepared. The tables and figures present the mean values together with the standard deviations.

Analytical methods

In the mixture before and after HC, the following parameters were analyzed: total and soluble chemical oxygen demand (COD and sCOD), total and volatile solids (TS and VS), dissolved and total organic carbon (DOC and TOC), phenols, ammonia nitrogen (TAN), and d-limonene. Each analysis was performed in at least triplicate.

Moreover, during the experiment, the pH vale and temperature (T) were monitored. A DR 3900 spectrophotometer (Hach Lange, Loveland, CO, USA) was used to determine the sCOD, COD, TAN and phenol contents. In turn, the VS and TS contents were analyzed according the procedure described in APHA (2012). The TOC content contents was determined using an RC 612 LECO analyzer (LECO, USA) . Moreover, a TOC-L analyzer (Shimadzu, Japan) was used to determine the DOC content. The sCOD and DOC contents were measured in the supernatant obtained by centrifuging the samples at a 4500 rpm for 25 min. The

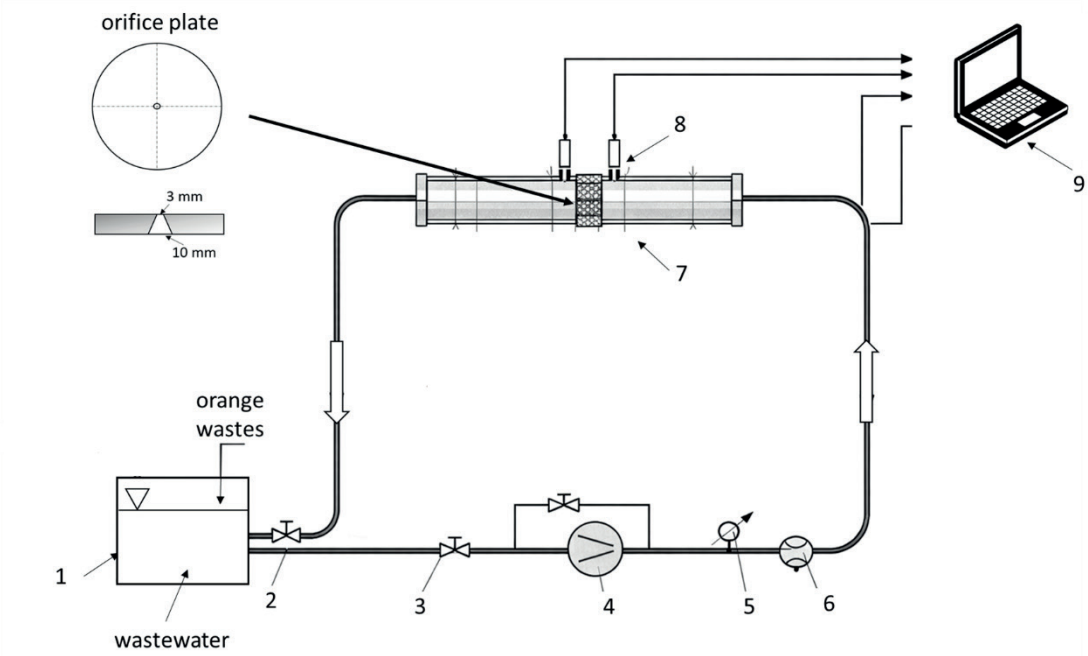


Fig 1. Laboratory installation for HC experiments 1– circulation tank, 2– pipe, 3 – valve, 4 – pump, 5 – manometer, 6 – electromagnetic flow meter, 7 – hydrodynamic cavitation reactor, 8 – piezoelectric pressure gauges, 9 – computer unit to collect data.

d-limonene content was determined using a Thermo GC Ultra PolarisQ Ion Trap gas chromatograph (Waldbron, Germany) equipped with an Equity-5MS capillary column (30 m x 0.25 mm ID x 0.25um df). Helium (99.99% purity) was used as carrier gas at a flow rate of 1.0 mL/min. The following temperature program was applied: an initial temperature of 40°C maintained for 2 min, followed by an isotherm increase of 10°C/min to 250°C, which was maintained for 3 min. The pH of the samples was measured using a pH meter (Elmetron CX-401, Poland) by directly immersing the electrode (EPS-1) into the liquid sample. Electrical conductivity was measured using a conductivity meter (Elmetron CX-401, Poland) equipped with an EC-60 conductometric electrode.

A Zetasizer Nano ZS (Malvern Instruments, UK) was used to determine the zeta potential of the samples. The electrophoretic mobility was converted to zeta potential using the Smoluchowski equation. All measurements were carried out at 25°C and repeated at least three times. The average particle size was determined using dynamic light scattering (DLS) with a Zetasizer Nano ZS (Malvern Instruments, UK). The mean particle size was expressed as the Z-average (intensity to noise ratio). The samples were sonicated for 5 min using a Sonics Vibra Cell ultrasonicator (Sonics & Materials, Inc.) and analyzed in disposable polystyrene cuvettes. The surface tension of the samples was determined at 25°C using the ring method with a K9 tensiometer (Krüss, Hamburg, Germany) . Before each measurement, the platinum ring was cleaned and flame-dried. It was then immersed in the sample (50 cm^3) and subsequently withdrawn to determine the surface tension. The surface tension values were calculated from the maximum force required to pull the ring through the liquid-air interface.

The structural transformations of the organic matter during HC were evaluated using Fourier-transform infrared spectroscopy (FT-IR). Before the measurements, all samples were subjected to freeze-drying (lyophilization) to remove water, which would otherwise interfere with the accurate interpretation of the spectroscopic results. The spectra were recorded at room temperature using a Nicolet 6700 spectrometer equipped with a Meridian Diamond ATR accessory (Harrick Scientific, USA). Data acquisition was performed over the spectral range of 3800-600 cm^{-1} with a resolution of 4 cm^{-1}. To ensure a high signal-to-noise ratio, each individual spectrum consisted of 128 scans. To confirm the reproducibility and reliability of the analytical data, each sample was measured at least three times. Furthermore, no smoothing functions were applied during spectral processing in order to preserve the integrity of the raw spectroscopic features for detailed structural evaluation.

HC parameters

The cavitation number was calculated according to the following equation:

$$C_V = \frac{p_2 - p_v}{0.5 \cdot g \cdot v_O^2}$$

Where: p_2 – the fully recovered downstream pressure measured by pressure gauges, Pa; p_v – the vapor pressure of the medium, Pa; ϱ – the density of the medium, kg/m^3;v_o – the velocity of the medium, m/s.

Both the fully recovered downstream pressure and the vapor pressure were recorded using Keller PR-33X pressure gauges with a resolution of 0.0001 MPa. The flow rate was measured using an electromagnetic flowmeter.

The energy usage (E) was calculated based on the pump inverter readings. The inverter displayed the current [I] and voltage [V] values; by multiplying these values, the power (P)

was determined. The energy usage was then calculated using the following equation:

$$E = P \cdot t \text{ [kWh]}$$

Multi-criteria decision support

A multi-criteria analysis was conducted according to the authors' Multi-Criteria Determination of Recommended Variants (MCDRV) method, following the procedure described by Montusiewicz et. al. (2024). The criteria selected for the analysis were as follows: DOC/TOC ratio (1), the concentration of d-limonene (2) (increased as a result of waste degradation), the sCOD/COD ratio (3), and energy consumption (4). The first three criteria were maximized, whereas the last one was minimized. Despite the negative impact of d-limonene on AD, this criterion was maximized due to its correlation with the DOC/TOC ratio (R^2 = 0.8767). Its increase is associated with the decomposition of complex cellular structures and, consequently, the release of readily biodegradable compounds; therefore, the more effective the decomposition, the higher the d-limonene content. The variables considered in the four-dimensional criteria space included the HC inlet pressure and the number of times the stream passed through the cavitation zone, corresponding to the experimental time intervals. In the first step, the Pareto-optimal (non-dominated) variants were identified. Subsequently, of the weighted min-max analysis procedure was implemented based on the following assumptions: (1) all criteria were equally important and assigned identical weights, and (2) the criteria were assigned different weights according to their technological or economic importance.

Results and discussion

The effect of HC on physicochemical parameters

The results of the HC physicochemical analyses and energy usage for the specified experimental variants are shown in Table 2. Due to the variable composition of OW and wastewater during the experiment, the characteristics of the untreated samples varied between the pressure conditions. However, in all analyzed cases, the application of HC resulted in effective destruction of complex organic matter, as indicated by reductions in TOC, COD, and TS. More favorable results were obtained at a pressure of 3 bar. At this pressure, the TOC content decreased from 30.3 to 21.4%, with the highest removal observed after the longest treatment time of 45 min; however, significant reductions were also achieved after 20 and 30 min. A similar trend was observed for TS and VS. The removal efficiencies of TS and VS ranged from 15.9 to 24.9% and from 18.4 to 28.8%, respectively. As in the case of TOC, the greatest reductions were recorded after the longest cavitation time. At a pressure of 5 bar, a less pronounced effect on TOC was observed. In this case, the TOC reduction ranged from 15.3 to 26.8%. The most notable effect was observed for VS, for which the highest removal efficiency of 32% was achieved after the longest treatment time. With regard to TS, only a slight effect of cavitation was observed. Analysis of the effect of cavitation on the VS/TS ratio revealed only a minor decrease, which was comparable for both pressure conditions.

During HC, the decomposition of complex organic matter was accompanied by simultaneous solubilization. This effect was observed at both pressures of 3 and 5 bar; however, it was more pronounced at the lower pressure of 3 bar. With regard to DOC, an increase of more than 1.5-fold was observed after only 5 min of treatment. The greatest increase was achieved after 10 and 20 min. Thereafter, a slight decrease in DOC concentration was noted. Importantly, the application of the higher pressure of 5 bar did not result in a greater release of DOC. In this case, the DOC concentration increased by 22.2-36.2%, with the highest increase observed after 20 min of treatment. Beyond this time, a slight decrease in DOC concentration was observed, which might indicate that the rate of DOC oxidation exceeded its releasing. These findings suggest that, during shorter treatment times, the physical (thermo-mechanical) effects of cavitation predominate, whereas prolonged treatment favors chemical transformations due to the increasing formation of hydroxyl radicals over time. This effect depended on both the inlet pressure and treatment time and was more pronounced at higher pressures. A similar effect was observed for sCOD. At a pressure of 3 bar, increasing the treatment time enhanced the release of soluble organic compounds. The increase in sCOD ranged from 17 to 30.7%. Importantly, comparable values were recorded within the treatment time interval of 10-45 min. Extending the treatment time did not result in a significant increase in sCOD, probably due to the oxidation of the soluble organic fraction. At a pressure of 5 bar, the effect was less pronounced, and only a slight increase in the sCOD value was observed.

Changes were also observed in the biodegradability index expressed as the DOC/TOC ratio. As previously mentioned, more favorable results were obtained at the lower pressure of 3 bar. Under these conditions, the DOC/TOC ratio doubled after only 5 min of treatment, with the highest value recorded after 20 min. Beyond this treatment time, a slight decrease in the DOC/TOC ratio was observed. A less pronounced effect on the biodegradability index was found at the higher pressure of 5 bar. Under these conditions, the DOC/TOC ratio increased by 55.2-68.8%, with the highest increase observed after 20 min of treatment. A similar trend was observed for the sCOD/COD ratio. At a pressure of 3 bar, this ratio doubled after only 10 min of treatment. At the higher pressure, the same effect was observed after 20 min of treatment. The observed destruction of complex and recalcitrant compounds, together with the accompanying solubilization, is particularly important because microorganisms involved in the AD process metabolize readily biodegradable substances more rapidly. Consequently, HC pretreatment may shorten the retention time and increase methane production, thereby reducing treatment costs and enabling an energy surplus (Yeneneh et al. 2024). The degradation of lignocellulosic biomass during HC occurs as a result of physical and chemical transformations taking place within the hotspot formed after the collapse of microbubbles, leading to a sudden local increase in temperature and pressure (Bimestre et al. 2022).

HC involves the generation, growth, and implosion of cavities resulting from spatial pressure variations within the liquid. Physical and chemical transformations occur in the hotspot region following the collapse of microbubbles, leading to intense localized temperatures and pressures. The physical effects include the action of shock waves, microjet streaming, and elevated temperatures, whereas the chemical effects involve the generation of free radicals (Das et al.

Table 2: The HC results of physicochemical analyses of and energy usage for the specified experimental variants

t	TOC	DOC	DOC/TOC	limonene	TS	VS	VS/TS	phenols	COD	sCOD	sCOD/ COD	$N\text{-}NH^{+}_{4}$	VFA	Energy	T	Variant number
min	g/kg	mg/L	-	µg/mL	g/kg	g/kg	-	mg/L	mg/L	mg/L	-	mg/L	mg/L	kWh	°C	
3 bar																
0	381.4±19.1	573.9±28.7	0.00147	17.1±0.9	5.11±0.26	4.24±0.21	0.83	15.87±0.78	6623.2±87.7	2490.0±54.1	0.376	84.8±4.1	230±5.7		11.8	v1
5	299.7±15.0	906.5±39.4	0.00302	148.5±3.7	4.30±0.21	3.47±0.17	0.81	27.20±1.35	4444.0±74.1	2915.0±37.4	0.656	80.9±3.7	329±6.6	0.041	12.4	v2
10	291.0±14.6	965.3±41.1	0.00332	159.1±8.0	4.22±0.21	3.39±0.16	0.80	30.20±1.51	4282.0±97.1	3137.0±78.3	0.733	80.3±5.1	307±5.8	0.082	13.2	v3
20	273.4±13.7	937.0±44.1	0.00361	140.5±7.1	4.02±0.20	3.20±0.16	0.80	32.40±1.62	4183.0±41.1	3214.0±41.1	0.768	80.1±6.4	305±10.1	0.164	14.1	v4
30	273.5±13.1	916.6±45.8	0.00348	137.2±6.9	3.99±0.16	3.18±0.17	0.80	36.20±1.81	3895.0±104.1	3201.0±68.4	0.822	80.2±7.4	287±11.4	0.246	15.0	v5
45	265.7±13.3	891.5±43.1	0.00329	155.1±7.8	3.84±0.15	3.02±0.21	0.79	35.20±2.1	3815.0±107.1	3255.0±47.1	0.853	80.3±9.7	336±9.7	0.369	16.9	v6
5 bar																
0	344.4±17.1	579.8±29.0	0.00168	36.9±1.8	4.57±0.23	3.73±0.78	0.82	13.78±1.2	8700.0±124.0	2275.0±57.1	0.261	73.7±7.7	220±10.4	0.0	16.8	v7
5	291.6±14.6	712.8±35.6	0.00262	112.9±5.6	4.56±0.22	3.77±0.89	0.83	20.48±2.1	6080.0±147.1	2303.0±78.4	0.379	83.4±5.6	295±14.1	0.059	17.3	v8
10	283.5±	740.6±37.0	0.00261	93.9±4.7	4.52±0.36	3.68±0.90	0.82	22.08±2.2	5190.0±87.2	2300.0±85.4	0.443	84.1±4.7	273±13.1	0.118	18.0	v9
20	277.9±14.2	789.7±39.5	0.00284	80.0±4.0	4.52±0.98	3.66±0.88	0.81	22.80±3.1	4310.0±97.7	2298.0±125.4	0.533	82.4±5.9	306±14.1	0.236	19.3	v10
30	256.5±12.8	708.8±35.4	0.00281	67.5±3.4	4.43±0.47	3.56±0.95	0.80	23.50±1.7	4240.0±157.1	2346.0±94.6	0.553	75.1±8.7	280±9.7	0.354	20.6	v11
45	252.0±12.6	747.8±37.4	0.00281	78.4±3.9	3.92±0.47	3.10±0.57	0.79	23.03±2.7	3880.0±75.4	2309.0±73.1	0.595	78.6±8.4	286±9.8	0.531	22.1	v12

2021). However, several factors may affect the effectiveness of HC, including cavitation intensity, inlet pressure, substrate composition, treatment duration, and the design of the HC reactor. Generally, higher cavitation intensity and longer treatment duration are associated with greater treatment efficiency because more violent reactions and an increased number of passes through the cavitation zone(Sun et al. 2022).

In the present study, the most favorable results were obtained at the lower pressure of 3 bar and treatment times of up to 20 min. It was hypothesized that an excessive increase in the inlet pressure may lead to the onset of supercavitation or the formation of dense cavitation clouds. Under such conditions, interactions between bubbles may result in a cushioning effect, in which the collapse intensity of individual cavities is reduced, thereby diminishing the overall mechanical and chemical efficiency of the process (Brennen, 2014). This mechanism could explain the lower degree of solubilization observed at 5 bar compared to 3 bar, despite the higher energy input.

Another important aspect that should be investigated when evaluating a particular pre-treatment strategy is the fate of inhibitory compounds. In this study, the concentrations of d-limonene, phenols, ammonia nitrogen, and volatile fatty acids (VFA) were analyzed, as all of these compounds may potentially inhibit AD. With regard to d-limonene, the application of HC promoted its release, with the greatest increase observed at a pressure of 3 bar. Under these conditions, an almost 9-fold increase in the d-limonene concentration was achieved after only 5 min of treatment intervals, although at a lower rate. Beyond 20 min, a slight decrease in d-limonene concentration was observed. At a pressure of 5 bar, a less pronounced release occurred, with the highest concentration recorded after 5 min of treatment. During the subsequent treatment intervals, a slight decrease in d-limonene concentration occurred; however, the values remained higher than those of the raw sample.

A similar effect was observed for phenols. At both pressures, a release of this component was noticed, with the greatest increase observed for the lower pressure of 3 bar. Under these conditions, from 20 min onwards, the phenol concentration in the pre-treated mixture was more than double that of the untreated sample. At the higher pressure of 5 bar, the phenol concentration increased by 49-70.6%, with the highest values observed after 30 and 45 min of treatment. Another adverse effect of HC was the release of VFA. As previously, greater VFA release was observed at a lower pressure of 3 bar. The smallest increase (24.8%) was recorded after 30 min of treatment, whereas moderate increases of approximately 33% were observed after 10 and 20 min, respectively. At a pressure of 5 bar, the lowest VFA release was observed after 10 and 30 min, and the increase did not exceed 30%. HC is a well-established method for the extraction of various natural compounds, such as pectin, polyphenols, and terpenes (Meneguzzo et al. 2019). This effect is associated with enhanced diffusion and mass transfer, which facilitate efficient solvent penetration into cells. The performance of HC depends on several operational variables, including solution pH and temperature, inlet pressure, HC reactor type and its geometry, as well as the concentration of pollutants (Panda et al. 2020). In contrast, at a pressure of 3 bar, a slight decrease of TAN was initially observed, whereas extending the treatment time did not result in any further decrease in its concentration. A different trend was observed at the pressure of 5 bar, where TAN concentration was observed during the treatment period from 5 to 20 min, after which the concentration decreased. Nevertheless, TAN concentrations remained higher than those measured in the untreated sample.

Differences in the release of individual inhibitors resulted from the different operating parameters of HC. This finding also demonstrates that HC requires time-consuming optimization studies conducted individually for each substrate. Due to the complexity of the transformations occurring during cavitation, a thorough analysis of the potential formation of toxic by-products should be carried out, particularly when treating complex mixtures. In many cases, establishing the optimal operating conditions of HC presents a technological challenge, highlighting the need to modify the proposed technology. When volatile toxic compounds are generated, it may be necessary to remove them by stripping with an inert gas before introducing the pre-treated biomass as a substrate for AD. Such a procedure was also applied in the present study for the removal of d-limonene.

Physicochemical properties of the medium also changed as a result of HC (Fig. 2). The results show that, regardless of the applied pressure, HC causes an increase in both pH (Fig. 2a) and electrical conductivity (Fig. 2b). These changes indicate that ionic alkaline substances were released during HC. The increase in pH may be attributed to the disruption of cell walls, which releases compounds contained within the plant tissues. Mineral salts (e.g., potassium, calcium, and magnesium) are released into the solution, often in the form of citrates, which may exhibit slightly alkaline properties (Chegukrishnamurthi et al. 2025). Nitrogen-containing compounds, such as amino acids, amines, and small amounts of ammonia, may also be released. These compounds can generate OH^- ions in aqueous solution, thereby increasing the pH(Balasundaram and Harrison 2006). Additionally, some organic acids present in the orange peel, such as citric acid, may undergo decomposition or oxidation during HC, thereby reducing the acidity of the solution (Chegukrishnamurthi et al. 2025).

Interestingly, at a pressure of 5 bar, the treated samples exhibited lower pH values compared to those cavitated at 3 bar, while their electrical conductivity was higher. This may indicate the release of both alkaline and acidic compounds under these operating conditions (Arya et al. 2023). Another observation was that the zeta potential became increasingly negative with increasing cavitation time (Fig. 2c). This behavior may also be attributed to the release of alkaline substances during HC (Chegukrishnamurthi et al. 2025). In addition, HC disrupts the cellular structures of the orange peels, promoting the release of anionic compounds into the solution. The principal compounds released include pectins, organic acids (e.g., citric or malic acid), and other compounds containing carboxyl groups. In water, these functional groups can dissociate into $-COO^-$ forms, increasing the density of negatively charged groups on the surfaces of colloidal particles (Yapias et al. 2025). Furthermore, fragments of cell walls and polysaccharides form fine colloidal particles whose surfaces are rich in negatively charged functional groups. As a result, the negative surface charge density increases, causing the zeta potential to shift toward more negative values (John et al. 2022).

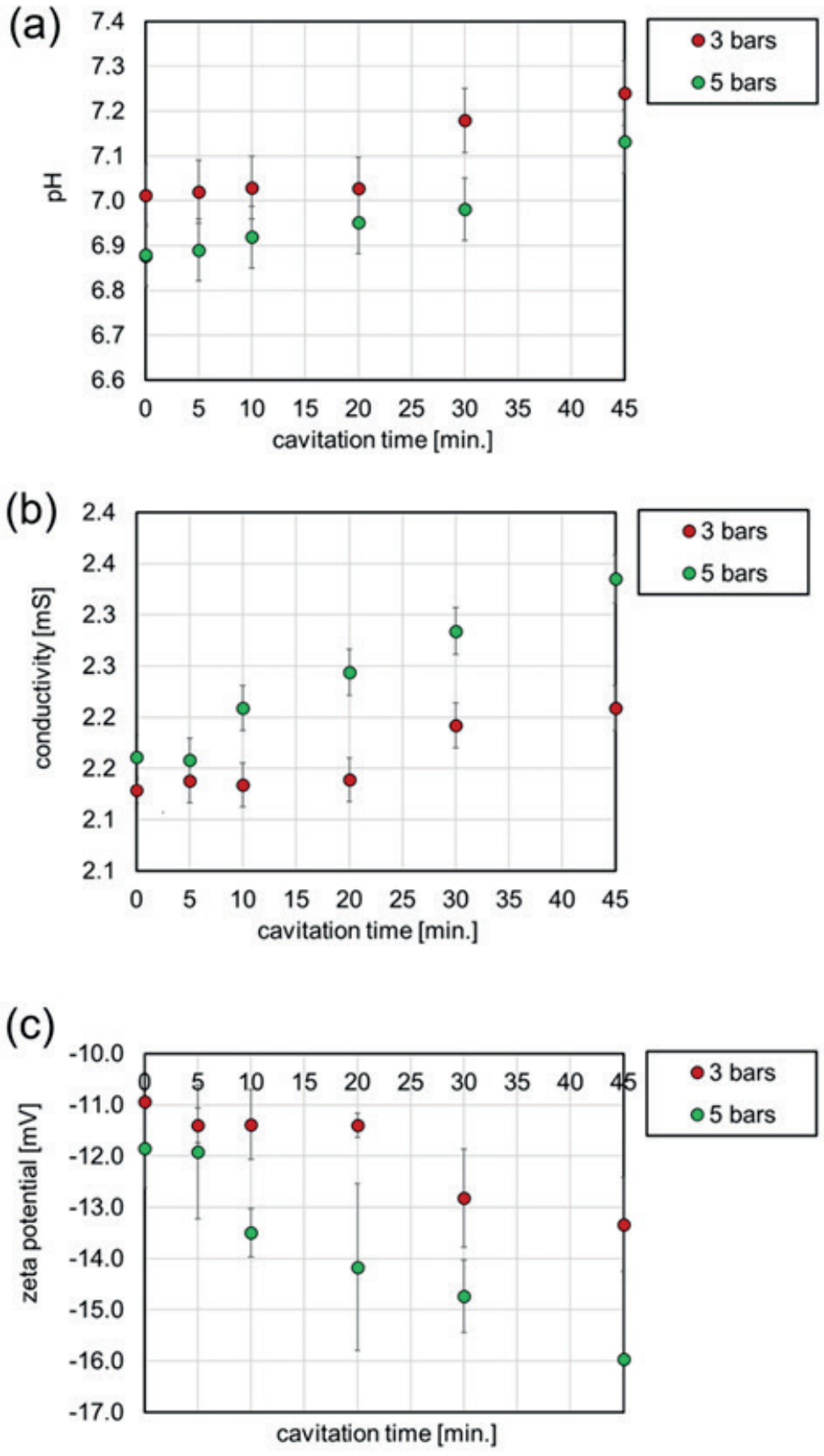


Fig 2. Influence of HC on physiochemical properties: (a) pH; (b) conductivity and (c) zeta potential of the studied samples.

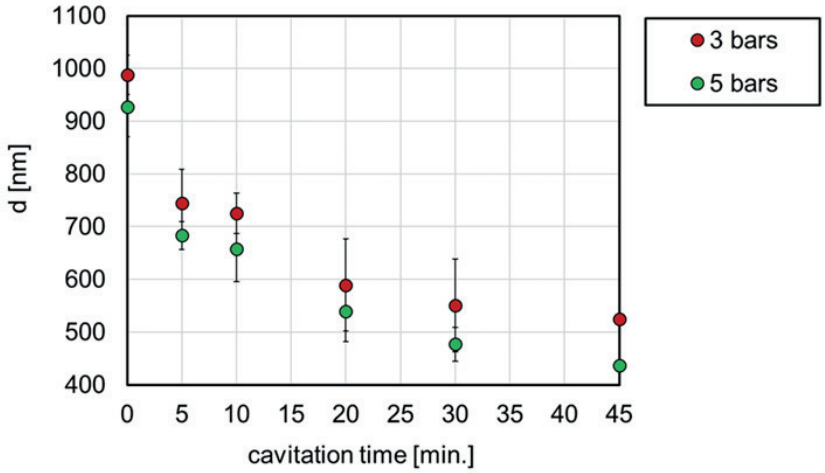


Fig 3. Influence of HC on the particle size of the studied samples.

Figure 3 shows the effect of HC on the particle size distribution of the studied samples. As can be seen from the results, extending the HC treatment time reduced the size of the particles present in the system, which is consistent with previous literature reports (Bałdyga et al. 2009). During HC, intense localized mechanical phenomena, including liquid microjets, shock waves, and high shear stresses, are generated within the system (Azadi and Nobes 2022). These forces disrupt particle aggregates and fragment larger particles into smaller ones. Furthermore, turbulence and intense mixing inhibit particle recombination, resulting in a decrease in the average particle size. A similar effect was observed at both applied pressures, although the higher pressure appeared to be slightly more effective in reducing the diameter of solid particles. The observed structural fragmentation was further confirmed by the changes in the DOC/TOC and sCOD/COD ratios, as well as by the FT-IR/ATR results.

Figure 4 shows the effect of HC on the surface tension of the studied samples. As the results indicate, increasing cavitation time promoted the release of surface-active compounds capable of reducing the surface tension. Consequently, the longer the treatment duration, the greater the concentration of these compounds in the system and the lower the surface tension.

Citrus peels contain essential oils (e.g., d-limonene), phospholipids, proteins, pectin fragments, and other polysaccharides. Many of these compounds are amphiphilic, meaning that they possess both hydrophilic and hydrophobic moieties (Braddock 1999). Consequently, they accumulate at the air-water interface, where they reduce the intermolecular forces between water molecules, thereby lowering the surface tension of the solution. Furthermore, cavitation causes particle fragmentation and better dispersion of the released compounds, increasing their availability at the surface and further enhancing the reduction in surface tension (Zhang et al. 2024). Regarding the effect of pressure, the results suggest that higher pressures are slightly more effective than lower pressures in promoting the release of these compounds .

FT-IR/ATR spectral analysis

The FTIR spectra of freeze-dried samples before and after HC are shown in Figures 5 and 6. The FT-IR spectra of the raw mixture (0 min, Figs. 5 and 6) exhibited characteristic absorption bands of a complex lignocellulosic and lipid-rich matrix. In the high-wavenumber region, a broad absorption at 3273 cm^{-1} is attributed to the hydrogen-bonded hydroxyl (O-H) groups in cellulose and lignin (Socrates 2004). Intense

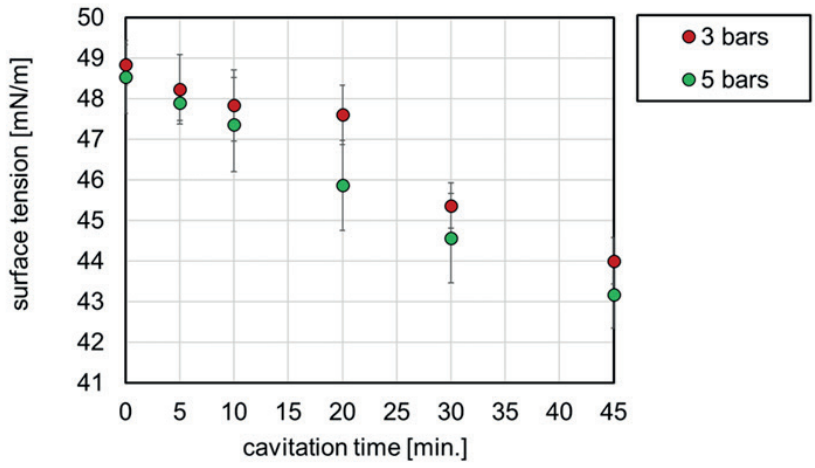


Fig 4. Influence of HC on the surface tension of the studied samples.

peaks at 2920 and 2852 cm^{-1} correspond to the asymmetric and symmetric stretching of aliphatic C-H groups, which are markers for both polysaccharides and terpenoid structures, specifically d-limonene. In the fingerprint region, the band at 1734 cm^{-1} is assigned to C=O stretching in the acetyl groups of hemicellulose or lignin carboxyls (Méndez-Durazno et al. 2025). Aromatic skeletal vibrations and C=C/C=O vibrations from lignin were identified at 1642, 1604, and 1521 cm^{-1}, while the band at 1547 cm^{-1} is associated with the amide II vibrations of proteins. Furthermore, the range of 1239-1010 cm^{-1} reflects C-O stretching and glycosidic linkages in cellulose and hemicellulose (Szaja et al., 2025). Specific peaks confirming the presence of inhibitors included the terminal methylene group of d-limonene at 892 cm^{-1} and phenolic compounds (O-H deformation and C-O stretching) at 1360 and 1239 cm^{-1} (Szaja et al. 2022).

Following 5 min of HC at 3 bar (Fig. 5), the spectra showed a decrease in the intensity of the peaks at 2920, 2852, and 1734 cm^{-1}. Concurrently, there was a significant decrease in the intensity of the lignin-associated bands (1642, 1604, 1547, and 1521 cm^{-1}) and the disappearance of bands at 1360, 1301, and 1276 cm^{-1}. The band at 892 cm^{-1} also decreased, indicating a major loss of d-limonene from the solid phase. Interestingly, a new peak emerged at 865 cm^{-1}, which may indicate the formation of oxidation intermediates, such as peroxy acids or organic peroxides (O−O stretching vibrations typically found in this region) (Socrates 2004). This emergence could be associated with advanced oxidation processes (AOPs) driven by the postulated generation of hydroxyl radicals (·OH) during the collapse of cavitation bubbles (Thanekar and Gogate 2018; Ozonek 2012) Beyond 10 min of HC treatment, the fingerprint region remained largely unchanged, suggesting that the maximum degree of structural matrix fragmentation was achieved in the early stages of the process.

The FT-IR spectra of the sample treated at 5 bar (Fig. 6) exhibited markedly different behavior from that observed at lower pressures, characterized by the relative structural stability of the insoluble matrix despite the high energy input. Unlike the 3 bar treatment, the characteristic bands in the 1239-1010 cm^{-1} range and the specific d-limonene marker at 892 cm^{-1} remained practically unchanged in both position and intensity throughout the 5-45 minute treatment period.

A significant phenomenon was observed in the carbonyl region, where the peak at 1734 cm^{-1} (ester linkages) exhibited less attenuation than at 3 bar and instead shifted and sharpened toward 1746 cm^{-1}. This shift is indicative of a change in the microenvironment of the C=O groups, likely reflecting a transition to a non-hydrogen-bonded state or a change in the coplanarity of these groups within the solid matrix without their physical cleavage from the lignocellulosic skeleton (Gregoriou and Braiman 2006). Furthermore, the aliphatic C-H stretching bands at 2920 and 2852 cm^{-1} showed a transient increase in

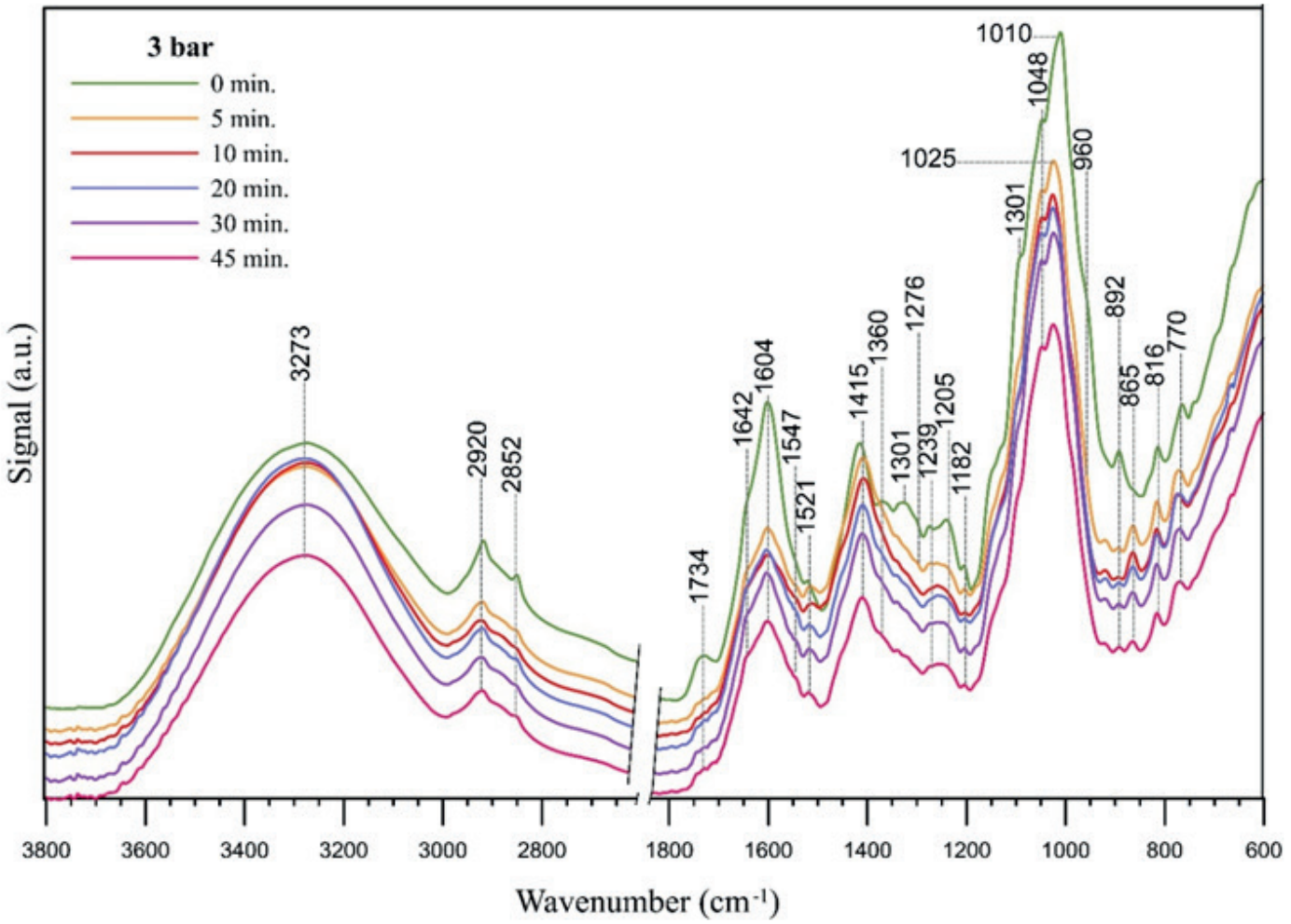


Fig 5. FT-IR/ATR spectra of the raw sample (0 min.) and sample cavitated at a pressure of 3.

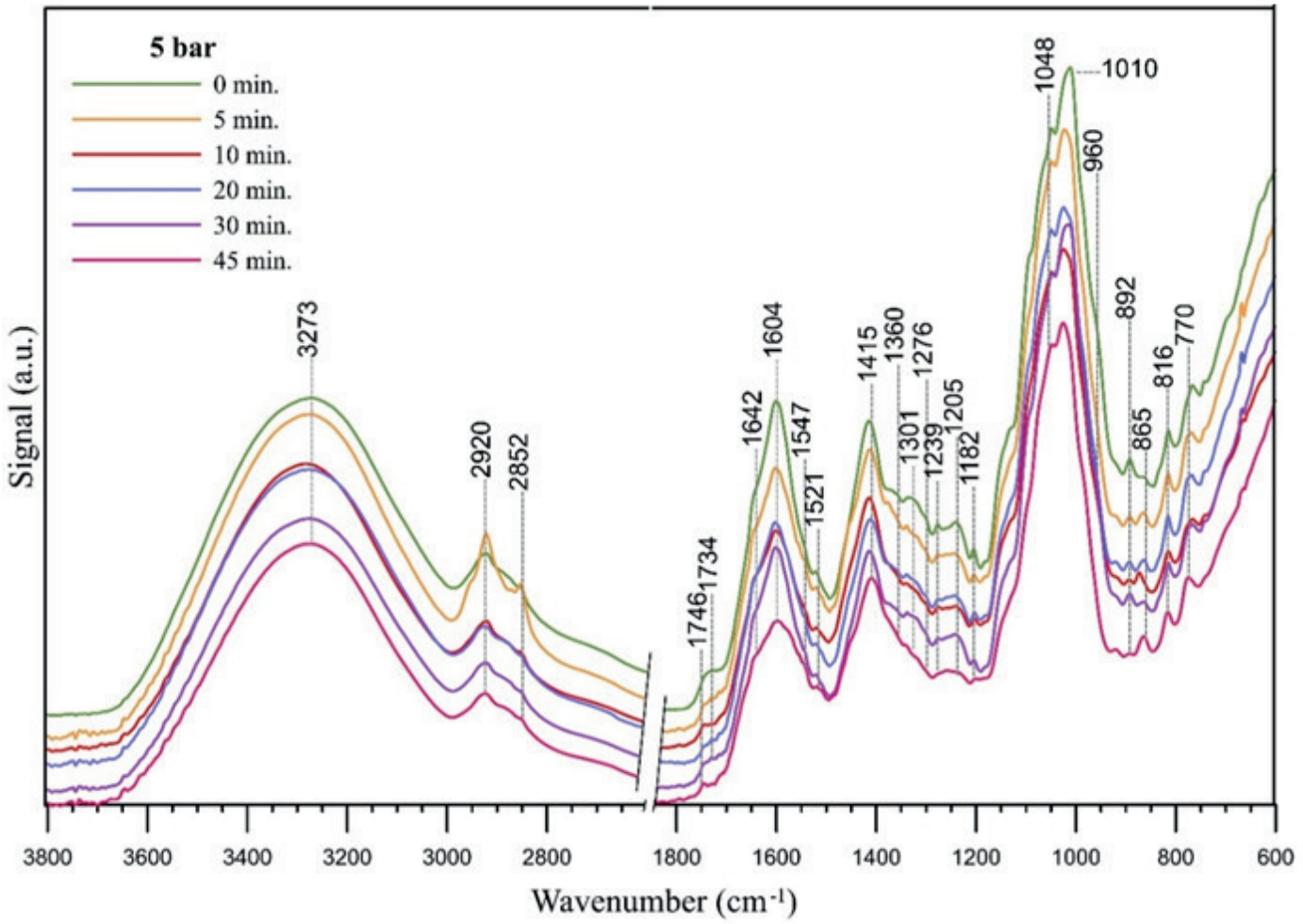


Fig 6. FT-IR/ATR spectra of the raw sample (0 min.) and sample cavitated at a pressure of 5 bar (5-45 min.).

intensity in the 5-minute sample before stabilizing. This apparent increase in the solid-phase spectrum suggests rapid surface erosion of the particles, which probably increases the specific surface area and exposes previously shielded aliphatic groups to the IR beam rather than reflecting a true increase in concentration. The most prominent spectral change over time was the growth of a band at ~865 cm^{-1}, which reached its maximum intensity at 45 min. Since this peak is attributed to O-O stretching vibrations in peroxides and intermediate oxidation products, its growth suggests a possible advanced chemical oxidation occurring on the matrix surface. Although radical species were not measured directly, the increase in this band, coupled with the observed decline in soluble d-limonene at 5 bar, is consistent with the oxidative mechanisms described in the cavitation literature (Ozonek 2012).

The analytical approach in this study targeted both the solid and liquid phases of the treated waste. FT-IR measurements were conducted on the freeze-dried matrix to evaluate its structural integrity, whereas physicochemical parameters were determined for the soluble fraction in order to quantify the release of organic matter and inhibitory compounds. Correlating these two phases reveals a highly efficient HC-driven solubilization mechanism. The sharp reduction in FT-IR peak intensities associated with d-limonene (2920, 2852, and 892 cm^{-1}) and phenolic compounds (1360 and 1239 cm^{-1}) in the solid matrix subjected to HC cavitation at a pressure of 3 bar (Fig. 5) directly corresponds to their rapid release into the liquid phase. Physicochemical data confirm this stripping effect: within the first 5 min of treatment at 3 bar, the soluble d-limonene concentration increased from 17.1 to 148.5 µg/ml, while the phenol concentration increased from 15.87 to 27.20 mg/L (Table 2). These results indicate that HC effectively disrupts the organic skeleton, liberating the inhibitors previously entrapped within the lignocellulosic structure. The efficiency of this redistribution is further supported by the increase in the sCOD/COD ratio from 0.376 to 0.656 in only 5 min, providing chemical evidence of the structural fragmentation (e.g., breakdown of ester and glycosidic linkages) observed in the FT-IR spectra. The concurrent increase in the DOC/TOC ratio further corroborates this interpretation.

The analytical approach adopted in this study targeted both the solid and liquid phases of the treated waste. FT-IR measurements were conducted on the freeze-dried matrix to evaluate its structural integrity, while physicochemical parameters were determined in the soluble fraction to quantify the release of organic matter and inhibitory compounds.

The relatively unchanged FT-IR fingerprint of the solid matrix at 5 bar, together with the physicochemical data, indicates a mechanism dominated by chemical oxidation (AOP) rather than physical solubilization. This is supported by the sCOD/COD ratio, which reached only 0.595 after 45 min at 5 bar, significantly lower than the value of 0.853

achieved at 3 bar (Table 2). This resistance to disintegration at higher pressure is likely attributable to the cushioning effect, whereby an excessive density of cavitation bubbles (super-cavitation) reduces the intensity of individual bubble collapses, thereby reducing the mechanical shear forces required for matrix fragmentation (Brennen, 2014). However, the 5 bar treatment showed a unique capacity for the extensive chemical degradation of inhibitors. Although the soluble d-limonene concentration increased sharply during the first 5 min (112.9 µg/ml), it subsequently declined to 78.4 µg/ml after 45 min. This decrease in the liquid phase coincided with the rising intensity of the 865 cm^{-1} (O-O bond) oxidation band in the FT-IR spectra. These observations suggest that the inhibitors released into the solution are further oxidized by hydroxyl radicals (·OH), leading to the formation of oxidation products that were subsequently re-deposited on the matrix.

Comparison of the two pressure regimes demonstrates that 3 bar is the optimal operating pressure for enhancing the biodegradability of OW. At 3 bar and short treatment times, HC acts as a liquefying pressure, maximizing solubilization, as reflected by the DOC/TOC and sCOD/COD ratios, and efficiently releasing inhibitors from the matrix within 10 min (Szaja et al. 2025). In contrast, treatment at 5 bar is dominated by oxidative process. Although this pressure promotes the secondary chemical degradation of inhibitors such as d-limonene, it is less effective for matrix disintegration due to the cushioning effect and potential super-cavitation that suppress the mechanical shear forces (Brennen 2014, Thanekar and Gogate 2018). Moreover, it requires substantially greater energy input (0.531 kWh vs. 0.369 kWh) while producing inferior solubilization. Overall, these findings indicate that HC treatment at 3 bar provides the best compromise between enhanced organic matter availability and reduced energy demand.

Multi-criteria decision support

HC generated a dataset, making it difficult to identify the most advantageous operating conditions because numerous performance indicators were obtained for different combinations of process variables. Selecting the HC parameters that maximize biodegradability while minimizing energy consumption therefore required a multi-criteria decision analysis (MCDA). The analysis was performed for the 12 experimental variants listed in Table 2. The Pareto-optimal set, consisting of 7 elements, included variants specified for a pressure of 3 bar, whereas the variants assigned to a higher pressure were excluded based on the multivariate dominance cone analysis. Assuming equal importance for all criteria (w= 0.25 for each criterion), variant 6 (pressure of 3 bar, HC time of 45 min) was identified as the optimal solution according to the min-max criterion.

In practice, however, the evaluation criteria do not have equal importance, and their weights should reflect their relative significance. Because criterion 1 DOC/TOC ratio and criterion 4 (energy consumption) were considered the most important, they were assigned higher weights than the remaining criteria. Four weighting scenarios were evaluated (w1, w2, w3, w4, the sum of the weights is always equal to 1): (1) 0.5, 0.1, 0.1 and 0.3; (2) 0.4, 0.1, 0.1 and 0.4; (3) 0.5, 0.1, 0.15 and 0.25, and (4) 0.5, 0.1, 0.2 and 0.2. Under all weighting scenarios, the first stage of the analysis identified variant 4 (3 bar, 20 min) as the optimal solution. Notably, this variant also achieved the highest DOC/TOC ratio. In the second stage, the optimal subset consisted of variants 5 and 3, corresponding ot==to HC treatment at 3 bar for 10 and 30 min, respectively.

Conclusions

The results of this study indicate that HC can be applied as an effective pre-treatment strategy to enhance the solubilization of organic matter in orange waste. Multi-criteria analysis showed that HC treatment at a pressure of 3 bar for 20 min can be considered as the optimal operating condition, providing the best balance between enhanced biodegradability and low energy consumption. This selection was further supported by the physicochemical characterization and FT-IR/ATR spectral analyses. Under these operating conditions, the DOC/TOC ratio increased by a factor of 2.45 compared to the untreated waste, while the corresponding energy consumption reached 0.164 kWh. In the second stage of the multi-criteria analysis, the optimal sub-set included HC treatment at 3 bar for 10 and 30 min, respectively, which produced only slightly lower DOC/TOC ratios than the optimal variant. Importantly, all operating conditions resulted in the release of both d-limonene and phenolic compounds, which may adversely affect the subsequent anaerobic digestion (AD) process. Therefore, further research in this area should be carried out.

Acknowledgements

This study was funded by the Ministry of Science and Higher Education of Poland under grant numbers FD-20/IS-6/036, FD-20/IS-6/023, FD-20/IS-6/020, and FD-20/IT-3/001).

References

Arya, S.S., More, P.R., Ladole, M.R., Pegu, K. & Pandit, A.B. (2023). Non-thermal, energy efficient hydrodynamic cavitation for food processing, process intensification and extraction of natural bioactives: A review, *Ultrasonics Sonochemistry*, 98, 106504. DOI:10.1016/j.ultsonch.2023.106504

Azadi, R. & Nobes, D.S. (2022). Hydrodynamic cavitation reduction in semidilute turbulent polymer solution flows, *Journal of Fluid Mechanics*, 952, A29. DOI:10.1017/jfm.2022.910

Bałdyga, J., Makowski, Ł., Orciuch, W., Sauter, C. & Schuchmann, H.P. (2009). Agglomerate dispersion in cavitating flows, *Chemical Engineering Research and Design*, 87, 4, pp. 474–484. DOI:10.1016/j.cherd.2008.12.015

Balasundaram, B. & Harrison, S.T.L. (2006). Disruption of brewers' yeast by hydrodynamic cavitation: Process variables and their influence on selective release, *Biotechnology and Bioengineering*, 94, pp. 303–311, DOI:10.1002/bit.20878

Bimestre, T.A., Júnior, J.A.M., Canettieri, E.V. et al. (2022). Hydrodynamic cavitation for lignocellulosic biomass pretreatment: A review of recent developments and future perspectives, *Bioresources and Bioprocessing*, 9, 7, pp. 1–16. DOI:10.1186/s40643-022-00499-2

Braddock, R.J. (1999). *Handbook of citrus by-products and processing technology*, John Wiley & Sons, New York 1999.

Brennen, C.E. (2014). *Cavitation and bubble dynamics*, Cambridge University Press, Cambridge (UK) 2014.

Chen, X., Zhang, X., Sun, C., Chen, Y., Xi, Z., Ma, G., Zhang, T., Zhang, Y., Zhou, X., Li, Y.-Y. & Kong, Z. (2024). New insights

into anaerobic digestion of lignocellulosic wastes towards carbon neutrality: A review of current advancement and future prospects, *Journal of Water Process Engineering*, 68, 106584. DOI:10.1016/j.jwpe.2024.106584

Chegukrishnamurthi, M., Nagarajan, S., Ravi, S. et al. (2025). Hydrodynamic cavitation mediated Spirulina valorisation with insights into phycocyanin extraction and biogas production, *Communications Biology*, 8, 326. DOI:10.1038/s42003-025-07702-y

Ciriminna, R., Scurria, A. & Pagliaro, M. (2023). Natural product extraction via hydrodynamic cavitation, *Sustainable Chemistry and Pharmacy*, 33, 101083. DOI: 10.1016/j.scp.2023.101083

Das, S., Bhat, A.P. & Gogate, P.R. (2021). Degradation of dyes using hydrodynamic cavitation: Process overview and cost estimation, *Journal of Water Process Engineering*, 42, 102126. DOI:10.1016/j.jwpe.2021.102126

Dauknys, R., Mažeikienė, A., & Paliulis, D. (2024). Evaluation of additive effect on anaerobic sewage sludge digestion. *Archives of Environmental Protection*, 50, 82–92. DOI 10.24425/aep.2024.152898

Galloni, M.G., Fabbrizio, V., Giannantonio, R., Falletta, E. & Bianchi, C.L. (2025). Applications and applicability of the cavitation technology, *Current Opinion in Chemical Engineering*, 48, 101129. DOI:10.1016/j.coche.2025.101129

Gregoriou, V.G. & Braiman, M.S. (Eds.) (2006). *Vibrational spectroscopy of biological and polymeric materials*, CRC Press, Boca Raton, FL 2006.

Hovorukha, V. (2024). The effect of fermentation modes on the efficiency of organic waste treatment in batch bioreactors, *Archives of Environmental Protection*, 50, 80–86. DOI:10.24425/aep.2024.149434

Kumar Prasad, R., Sharma, A., Mazumder, P.B. & Dhussa, A. (2024). A comprehensive pre-treatment strategy evaluation of ligno-hemicellulosic biomass to enhance biogas potential in the anaerobic digestion process, *RSC Sustainability*, 2, pp. 2444–2467. DOI:10.1039/D4SU00099D

Mankar, A.R., Pandey, A., Modak, A. & Pant, K.K. (2021). Pretreatment of lignocellulosic biomass: A review on recent advances, *Bioresource Technology*, 334, 125235. DOI:10.1016/j.biortech.2021.125235

Méndez-Durazno, C., Ramírez, V., Robles Carrillo, N.M., Flores Enríquez, M.F., Velalcázar Rhea, C.M. & Narváez, R.A. (2025). Comprehensive characterization of Ecuadorian lignocellulosic biomass in terms of their candidacy for bioenergy purposes, *Clean Energy*, 9, 3, pp. 128–145. DOI:10.1093/ce/zkaf008

Montusiewicz, J., Szaja, A., Montusiewicz, A. & Lebiocka, M. (2024). Multi-criteria decision support in the evaluation of hydrodynamic cavitation effects – a case study, *Advances in Science and Technology Research Journal*, 18, 8, pp. 341–350. DOI:10.12913/22998624/193789

Muhandiram, D.I. & Rudra, S. (2025). Coupled hydrodynamic cavitation–hydrothermal separation for biomass valorization: Simulation and experimental validation, and techno-economic assessment, *Bioresource Technology Reports*, 32, 102450. DOI:10.1016/j.biteb.2025.102450

Ozonek, J. (2012). Application of Hydrodynamic Cavitation in Environmental Engineering. Boca Raton: CRC Press, Taylor & Francis Group.

Panda, D., Saharan, V.K. & Manickam, S. (2020). Controlled hydrodynamic cavitation: A review of recent advances and perspectives for greener processing, *Processes*, 8, 2, 220. DOI:10.3390/pr8020220

Ponzelli, M., Koch, K., Drewes, J.E., Radjenovic, J. & Vinardell, S. (2024). The ambivalent role of graphene oxide in anaerobic digestion: A review, *Bioresource Technology*, 414, 131663. DOI:10.1016/j.biortech.2024.131663

Roy, S., Rudra, S., Muhandiram, D. & Roshid, M.M. (2025). Numerical modelling and experimental validation of an orifice plate-based hydrodynamic cavitation process for improving the biomass pretreatment, *Biotechnology Reports*, 48, e00925. DOI:10.1016/j.btre.2025.e00925

Song, P., Huang, Y., Li, J., Shan, S., Zhou, Z., Cao, H. & Zhao, C. (2024). The influence of processing technologies on the biological activity of carbohydrates in food, *Food Chemistry: X*, 23, 101590. DOI:10.1016/j.fochx.2024.101590

Szaja, A., Montusiewicz, A., Pasieczna-Patkowska, S. & Lebiocka, M. (2022). Technological and energetic aspects of multi-component co-digestion of the beverage industry wastes and municipal sewage sludge, *Energies*, 15, 15, 5395. DOI:10.3390/en15155395

Szaja, A., Montusiewicz, A., Cydzik-Kwiatkowska, A., Pasieczna-Patkowska, S. & Lebiocka, M. (2025). Enhancing methane production through co-digestion of sewage sludge, citrus waste and brewery spend grain with natural zeolite: Mechanisms and microbiome analysis, *GCB Bioenergy*, 17, 1, e70029. DOI:10.1111/gcbb.70029

Sun, X., Liu, S., Zhang, X., Wang, H., Chen, Y., Li, J. (2022). Recent advances in hydrodynamic cavitation-based pretreatments of lignocellulosic biomass for valorization, *Bioresource Technology*, 345, 126251. DOI:10.1016/j.biortech.2021.126251

Thanekar, P. & Gogate, P. (2018). Application of hydrodynamic cavitation reactors for treatment of wastewater containing organic pollutants: Intensification using hybrid approaches, *Fluids*, 3, 4, 98. DOI:10.3390/fluids3040098

Vasconcellos, M.S., Saavedra, Y.M.B. (2026). Systematic literature review of orange waste management from the environmental life cycle perspective, *Biomass and Bioenergy*, 213, 109353. DOI:10.1016/j.biombioe.2026.109353

Wang, Y., Nie, M.-Z., Shi, P., Liu, Y.-S., Lan, W.-B., Dai, Z.-R., Adeel, M. & Javed, H.U. (2026). From waste to wellness: Citrus by-products as nutritional and immunological enhancers in aquaculture, *Food Chemistry: X*, 33, 103523. DOI:10.1016/j.fochx.2026.103523

Yeneneh, A.M., Al Balushi, K., Jafary, T. & Al Marshudi, A.S. (2024). Hydrodynamic cavitation and advanced oxidation for enhanced degradation of persistent organic pollutants: A review, *Sustainability*, 16, 4601. DOI:10.3390/su16114601

Zhang, H., Fan, C., Wang, L., Lu, W. & Li, D. (2024). The generation methods and applications of cavitating jet by using bubble collapse energy, *Energies*, 17, 23, 5902. DOI:10.3390/en17235902

Kawitacja hydrodynamiczna jako metoda poprawiająca rozpuszczalność materii organicznej w odpadach pomarańczowych przed procesem fermentacji metanowej

Streszczenie: W niniejszym badaniu oceniono skuteczność zastosowania kawitacji hydrodynamicznej (KH) jako metody wstępnej obróbki odpadów z pomarańczy. W przeprowadzonych badaniach zastosowano dwa ciśnienia 3 i 5 barów oraz następujące czasy 5, 10, 20, 30 i 45 min. Jako induktor kawitacji zastosowano płytę kryzową z jednym stożkowym otworem koncentrycznym (3/10 mm). Spośród wszystkich analizowanych przypadków wyniki analizy wielokryterialnej wykazały, że najkorzystniejszym wariantem pod względem poprawy solubilizacji materii organicznej i zużycia energii jest ciśnienie 3 barów i czas kawitacji 20 minut, w tym przypadku stosunek rozpuszczonego do całkowitego węgla organicznego (RWO/WO) wzrósł 2.45-krotnie, dodatkowo uzyskano dwukrotny wzrost sChZT/ChZT (rozpuszczonego do całkowitego chemicznego zapotrzebowania tlenu) przy zużyciu energii 0,164 kWh. Jako kolejne korzystne warianty analiza wielokryterialna wykazała ciśnienie 3 bar i czasy kawitacji wynoszące odpowiednio 10 i 30 min. Co ważne, we wszystkich przypadkach zaobserwowano uwalnianie zarówno d-limonenu, jak i fenoli, co potencjalnie może hamować późniejszą fermentację metanową tych odpadów.

Archives of Environmental Protection
Vol. 52 no. 3 pp. 121–129

PL ISSN 2083-4772
DOI: 10.24425/aep.2026.3681



© 2026. The Author(s). This is an open-access article distributed under the terms of the Creative Commons Attribution-ShareAlike 4.0 International Public License (CC BY SA 4.0, https:// creativecommons.org/licenses/by-sa/4.0/legalcode), which permits use, distribution, and reproduction in any medium, provided that the article is properly cited.

Research on the properties of waste from streets cleaning

Anna Wassilkowska, Agnieszka Generowicz*, Anna Młyńska

Cracow University of Technology, Faculty of Environmental Engineering and Energy, Poland

*Corresponding author. E-mail: agnieszka.generowicz@pk.edu.pl

Keywords: elemental composition, electron microscopy, street sweepings, street cleaning, waste fraction

Abstract: Nowadays, environmental pollution is a common problem influenced by, among other factors, the increased accumulation of waste of different types and with different impacts on the environment. Streets sweeping, especially in urban areas, collects dust of various origins, compositions, and properties. Dust accumulation on streets and sidewalks may cause a significant deterioration of the natural environment, influencing not only water, soil and air, but also human life and health. In the literature, there are many studies describing the impact of street waste on the natural environment, e.g., on greenery and roadside trees, secondary emissions causing high human exposure, rainwater pollution, and consequently, surface water pollution. Street cleaning is one of the elements of urban area management within the broader concept of "smart city" management. The aim of this study was to investigate waste from the city streets (sweeping residues) using SEM-EDS microscopic examination. Waste was collected from the streets and sidewalks of a large city. Based on the results, it is possible to evaluate the quality of the urban space.

Introduction

Street sweepings, i.e., road-deposited sediments, are municipal waste systematically removed by sweeper vehicles in order to prevent them from reaching the aquatic environment and to reduce the harmful effects of dust on human health (Lloyd et al. 2018, Yang et al. 2016, Operacz et al. 2023). The primary European Waste Catalogue (EWC) code for street sweepings is 20 03 03 (street-cleaning residues). Sweeper vehicles belonging to the Municipal Cleaning Company (MPO) in Cracow, Poland, operate with a closed-circuit water spray system and are certified according to the EUnited PM10 standard. The study by Kryłów and Generowicz (2019) confirmed that the current technology of streets cleaning and washing contributes to the reduction of suspended dust in the air with a particle size below 10 μm. Dry matter, mineral and organic substances and heavy metals have been determined in street sweepings (Generowicz et al. 2023, Gronba-Chyła et al, 2025, Gronba-Chyła et al, 2021). In the literature (Bi et al. 2013, Adamiec et al. 2016, Fang et al. 2017), attention has been paid to the grain size classification of street dust. Particle size is an important parameter influencing the accumulation of heavy metals on roads (Hengren et al. 2006). Heavy metal concentrations in street dust increase significantly as particle size decreases (Li et al. 2010). The largest mass of pollutants was associated with particles in the size range of 100–250 μm (Lau and Stenstrom 2005). Samples are collected using a modified vacuum cleaner, and the dust passes through filters and sieves. In the study by Adamiec et al. (2016), it was found that individual particles are, on average, no larger than 65 μm; however, they actually form agglomerates with diameters of 1000–2000 μm. In the study by Gunawardana et al. (2014), X-ray diffraction analysis revealed that road dust consisted mainly of silicates and aluminosilicates, including quartz (SiO_2), constituting more than 70% of the volume, albite ($NaAlSi_3O_8$), microcline ($KAlSi_3O_8$), chlorite ($H_8Mg_6O_{18}Si_4$), and muscovite ($H_2KAl_3(SiO_4)_3$). The authors stated that the differences in the physical and chemical properties of particles in the size ranges <75 μm and 75–150 μm result from different proportions of minerals and organic matter, whereas for larger particles (150–300 μm and 300–425 μm), the adsorption properties of pollutants are similar due to significantly high quartz content.

The determination of the level of contamination of street sweepings with heavy metals such as Zn, Cd, Cu, Pb, Ni and Cr is important (Li et al. 2010, Isa et al. 2008), as some of these metals are considered toxic, while others, e.g., Fe, Ca, Ba and Mn, are mainly associated with the Earth's crust. Typically, metal concentrations are determined by atomic absorption spectrometry (Rashed 2008, Skorbiłowicz and Skorbiłowicz, 2019), although other methods, such as inductively coupled plasma-optical emission spectrometry, have also been used (Isa et al. 2008, Fang et al. 2017). Common pollutants in streets dust include Pb, Mn, and Fe (Rashed 2008). In the study by Lau and Stenstrom (2005), the metal content of street sweepings was determined. The particle-size fraction of of 125–250 μm was the richest in metals. Furthermore,

the authors stated that street-sweeping technologies available in the 1970s were not able to remove particles containing the highest metal loads. Generowicz et al. (2020) found that 60% of the road dust consisted of minerals of a terrestrial origin, of which 40–50 % was quartz, 10–20 % was clay, and the organic fraction accounted for 2% of the volume. Recently, scanning electron microscopy coupled with energy-dispersive X-ray spectroscopy (SEM-EDS) has been applied to the analysis of trace elements in atmospheric particles separated by size on glass fiber filters (Sevimoglu and Kuzu 2025, Kwaśnicki et al, 2024). Yang et al. (2016) also reported that, prior to microstructural analysis, street sweepings were divided into aerosolized and bulk dust fractions.

The aim of this study was to identify and describe the microscopic characteristics of street cleaning residues, with particular emphasis on developing an analytical approach that does not require prior separation of the entire sample into particle-size classes before SEM analysis. This objective is important because street cleaning residues are highly heterogeneous materials composed of particles of different origins, sizes, morphologies, and chemical compositions. Conventional size-fractionation procedures may be time-consuming and can potentially disturb the original structure of the collected material, thereby limiting the ability to assess the sample as it actually occurs in urban environments.

Therefore, this study focused on detecting and precisely documenting whether individual particle-size fractions exhibit significant differences in elemental composition, as well as identifying clear compositional trends based on the examination of a statistically large number of particles. Such an approach makes it possible to obtain a more representative and comprehensive characterization of street cleaning residues, including particles that may be of environmental or health significance because of their chemical composition or small size.

The justification for this research lies in the need to better understand the actual composition of material removed from urban streets by mechanical cleaning systems. By characterizing the microscopic and elemental properties of the collected residues, this study provides a basis for assessing the actual efficiency of street sweepers in capturing different types of particulate matter. The results may also support the optimization of street-cleaning strategies and contribute to a more accurate evaluation of their role in reducing urban dust pollution.

Research papers available in the literature present both potential technical solutions for street-cleaning systems and analyses of their environmental effects, ranging from technological descriptions of the equipment and its capabilities, through descriptions of complete cleaning and sweeping systems, to analyses of the changes occurring in the human environment as a result of streets cleaning. Many scientific publications characterize and analyze the composition of waste collected from streets (Järlskog et al. 2020, Lloyed et al. 2018, Kladnik et al. 2024, Gronba-Chyła, 2026, Kochanek et al. 2025).

Investigations conducted in Cracow have so far aimed to demonstrate the positive changes in environmental quality resulting from streets cleaning, including improvements in resident's quality of life and the aesthetics of the urban area. The results clearly demonstrate environmental improvements, including waste reduction, enhanced quality of urban infrastructure (sidewalks and streets), reduced amounts of pollutants transported by stormwater, and improved air quality throughout the studied city areas. Studies of streets-cleaning residues (Gronba-Chyła et al. 2022, Generowicz et al. 2020) indicate the presence of heavy metals. Their removal from urban areas and the identification of appropriate disposal options constitute a difficult and challenging interdisciplinary task. This article also aims to confirm previous research findings regarding the quality of street-cleaning residues and the environmental changes occurring in urban areas as a result of street cleaning.

Materials and methods

The material for this study consisted of street waste collected in March and April 2025 in the city of Cracow by the Municipal Cleaning Company (MPO) using sweeper vehicles on three streets (a total of four samples) (Table 1). The streets were first swept, after which samples of solid waste were collected from the sweepers (designated as *street sweepings* and *sidewalk sweepings*). The streets were subsequently washed, and samples of wastewater were collected from the sweepers (designated as *sweeper wastewater*).

Krasińskiego Street is located in the center of Cracow, whereas Stella-Sawickiego Street is situated in the eastern part of the city. Both streets serve as main thoroughfares. They consist of two carriageways, each with three traffic lanes separated by a green median strip, and are characterized by high-traffic volumes. Kujawska Street is located to the west of Cracow city center. It is a local street with moderate traffic, primarily serving as access to nearby buildings, and consists of a single carriageway and two lanes. The samples day from Krasińskiego Street were collected on 24 March 2025. The weather was cloudy, with no precipitation, and the maximum air temperature reached 14°C. The samples from Stella-Sawickiego Street and Kujawska Street were collected on 25 April 2025. On that day, the weather was cloudy with light rainfall, and the maximum air temperature reached 14°C.

Table 1: Collected and tested samples of the street waste.

No.	Sample	Street	Date of collection	Sample type/form
1	Kr24z	Krasińskiego	24 March 2025	Sweepings from street
2	Kr24s			Sewage from sweeper
3	SS	Stella-Sawickiego	25 April 2025	Sweepings from sidewalk
4	Ku	Kujawska		Sweepings from street

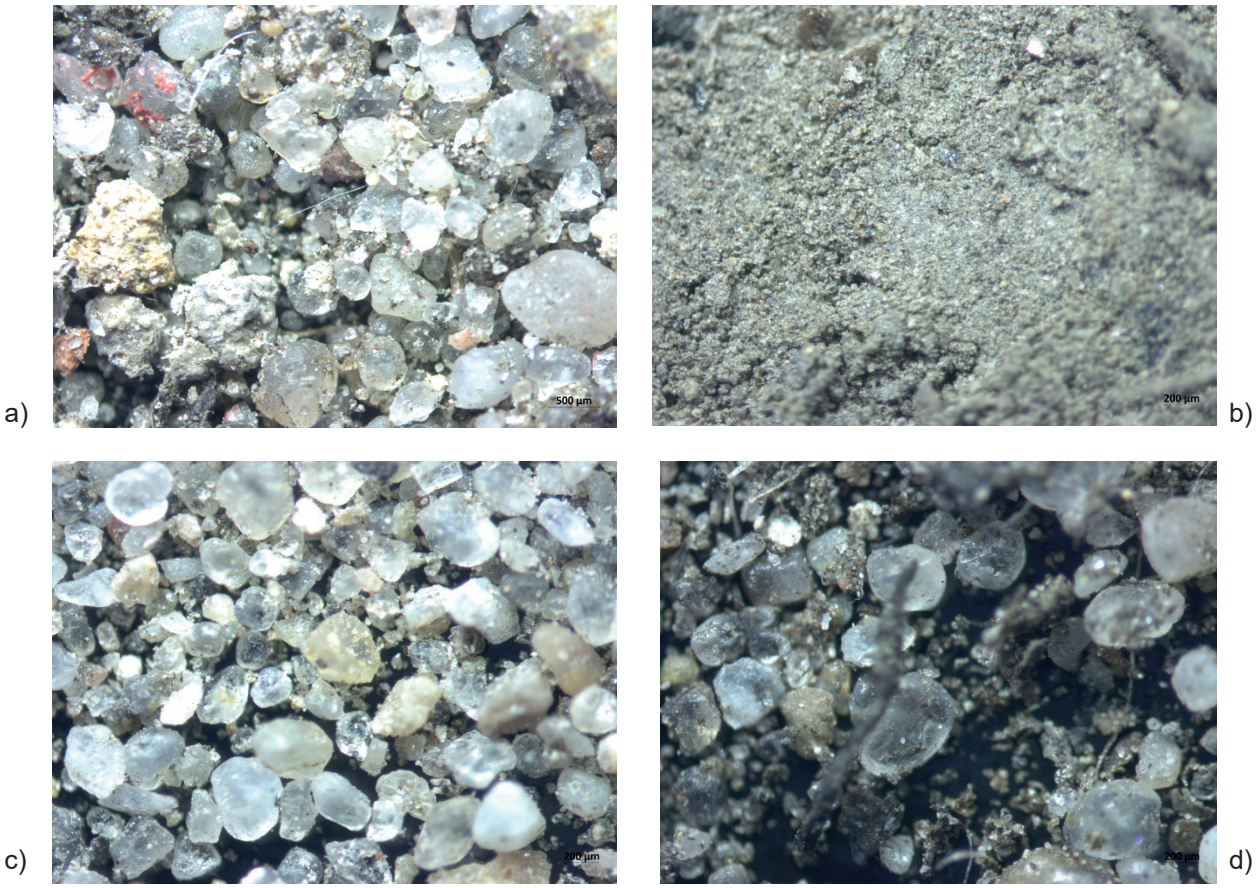


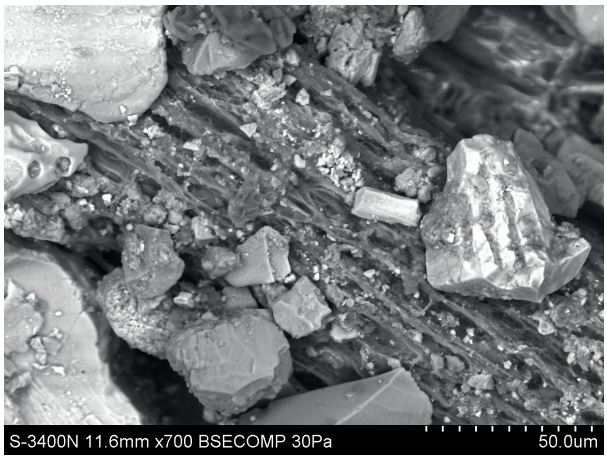
Fig 1. Optical microscope images of the granular microstructure of street sweepings residues in nominal magnification of x30: a) sample Kr24z – quartz, b) sample Kr24s – dust, c) sample SS – quartz and dust, d) sample Ku – quartz and soot.

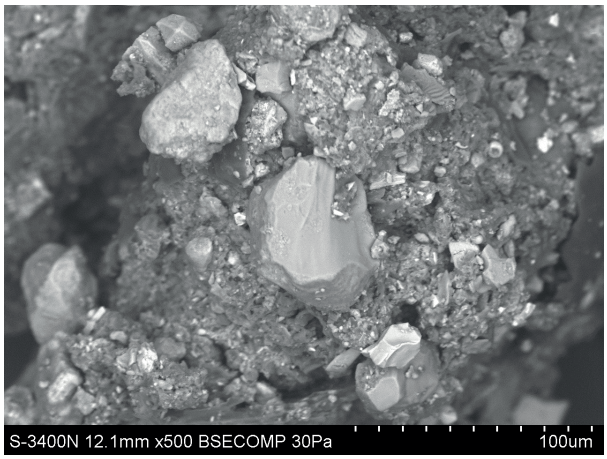
Small wet samples of the collected waste were placed in plastic bags and subsequently dried under ambient laboratory conditions. The dried waste particles were placed on stubs and then photographed and analyzed for their size, shape, and composition. Optical microscopy was used for the preliminary assessment of larger particles (Figure 1) using a Zeiss Stemi 508 stereoscopic microscope . SEM-EDS examination was performed using a Hitachi S-3400N scanning electron microscope at magnifications of x50, x100, x500, x700, x1000, x2000, and x5000. Microscopic images of waste particles were acquired under a vacuum of 25–30 Pa at an electron-beam accelerating voltage of 15 kV using a backscattered electron detector (BSE). Spectrometric analysis was performed on eighteen randomly selected individual particles with grain sizes above 10 µm, as well as on ten micro-areas measuring 20×20 µm^2 containing fine dust, using an EDS system from Thermo Scientific.

Several limitations of this study should be acknowledged. First, the research was based on a relatively small number of samples. The material was collected from three streets in Cracow, with a total of four samples obtained during two sampling campaigns conducted in March and April 2025. Although the selected streets represent different traffic conditions and urban settings, the limited number of sampling locations and collection dates restricts the generalizability of the results to the entire city or to other seasons. Street cleaning residues may vary considerably depending on traffic intensity, meteorological conditions, road surface characteristics, surrounding land use, and the time elapsed since the last street cleaning or rainfall event. Therefore, the results should be interpreted as an initial microscopic and elemental characterization of selected street cleaning residues rather than as a comprehensive and representative assessment of all urban street waste in Cracow.

Another limitation is related to the SEM-EDS analytical method. SEM-EDS is a valuable technique for identifying particle morphology and determining the elemental composition of individual particles or selected micro-areas. However, it provides primarily semi-quantitative elemental data and does not allow the direct identification of mineralogical phases or chemical compounds. The accuracy of EDS analysis may also be affected by particle geometry, surface roughness, sample heterogeneity, matrix effects, and the small analyzed area. Moreover, light elements may be detected with lower accuracy, whereas elements present at very low concentrations may remain below the detection limit of the method.

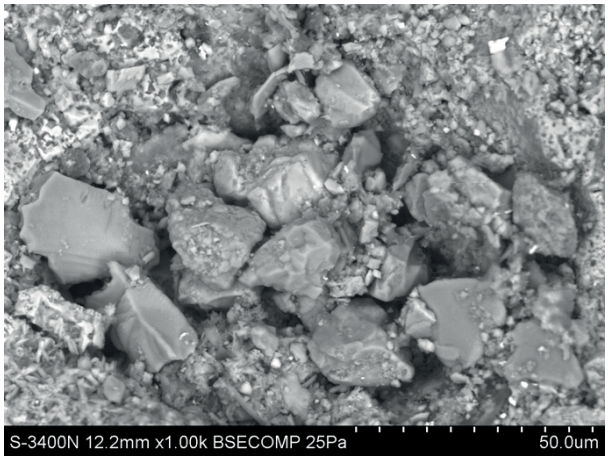
In this study, EDS measurements were performed on randomly selected particles larger than 10 µm and on selected micro-areas containing fine dust. As a result, the obtained data describe the composition of analyzed particles and micro-areas but may not fully represent the bulk chemical composition of the entire sample. The lack of prior separation of the whole material into particle-size classes allowed the residues to be analyzed in a form closer to their actual collected state;

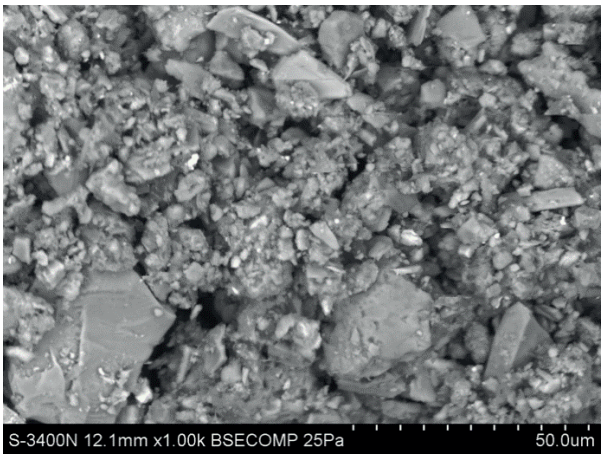
a) 



b)

Fig 2. BSE waste microstructure images: a) sample SS at nominal magnification of x700, b) sample Ku at nominal magnification of x500 indicating fine-grained irregular-shape particles into dust background.

a) 



b)

Fig 3. BSE waste microstructure images: a) sample Kr24z, b) sample Kr24s at nominal magnification of x1000 indicating clumped particles into loose dust.

however, it also limited the possibility of directly comparing the chemical composition of strictly defined particle-size fractions. Consequently, the findings should be regarded as indicative of compositional trends and particle-level variability rather than as a comprehensive quantitative geochemical characterization of street cleaning residues. The presented study is preliminary, and future research should include a larger number of samples collected different seasons and complement SEM-EDS with additional analytical techniques, such as XRD analysis, ICP-OES/ICP-MS, and sieve analysis.

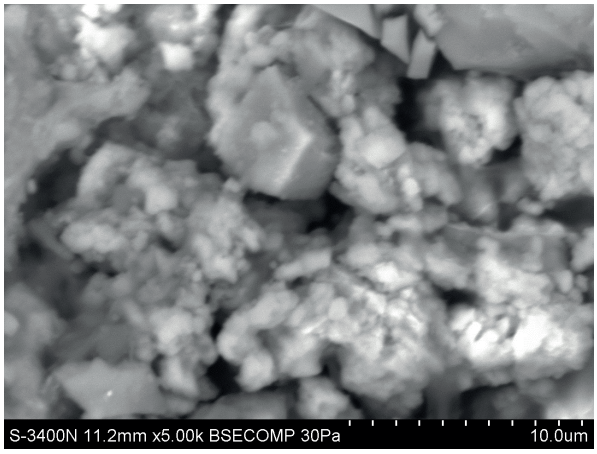
Results and discussion

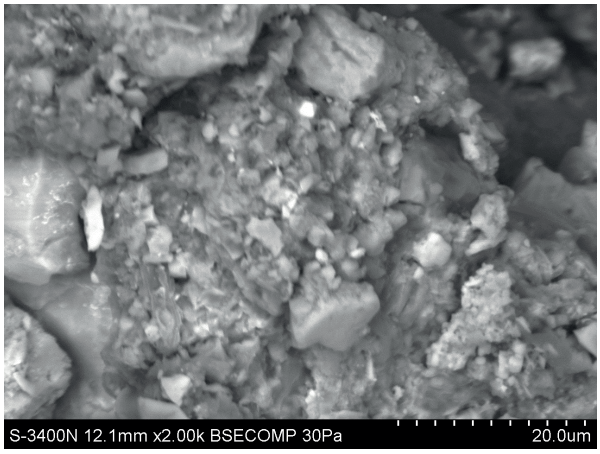
The research aimed to characterize the particle size and chemical composition of waste collected from urban streets and, subsequently, to indicate its potential negative impact on the environment and the associated consequences for human life and health. The results were presented accordingly.

Drying the waste samples under ambient laboratory conditions produced samples of good quality in terms of their final moisture content and granulation. Figures 1a and 1b clearly shows that the street-spraying technology enables the street sweeper to separate quartz particles and dust particles *in situ*, while the sweeper is collecting street sweepings.

Table 2: Grain-size estimation in sweepings samples using optical and electron microscopes.

No.	Sample	Coarse-grained fraction (mm)	Fine-grained fraction (mm)	Compact dust particles (μm)	Loose dust particles (μm)
1	Kr24z	0.8; 0.6; 0.3	< 0.2 (sand)	< 50	< 10
2	Kr24s	–	–	< 50	< 10
3	SS	1.0; 0.7; 0.4	< 0.2	< 50	< 10
4	Ku	< 0.8	< 0.2 (coal)	Inclusions in coal	< 10

a) 



b)

Fig 4. BSE waste microstructure images: a) sample SS at nominal magnification of x5000, b) sample Ku at nominal magnification of x2000 indicating particles of sizes below 5 μm.

The following characteristics of the collected samples were observed: the street sweepings sample Kr24z was composed mainly of quartz with different particle sizes (max. grain size of 0.8 mm), whereas sample Kr24s contained only the fine dust fraction (max. particle size of 50 μm). The particulate matter was classified into four particle-size fractions (Table 2) by measuring particles in BSE images acquired at seven different magnifications ranging from x50 to x5000.

Based on the examination of the microstructure of the street waste, BSE images of the sweepings were obtained at magnifications that allowed their visual classification into particle- size classes (Figures 2–4). The corresponding energy-dispersive X-ray (EDS) spectra (Figure 5) were then used to determine the elemental composition of selected micro-areas within the samples (Table 3–6).

According to Table 2, the coarse-grained fraction included all particles in the range of 0.2–1.0 mm. Particles with sizes ranging from 50 to 200 μm were classified as the fine-grained fraction (Figure 2). Compact dust consists of particles in the size range of 10–50 μm (Figure 3), whereas particles smaller than 10 μm were classified as loose dust (Figure 4). Morphologically, the dust particles are non-spherical. The ultrafine particles have dimensions of approximately 0.5 μm. Based on this visual classification of particle-size fractions, elemental composition analysis was then performed on randomly selected individual particles (Tables 3–5) or on micro-areas composed of dust (Table 6). Tables 3-6 present representative examples of EDS measurements (selected analyses for individual samples), whereas representative EDS spectra are shown in Figure 5. Based on simulations, it was assumed that the X-ray interaction depth for EDS is approximately 5 μm (Wassilkowska at al. 2014). Therefore particles smaller than 5 μm are too small for reliable point analysis and should instead be analyzed as part of aggregated dust micro-areas .

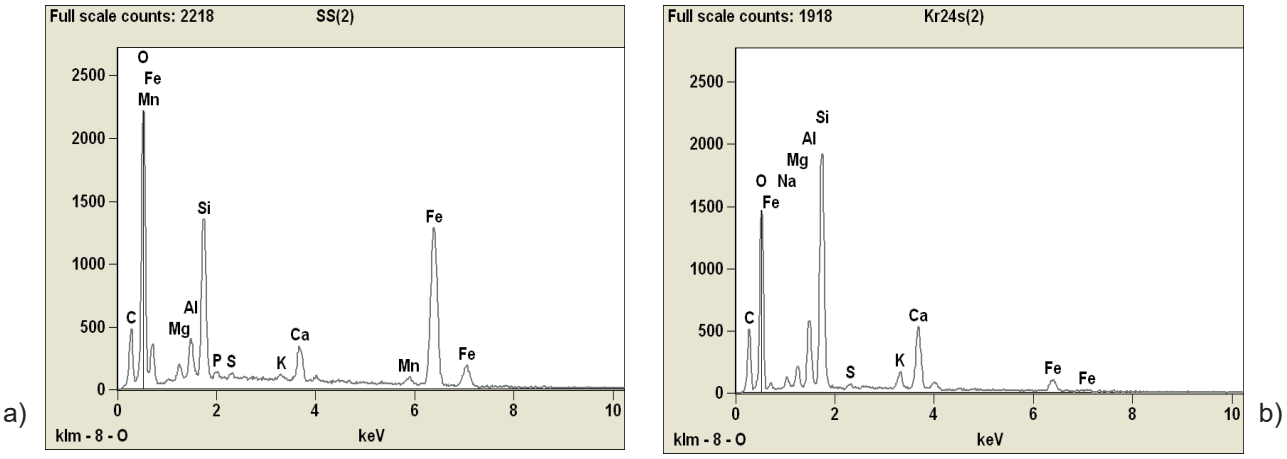
Regardless of the form of the analyzed samples, where sample Kr24z constituted of street sweepings and sample Kr24s consisted of wastewater from the sweeper, the dust fraction appeared similar in all cases. It contained fine agglomerates measuring 10–50 μm and particles smaller than 10 μm and was characterized by high porosity (Figure 3). In the study by Gunawardana et al. (2014), it was found that the fine particles smaller than 75 μm constitute an amorphous fraction composed of a small proportion of clay minerals, such as illite, kaolinite, and chlorite, although these minerals also

Table 3: EDS analysis of the elemental composition of the coarse grains (above 200 μm).

Test number in sample	Chemical element (weight %)												
	C	O	Na	Mg	Al	Si	P	S	K	Ca	Ti	Mn	Fe
Kr24z(3)	17.8	58.4	–	–	0.2	23.3	–	–	–	0.4	–	–	–
Kr24z(15)	9.5	62.2	–	–	0.6	26.6	–	–	–	1.2	–	–	–
SS(4)	–	65.3	–	–	–	34.7	–	–	–	–	–	–	–
Ku(6)	27.3	57.1	–	–	0.3	15.3	–	–	–	–	–	–	–

Table 4: EDS analysis of the elemental composition of selected particles with dark BSE contrast of sample Ku.

Test number in sample	**Chemical element (weight %)**												
	C	**O**	**Na**	**Mg**	**Al**	**Si**	**P**	**S**	**K**	**Ca**	**Ti**	**Mn**	**Fe**
Ku(7)	77.6	19.5	–	0.1	0.4	0.8	–	0.2	–	1.5	–	–	–
Ku(9)	86.8	12.7	–	0.0	0.1	0.3	–	0.0	–	0.2	–	–	–



a) b)

Fig 5. Examples of EDS spectra: a) from a random fine particle with bright BSE contrast, b) from the dust area of 20×20 μm^2.

occur i crystalline form. An important parameter governing the adsorption of pollutants by dust particles is their specific surface area, which, for particles smaller than 75 μm, is four times greater than that for particles larger than 300 μm.

The results of EDS measurements summarized in Tables 3–6 confirm distinct differences in the composition of the identified particle-size fractions. Based on the presence of the elements such as Si, Al, Ca, and O, it can be concluded that large particles with diameters of 0.2–1.0 mm represent a mineral fraction composed of quartz (Table 3). According to Gunawardana et al. (2014), quartz is the dominant component of street sweepings with particle sizes greater than 150 μm because of its low abrasiveness. Crystalline silica is a mineral that is present in sand, rocks and construction materials. Inhalation of airborne particles containing crystalline silica, particularly those with aerodynamic diameters in the PM10 and PM2.5 size ranges, may pose a significant risk to human health.

In sample Ku, consisting of street sweepings collected from Kujawska Street, soot particles with dust inclusions and diameters of 0.2 mm were identified. The sample was composed predominantly of carbon (Table 4). Carbon in street dust originates from both organic carbon and elemental carbon (soot), with its main sources including vehicle exhaust, tire wear particles, biomass burning, and industrial emissions. Soot is a significant component of street dust and is associated with various health hazards, such as respiratory irritation.

Fine particles with sizes ranging from 50 to 200 μm were analyzed in samples Kr24z and SS, in which this particle-size fraction was more abundant than in samples Kr24s and Ku. In addition to oxygen and carbon, these samples contained elements including Al, Ca, Fe, K, Mg, Mn, and Si, whereas sample SS also contained Ti (Table 5). As shown in Table 5, these elements occur mainly in the form of calcium, iron, and silicon oxides, with occasional occurrences of Mn, S and P.

Calcium is a naturally occurring element commonly found in building materials, such as cement. Calcium-containing compounds, such as $CaCO_3$, $CaSO_4$, and CaO, are common constituents of dust (Yang et al. 2016). Calcium phosphate in the form of hydroxyapatite ($Ca_5(PO_4)_3(OH)$) has been

Table 5: EDS analysis of the elemental composition of grains with size fraction 50–200 μm.

Test number in sample	Chemical element (weight %)												
	C	O	Na	Mg	Al	Si	P	S	K	Ca	Ti	Mn	Fe
Kr24z(1)	37.1	39.5	–	0.9	1.1	6.8	–	–	0.3	5.6	–	1.1	7.6
Kr24z(2)	33.3	49.5	–	0.3	0.6	2.2	–	–	–	13.2	–	–	0.8
Kr24z(4)	23.5	42.3	–	1.5	0.3	8.6	0.4	–	–	10.7	–	4.5	8.1
Kr24z(5)	32.1	35.8	–	0.4	2.2	8.4	–	0.2	0.5	12.2	–	0.7	7.5
Kr24z(6)	37.6	49.4	–	0.1	0.4	5.7	–	–	–	6.7	–	–	0.0
Kr24z(9)	35.8	47.9	–	0.3	1.1	2.6	–	0.1	0.2	11.4	–	–	0.7
Kr24z(14)	19.9	37.6	–	0.8	2.3	9.0	0.6	–	0.2	17.6	–	1.3	10.8
Kr24z(16)	36.3	48.4	–	2.7	0.7	2.2	–	–	0.1	8.9	–	–	0.7
SS(2)	32.1	31.0	–	0.4	1.0	3.9	0.2	0.1	0.2	1.7	–	1.0	28.5
SS(7)	35.9	38.9	–	1.2	0.9	2.8	–	0.1	0.2	3.6	4.0	–	12.4
SS(9)	23.9	44.5	–	0.0	0.9	1.9	–	–	0.1	0.3	7.5	–	21.1
SS(11)	25.0	35.7	–	0.3	0.8	3.3	–	–	–	0.7	–	–	34.3

Table 6: EDS analysis of the elemental composition of the dust fraction.

Test number in sample	Chemical element (weight %)												
	C	O	Na	Mg	Al	Si	P	S	K	Ca	Ti	Mn	Fe
Kr24z(10)	44.3	39.6	0.2	0.5	2.3	7.6	–	0.1	0.5	2.7	–	–	2.4
Kr24z(13)	35.6	43.5	0.1	0.5	2.5	10.3	–	0.2	1.0	3.6	–	–	2.8
Kr24s(1)	64.3	28.6	0.2	0.3	0.9	2.6	–	0.2	0.2	1.4	–	–	1.3
Kr24s(2)	43.6	37.7	0.5	0.7	2.1	7.2	–	0.2	0.9	4.3	–	–	2.9
Kr25s(4)	40.0	41.7	0.5	0.8	2.1	7.6	–	0.3	0.8	3.6	–	–	2.7
Kr25s(6)	41.0	40.7	0.5	1.0	2.7	7.3	–	0.3	0.8	3.5	–	–	2.4
SS(3)	50.4	37.1	0.2	0.2	0.8	6.3	0.1	0.1	0.4	3.0	–	–	1.4
SS(6)	64.7	31.1	0.1	0.2	0.4	2.3	0.1	0.1	0.2	0.6	–	–	0.5
Ku(2)	66.0	29.3	0.1	0.2	0.5	2.2	–	0.1	0.2	1.0	–	–	0.5
Ku(10)	46.8	35.3	0.9	0.4	2.8	8.4	–	0.3	0.3	3.0	–	–	1.9

identified in aerosolized dust samples with particle sizes of 30–90 nm and a spherical morphology (Yang et al. 2016). Iron is a common element present in the environment as a result of corrosion processes. Aluminum is one of the most abundant inorganic elements in the Earth's crust, along with calcium, magnesium, potassium, and sodium. However, in the study by Skorbiłowicz and Skorbiłowicz (2019), aluminum was not identified as an component of street sweepings.

Manganese is a component of fine dust particles (50–200 μm), which consist of a mixture of dirt, tire wear debris, and road surface material. Sulphur originates from vehicle exhaust emissions and the wear and tear of vehicle parts such as tires and brakes. Phosphorus is derived primarily from leaf litter and other organic pollutants. Potassium is a naturally occurring crustal element but may also originate from anthropogenic sources, such as construction activities or the decomposition of organic materials. Titanium dioxide is added to concrete and asphalt road surfaces as a photocatalyst to reduce air pollution (e.g., volatile organic compounds), when exposed to sunlight.

Based on the SEM examination, it was concludes that the dust fraction consists of irregular particles with dimensions smaller than 50 μm. Since the dust occurred in both agglomerated and loose forms, morphologically homogeneous areas measuring 20×20 μm^2 were selected for EDS analysis. These micro-areas contained clusters of particles smaller than 10 μm, including ultrafine particles with dimensions of approximately 0.5 μm. The EDS results are summarized in Table 6. Similar elemental compositions (expressed as averaged weight percentages were found in all analyzed samples. The average contents were approximately: Si – 6.2%, Ca – 2.7%, Fe – 1.9%, Al – 1.7%, Mg – 0.5%, K – 0.5%, Na – 0.3%, S – 0.2%, C – 49.7%, O – 36.5%, and P – 0.1% (detected only in sample SS). The conducted study indicates that Na was detected only in the dust fraction. Sodium-containing compounds are natural components of asphalt and engine oil. As these materials undergo mechanical wear, they break down into smaller particles that become mixed with street dust. By removing sodium-containing particles together with other pollutants, street sweepers prevent their transport into stormwater drainage systems and surface waters, thereby reducing environmental pollution.

Heavy metals associated with road traffic, such as those originating from tire wear, including Cu, Zn, Ni, and Pb, have often been detected in EDS studies (Gunawardana et al. 2014, Generowicz et al. 2020). In the present EDS analysis (Figure 5), however, these elements were missing in either the fine-grained fraction or the dust fraction (Table 5–6), which may be related to the detection limit of 0.1 weight % for multicomponent, porous materials.

Street sweepings pose a threat to the natural environment, including water, soil, and human health, when their mineral fraction is contaminated with harmful substances. Based on the present analysis of street sweepings collected from three streets in Cracow, it was found that the key components, including Fe, Mn and Ca, occurred predominantly in particles larger than 50 μm, whereas the dust fraction also exhibited relatively higher contents of S and Na.

Conclusions

Street sweepings collected from the city streets were classified into particle-size fractions using the magnification scale on the BSE images obtained by scanning electron microscope. Dust particles with sizes of approximately 50 μm exhibited irregular shapes and were embedded in a background matter composed of particles smaller than 10 μm. The dust fraction containing particles smaller than 10 μm consisted of Si, Al, Fe, Ca, Na, Mg, S, and K. EDS measurements of selected micro-areas showed that particles in the size range of 50–200 μm were characterized by higher contents of Si, Ca, and Fe and occasionally contained Mn, most likely in the form of oxides. The heavy metals identified in the analyzed samples included Fe and Mn, whereas the light metals included Al and Ti. The presented SEM-EDS analysis demonstrated that modern sweepers are capable of effectively removing dust fractions smaller than 10 μm from streets. These particles may act as carriers of heavy metals and organic pollutants.

Acknowledgements

The research was carried out through the co-operation between the Municipal Cleaning Company (MPO) in Cracow

and the Cracow University of Technology. The authors would like to express their sincere gratitude to President Andrzej Natkaniec and Director Jacek Sobczyk for making this research and associated analyses possible.

References

Adamiec, E., Jarosz-Krzemińska, E. & Wieszała, R. (2016). Heavy metals from non-exhaust vehicle emissions in urban and motorway road dusts, *Environ. Monit. Assess*, 188, 369, pp. 1-12. https://doi.org/10.1007/s10661-016-5377-1

Bi, X., Liang, S. & Li, X. (2013). A novel in situ method for sampling urban soil dust: Particle size distribution, trace metal concentrations, and stable lead isotopes, *Environmental Pollution*, 177, pp. 48-57. https://doi.org/10.1016/j.envpol.2013.01.045

Fang, F., Li, Y., Lin, Y. & Xu, M. (2017). Grain-size distribution and chemical speciation of heavy metals in Chinese street dust, *Pol. J. Environ. Stud*, 26(4), 1501-1509. https://doi.org/10.15244/pjoes/68884

Generowicz, A., Wassilkowska, A. & Kryłów, M. (2020). Qualitative composition of waste from street cleaning on the example of research carried out in Krakow. *Przemysł Chemiczny*, 99/9, pp. 1312-1314. https:/doi.org/10.15199/62.2020.9.8 (in Polish)

Generowicz, A., Gronba-Chyła, A., Kulczycka, J., Harazin, P., Gaska, K., Ciuła, J. & Ocłoń, P. (2023). Life Cycle Assessment for the environmental impact assessment of a city' cleaning system. The case of Cracow (Poland), *Journal of Cleaner Production*, 382, 135184. https://doi.org/10.1016/j.jclepro.2022.135184

Gronba-Chyła, A., (2026). Seasonal dynamics of particle size distribution, morphology and nanofractions in street sweeping residues, *Environmental Pollution*, 405,128469. https://doi.org/10.1016/j.envpol.2026.128469

Gronba-Chyła, A., Generowicz, A., Kramek, A., (2021). Using Selected Types of Waste to Produce New Light Ceramic Material, *Polish Journal of Environmental Studies*, 30(3), DOI: 10.15244/pjoes/126496

Gronba-Chyła, A., Generowicz, A., Kwaśnicki, P., Cycoń, D., Kwaśny, J., Grąz, K., Gaska, K. & Ciuła, J. (2022). Determining the Effectiveness of Street Cleaning with the Use of Decision Analysis and Research on the Reduction in Chloride in Waste, *Energies*, 15, 3538, https://doi.org/10.3390/en15103538

Gronba-Chyła, A., Generowicz, A., Kwaśnicki, P. & Kochanek, A. (2025). Recovery and Recycling of Selected Waste Fractions with a Grain Size Below 10 mm. *Sustainability*, *17*, 1612. https://doi.org/10.3390/su17041612

Gunawardana, C., Egodawatta, P. & Goonetilleke, A. (2014). Role of particle size and composition in metal adsorption by solids deposited on urban road surfaces, *Environmental Pollution*, 184, pp. 44-53. https://doi.org/10.1016/j.envpol.2013.08.010

Herngren, L., Goonetilleke, A. & Ayoko, G. (2006). Analysis of Heavy Metals in Road-Deposited Sediments, *Analytica Chimica Acta*, 571, 2, pp. 270-278. https://doi.org/10.1016/j.aca.2006.04.064

Isa, N., Darus, F.M., Arsih, W. & Laiman, R. (2008). Heavy metal concentration in street dust of Shah Alam City, Selangor, in*: Human Habitat and Environmental Change,* Jamaluddin, Md. J., Aiyub, K., Razman, M.R., Ariffin, K. & Awang, A. (Eds.). UKM Press, pp. 171–180. ISBN: 978-983-42514-1-3

Järlskog, I., Strömvall, A.M., Magnusson, K., Gustafsson, M., Polukarova, M., Galfi, H., Aronsson, M., & Andersson-Sköld, Y. (2020). Occurrence of tire and bitumen wear microplastics on urban streets and in sweepsand and washwater, *Science of the Total Environment*, 729, 138950. https://doi.org/10.1016/j.scitotenv.2020.138950

Kladnik, V., Dworak, S. & Schwarzb¨ock, T. (2024). Composition of public waste - a case study from Austria, *Waste Management*, 178, pp. 210-220. https://doi.org/10.1016/j.wasman.2024.02.031

Kochanek, A., Zaclona, T., Pietrucha, I., Petryk, A., Ziemianczyk, U., Basak, Z., Guzdek, P., Akbulut, L., Atilgan, A., Wozniak, A.D., Renewable Energy Integration in Sustainable Transport: A Review of Emerging Propulsion Technologies and Energy Transition Mechanisms, Energies 2025, 18(24), 6610; https://doi.org/10.3390/en18246610

Kryłów, M. & Generowicz, A. (2019). Impact of Street Sweeping and Washing on the PM10 and PM2.5 Concentrations in Cracow (Poland), *Middle Pomeranian Scientific Socjety of the Environment Protection, Rocznik Ochrona Środowiska*, 21, pp. 691-711. ISSN 1506-218X

Kwaśnicki P., Gronba-Chyła A., Generowicz A., Ciuła J., Makara A., Kowalski., Z., (2024). Characterization of the TCO Layer on a Glass Surface for PV IInd and IIIrd Generation Applications, Energies, 17, 3122. https://doi.org/10.3390/en17133122

Lau, S. L. & Stenstrom, M. K. (2005). Metals and PAHs adsorbed to street particles, *Water Research*, 39, pp. 4083–4092. doi:10.1016/j.watres.2005.08.002

Li, X., Li, Y., Zhifeng, Y. & Jianghong S. (2010). Seasonal difference and availability of heavy metals in street dust in Beijing, *Journal of Environmental Science and Health*, Part A, 45, 9, pp. 1092-1100. DOI: 10.1080/10934529.2010.486340

Lloyd, L.N., Fitch, G.M., Singh, T. S. & Smith, J.A. (2018). Characterization of residuals collected from street sweeping operations, Report No.: FHWA/VTRC 18-R20, Virginia Transportation Research Council, www.virginiadot.org/vtrc/main/online_reports/ pdf/18-r20.pdf

Operacz, A., Jóźwiakowski, K., Rodziewicz, J., Janczukowicz, W. & Bugajski, P. (2023). Impact of Climate Conditions on Pollutant Concentrations in the Effluent from a One-Stage Constructed Wetland: A Case Study. *Sustainability*, 15, 17, 13173. https://doi.org/10.3390/su151713173

Rashed, M.N. (2008). Total and Extractable Heavy Metals in Indoor, Outdoor and Street Dust from Aswan City, Egypt, *Clean*, 36, pp. 850-857. DOI: 10.1002/clen.200800062

Sevimoglu, O. & Kuzu, S.L. (2025). Characterization of trace elements in size-segregated atmospheric particles: Insights from SEM-EDS analysis, *Urban Climate*, 62, 102517. https://doi.org/10.1016/j.uclim.2025.102517

Skorbiłowicz, M. & Skorbiłowicz, E. (2019). Content of Calcium, Magnesium, Sodium and Potassium in the Street Dust from the Area of Białystok (Poland), *Journal of Ecological Engineering*, 20, 10, pp. 125–131. https://doi.org/10.12911/22998993/113145

Wassilkowska, A., Czaplicka, A., Zielina, M. & Bielski A. (2014). An analysis of the elemental composition of micro-samples using EDS technique, *Technical Transactions*, 1-Ch, pp. 133-148.

Yang, Yi, Vance, M., Tou, F., Tiwari, A., Liua, M. & Hochella, M.F. Jr. (2016). Nanoparticles in road dust from impervious urban surfaces: distribution, identification, and environmental implications, *Environmental Science: Nano*, 3, pp. 534-544. https://doi.org/10.1039/c6en00056h

Badania właściwości odpadów pochodzących z czyszczenia ulic

Streszczenie. Celem niniejszego badania było zbadanie odpadów z ulic miasta (pozostałości po zamiataniu) z wykorzystaniem mikroskopii SEM-EDS. Odpady zebrano z ulic i chodników dużego miasta. Na podstawie uzyskanych wyników możliwa jest ocena jakości przestrzeni miejskiej. Materiał badawczy stanowiły odpady uliczne zebrane w marcu i kwietniu 2025 roku na terenie miasta Krakowa przez Miejskie Przedsiębiorstwo Oczyszczania Miasta z wykorzystaniem zamiatarek na trzech ulicach. Do wstępnej oceny większych cząstek wykorzystano mikroskopię optyczną z wykorzystaniem stereoskopowego mikroskopu optycznego Stemi 508 firmy Zeiss. Badania SEM-EDS wykonano przy użyciu skaningowego mikroskopu elektronowego Hitachi S-3400N przy powiększeniach x50, x100, x500, x700, x1000, x2000 i x5000. Rozkład wielkości cząstek poszczególnych grup frakcyjnych zawartych w zmiotkach ma kluczowe znaczenie dla opracowania koncepcji oczyszczania dla różnych klas wielkości cząstek. Na podstawie aktualnej analizy zmiotek z trzech ulic w Krakowie stwierdzono, że kluczowe składniki, takie jak Fe, Mn i Ca, występują najczęściej w cząstkach o wielkości powyżej 50 µm, a pył charakteryzuje się również wyraźnymi pikami zawartości S i Na. Przedstawiona analiza SEM-EDS dowiodła, że nowoczesne zamiatarki samochodowe są w stanie skutecznie usuwać z ulic pyły o wielkości poniżej 10 µm.

Archives of Environmental Protection

Instructions for Authors

Archives of Environmental Protection is a quarterly published jointly by the Institute of Environmental Engineering of the Polish Academy of Sciences and the Committee of Environmental Engineering of the Polish Academy of Sciences. Thanks to the cooperation with outstanding scientists from all over the world we are able to provide our readers with carefully selected, most interesting and most valuable texts, presenting the latest state of research in the field of engineering and environmental protection.

Scope

The Journal principally accepts for publication original research papers covering such topics as:
– Air quality, air pollution prevention and treatment;
– Wastewater treatment and utilization;
– Waste management;
– Hydrology and water quality, water treatment;
– Soil protection and remediation;
– Transformations and transport of organic/inorganic pollutants in the environment;
– Measurement techniques used in environmental engineering and monitoring;
– Other topics directly related to environmental engineering and environment protection.

The Journal accepts also authoritative and critical reviews of the current state of knowledge in the topic directly relating to the environment protection.

If unsure whether the article is within the scope of the Journal, please send an abstract via e-mail to:
aep@ipispan.edu.pl

Preparation of the manuscript

The following are the requirements for manuscripts submitted for publication:

- The manuscript (with illustr ations, tables, abstract and references) should not exceed 20 pages. In case the manuscript exceeds the required number of pages, we suggest contacting the Editor.
- The manuscript should be written in good English.
- The manuscript ought to be submitted in doc or docx format in three files:

– text.doc – file containing the entire text, without title, keywords, authors names and affiliations, and without tables and figures;
– figures.doc – file containing illustrations with legends;
– tables.doc – file containing tables with legends;

- The text should be prepared in A4 format, 2.5 cm margins, 1.5 spaced, preferably using Time New Roman font, 12 point. The text should be divided into sections and subsections according to general rules of manuscript editing. The proposed place of tables and figures insertion should be marked in the text.
- Legends in the figures should be concise and legible, using a proper font size so as to maintain their legibility after decreasing the font size. Please avoid using descriptions in figures, these should be used in legends or in the text of the article. Figures should be placed without the box. Legends should be placed under the figure and also without box.
- Tables should always be divided into columns. When there are many results presented in the table it should also be divided into lines.
- References should be cited in the text of an article by providing the name and publication year in brackets, e.g. (Nowak 2019). When a cited paper has two authors, both surnames connected with the word “and” should be provided, e.g. (Nowak and Kowalski 2019). When a cited paper has more than two author, surname of its first author, abbreviation ‘et al.’ and publication year should be provided, e.g. (Kowalski et al. 2019). When there are more than two publications cited in one place they should be divided with a coma, e.g. (Kowalski et al. 2019, Nowak 2019, Nowak and Kowalski 2019). Internet sources should be cited like other texts - providing the name and publication year in brackets.
- The Authors should avoid extensive citations. The number of literature references must not exceed 30 including a maximum of 6 own papers. Only in review articles the number of literature references can exceed 30.
- References should be listed at the end of the article ordered alphabetically by surname of the first author. References should be made according to the following rules:

1. Journal:

Surnames and initials. (publication year). Title of the article, ***Journal Name,*** **volume, number, pages. DOI:.**

For example:

Nowak, S.W., Smith, A.J. & Taylor, K.T. (2019). Title of the article, *Archives of Environmental Protection*, 10, 2, pp. 93–98. DOI:10.24425/aep.2019.126330

If the article has been assigned DOI, it should be provided and linked with the website on which it is made available.

2. Book:

Surnames and initials. (publication year). *Title*, Publisher, Place and publishing year.

For example:

Kraszewski, J. & Kinecki, K. (2019). *Title of book*, Work & Sudies, Zabrze 2019.

3. Edited book:

Surnames and initials of text authors. (publishing year). Title of cited chapter, in: *Title of the book*, Surnames and initials of editor (s). (Ed.)/ (Eds.). Publisher, Place, pages.
For example:

Reynor, J. & Taylor, K.T. (2019). Title of chapter, in: *Title of the cited book*, Kaźmierski, I. & Jasiński, C. (Eds.). Work & Studies, Zabrze, pp. 145–189.

4. Internet sources:

Surnames and initials or the name of the institution which published the text. (publication year). Title, (website address (accessed on)).
For example:

Kowalski, M. (2018). Title, (http://www.krakow.pios.gov.pl/publikacje/2009/ (03.12.2018)).

5. Patents:

Orszulik, E. (2009). Palenisko fluidalne, Patent polski: nr PL20070383311 20070910 z 16 marca 2009.
Smith, I.M. (1988). U.S. Patent No. 123,445. Washington, D.C.: U.S. Patent and Trademark Office.

6. Materials published in language other than English:

Titles of cited materials should be translated into English. Information of the language the materials were published in should be provided at the end.
For example:

Nowak, S.W. & Taylor, K.T. (2019). Title of article, *Journal Name*, 10, 2, pp. 93–98, DOI: 10.24425/aep.2019.126330. (in Polish)

Not more than 30 references should be cited in the original research paper.

Submission of the manuscript

By submitting the manuscript Author (s) warrant (s) that the article has not been previously published and is not under consideration by another journal. Authors claim responsibility and liability for the submitted article.
The article is freely available and distributed under the terms of Creative Commons Attribution-ShareAlike 4.0 International Public License (CC BY SA 4.0, https: // creativecommons.org/licenses/by-sa/4.0/legalcode), which permits use, distribution and reproduction in any medium provided the article is properly cited, is not used for commercial purposes and no modification or adaptation are made.

© 2026. The Author(s). This is an open-access article distributed under the terms of the Creative Commons Attribution-ShareAlike 4.0 International Public License (CC BY SA 4.0, https:// creativecommons.org/licenses/by-sa/4.0/legalcode), which permits use, distribution, and reproduction in any medium, provided that the article is properly cited.

The manuscripts should be submitted on-line using the Editorial System available at https://wydawnictwo.pan.pl/index.php/aep. The journal does not have article processing charges (APCs) nor article submission charges.

Review Process

All the submitted articles are assessed by the Editorial Board. If positively assessed by at least two editors, Editor in Chief, along with department editors selects two independent reviewers from recognized authorities in the discipline. Review process usually lasts from 1 to 4 months.
After completion of the review process Authors are informed of the results and - if both reviews are positive - asked to correct the text according to reviewers' comments. Next, the revised work is verified by the editorial staff for factual and editorial content.

Acceptance of the manuscript

The manuscript is accepted for publication on grounds of the opinions of independent reviewers and approval of Editorial Board. Authors are informed about the decision and also asked to pay processing charges and to send completed declaration of the transfer of copyright to the editorial office.

Proofreading and Author Correction

All articles published in the *Archives of Environmental Protection* go through professional proofreading process. If there are too many language

errors that prevent understanding of the text, the article is sent back to Authors with a request to correct the indicated fragments or - in extreme cases – to re-translate the text.
After proofreading the manuscript is prepared for publishing. The final stage of the publishing process is Author correction. Authors receive a page proof copy of the article with a request to make final corrections.

Article publication charges

The publication fee in the Journal of an article up to 20 pages of a manuscript is **520 EUR/2500** zł
Payments in Polish zlotys
Bank BGK
Account no.: 20 1130 1091 0003 9111 7820 0001

Payments in Euros
Bank BGK
Account no.: 20 1130 1091 0003 9111 7820 0001
IBAN: PL 20 1130 1091 0003 9111 7820 0001
SWIFT: GOSKPLPW

Authors are kindly requested to inform the editorial office of making payment for the publication, as well as to send all necessary data for issuing an invoice.

PL ISSN 2083-4772